POLITECNICO DI MILANO

School of Industrial and Information Engineering

Master of Science in Energy Engineering
Energy Department

An innovative methodology to estimate the parameters of a lithium-ion battery physical model

Supervisor: Prof. Andrea CASALEGNO

Co-supervisor: Dr. Claudio RABISSI

Co-supervisor: Ing. Gabriele SORDI

Co-supervisor: Prof. Massimo SANTARELLI

Master Thesis by:

Alessandro INNOCENTI ID 900021

Academic Year 2018 - 2019

Alessandro Innocenti: *An innovative methodology to estimate the parameters of a lithium-ion battery physical model* | Master of Science Thesis in Energy Engineering, Politecnico di Milano.

Politecnico di Milano:
www.polimi.it/en/

School of Industrial and Information Engineering:
www.ingindinf.polimi.it/en/

Department of Energy:
www.energia.polimi.it/en/energy-department/

Extended abstract

Introduction

Global warming is a pressing challenge that our world has to face in the next years, and all the sectors of human economy are expected to gradually move towards a near zero-emissions operation [1]. The energy storage is a key component of the transition towards a decarbonized power generation and a cleaner transportation system [2]. Among the available energy storage technologies, lithium-ion batteries (LIB) have the highest share of stationary energy storage installations, owning 88% of 2016 new capacity and scoring a steady growth in the last five years [2]. They are also the leading technology in the electric vehicles (EV) field and consumer electronics, thanks to their advantageous properties compared to other kinds of storage systems: high energy and power density, long cycle life and low self-discharge rate [3]. Nevertheless, several challenges have to be faced in order to make LIBs a fully stable, performant and sustainable technology.

One of these issues is the final part of the LIB lifecycle: the growth of the EV market is leading to an increasing number of aged lithium-ion batteries that are retired after their end-of-life in electric cars [4], with potential problems for the currently low capability and cost-effectiveness of their recycling process [5]. Nevertheless, these LIBs still retain a useful capacity that can be exploited in less demanding applications. In order to recover these aged batteries and to assess their residual economic value, enabling a circular economy framework, a diagnostic procedure that measure the capacity and remaining useful lifetime is of foremost importance.

This work has the objective of defining a novel methodology for the estimation of the physical parameters of a lithium-ion battery, combining different experimental techniques and a mechanistic model. In a future work, these parameters could be related to the extent of degradation of the lithium-ion battery [6], obtaining detailed information about its state of health.

The activities that are carried out to achieve this objective are:

1. execution of an **experimental campaign** on commercial battery samples, to understand the information that are provided by three diagnostic techniques in different operative conditions (see Thesis Chapter 3);

2. realization of a **sensitivity analysis** of the LIB physical model with respect to the battery parameters, simulating a wide operative condition matrix of the three diagnostic tests. Using the results of the analysis, we formulated the **methodology** (see Thesis Chapter 4);

3. validation of the **methodology** with the implementation in a parameter estimation process using Particle Swarm Optimization (PSO), with the utilization of both simulated and experimental datasets (see Thesis Chapter 5).

1. State of the art

1.1 Lithium-ion battery description

A lithium-ion battery (LIB) is an energy storage system based on the electrochemical reactions of lithium ions, able to store and release electrical energy. It is a closed system, implying that reactants and products of the electrochemical reactions are stored inside the battery.

The lithium-ion battery operates at a certain voltage V depending on the constituent materials and on the thermodynamic conditions. During operation, a current I is applied, charging or discharging the battery. The amount of charge that the LIB can store or release is defined as its capacity Q, with a nominal value Q_{nom} that is measured by the manufacturer with standard test procedures [7]. The available capacity Q of the battery is usually expressed in a dimensionless form as the battery state of charge, or SOC, defined as the fraction of charge stored in the battery with respect to the nominal capacity. The operating current I is related to the nominal capacity through the current rate, or C-rate, C, defined as the ratio between I and Q_{nom}.

The simplest element of a LIB is the cell (figure 1), composed of two porous electrodes, i.e. the anode and the cathode, a liquid electrolyte and a separator. The oxidation reaction (lithium deintercalation) releases the lithium ions from the particles of one electrode, which flow through the electrolyte, and the reduction reaction (lithium intercalaction) inserts them into the particles of the other electrode. Instead, the electrons flow through the external circuit that connects the anode and cathode current collectors. The direction of the charges' flow depends on whether the battery is charged or discharged.

During these reactions, the concentration of lithium in the electrodes changes, and the battery voltage V changes too, according to the open circuit potential (OCP) characteristics of the electrodes. In fact, V is the difference between the OCPs of the two electrode. The cathode, with the higher potential, is commonly made of transition metal oxides or polyanion compounds, while the material of choice for the low-potential anode is graphite [8].

1.2 Battery degradation and diagnostics

During their operation, lithium-ion batteries are subject to degradation. The electrodes and the electrolyte properties continuously change since the battery beginning of life, due to unwanted side reactions that degrade in various ways these components [10], such as solid electrolyte interphase (SEI)

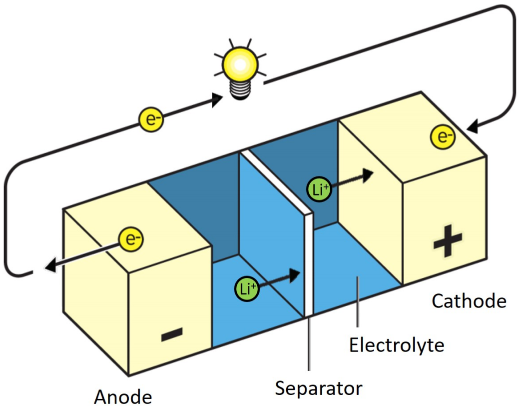

Figure 1. *Depiction of a lithium-ion cell during a discharge, with the indications of its main components (Adapted from [9])*

growth, electrolyte decomposition, particle cracking, graphite exfoliation, current collector corrosion and lithium deposition. These phenomena induce loss of cyclable lithium (a capacity fade) and an increase of the overall impedance of the battery (a power fade). In the EV industry, the standard threshold for the end-of-life of a LIB is when it retains only 80% of the initial capacity or of the initial power [11]. There is the possibility of employing these aged LIBs in a second life cycle in less intensive applications, such as stationary energy storage systems for renewable power plants or light-duty EVs [12], with benefits for the in terms of reduction of the environmental impact of used LIBs and lower investment costs for energy storage systems.

Nevertheless, this concept faces some challenges that needs to be solved for an economically viable and scalable implementation [13]. In particular, in this work we deal with the identification of the battery degradation, since a high uncertainty on the state of health can hinder the battery second use, and with the standardization of the diagnostic procedure, to decrease the costs of refurbishment and to achieve the full comparability of the diagnostic results.

The stressors of battery degradation are numerous [10], such as the ambient temperature, the storage SOC, the number of charge and discharge cycles, and the current rate. Very different degradation mechanisms can be due to the same stressors, and they can bring to the same degradation effects, i.e. capacity and power fade. The inherent complexity of degradation is commonly summarized in a parameter called state of health (SOH). This indicator has not a standardized definition: the simplest one refers to the ratio between the actual maximum dischargeable capacity Q_{max} measured with the same conditions of the nominal capacity, and the nominal capacity Q_{nom} [14].

The state of health determination stems from the execution of diagnostic tests, after which the SOH can be calculated or estimated with a variety of techniques. There are different types of diagnostic tests too [15], that can provide information on the LIB characteristics with varying degrees of accuracy and speed. In literature and in diagnostic standards, it is often used only one kind of test to characterize a LIB, usually the capacity test at different temperatures and current rates [16]. Nevertheless, it has also been shown how the use of more advanced techniques and the combination of them permit to understand much better the nature of a complex phenomenon such as degradation [15, 17]. In fact, the most correct and comprehensive approach to a complex problem like the one of battery degradation should be the one that combines these techniques to obtain the maximum amount of useful information in a reasonable time frame.

2. Methodology

2.1 Experimental techniques

The selected experimental techniques that are then applied on commercial battery samples are the capacity test, the relaxation test and the electrochemical impedance spectroscopy (EIS).

Capacity test The capacity test is commonly applied to measure the amount of charge that can be exchanged with the battery, by charging and/or discharging the LIB. With this test, it is possible to obtain the voltage-capacity relationship of the battery, which depends on the current rate and on the ambient temperature at which the test is made. For the sake of degradation diagnostics, this kind of test is useful to understand the remaining capacity of the LIB and estimate the impact of the increased overpotentials on the voltage-capacity curve. The chosen current rate determines the aspects that emerge more from the capacity test. The higher the current rate, the higher the influence of the kinetic parameters of the battery that induce overpotentials [18], i.e. the ohmic resistance, the charge transfer resistance and the lithium concentration disequilibria, with a decrease of the exchanged charge. For low current rates, the voltage losses are lower, hence allowing the battery to receive or release more energy, obtaining a more accurate evaluation of the actual battery capacity. In fact, Q_{nom} is commonly measured at a low C-rate, between 0.2C and 1C. To start the capacity test in the discharge mode, the battery is first charged up to 100% SOC with a constant current step and a constant voltage step, reaching the upper limit of the voltage range in which the battery operation is safe. Then, according to the desired current rate, a discharge current is applied on the battery, whose voltage decreases down to the lower voltage limit. The capacity is commonly calculated with the coulomb-counting method, integrating the applied current in time with a certain discretization according to the data acquisition timestep.

Relaxation test During a current pulse, lithium concentration gradients easily develop in the electrolyte and in the solid particles of the two electrodes, due to the low lithium diffusion coefficient in these media. The higher the current and the pulse duration, the steeper these concentration gradients.

When the current is set to zero, these gradient tend to reduce with a combination of diffusion processes and electrochemical reactions happening in the electrodes and the the electrolyte [19]. The relaxation of the gradients makes the battery voltage increase after the end of a discharge, and decrease after the end of a charge, in both cases with a trend that resembles a decaying exponential.

The trend of the voltage during this relaxation phase can give useful insights about the structure and the behavior of the lithium-ion battery, since it depends on the the geometry of the battery, the composition of the electrolyte, the physical structure and the chemistry of the electrodes. These information can be very useful for the degradation detection, but the study of the relaxation curve with this purpose is seldom seen in literature [20].

To perform this test, the battery is brought to the desired starting SOC and ambient temperature. Then, a current pulse is applied, whose current rate and depth of discharge (DOD), i.e. the percentage of exchanged charge with respect to the nominal one, define the duration of the pulse itself. When the circuit is opened, the voltage is measured until its rise or decrease is lower than the experimental uncertainty. In fact, concentration gradients need a sufficiently extended and intense current pulse to be developed, but their complete homogenization can require a very long time (up to 10^5 s) considering that the driving force of diffusion gradually decreases [21–23].

Electrochemical Impedance Spectroscopy The internal resistance of a lithium-ion battery is not an univocal concept. Its value and its physical meaning depend on the nature of the current pulse with which it is measured, i.e. direct current (DC) or alternate current (AC) [24]. By using AC, the current frequency ω determines the impedance Z, composed by a real part and by an imaginary part:

$$Z(\omega) = \frac{V(\omega)}{I(\omega)} = Z_0[cos(\phi(\omega)) + i\,sin(\phi(\omega))] \qquad (1)$$

where Z_0 is the module of the impedance, which represents the ratio between the amplitudes of voltage and current, while ϕ is the phase shift between the voltage and current sinusoids. In the electrochemical impedance spectroscopy (EIS), each frequency represents the characteristic time of a phenomenon taking place inside the battery, obtaining the resistance associated to each of them together [25–27]:

- **Inductive behavior** (ω >2000 Hz): in this region there is a purely imaginary contribution given by the wiring and cables inductance;
- **Ohmic behavior** (2000 Hz< ω <500 Hz): where the imaginary part changes sign and it is equal to zero, the real part is called high frequency resistance (HFR), and it is associated to the ohmic resistances of the battery;
- **Kinetic behavior** (500 Hz< ω <1 Hz): frequency range attributed to the kinetics of the interfacial reactions between the electrolyte and the electrodes, and to the double layer capacitance of the solid/liquid interfaces, called charge transfer resistance;
- **Diffusive behavior** (ω >1 Hz): at low frequencies, the concentration of lithium in the electrolyte and in the solid particles is perturbed, since we reach the diffusion characteristic timescales.

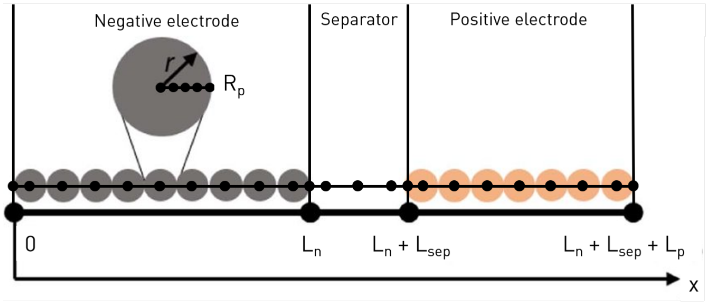

Figure 2. *Representation of the Fuller-Doyle-Newman P2D model domain*

The EIS is very useful for the detection of degradation since it can show the changes of the single components of the LIB resistance, and these changes can be then related to different degradation modes [17].

2.2 Model description

The model employed in this work is the Doyle-Fuller-Newman pseudo-two dimensional (P2D) electrochemical model [28, 29] (see Thesis Chapter 2.2).

The parts of the battery that are modeled are the negative electrode, the separator and the positive electrode (figure 2), with a mechanistic approach. Each of them has several nodes that form a 1D mesh, where the model's partial differential equations (PDE) are applied and solved. The model is labeled as pseudo-two dimensional since the points in which the PDEs are solved are placed along a linear dimension x, but in every point except for the separator, there is an additional radial dimension r which represents the solid particles of the electrodes. These particles are usually modeled as spheres, and the Fick's law of diffusion is solved in the additional nodes along their radial dimension.

The solved partial differential equations are the material balance in the electrolyte and in the electrodes, the Bulter-Volmer electrochemical kinetics, the charge conservation in the electrolyte and in the electrode, and the double layer charge or discharge.

This basic P2D formulation is isothermal and the model parameters do not depend on the temperature. To take into account the variation of ambient temperature and the heating of the battery during operation, the model has been extended in order to include the heat transfer, and hence the influence of temperature on the battery behavior. The thermal model geometry is a 2D representation of a cylindrical lithium-ion battery, like the ones that have been experimentally studied. The model coordinates are the along the radius and the axis of the cylinder, since the heat conduction in the angular direction can be neglected [30].

The heat conduction equation is solved numerically in each of the nodes of a 2D mesh, with a convective boundary condition on the battery surfaces, and the model provides the temperature distribution in the domain. However, the electrochemical model takes as input only a single temperature value for its whole domain, hence each timestep the 2D temperature distribution is averaged over the battery area and given as input to the electrochemical model. The only unknown quantity of the thermal model is the volumetric heat generation term, which is determined by the electrochemical model as sum of the ohmic, the reaction and the reversible heat generations [31]. The volumetric heat generation is calculated in each node of the 1D electrochemical model, but the 2D thermal model can only accept a single volumetric heat generation term. Therefore, on each timestep, it is averaged along the length of the electrochemical model domain and given as input to the thermal model. We also added an Arrhenius temperature dependence for the physical quantities that are influenced by this parameter, as the diffusion coefficients and the rate constants.

The whole model is implemented in COMSOL Multiphysics®, while the control of the simulations and the analysis of the outputs are done with MATLAB.

3. Experimental campaign

The test bench on which the experimental campaign is carried out was designed and assembled during the previous thesis work on the same project [32]. It allows the testing of LIBs in four independent channels, each equipped with a Chroma UM 63640-80-80 electronic load. A NI DAQ USB 6218 acquisition board is used to measure voltage oscillations during EIS's and to check the voltage read by the electronic loads, while the power supply NI RMX-4124 acts as battery charger. The batteries are placed in a Binder KT 53 climatic chamber, that controls the ambient temperature. The surface temperature of each LIB is measured through four RS PRO type K thermocouples, with a NI CDAQ 9211 as temperature acquisition board. In addition to this fixed setup, an Autolab PGSTAT30 with a FRA2 module is employed to perform high-precision EIS's. The whole setup is controlled through the software LabView®.

The measurement uncertainty is evaluated on the experimental outputs, i.e. the battery voltage, surface temperature and impedance (see Thesis Chapter 3.1.2).

The tested lithium-ion batteries are commercially available products, in accordance to the scope of the thesis project, directed towards the second use of commercial batteries. In particular, we employed a total of four batteries: a pristine and an aged Sony US26650VT, and a pristine and an aged Sony US18650V3, whose technical features are reported in table 1.

Characteristic	**US**26650**VT**	**US**18650**V**3
Cathode chemistry	NMC+LMO	NMC
Anode chemistry	Graphite	Graphite
Nominal capacity	2600 mAh	2250 mAh
Maximum charge current	2.6 A	2.25 A
Maximum discharge current	26 A	10 A
Nominal voltage	3.7 V	3.7 V
Maximum voltage	4.2 V	4.2 V
Minimum voltage	2.8 V	2.5 V
Temperature range (charge)	0 – 40° C	0 – 45° C
Temperature range (discharge)	−10 – 45° C	−20 – 60° C
Weight	85 g	44 g
Dimensions (D x H)	26 mm x 65 mm	18 mm x 65 mm

Table 1. Characteristics of the tested battery samples

3.1 Capacity test

The experimental matrix for the capacity tests is composed by:

- three values of ambient temperature: $T_{amb} \in \{10°C, 25°C, 40°C\}$;
- four values of current rate: $C \in \{0.5C, 1C, 2C, 3C\}$;

All the combinations of current rates and ambient temperatures are tested, with the purpose of exploring the impact of these two operative parameters on the results of this diagnostic procedure. As an example of these tests, in figure 3 it is shown the variation of the discharge curve of the new US26650VT at 25°C with the current rate.

The observations that can be made with the results of the capacity tests are (see Thesis Chapter 3.2.1):

- an increase of the **current rate** corresponds to a lower exchanged capacity, and in general this is true for all the tested batteries and for all the employed ambient temperatures. For instance, in figure 3 the pristine US26650VT passes from 2501 mAh at 0.5C to 2357 mAh at 3C.
  An higher current rate implies an increased extent of the electrochemical reaction, which consequently increases the activation overpotential, according to the Butler-Volmer kinetics [18]. Also, the ohmic losses are higher, being the current higher too. These losses are individuated as an increased initial voltage drop at the beginning of the discharge, with a vertical shift of the voltage-capacity curve. The lithium concentration gradients in the electrolyte and in the electrode are enhanced too, due to the higher molar flow rate of lithium transported in the cell. This overpotential can be visualized as a contraction towards lower capacities of the dischare curve;

- a decrease of the **ambient temperature** makes the exchanged charge decrease too. This effect is enhanced at higher current rates. For example, in the pristine US26650VT the capacity in a discharge curve at 0.5C passes from 2503 mAh at 40°C to 2377 mAh at 10°C, with a difference of 126 mAh. Instead, the capacity in a discharge curve at 3C changes from 2406 mAh at 40°C

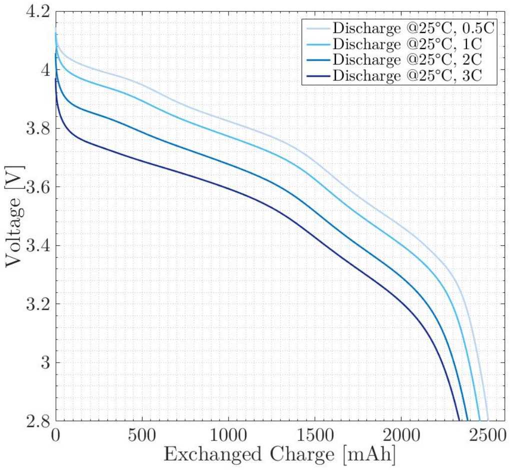

Figure 3. *Discharge curves of the pristine US26650VT, @25°C, voltage variation with current rate*

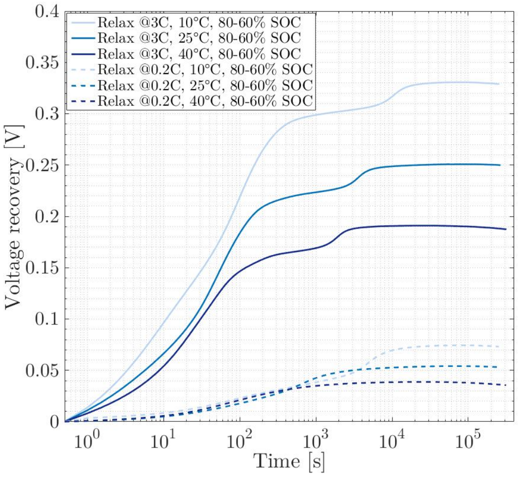

Figure 4. *Voltage recovery during relaxation for the pristine US18650V3, after a current pulse from 80% to 60% SOC, voltage variation with current rate and ambient temperature*

to 2146 mAh at 10°C, a delta of 260 mAh.
The lower operating temperature has the effect of slowing the kinetics of the electrochemical reactions, as well as lowering the ionic conductivity of the electrolyte [33], with an increase of the activation and ohmic overpotentials. The lithium diffusion is more sluggish at lower temperatures, bringing to the same phenomenon described in the previous bullet point. These effects have an higher impact on the capacity test if the current rate is higher too;

- as expected, the effect of **battery aging** implies a lower exchanged charge, due to the capacity fade. Comparing the capacity tests of the pristine and the aged US26650VT, we have 2503 mAh against 2381 mAh at 0.5C and 40°C, and 2146 mAh against 1989 mAh at 3C and 10°C. The latter test show how increased ohmic and activation losses are present in the aged battery, probably due to the additional resistance created by the SEI layer, by the lower ionic conductivity caused by the electrolyte degradation, and by the lower specific active area in the electrodes due to particle cracking and structural disordering [10, 34]. Nevertheless, it is not possible to be sure of this interpretation only with the capacity test, since the overpotentials are not effectively distinguishable with this technique.

3.2 Relaxation test

The relaxation voltage profile is measured after a current pulse that discharges the battery with a depth of discharge of 20%, starting from 100% SOC down to 20% SOC. After each pulse, the battery is allowed to relax for at least three days. The experimental matrix for the relaxation tests is composed of:

- three values of ambient temperature: $T_{amb} \in \{10°C, 25°C, 40°C\}$;
- two values of current rate in the pulse: $C \in \{0.2C, 3C\}$;

In figure 4 are reported the variation with current rate and ambient temperature of the voltage recovery of the pristine US18650V3, after a current pulse from 80% to 60% SOC. The voltage recovery is obtained by subtracting the voltage measurement of the first data point after the current is set to zero from the voltage profile during relaxation.
The main trends in the relaxation tests are (see Thesis Chapter 3.2.2):

- the extent of the voltage recovery depends on the **current rate** at which the previous discharge is performed. In the pristine US18650V3, the voltage recovery for the 3C pulse is 5 times higher than the 0.2C pulse for the discharge from 80% to 60% SOC, while it is 10 times higher in case of the discharge from 40% to 20% SOC. The higher concentration disequilibria caused by the high current corresponds to higher voltage losses during discharge, that have to be recovered during relaxation;
- the **ambient temperature** has an impact both on the magnitude and on the dynamic of the voltage recovery, because of its influence on the diffusion processes. For instance, the voltage recovery after a $3C$ pulse between 80% and 60% SOC passes from 25 mV in $5 \cdot 10^4$ s to to 33 mV in $8 \cdot 10^4$ s (figure 4). A lower temperature correspond to higher concentration gradients during the discharge pulse and to a slower voltage recovery, because of the decrease of the lithium diffusion coefficients in the electrolyte and in the electrodes.
- the effect of **battery aging** can be individuated since at same exchanged charge in the current pulse, the voltage reached at the end of the relaxation depends only on the battery open circuit voltage, and the degradation changes this thermodynamic characteristic [35]. In fact,

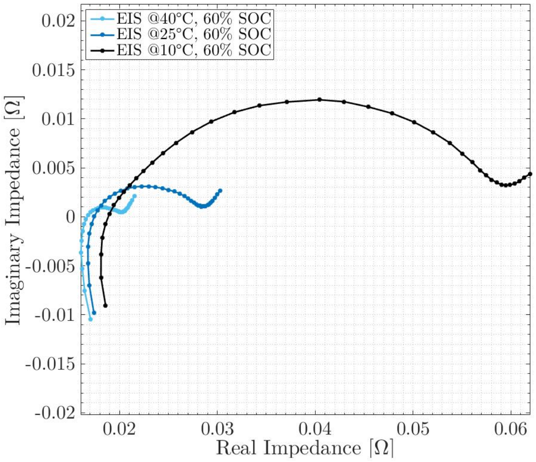

Figure 5. *Impedance spectra of the new US*26650*VT obtained with EIS at* 60% *SOC, ambient temperature variation*

the voltage recovery after a 3C pulse at 25°C between 60% and 40% SOC passed from 0.21 V in the pristine US18650V3 to 0.24 V in the aged one, coherent with a change in the graphite OCP [36].

3.3 Electrochemical impedance spectroscopy

The battery impedance spectra obtained with the EIS are measured at steady state, in the 10000-0.05 Hz range with 40 logarithmically spaced frequency points, and a 0.15 A amplitude of the current sinusoid. The experimental matrix is:

- three values of ambient temperature: $T_{amb} \in \{10°C, 25°C, 40°C\}$;
- four values of state of charge: $SOC \in \{100\%, 80\%, 60\%, 40\%, 20\%\}$;

Figure 5 shows three impedance spectra obtained at different ambient temperatures with the pristine US26650VT at 60% SOC. The obtained impedance spectra suggest that (see Thesis Chapter 3.2.3):

- the variation of the battery impedance with the **state of charge** is quite complex. At 100% SOC, the impedance shows a relevant diffusion-related impedance at low frequency, whose extent can be explained with limitations in the lithium diffusion due to phase transformations [37, 38] and to the high slope of the open circuit potential [25]. Instead, at 20% SOC, an additional charge transfer impedance appears at low frequencies, probably caused by the shift from the metallic to semimetallic behavior of the cathode material when near the fully lithiated state [27, 37], with a more limited kinetics;
- the impedance spectra show evidently the effects of **battery aging**. The aged US26650VT shows an HFR equal to 19 mΩ, while the HFR of the pristine one is 17.5 mΩ. The high frequency resistance increase with aging is mainly due to the formation of the SEI, which adds a resistive layer around the anode particles. Moreover, at 20% SOC, the aged battery has a semicircle in the low frequency region which is about 7 times larger than the same semicircle of the pristine battery;
- for what concerns the **ambient temperature** variation, we see in figure 5 how a lower temperature makes the overall impedance grow. The high frequency resistance increases from 16.7 mΩ at 40°C to 18.5 mΩ at 10°C, since there is also a decrease of the ionic conductivity of the electrolyte with the temperature [33]. Also, the charge transfer resistance has a strong growth when temperature decreases, about 4 times every 15°C, due to Arrhenius-type dependence with temperature of the reactions' kinetics;

4. Sensitivity analysis

We saw how the three experimental techniques they can provide insights on all the defining phenomena of the lithium-ion battery. Also, aged batteries can be distinguished from pristine ones in each of these techniques. Their combination can be used to obtain complete overview on the battery dynamic performances, and as far as the author's knowledge this concept has not been explored in literature.

To optimize the number and the types of tests that are needed for the battery characterization, it is important to understand the conditions in which these techniques can give the higher amount of information on the battery. Therefore, we carry out a **sensitivity analysis** on the lithium-ion battery model, in order to understand the effect of the variations of the model parameters on the simulations of the diagnostic tests' outputs, and to recognize the experimental tests that can better identify a parameter by assessing its effect on the test outputs.

4.1 Sensitivity analysis methodology

The chosen sensitivity analysis methodology is the one-factor-at-time (OFAT) [39], where the model parameters are set to nominal values, and they are varied one at a time while keeping the others fixed. With this type of analysis, it is easier to understand the underlying physical processes that are influenced by the model parameters. Also, its has a lower computational burden with respect to other techniques.

The 28 parameters on which the sensitivity analysis is performed are the ones related to the dynamic performances of the battery. The parameters linked to its thermodynamic behavior and to its geometry, i.e. the ones that defines its maximum capacity, are kept constant, since they are evaluated in with other experimental techniques than the ones discussed here, such as the incremental capacity [32, 35, 40].

The validity range for the 28 varied parameters are defined after thorough literature review [41–55], with the pristine US26650VT as reference battery type. Five values for each parameter are used in the simulations, which explore the whole available range. For each value of the parameters, 190 dis-

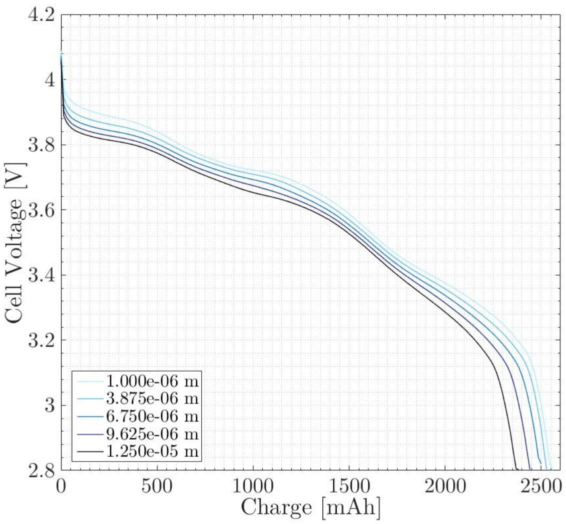

Figure 6. *Sensitivity of the complete discharge curve 2C and 25°C to the negative electrode particle radius*

charge curves, 96 relaxation curves and 20 impedance spectra are simulated in various combinations of ambient temperature, current rate, state of charge and depth of discharge. The model outputs are the battery voltage and surface temperature in the capacity test and in the relaxation test simulations, and the real and imaginary impedance in the EIS simulations. In total, the sensitivity analysis is based on 38140 simulated conditions. In figure 6, there is an example of the obtained results, with the sensitivity of the complete discharge curve at 2C and 25°C to the variations of the negative electrode particle radius.

Following the works of Zhang et al. [31] and of Edouard et al. [56], the great amount of data that is obtained by this wide simulation matrix is summarized through the standard deviation, which estimates the dispersion of an output due to the variation of a parameter (see Thesis Chapter 4.1.1). The steps of the analysis are briefly explained in figure 7, and the final results are:

- a classification of the model parameters according to four categories based sensitivity of each model output to them: Insensitive, Low Sensitivity, Mid Sensitivity and High Sensitivity (see Thesis Chapter 4.2.2). The classification is made by comparing the mean of the average standard deviations of a parameter and the maximum average standard deviation for each model output with a minimum limit value, whose value derives from the measurement uncertainty analysis. The purpose is to obtain a qualitative assessment of the degree of sensitivity of the outputs to the model parameters;

- a comparison of the sensitivities associated to each model parameters in each operative condition, for all the outputs of the three simulated techniques. This comparison is made thanks to a clustering algorithm (Fuzzy C-Means clustering) that associates the standard deviations of all the parameters in each operative condition to three clusters: Low Sensitivity, Mid Sensitivity and High Sensitivity (see Thesis Chapter 4.2.3). The purpose is the comparative evaluation of the trend of the parameters' standard deviation while varying the operative conditions, to select experiments where one or more parameters are much more relevant than others;

4.2 Sensitivity analysis results

Some general considerations that can be made from the sensitivity analysis results are:

- some model parameters have a negligible impact in certain operative conditions, while they are very impactful in others. This **mixed impact** is very interesting for the purpose of our analysis, since it implies the possibility to exclude or isolate the effect of a parameter. An example are the variations of the double layer capacities of the positive and negative electrodes. They are not relevant in the capacity test and in the relaxation test, while the EIS impedance shows a great sensitivity to them, since these parameters define the characteristic frequency of the charge transfer resistance;

- some parameters show an **uniform impact** on practically all the explored conditions. This feature is not desirable for the parameter estimation, since there are no conditions where a parameter can be effectively isolated.
  A notable example is the effect of the positive and negative particle radii. A variation of these parameters leads to high dispersions in all the outputs of the capacity test, of the relaxation curve and of the EIS, since the particle radii define all the battery overpotentials, with a linear relationship with the ohmic and activation overpotentials and a quadratic relationship with the concentration overpotential;

- some parameters have a **negligible impact** in every simulated condition. By comparing their standard deviations with the minimum limit values, we observe that they are always below these thresholds. Therefore, these parameters can be excluded from the parameter estimation process and kept constant at a reasonable value taken from literature. In total, four of the model parameters are classified in this category: the electrolyte fraction in the separator, the film resistance on the positive electrode, the axial thermal conductivity and the electronic conductivity in the negative electrode.

After analyzing all the information obtained from the sensitivity analysis and the clustering of the results, we propose this experimental methodology, designed as a series of concatenated tests with a limited duration that are able to give information about all the relevant model parameters (see Thesis Chapter 4.3):

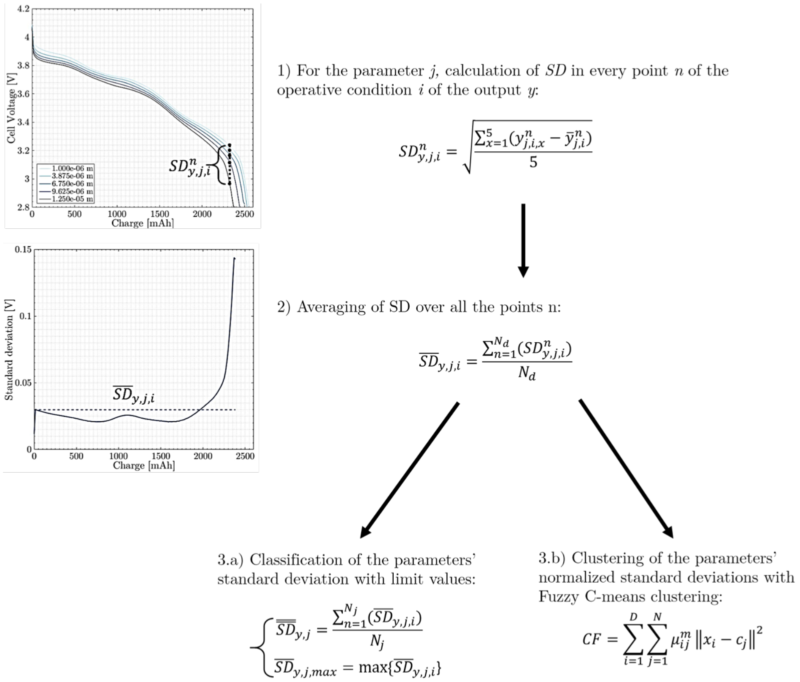

Figure 7. *Scheme of the sensitivity analysis*

1. starting from 10°C and 100% SOC, the impedance spectrum is measured with an **EIS**, in the 4000-1 Hz range with 20 logarithmically spaced frequencies applying two sinusoids (time employed: around 2 minutes);

2. then, the battery is **discharged** for three quarters of its nominal capacity (75% DOD) with a current rate equal to 3*C*, reaching 25% SOC (time employed: around 15 minutes);

3. the current is set to zero and the battery **relaxation** process starts. The cell voltage and the battery surface temperature are measured for 1000 s, and then the ambient temperature is modified to 25°C. A certain amount of time has to be waited to allow the heating of the battery and to obtain a sufficiently homogeneous temperature profile. With the battery samples employed in this work, half an hour is sufficient for this purpose (time employed: around 45 minutes);

4. a second **EIS** is performed, at 25°C and 25% SOC, with the same frequency range and spacing of the first one (time employed: around 2 minutes);

5. the battery is **discharged** down to the minimum voltage limit with a 1C current rate and a theoretical 25% DOD, at 25°C and starting from 25% SOC (time employed: around 15 minutes).

With these five experiments, we expect to obtain information on all the defining characteristics of the lithium-ion battery.

5. Calibration and validation

The data obtained from the application of the described methodology are used as the training dataset for an optimization algorithm that has to objective to fit the results of the physical LIB model to this dataset.

The employed algorithm is the Particle Swarm Optimization (PSO), a gradient-free algorithm that is simple to implement and robust. Being a mechanistic formulation, the P2D lithium-ion battery model has complex non-linear relations between the outputs and the inputs. Moreover, it is not easy to guess an initial point that can be near to the cost function minimum, due to the presence of an high number of parameters and to the uncertainty about their actual value, that can span orders of magnitude in some cases.

The solution space is defined by the number of model parameters included in the optimization and by the ranges in which the values of these parameters can lie (see Thesis Chapter 5.1). The cost function is a weighted sum of the root-mean-square errors (RMSEs) between the results of the model and the training dataset. According to the methodology, the number of experimental outputs included in the optimization is equal to 7: the battery voltage of the two discharge curve and of the relaxation test, and the real and imaginary impedances of the two EIS's. The battery surface temperature is not included to low accuracy and reliability of this experimental output (see Thesis Chapter 5.1.1).

5.1 Calibration

To perform the tuning of the data fitting algorithm and to confirm the capability of the said algorithm of obtaining an accurate result for what concerns the values of the model

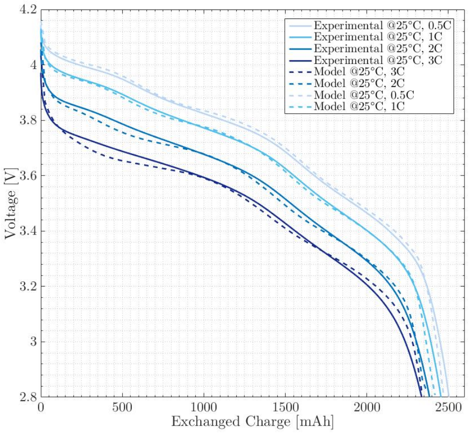

Figure 8. *Validation dataset: Discharge curves at 25°C, from 100% SOC to 0% SOC, current rate variation*

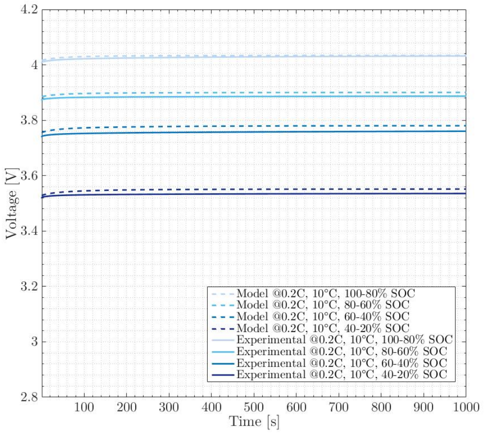

Figure 9. *Validation dataset: Relaxation curves after discharges at 0.2C, 10°C, with 20% DOD, starting SOC variation*

parameters, we use two simulated training datasets obtained from the model with two different sets of assumed model parameters (see Thesis Chapter 5.2). Both the sets of parameters found by the algorithm fit well the simulated datasets, but only the one associated to the first dataset is similar to the actual values given as input to the model to simulate that dataset.

The first simulated dataset represents a battery whose electrodes have different properties, with the positive one that has a charge transfer resistance about four times higher than the negative one, and a much lower characteristic frequency of this resistance in the impedance spectrum. Instead, the simulated dataset 2 represents a battery whose electrodes show very similar properties. In this situation, the fitting parameter set does not represent the real one in a satisfactory way, even if this combination of wrong parameters reproduces well the training dataset.

From this test we understood that the particle radii of the electrodes have to be fixed in order to be sure to obtain a correct set of parameters, due to their strong influence on all the components of the battery impedance. Also, we recognized the need for more accurate correlations for the parameters that determine the battery high frequency resistance, in order to better distinguish the single contributions to this important characteristic.

The final step of the calibration is the use of an experimental dataset in the fitting algorithm as training dataset, to understand if it is possible to find a set of parameters that reproduces the behavior of a real battery only using the data obtained with the proposed methodology (see Thesis Chapter 5.3).

5.2 Validation

After the experimental training dataset is applied, the set of parameters obtained from the algorithm is then used to simulate different operative conditions in all the three techniques. This validation dataset is composed of tests made during the experimental campaign. The battery sample on which the tests of the training dataset and of the validation dataset are performed is the pristine US26650VT.

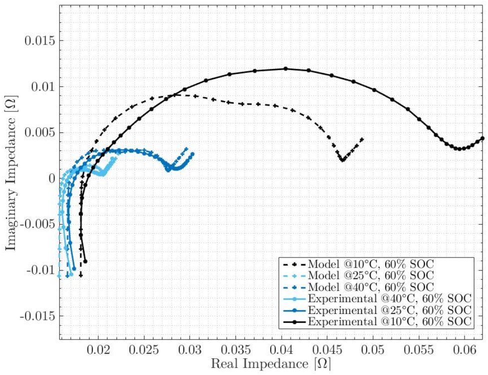

Figure 10. *Validation dataset: Impedance spectra at* 60% *SOC, temperature variation*

The RMSE of all the tests in the validation dataset are shown in table 2, while in the figures 8, 9 and 10 it is possible to compare some of the results of the model with the experimental data of discharge curves, relaxation tests and EIS's. We briefly report some of the performances of other parameter estimation methodologies found in the relevant literature, to have a benchmark to compare the results reported in table 2. As far as the author's knowledge, in the literature concerning the parameter estimation made with an analogous model, the reported root-mean-square errors are only related to capacity tests or to driving cycles profiles, a kind of test that is not included in this work.

Zhang et al. [31] reported RMSEs between 8 and 24 mV for discharge curves between 0.5C and 2*C* at 30°C, and between 20 and 37 mV for discharge curves between 0.5C and 2*C* at 15°C, on $LiCoO_2$ batteries. Park et al. [57] obtained RMSEs of 11.8 mV and 25.5 mV, respectively for a 0.5C and 1C discharge at 25°C, with a NCA battery. Li et al. [58] worked

Technique	Operative condition	RMSE
Discharge curve	0.5C, 25°C, 100 – 0% SOC	20.6 mV
	1C, 25°C, 100 – 0% SOC	20.3 mV
	2C, 25°C, 100 – 0% SOC	18.3 mV
	3C, 25°C, 100 – 0% SOC	26.6 mV
	0.5C, 10°C, 100 – 0% SOC	37.8 mV
	0.5C, 40°C, 100 – 0% SOC	22.9 mV
	3C, 10°C, 100 – 0% SOC	60.5 mV
	3C, 40°C, 100 – 0% SOC	30.9 mV
Relaxation test	0.2C, 10°C, 100 – 80% SOC	6.5 mV
	0.2C, 10°C, 80 – 60% SOC	12.0 mV
	0.2C, 10°C, 60 – 40% SOC	17.1 mV
	0.2C, 10°C, 40 – 20% SOC	11.6 mV
	3C, 40°C, 100 – 80% SOC	18.6 mV
	3C, 40°C, 80 – 60% SOC	28.8 mV
	3C, 40°C, 60 – 40% SOC	35.7 mV
	3C, 40°C, 40 – 20% SOC	38.8 mV
EIS	25°C, 100% SOC	Z_R: 1.28 mΩ Z_I: 1.43 mΩ
	25°C, 60% SOC	Z_R: 1.27 mΩ Z_I: 0.606 mΩ
	25°C, 20% SOC	Z_R: 2.69 mΩ Z_I: 1.00 mΩ
	40°C, 60% SOC	Z_R: 0.501 mΩ Z_I: 0.313 mΩ
	10°C, 60% SOC	Z_R: 8.54 mΩ Z_I: 1.95 mΩ

Table 2. *Summary of the RMSE between the model data and the experimental data in the validation dataset*

on a LMO battery, achieving RMSEs between 6.4 mV and 12.9 mV for discharge curves between 0.5C and 3C, at 25°C. Yang et al. [59] reported RMSEs of 15.6 mV and 21.6 mV, respectively for a 1C and a 2C discharge curve, at 25°C, with a NMC battery. We can see how in the same operative conditions, our results are aligned with the literature, also including in our work a much wider range of operative conditions and techniques.

The zones where the model performed less well were the ones of low/very low states of charge and low temperatures, probably due to a non-optimal fitting of the thermodynamic characteristic of the battery, and of correlations that are not suitable for highly non-linear effects like the ones found at low SOC and low ambient temperature. Moreover, there is the need to improve the speed of the simulations, in order to increase the number of iterations made by the algorithm, obtaining more accurate results. Nevertheless, the results obtained with the application of the proposed experimental methodology suggest that the combination of discharge curves, relaxation tests and EIS can be a powerful tool for the parameter estimation of a lithium-ion battery in a physical model. This novel and comprehensive approach to battery characterization can be a stepping stone in the definition of a complete diagnostic procedure of aged lithium-ion batteries.

Conclusions

By studying and applying capacity tests, relaxation tests and EIS's on pristine and aged commercial battery samples, we understood how the smart combination of these different techniques can be a powerful tool to obtain a complete dataset on the battery behavior.

A sensitivity analysis on a physical LIB model was used to design the experimental methodology, balancing the trade off between the amount of obtained data and the tests' duration.

The methodology was then implemented and tested in a parameter estimation process, where a metaheuristic Particle Swarm Optimization algorithm was employed to fit the model results to the training dataset. Two simulated datasets and one experimental dataset were used for the calibration and validation of the methodology.

We showed how the validation dataset is well reproduced with the estimated parameters in the majority of the conditions not included in the training dataset, obtaining RMSEs that are aligned with the relevant literature on the topic. The calibration was performed on a very limited set of experiments if compared to the validation datasets, and we considered a much wider range of operative conditions and experimental techniques than the literature.

We observed some limitations in the operative conditions where the battery SOC and the ambient temperature are low. It was highlighted the necessity of a proper fitting of the thermodynamic characteristic of the battery to obtain a fully reliable set of parameters.

The proposed methodology has shown promising results, and it confirmed how the combination of different experimental techniques and of a physical model can be a powerful tool for a comprehensive battery characterization. The next important step for the definition of a complete diagnostic procedure will be the correlation of the values of the physical parameters with the degradation sustained by the aged lithium-ion battery.

Bibliography

[1] *CAIT Climate Data Explorer*. *https://www.climatewatchdata.org/ghg-emissions*. 2019 (cit. on p. 1).

[2] *IEA - Tracking Energy Integration*. *https://www.iea.org/reports/tracking-energy-integration*. 2019 (cit. on p. 1).

[3] John T Warner. *The Handbook of Lithium-Ion Battery Pack Design: Chemistry, Components, Types and Terminology*. en. Elsevier, May 2015 (cit. on p. 1).

[4] H E Melin. “The Lithium-Ion Battery End-of-Life Market—A Baseline Study”. In: *World Economic Forum: Cologny, Switzerland*. 2018, pp. 1–11 (cit. on p. 1).

[5] Rebecca E Ciez and J F Whitacre. “Examining different recycling processes for lithium-ion batteries”. In: *Nature Sustainability* 2.2 (Feb. 2019), pp. 148–156 (cit. on p. 1).

[6] Venkatasailanathan Ramadesigan et al. “Parameter Estimation and Capacity Fade Analysis of Lithium-Ion Batteries Using Reformulated Models”. In: *J. Electrochem. Soc.* 158.9 (2011) (cit. on p. 1).

[7] International Organization for Standardization (ISO). *Electrically propelled road vehicles — Test specification for lithium-ion traction battery packs and systems*. Tech. rep. 12405-4. 2018 (cit. on p. 1).

[8] Naoki Nitta et al. “Li-ion battery materials: present and future”. In: *Materials Today* 18.5 (June 2015), pp. 252–264 (cit. on p. 1).

[9] *The Nobel Prize in Chemistry 2019. https://www.nobelprize.org/prizes/chemistry/2019/press-release/.* 2019 (cit. on p. 2).

[10] Christoph R Birkl et al. “Degradation diagnostics for lithium ion cells”. In: *Journal of power sources* 341 (Feb. 2017), pp. 373–386 (cit. on pp. 1, 2, 5).

[11] Lockheed Idaho Technologies Co. *USABC electric vehicle Battery Test Procedures Manual. Revision 2*. 1996 (cit. on p. 2).

[12] Robert Reinhardt et al. “Towards sustainable business models for electric vehicle battery second use: A critical review”. en. In: *Journal of environmental management* 245 (Sept. 2019), pp. 432–446 (cit. on p. 2).

[13] E Martinez-Laserna et al. “Battery second life: Hype, hope or reality? A critical review of the state of the art”. In: *Renewable and Sustainable Energy Reviews* 93 (Oct. 2018), pp. 701–718 (cit. on p. 2).

[14] M S Hossain Lipu et al. “A review of state of health and remaining useful life estimation methods for lithium-ion battery in electric vehicles: Challenges and recommendations”. In: *Journal of cleaner production* 205 (Dec. 2018), pp. 115–133 (cit. on p. 2).

[15] Anup Barai et al. “A comparison of methodologies for the non-invasive characterisation of commercial Li-ion cells”. In: *Progress in Energy and Combustion Science* 72 (2019), pp. 1–31 (cit. on p. 2).

[16] Grietus Mulder et al. “Enhanced test methods to characterise automotive battery cells”. In: *Journal of power sources* 196.23 (Dec. 2011), pp. 10079–10087 (cit. on p. 2).

[17] Carlos Pastor-Fernández et al. “A Comparison between Electrochemical Impedance Spectroscopy and Incremental Capacity-Differential Voltage as Li-ion Diagnostic Techniques to Identify and Quantify the Effects of Degradation Modes within Battery Management Systems”. In: *Journal of Power Sources* 360 (2017), pp. 301–318 (cit. on pp. 2, 3).

[18] Wladislaw Waag, Stefan Käbitz, and Dirk Uwe Sauer. “Experimental investigation of the lithium-ion battery impedance characteristic at various conditions and aging states and its influence on the application”. In: *Applied energy* 102 (Feb. 2013), pp. 885–897 (cit. on pp. 2, 4).

[19] Kandler Smith and Chao-Yang Wang. “Solid-state diffusion limitations on pulse operation of a lithium ion cell for hybrid electric vehicles”. In: *Journal of Power Sources* 161.1 (2006), pp. 628–639 (cit. on p. 3).

[20] Stefan Schindler et al. “Voltage relaxation and impedance spectroscopy as in-operando methods for the detection of lithium plating on graphitic anodes in commercial lithium-ion cells”. In: *Journal of power sources* 304 (Feb. 2016), pp. 170–180 (cit. on p. 3).

[21] Anup Barai et al. “A study on the impact of lithium-ion cell relaxation on electrochemical impedance spectroscopy”. In: *Journal of power sources* 280 (Apr. 2015), pp. 74–80 (cit. on p. 3).

[22] Frank M Kindermann et al. “Measurements of lithium-ion concentration equilibration processes inside graphite electrodes”. In: *Journal of power sources* 342 (Feb. 2017), pp. 638–643 (cit. on p. 3).

[23] Veronika Zinth et al. “Inhomogeneity and relaxation phenomena in the graphite anode of a lithium-ion battery probed by in situ neutron diffraction”. In: *Journal of Power Sources* 361 (2017), pp. 54–60 (cit. on p. 3).

[24] Anup Barai et al. “A study of the influence of measurement timescale on internal resistance characterisation methodologies for lithium-ion cells”. en. In: *Scientific reports* 8.1 (Jan. 2018), p. 21 (cit. on p. 3).

[25] Jeremy P Meyers et al. “The Impedance Response of a Porous Electrode Composed of Intercalation Particles”. In: *Journal of the Electrochemical Society* 147.8 (Aug. 2000), pp. 2930–2940 (cit. on pp. 3, 6).

[26] Isabel Jiménez Gordon et al. “Electrode contributions to the impedance of a high-energy density Li-ion cell designed for EV applications”. In: *Solid State Ionics* 237 (Apr. 2013), pp. 50–55 (cit. on p. 3).

[27] I A Jiménez Gordon et al. “Electrochemical Impedance Spectroscopy response study of a commercial graphite-based negative electrode for Li-ion batteries as function of the cell state of charge and ageing”. In: *Electrochimica acta* 223 (Jan. 2017), pp. 63–73 (cit. on pp. 3, 6).

[28] Thomas F Fuller, Marc Doyle, and John Newman. “Simulation and optimization of the dual lithium ion insertion cell”. In: *Journal of the Electrochemical Society* 141.1 (1994), pp. 1–10 (cit. on p. 3).

[29] Gregory L Plett. *Battery Management Systems, Volume I: Battery Modeling*. en. Artech House, Sept. 2015 (cit. on p. 3).

[30] Parthasarathy M Gomadam, Ralph E White, and John W Weidner. “Modeling Heat Conduction in Spiral Geometries”. en. In: *Journal of the Electrochemical Society* 150.10 (Aug. 2003), A1339 (cit. on p. 4).

[31] Liqiang Zhang et al. “Parameter Sensitivity Analysis of Cylindrical LiFePO4 Battery Performance Using Multi-Physics Modeling”. In: *Journal of the Electrochemical Society* 161.5 (Jan. 2014), A762–A776 (cit. on pp. 4, 7, 9).

[32] Gabriele Sordi. “Thermodynamic and kinetic analysis of commercial lithium ion battery for identification of degradation mechanisms”. MA thesis. Polytechnic of Milan, Apr. 2019 (cit. on pp. 4, 6).

[33] Lars Ole Valøen and Jan N Reimers. “Transport Properties of LiPF6-Based Li-Ion Battery Electrolytes”. en. In: *Journal of the Electrochemical Society* 152.5 (Mar. 2005), A882 (cit. on pp. 5, 6).

[34] Cheng Lin et al. “Aging Mechanisms of Electrode Materials in Lithium-Ion Batteries for Electric Vehicles”. en. In: *Journal of chemistry and chemical engineering* 2015 (June 2015) (cit. on p. 5).

[35] Matthieu Dubarry, Cyril Truchot, and Bor Yann Liaw. “Cell degradation in commercial LiFePO4 cells with high-power and high-energy designs”. In: *Journal of power sources* 258 (July 2014), pp. 408–419 (cit. on pp. 5, 6).

[36] J R Dahn. “Phase diagram of LixC6”. en. In: *Physical review. B, Condensed matter* 44.17 (Nov. 1991), pp. 9170–9177 (cit. on p. 6).

[37] K M Shaju, G V Subba Rao, and B V R Chowdari. “Li ion kinetic studies on spinel cathodes, Li (M 1/6 Mn 11/6) O 4 (M= Mn, Co, CoAl) by GITT and EIS”. In: *Journal of materials chemistry* 13.1 (2003), pp. 106–113 (cit. on p. 6).

[38] Young-Min Choi and Su-Il Pyun. “Effects of intercalation-induced stress on lithium transport through porous LiCoO2 electrode”. In: *Solid State Ionics* 99.3 (Aug. 1997), pp. 173–183 (cit. on p. 6).

[39] Guus Ten Broeke, George Van Voorn, and Arend Ligtenberg. “Which sensitivity analysis method should I use for my agent-based model?” In: *Journal of Artificial Societies and Social Simulation* 19.1 (2016) (cit. on p. 6).

[40] Ning Jin et al. “Parameter estimation of an electrochemistry-based lithium-ion battery model using a two-step procedure and a parameter sensitivity analysis”. In: *International Journal of Energy Research* 42.7 (2018), pp. 2417–2430 (cit. on p. 6).

[41] Johannes Schmalstieg and Dirk Uwe Sauer. “Full Cell Parameterization of a High-Power Lithium-Ion Battery for a Physico-Chemical Model: Part II. Thermal Parameters and Validation”. In: *Journal of The Electrochemical Society* 165.16 (2018), A3811–A3819 (cit. on p. 6).

[42] Johannes Schmalstieg et al. “Full Cell Parameterization of a High-Power Lithium-Ion Battery for a Physico-Chemical Model: Part I. Physical and Electrochemical Parameters”. In: *Journal of The Electrochemical Society* 165.16 (2018), A3799–A3810 (cit. on p. 6).

[43] Michael J Lain, James Brandon, and Emma Kendrick. “Design Strategies for High Power vs. High Energy Lithium Ion Cells”. en. In: *Batteries* 5.4 (Oct. 2019), p. 64 (cit. on p. 6).

[44] Jason B Quinn et al. “Energy density of cylindrical Li-ion cells: A comparison of commercial 18650 to the 21700 cells”. In: *Journal of the Electrochemical Society* 165.14 (2018), A3284–A3291 (cit. on p. 6).

[45] Chia-Chin Chang, Sin-Yi Huang, and Wei-Hsin Chen. “Thermal and solid electrolyte interphase characterization of lithium-ion battery”. In: *Energy* 174 (May 2019), pp. 999–1011 (cit. on p. 6).

[46] Atsushi Funabiki et al. “Impedance study on the electrochemical lithium intercalation into natural graphite powder”. In: *Journal of the Electrochemical Society* 145.1 (1998), pp. 172–178 (cit. on p. 6).

[47] A Van der Ven and G Ceder. “Lithium Diffusion in Layered Li x CoO2”. en. In: *Electrochemical and Solid State Letters* 3.7 (May 2000), p. 301 (cit. on p. 6).

[48] Jaephil Cho et al. “Electrochemical Properties and Thermal Stability of Li a Ni1- x CO x O 2 Cathode Materials”. In: *Journal of the Electrochemical Society* 147.1 (2000), pp. 15–20 (cit. on p. 6).

[49] Ajit Kumar Dutta. “Electrical Conductivity of Single Crystals of Graphite”. In: *Physics Review* 90.2 (Apr. 1953), pp. 187–192 (cit. on p. 6).

[50] M Wakihara et al. “Chemical diffusion coefficients of lithium in LiMyMn2- yO4 (M= Co and Cr)”. In: *Solid State Ionics* 86 (1996), pp. 907–909 (cit. on p. 6).

[51] J Marzec et al. “Conduction mechanism in operating a LiMn2O4 cathode”. In: *Solid State Ionics* 146.3 (Feb. 2002), pp. 225–237 (cit. on p. 6).

[52] Dany Carlier, Michel Ménétrier, and Claude Delmas. “7Li MAS NMR study of electrochemically deintercalated LixNi0.30Co0.70O2 phases: evidence of electronic and ionic mobility, and redox processes”. en. In: *Journal of materials chemistry* 11.2 (2001), pp. 594–603 (cit. on p. 6).

[53] Sang Woo Han. “Transport and Kinetic Phenomena Linked to Power Performance of Lithium-Ion Batteries”. PhD thesis. 2014 (cit. on p. 6).

[54] Sarah Stewart and John Newman. “Measuring the Salt Activity Coefficient in Lithium-Battery Electrolytes”. en. In: *Journal of the Electrochemical Society* 155.6 (Apr. 2008), A458 (cit. on p. 6).

[55] Moses Ender et al. “Anode microstructures from high-energy and high-power lithium-ion cylindrical cells obtained by X-ray nano-tomography”. In: *Journal of power sources* 269 (Dec. 2014), pp. 912–919 (cit. on p. 6).

[56] C Edouard et al. “Parameter sensitivity analysis of a simplified electrochemical and thermal model for Li-ion batteries aging”. In: *Journal of power sources* 325 (Sept. 2016), pp. 482–494 (cit. on p. 7).

[57] Saehong Park et al. “Optimal Experimental Design for Parameterization of an Electrochemical Lithium-Ion Battery Model”. In: *Journal of the Electrochemical Society* 165.7 (Jan. 2018), A1309–A1323 (cit. on p. 9).

[58] Jun Li et al. “Parameter Identification of Lithium-Ion Batteries Model to Predict Discharge Behaviors Using Heuristic Algorithm”. In: *Journal of the Electrochemical Society* 163.8 (Jan. 2016), A1646–A1652 (cit. on p. 9).

[59] Xiao Yang et al. “Parameter Identification of Electrochemical Model for Vehicular Lithium-Ion Battery Based on Particle Swarm Optimization”. In: *Energies* 10.11 (2017), p. 1811 (cit. on p. 10).

Ringraziamenti

Quello che termina con questa tesi è un percorso intenso, lungo cinque anni e mezzo e durante quale io sono diventato un'altra persona. Una manciata di righe non potrà mai rendere giustizia a tutte le persone conosciute e a tutte le esperienze vissute in questo periodo, ma ci proverò lo stesso.

Ringrazio il professor Andrea Casalegno, il professor Claudio Rabissi, l'ormai dottorando Gabriele Sordi e tutte le altre persone del gruppo MRT Fuel Cell and Battery (!) Lab. Questo lungo lavoro e quello che arriverà dopo è stato possibile soprattutto grazie al loro prezioso aiuto e alla loro guida.

Ringrazio tutti i miei compagni di università e di Alta Scuola Politecnica, coi quali condividere questi cinque anni è stata un'occasione unica per me per passare dei bellissimi momenti, per imparare molto di sè stessi, e per migliorare come persona e come ingegnere.

Ringrazio i tutti miei amici, sia i vecchi di giù e che i nuovi di su, come piace dire a me. Che fossi in Via Nuova 118/A o in Via Mozart Amadeus 14, mi sono sempre sentito a casa.

Ringrazio la mia famiglia, Simone, Barbara, Lorenzo, Gianmarco e Cesira, che ha fatto davvero davvero tanto per darmi questa opportunità. Ringrazio anche Aldo e Chantal, che fin da subito sono diventati la mia seconda famiglia qua a Milano.

Infine ringrazio Monica, che ha dato e continua a dare un motivo e un senso a tutto questo.

Milano, 29 Aprile 2020 A. I.

Dilige veritatem

Contents

List of Figures

List of Tables

Sommario

La crescita del mercato dei veicoli elettrici sta rendendo disponibile un grande numero di batterie agli ioni di litio invecchiate, ritirate dopo la fine della loro vita utile nei veicoli elettrici. In realtà, queste batterie possiedono ancora una capacità residua che può essere sfruttata per applicazioni meno impegnative. Per permetterne il riuso, è importante misurare il loro stato di salute e la vita utile rimanente. L'obiettivo di questo lavoro è definire una metodologia innovativa per la stima dei parametri fisici di una batteria agli ioni di litio, attraverso l'uso di un modello elettrochimico e termico. I valori dei parametri fisici possono essere poi associati agli effetti dell'invecchiamento.

La prima attività è una campagna sperimentale su batterie commerciali nuove e invecchiate, nella quale tre tecniche di diagnostica sono utilizzate: test di capacità, test di rilassamento e spettroscopie elettrochimiche di impedenza (EIS). Si è capito come ogni tecnica può evidenziare in modi diversi gli effetti della degradazione sulle batterie agli ioni di litio, e tutte e tre si sono dimostrate validi strumenti per la stima dei parametri, specialmente se combinate assieme.

La seconda attività è un'analisi di sensitività one-factor-at-time del modello fisico della batteria, dove le tre tecniche di diagnostica sono simulate in molte condizioni operative, e 28 parametri del modello sono variati in un range definito da un'analisi di letteratura. Il risultato è una classificazione dei parametri a seconda della sensitività dei risultati del modello a una loro variazione. Da questa analisi, si è formulata una metodologia sperimentale che bilancia la quantità di informazioni ottenibili per la stima dei parametri e la durata dei test.

Infine, la metodologià è implementata e testata con un algoritmo di fitting Particle Swarm Optimization (PSO). Due dataset simulati e un dataset sperimentale ottenuto da una batteria commerciale da 2.6 Ah sono utilizzati per la calibrazione e la validazione della metodologia. I risultati mostrano come i parameteri stimati riproducono il comportamento della batteria in condizioni non comprese nel dataset di allenamento, e come questa metodologia può essere un passo fondamentale per la formulazione di una procedura di diagnostica completa per batterie agli ioni di litio invecchiate.

Parole chiave: batterie agli ioni di litio, degradazione, modello fisico, metodologia

Abstract

The growth of the electric vehicle (EV) market is leading to an increasing number of aged lithium-ion batteries (LIB) that are retired after their end of life in EVs. Nevertheless, these LIBs still retain a useful capacity that can be exploited in less demanding applications. To enable the reuse of such batteries, it is important to measure their state of health and the remaining lifetime. The purpose of this work is to define an innovative methodology for the estimation of the physical parameters of a lithium-ion battery, through the use of an electrochemical-thermal model. The values of the physical parameters can be then linked to the effects of aging.

The first activity is an experimental campaign on pristine and aged commercial battery samples, where three diagnostic techniques are used: capacity tests, relaxation tests, and electrochemical impedance spectroscopies (EIS). We understood how each technique can highlight in different ways the effects of degradation on LIBs, and all of them have proven to be valid tools for the parameter estimation, especially if combined together.

The second activity is a one-factor-at-time sensitivity analysis of the LIB physical model, where the three diagnostic techniques are simulated in a variety of operative conditions and 28 model parameters are varied within sensible ranges defined by a literature review. The result is a classification of the model parameters according to the sensitivity of the model outputs to their variations. From this analysis, we formulated an experimental methodology that balanced the amount of information obtainable for the parameter estimation and the tests' duration.

Finally, the methodology is implemented and tested with a Particle Swarm Optimization (PSO) fitting algorithm. Two simulated datasets and one experimental dataset obtained from a 2.6 Ah commercial battery sample are used for the calibration and validation of the methodology. The results show how the estimated parameters reproduce the battery behavior in conditions not included in the training dataset, and how this methodology can be a stepping stone for the formulation of a full diagnostic procedure for aged LIBs.

Keywords: lithium-ion batteries, degradation, physical model, methodology

Introduction

The necessity of reducing greenhouse gases emissions is one of the most pressing issues that our world is facing. To mitigate the impact of climate change and to contain the temperature increase within safe values, there has to be a concerted effort on all the main sectors of human economy. The most impactful sector is the energy one, accounting for 71.2% of overall annual GHG emissions in 2016 [1]. This number includes electricity and heat generation in power plants and buildings, transportation, manufacturing/construction energy needs and emissions related to fossil fuels production. Therefore, the shift towards a decarbonized energy mix is the key to achieve a serious decrease of GHG emissions, but this shift has to happen in a relatively small amount of years. According to IPCC [2], the annual emissions should peak in the next ten years, aiming to a zero-carbon economy by 2050.

The enabling technologies for such a switch are available: solar, wind, hydro, biomass and nuclear power generation allow a near-zero carbon energy generation. In particular, solar and wind energy have seen a continuous double-digit growth in the installed capacity in the last years [3]. However, these two intermittent and non-programmable renewable sources have to be coupled to an adequate integration system in order to be exploited in a way that resembles the programmable fossil fuel ones. Energy storage is the capstone of the integration technologies, allowing a delay in the utilization of the generated power, increasing the flexibility of the electric grid and facilitating the participation of the consumers in the grid operation. Moreover, the extent of its development makes it one of the few energy technologies on track to meet the requirements for the Sustainable Development Scenario [4].

In parallel with this, the transportation sector is being transformed by the use of electric motors as prime or auxiliary movers, with a steadily increasing adoption of hybrid electric vehicles (HEV) and battery electric vehicles (BEV). The replacement of the internal combustion engine, combined with a clean energy mix as input for the production and use phases, could decrease the life cycle GHG emissions and the toxicity indicators of a car [5], with evident benefits for the environment and for the human health. Of course, these kinds of vehicles require an on-board storage system that collects and delivers electric energy to the drivetrain, with strict requirements about safety, compactness and weight.

Lithium-ion batteries (LIB) represent the vast majority of stationary energy storage installations, owning 88% of 2016 new capacity and growing with a firm rate in the last five years [4]. They are also the leading technology in the EV field, after they rapidly replaced lead-acid and nickel-metal hydride batteries in the 1990s, and consumer electronics. This fact can be explained by their advantageous properties compared to other kinds of electrochemical storage systems: high energy and power density, long cycle life, low self-discharge rate and high cell voltage [6]. Hence, lithium-ion batteries have the potential to avoid a significant share of greenhouse gases emission, helping to reach the IPCC objectives. Nevertheless, several challenges have to be faced in order to make LIBs a fully stable, performant and sustainable technology. Safety issues, toxicity of some materials and end-of-life (EOL) destination are among the most pressing ones [6].

This thesis will focus on the possibility of reusing lithium-ion batteries coming from electric vehicles after their automotive end-of-life, in a circular economy framework. In particular, it will deal with the development of an innovative methodology for the testing of LIBs, in order to reproduce their behavior with a mechanistic model and a set of physical parameters. This work goes into the direction of a formulation of a diagnostic procedure that measures the EOL state of health and predicts the remaining useful lifetime of aged lithium-ion batteries.

Outline

The structure of this thesis is:

Chapter 1 describes the state of the art of second-life lithium-ion batteries, focussing on the technical challenges of such a concept, and it presents the research question of the thesis.

Chapter 2 explains the diagnostic techniques used in the experimental campaign, as well as the employed physical model.

Chapter 3 reports the results of the experimental campaign made on four battery samples, where three diagnostic techniques are employed: capacity tests, relaxation tests and electrochemical impedance spectroscopies.

Chapter 4 explains the methodology and the results of the sensitivity analysis made on the LIB physical model.

Chapter 5 reports the results of the fitting of LIB experimental data obtained with the application of the proposed methodology.

Chapter 1

State of the art

1.1 Lithium-ion battery: Introduction

A lithium-ion battery (LIB) is an electrochemical energy storage system that exploits the reduction/oxidation reactions of lithium ions to store and release electrical energy. The concept was mainly developed during the 1970s and the 1980s by John Goodenough, Stanley Whittingham and Akira Yoshino, who received the 2019 Nobel Prize for Chemistry for their work on the subject [7]. It was firstly commercialized by Sony in 1991 as rechargeable battery for mobile phones, and in the following decades it has become the standard for consumer electronics, electric vehicles and stationary energy storage.

The main benefit of using lithium as reacting species is its advantageous standard electrode potential, equal to -3.0141 V vs. Standard Hydrogen Electrode (SHE), one of the lowest among the periodic table elements [8]. This strong reactivity allows the manufacturing of high-voltage cells, up to 3.8 V as nominal voltage. In addition, lithium is the lightest existing metal thanks to its low atomic mass and hence it assures high specific energy and power if compared to other chemistries.

Lithium-ion batteries are closed systems, implying that reactants and products of the electrochemical reactions are stored inside the battery. Therefore, the energy and power density of the battery are strictly correlated, and they are linked to the size of the device. Moreover, during normal operation there are no stationary conditions in a LIB, due to the strong coupling between voltage, current, temperature and the concentrations of reactants and products in the battery. As we will see in the next sections, this inherent transient behavior of LIBs, with a wide range of characteristic timescales involved, has several implications for their experimental study and their modeling.

The simplest element is the lithium-ion cell (see figure 1.1), that operates at a certain voltage V depending on the constituent materials and on its actual thermodynamic conditions. It can be discharged or charged a current I, defined as the rate of flow of electrons in the electric circuit of the battery. Its magnitude is chosen according to the battery manufacturer specifications.

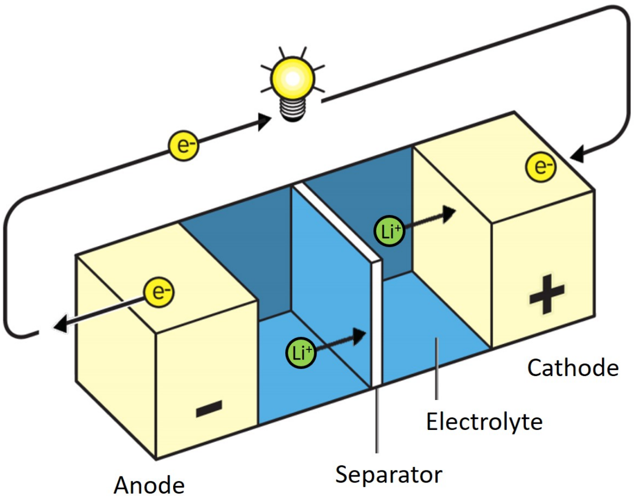

Figure 1.1: *Depiction of a lithium-ion cell with its main components (Adapted from [7])*

By integrating the operating current in time, it is obtained the number of the electric charges that are exchanged with the battery, i.e. the exchanged capacity Q usually measured in milliampere per hour (mAh):

$$Q = \int_0^t I dt \tag{1.1}$$

By inserting the voltage V in the integral, we can obtain the exchanged energy J:

$$J = \int_0^t V I dt \tag{1.2}$$

Cells can be connected together in modules: a series connection between cells increases the voltage of the module, while a parallel connection increases its capacity. One or more linked modules form a lithium-ion battery pack.

On every cell it is indicated the nominal capacity Q_{nom}, obtained with standard test procedures [9]. This quantity gives an approximate estimate of the maximum amount of energy that can be exchanged with the cell. The available capacity of the battery is usually expressed in a dimensionless form using the battery state of charge, or SOC, defined as:

$$SOC = \frac{Q}{Q_{nom}} \tag{1.3}$$

where Q is the available capacity. Using the SOC as parameter, it is possible to study together batteries of different nominal capacity. The state of charge can be expressed as absolute number (0–1 range) or as a percentage (0%–100% range) by multiplying the definition of equation 1.3 by 100.

A LIB operates in a fixed voltage range to avoid safety problems and side reactions. Typical limits are 4.2 V as upper value and 2.8 V as bottom value at 25°C, but they can vary according to the chemistry of the electrodes. The minimum and maximum value of the battery state of charge are defined according to these limits: at rest and at the standard temperature, a battery at the upper voltage limit has SOC equal to 1, while a battery at the lower voltage limit has SOC equal to 0.

As it is common in electrochemistry, the current density i could be used for lithium ion batteries:

$$i = \frac{I}{A_{el}} \tag{1.4}$$

where A_{el} is the surface area of the electrodes. With this quantity, the performance of batteries of different size could be easily compared. However, in commercial batteries the actual electrode area is usually quite difficult to evaluate, and hence the current density is not generally employed.

The current at which a LIB work is related to its nominal capacity through the current rate, or C-rate, C, defined as:

$$C = \frac{I}{Q_{nom}} \tag{1.5}$$

The C-rate is the inverse of the number of hours that are needed to completely charge or discharge the nominal capacity Q_{nom} with a current I. For instance, a C-rate equal to 2 h^{-1}, more commonly written as 2C, means that the battery is completely discharged in half an hour.

Usually, for high currents the real amount of time needed is lower than the C-rate inverse. The lower or upper voltage limits are reached without fully exploiting the battery nominal capacity, due to additional voltage losses that are not considered in standard test conditions. The C-rate can partially substitute the current density as way of comparing the performances of batteries with different size and nominal currents. However, the information about the distribution of the current inside the battery is lost.

For what concerns the efficiency of a lithium ion battery, it is possible to distinguish between:

- coulombic efficiency, or faradaic efficiency η_c, which is defined as:

  $$\eta_c = \frac{\int_{dis} Q_{nom} dSOC}{\int_{ch} Q_{nom} dSOC} \tag{1.6}$$

  It is the ratio of the electric charge extracted during a discharge and the electric charge put into the battery during the charge needed to get that discharge, in a closed cycle [10]. This efficiency accounts for irreversible charge losses between cycles, due to unwanted side reactions of the cyclable lithium with other elements of the battery. Generally, this parameter lays between 99.5% and 99.99%, and it is very influenced by the thermodynamic state of the LIB. High or very low temperatures, high SOC and high C-rates are detrimental for the coulombic efficiency;

- energy efficiency or round trip efficiency, η_e, defined as:

$$\eta_e = \frac{\int_{dis} VQ_{nom} dSOC}{\int_{ch} VQ_{nom} dSOC} \tag{1.7}$$

It is the ratio of the energy extracted during a discharge and the energy put into the battery during a charge needed to get that discharge, in a closed cycle [11]. It is mostly determined by the current at which the charge and discharge are performed. In the most common LIB operating conditions, the energy efficiency is usually in the 60%-90% range. It is also possible to separately define the discharge energy efficiency $\eta_{e,dis}$ and the charge energy efficiency $\eta_{e,ch}$ as:

$$\eta_{e,dis} = \frac{\int_{dis} VQ_{nom} dSOC}{\int_{OCV} VQ_{nom} dSOC} \tag{1.8}$$

$$\eta_{e,ch} = \frac{\int_{OCV} VQ_{nom} dSOC}{\int_{ch} VQ_{nom} dSOC} \tag{1.9}$$

They are calculated with respect to the energy that is actually present in the battery before the discharge or after the charge, calculated as the integral of the open circuit voltage-state of charge curve (see section 1.1.1). The product of the two efficiencies is the round trip efficiency, if they are calculated on the same charge-discharge cycle. As the round trip efficiency, they are strongly linked to the operating current, and they generally lay in the 80%-95% range.

Rigorously, in electrochemistry the anode is the electrode that is oxidizing, while the cathode is the one that is reducing, so the name of the electrodes should switch in case we are considering a discharge or a charge. Actually, in LIBs jargon the negative electrode is always called “anode”, while the positive electrode is always called “cathode”, hence taking the discharge condition as reference. We will always use this convention in the following sections.

1.1.1 Open Circuit Voltage

The voltage-SOC curve is obtained by discharging/charging a battery with a certain current rate between the voltage limits. If this current is low, it is possible to reduce the impact of the induced voltage losses, i.e. the irreversibilities, or overpotentials (see section 1.1.2). In the limit case, a near-zero current with an extremely slow discharge/charge can approximate a reversible process, and in this case the measured voltage trend is named open circuit voltage (OCV). The OCV represents the thermodynamic characteristic of the battery, and it is the result of the difference between the cathode and anode open circuit potentials (OCP).

To understand its meaning, we have to look at the lithium-ion batteries fundamental working principle. In almost all the commercially available LIBs, during operation lithium ions move from the negative electrode to the positive electrode and vice versa with a mechanism called intercalation. It is defined as the reversible inclusion of a species into a hosting structure, whose chemical bonds are not altered in the reactions involving the intercalating species. Some proposed LIB chemistries involve conversion electrodes, i.e. materials that partake in the lithium redox reaction modifying their structure, but they are still in a research and development phase [12, 13].

When a battery is fully charged, most of the lithium is hosted in the anode structure, while the cathode structure is depleted of it, and the system is in disequilibrium due to this species unbalance. The electrolyte that permeates the two electrodes allow only the movement of ions, whereas the external circuit permits only the flow of electrons. Hence, the equilibrium can be reestablished when the external circuit is closed and the lithium is separated in ions and electrons with the anode redox reaction:

$$\mathrm{LiN} \xrightleftharpoons[\text{charge}]{\text{discharge}} \mathrm{xLi^+ + xe^- + Li_{1\text{-}x}N}$$

where N is the anode host material. The lithium deintercalates from the anode and reaches the cathode by moving in the electrolyte by diffusion and migration, while the electrons flow in the external circuit creating an electric current.

Ions and electrons recombine thanks to the cathode redox reaction:

$$\mathrm{xLi^+ + xe^- + Li_{1\text{-}x}P} \xrightleftharpoons[\text{charge}]{\text{discharge}} \mathrm{LiP}$$

and lithium intercalates in the cathode host material P. In this way, the battery is discharged, with a spontaneous process that converts the energy of lithium chemical bonds into electrical work. The anode gets delithiated, i.e. the concentration of lithium decreases, while the cathode gets lithiated, i.e. the concentration of lithium increases. The opposite mechanism happens during the charge process, which is not a spontaneous process and requires the provision of an external work (i.e. a battery charger) in order to convert electric energy into chemical energy.

The intercalation and deintercalation process of lithium ions is driven by the chemical potential difference between anode and cathode [10]. In fact, according to Nernst equation, we have that at equilibrium the open circuit voltage difference E_{ocv} between cathode and anode is:

$$E_{ocv} = -\frac{\mu_{Li,p} - \mu_{Li,n}}{F} \tag{1.10}$$

where $\mu_{Li,p}$ and $\mu_{Li,n}$ are respectively the cathode and anode lithium chemical potentials, and F is the Faraday constant. Reminding the definition of μ, we can write the chemical potential of lithium in the interstices of the host material as:

$$\mu_{Li} = \left.\frac{\partial G(c_{Li})}{\partial c_{Li}}\right|_{T,P} \tag{1.11}$$

which is the derivative of the Gibbs free energy of the Li-host compound G with respect to the concentration of lithium in the host material c_{Li}, i.e. the fraction of available interstitial sites occupied by lithium [15]. In the ideal case, where the

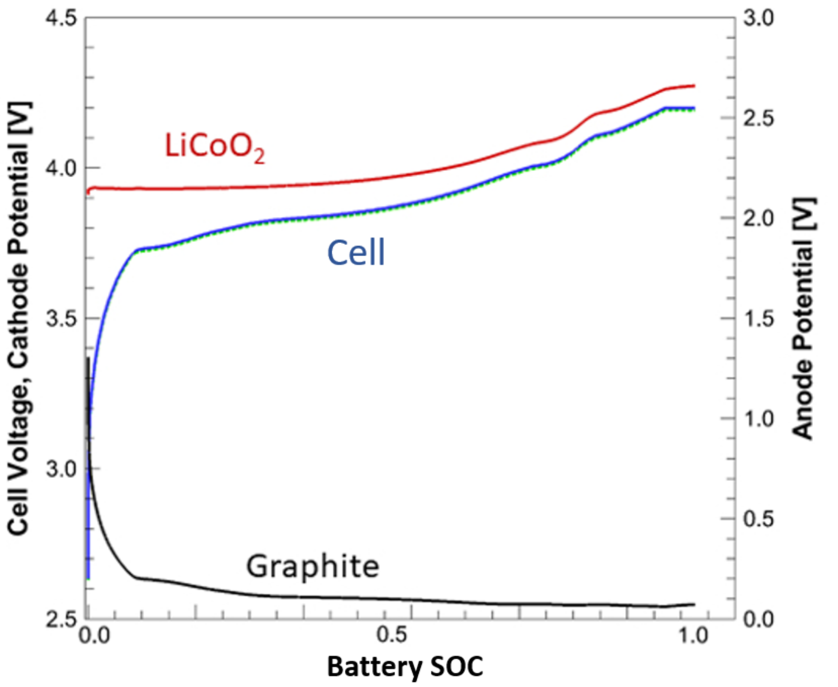

Figure 1.2: *Anode (graphite) and cathode ($LiCoO_2$) potentials, with the resulting battery voltage as function of the battery SOC (adapted from [14])*

interactions between lithium and the host structure are neglected, we would have that the Gibbs free energy is a concentration-dependent quantity equal to:

$$G(c_{Li}) = G_0 + c_{Li}\Delta G_0 + RT[c_{Li}\ln(c_{Li}) + (1 - c_{Li})\ln(1 - c_{Li})] \tag{1.12}$$

where G_o is the free energy of the host material without lithium, ΔG_o is the free energy change without configurational entropy per mole of lithium added and the last term is the free energy change coming from the possible configurations of the lithium in the interstitial sites of the host material, i.e. the configurational entropy dependent term. Deriving with respect to c_{Li} for both anode and cathode and putting the result in 1.10, we get:

$$\begin{aligned} E_{ocv} = -\left[\Delta G_{0,p} + RT\ln\left(\frac{c_{Li,p}}{1 - c_{Li,p}}\right)\right] - \left[\Delta G_{0,n} + RTln\left(\frac{c_{Li,n}}{1 - c_{Li,n}}\right)\right] = \\ = E_{0,p} - E_{0,n} + RT\ln\left[\frac{c_{Li,n}(1 - c_{Li,p})}{c_{Li,p}(1 - c_{Li,n})}\right] \end{aligned} \tag{1.13}$$

where $E_{o,p}$ and $E_{o,n}$ are the standard reduction potentials of the cathode and of the anode, and the third term is the concentration-related term of the cell open circuit potential. The standard reduction potential terms are obtained via the relation:

$$\Delta G_0 = -nFE_0 \tag{1.14}$$

with n equal to the number of moles of electrons transferred in the reaction, that in our case is equal to 1. From equation 1.13 we can see how E_{ocv} is related to the thermodynamic condition of the lithium ion battery at equilibrium conditions:

- the higher the temperature, the higher the battery voltage;
- the higher the concentration of lithium in the cathode and the lower the concentration of lithium in the anode, the lower the battery voltage. This explains why voltage decreases while discharging the battery and vice versa;
- the higher the difference between cathode and anode standard electrode potentials, the higher the battery voltage. This fact highlights the importance of the choice of the electrode materials.

Even when removing the ideality constraints, these considerations still hold true. During operation there will be additional voltage losses due to the effect of current, but the main trend will be dictated by the OCV.

An electrode open circuit potential curve (see figure 1.2) is measured against a reference lithium metal anode, whose constant chemical potential does not interfere with the trend of the cathode one. In this case, the anode-related terms in equation 1.13 are substituted with the lithium metal standard electrode potential, equal to 0 V, and we obtain only the OCP-SOC relation of the studied electrode material. The concentration of lithium in the electrode can be expressed in a dimensionless form as the electrode absolute state of charge SOC_{el}, through the relation:

$$SOC_{el} = \frac{c_{Li}}{c_{Li,max}} \tag{1.15}$$

where $c_{Li,max}$ is the maximum concentration of lithium that can be accepted by the electrode material. c_{Li} is the concentration on the surface of the particles of the electrode material.

The presence of voltage limits avoids the complete filling or emptying of an electrode, and the concentration of lithium that is present in the host at these limits can be expressed in a dimensionless form as:

$$\begin{cases} SOC_{min,n} = \frac{c_{Li,n}}{c_{Li,max,n}}\Big|_{V_{min},25°C} \\ SOC_{max,n} = \frac{c_{Li,n}}{c_{Li,max,n}}\Big|_{V_{max},25°C} \\ SOC_{max,p} = \frac{c_{Li,p}}{c_{Li,max,p}}\Big|_{V_{min},25°C} \\ SOC_{min,p} = \frac{c_{Li,p}}{c_{Li,max,p}}\Big|_{V_{max},25°C} \end{cases} \tag{1.16}$$

where V_{min} and V_{max} are the battery voltage limits, specific to the cell chemistry, measured at $25°C$ in equilibrium conditions.
The electrode absolute state of charge SOC_{el} can be rescaled in the 0−1 range as the electrode relative state of charge $SOC_{el}{}'$ if we take into account the amount of lithium that is present in the electrode when the voltage limits are reached, according to the formula:

$$SOC_{el}' = \frac{SOC_{el} - SOC_{el,min}}{SOC_{el,max} - SOC_{el,min}} \tag{1.17}$$

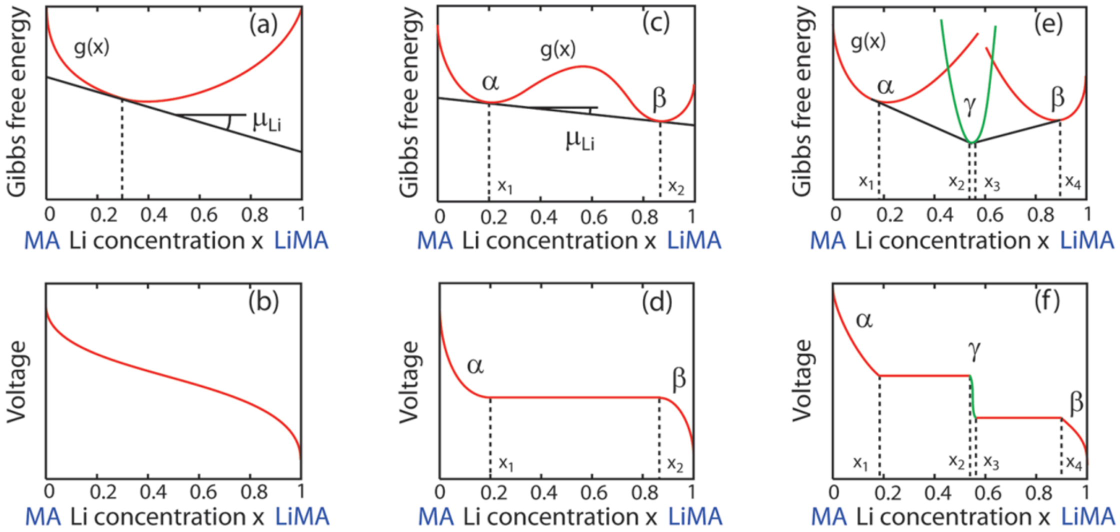

Figure 1.3: *Examples of different open circuit potential curves, showing their correlation with the Gibbs free energy of the Li-host compound. (a) and (b): single phase solid solution; (c) and (d): two phase solid solution; (e) and (f): two phase solid solution with intermediate single phase (Taken from [16])*

It is important to notice that at the upper voltage limit the anode relative state of charge is 1 while the cathode relative state of charge is 0, since almost all the available lithium is in the negative electrode. Vice versa at the lower voltage limit. Reminding the definition of battery SOC given with equation 1.3, we see that the anode relative SOC is equal to the battery SOC, while the cathode relative SOC is its complementary number.

Looking at figure 1.3, it is possible to notice how in reality the open circuit potential can strongly deviate from the ideal formulation described in equation 1.13, due to the effect of the interactions between the constituents of the electrodes and the cyclable lithium. According to the behaviour of the solid mixture(s) formed by lithium and the host material, there can be several cases [16]. Some examples are:

- a single solid solution, as in figures 1.3.(a) and 1.3.(b). The OCP curve is monotonously decreasing, quite similar to the ideal case;
- two phase solid solution, as in figures 1.3.(c) and 1.3.(d). The OCP curve shows a constant voltage part, due to the two phase behaviour of the solid solution between the Li-poor phase α and the Li-rich phase β, where μ_α=μ_β=constant;
- two phase solid solution with intermediate phase, as in figures 1.3.(e) and 1.3.(f). The OCP curve shows a two constant voltage part with an intermediate single phase behaviour. In between the Li-poor phase α and the Li-rich phase β there is a stable intermediate phase γ.

1.1.2 Overpotentials

When a current is applied to a lithium-ion battery, the trend of the voltage is still dictated by the OCV curve, but there is the addition of voltage losses that increases with current, also called overpotentials. These overpotential stem from the irreversibilities caused by the movement of a charged species in one or more media, and they can have three different natures [17]:

- **ohmic overpotential**: this voltage loss derives from the ohmic resistances inside the cell, and implies an instantaneous voltage drop/rise after the discharge/charge starts. It follows Ohm's law, and hence it is proportional to the applied current;

- **charge transfer overpotential**: when the electrochemical reactions are activated, in an electrode the electrons and the ions, i.e. the charges, are transferred between the different phases. This charge transfer reaction has a certain rate, and it requires the overcoming of an energy barrier (activation energy), which depends on the temperature, on the kind of reaction and on the requested current, proportional to the reaction rate. The higher the current, the higher the activation energy, which corresponds to an additional voltage drop. Also, the formation of space charge layers, also called double layer in solid/liquid interfaces, has to be taken into account [18, 19]. This layers act like capacitances, and hence they smooth the voltage profile of the cell during the first instants of the charge/discharge;

- **diffusion overpotential**: at high current rates, the diffusion processes of lithium in the liquid electrolyte and, more often, in the solid electrodes become dominant. The concentration of lithium on the surface of the solid particles, which controls the open circuit potential of the electrode, becomes different from the concentration of lithium in the bulk of the particles. Therefore, not all the available lithium will be utilized for the reactions due to the limitations induced by diffusion. The battery will reach the voltage limits with a lower exchanged charge with respect to the equilibrium. Please note that this is not a real overpotential that increases the irreversibilities of the reactions, but it can be seen as a "faster movement" on the OCV curve of the electrode(s) where the diffusion is limiting the flow of lithium inside or outside the solid particle (see Chapter 1.2), hence creating an unbalance between the surface and the bulk concentration.

1.2 Lithium-ion battery: components

After having defined the basic quantities in the previous section, we can analyse more in depth the lithium-ion battery structure, understanding better its advantages and its limits. Lithium-ion batteries are composed by an anode, a cathode, an electrolyte and a separator, plus the metallic current collectors that are necessary to connect the battery to the external load or charger.

1.2.1 Electrodes

The desirable characteristics for the LIB electrodes are:

- **high gravimetric capacity (or specific capacity)**: the capacity of lithium per unit weight that can be accepted by the anode material, measured in mAh/g. It is directly linked to the amount of energy that can be stored in the battery;
- **high volumetric capacity (or energy density)**: the capacity of lithium per unit volume that can be accepted by the electrode material, measured in mAh/cm^3. An high value of this quantity corresponds to smaller batteries for the same capacity;
- **low electrode potential**: to obtain an high cell voltage, the anode potential should be the lowest possible, while the cathode one should be the highest possible. The electrodes' voltages are measured taking as reference the lithium standard electrode potential of -3.0141 V, using V vs. Li/Li$^+$ as unit of measure. Therefore, the lithium standard electrode potential will be 0 V vs. Li/Li$^+$. We will always use this convention, but for the sake of brevity we will keep the symbol V;
- **high electronic conductivity**: the electrode should offer the lowest possible resistance to the electron flow, to avoid an excessive voltage drop;
- **high mechanical stability**: the continuous bidirectional reaction with lithium ions cause volume changes to the electrode, inducing mechanical stresses and eventually disordering the electrode structure. Therefore, the volume change during charge and discharge should be reduced to minimum;
- **high lithium solid diffusion coefficient**: in many materials, lithium needs to diffuse into and out the solid electrode structure during charge and discharge. If the solid diffusion is sluggish, there can be severe performance limitations with high current densities;
- **high thermal stability**: the electrode should be stable at high temperatures, with a marginal impact of thermally activated decomposition side reactions;
- **no side reactions with the electrolyte**: the electrode is always in contact with the electrolyte, and they should not cause undesired reactions that consume both electrode material and cyclable lithium;

- **no side reactions with lithium ions**: lithium ions can form inactive metallic lithium and lithium dendrites, which both imply power and capacity loss and safety issues. The electrode material nature and structure should not favour these reactions;
- **no toxicity and flammability**: these properties are fundamental for the safety of the lithium-ion battery in all the phases of its lifecycle;
- **low cost**

Anode

The anode is the negative electrode of a lithium-ion battery. As previously discusses, in this electrode, we observe an oxidation reaction during discharge and a reduction reaction during charge.
The most obvious choice would be the use of lithium metal as anode material, thanks to its very low and constant electrochemical potential (0 V), its very high gravimetric capacity (3860 mAh/g) and low density (0.534 kg/m³) [20]. Despite its lightness, it still retain an high volumetric capacity (≈1900 mAh/cm³). The straightforward redox reaction is:

$$\mathrm{Li}^{(s)} \xrightleftharpoons[\text{charge}]{\text{discharge}} \mathrm{Li}^{+} + \mathrm{e}^{-}$$

However, ionic lithium tends to deposit in an irregular way on the lithium metal anode surface, becoming inactive and reducing the cell capacity. In fact, this kind of anode has a low coulombic efficiency. Moreover, the deposited lithium forms needle-shaped structures called dendrites, that cause severe safety problems: dendrites can short-circuit the battery by piercing the separator and connecting the anode with the cathode [21]. For these two key problems, lithium metal anodes are not currently in use in LIBs, except in laboratory coin cells as reference electrodes for cathode materials.

Instead, carbon-based materials have established themselves as anode material of choice [22], thanks to their good theoretical gravimetric capacity (372 mAh/g), low potential (0.05-0.8 V) and the high reversibility of the intercalation reaction, corresponding to very high coulombic efficiency. In particular, graphite is now the leader in commercial batteries, owning 89% of the anode materials market share as of 2016 [13]. Graphite has a regular and stable layered structure, that favours the ordered insertion and deinsertion of lithium between parallel carbon layers. In this case, a possible intercalation reaction in the anode is:

$$\mathrm{LiC_6} \xrightleftharpoons[\text{charge}]{\text{discharge}} \mathrm{xLi}^{+} + \mathrm{xe}^{-} + \mathrm{Li_{1\text{-}x}C_6}$$

Intercalation in graphite is one of the most studied phenomena of lithium-ion batteries, and it results in a quite complex OCV curve, the outcome of the process called staging [24, 25]. Lithium firstly occupies interlayers that are distant to each other due to repulsion effects, before occupying more and more neighboring interlayers. This mechanism creates distinct Li-C solid phases, with large two-phase

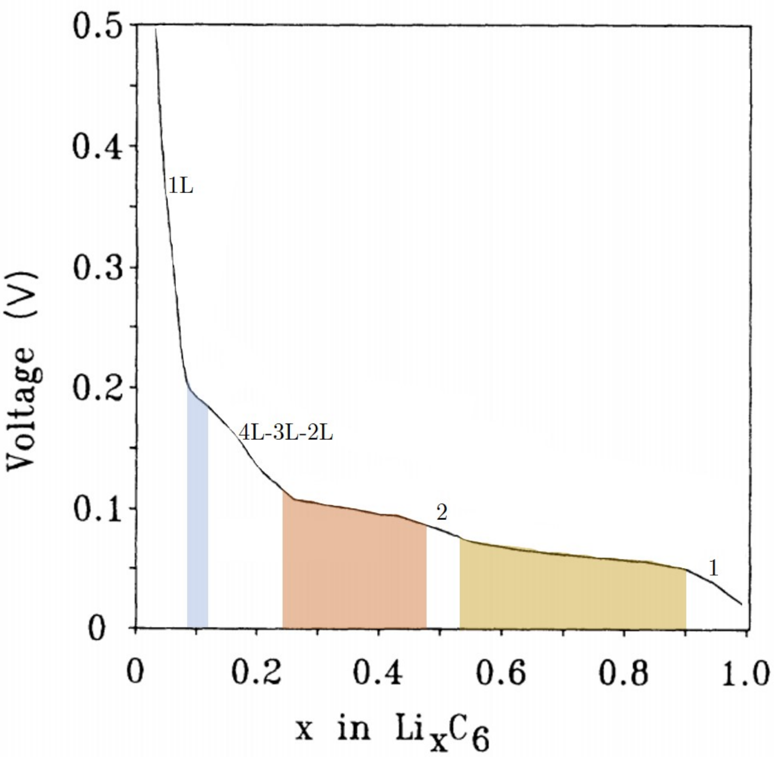

Figure 1.4: *Example of OCV curve of graphite, where the single phases are labelled with their name and the phase transitions are highlighted with different colours (Adapted from [23])*

transition regions that regularly occur at determined voltages. These phases are named with a number according to the nth interlayer that is occupied by lithium, and eventually a letter L that indicates a disordered, liquid-like behaviour of lithium in the interlayers if compared to the ordered behaviour in normal phases.

According to the literature on the topic [26, 27], at ambient temperature up to six different phases can be present (*figure 1.4*):

- **1L (≈LiC_{72})**: also called graphite solid solution. When lithiation begins, lithium occupies every available interlayer in a disordered manner. It is followed by a small phase transition towards the stage 4L;
- **4L, 3L, 2L (≈LiC_{36}, ≈LiC_{27}, ≈LiC_{18})**: increasing the concentration, lithium starts to occupy every fourth, then every third and then every second interlayer available, with a liquid-like behaviour. There are not distinct phase transitions between these three stages, and it seems that usually it exists a superposition of them [27];
- **2 (LiC_{12})**: the transition from the stages 4L/3L/2L to the ordered stage 2 is quite evident, and it can be identified as a voltage plateau at around 100-120 mV.
- **1 (LiC_6)**: the transition from stage 2 to stage 1 is well understood, and it sits around 85 mV.

Their presence strongly depends on the current rate at which the OCV curve is measured, since some phases are formed only with extremely slow lithiation. For instance, Dahn et al. [23] observed the formation of only four different phases with 1/80C, an 80 h discharge. In a subsequent work, Dahn [24] identified all the six phases with 1/800C, which corresponds to a 800 h discharge, but the 2L phase was very short-lived.

The disadvantages of the graphitic anode are its quite low volumetric capacity (330-440 mAh/cm^3), a not negligible 10% volume change during cycling and, most of all, the formation of a relevant solid electrolyte interphase (SEI) on the graphite-electrolyte interface. This layer consumes available lithium, reducing the cell capacity, and increases the overall resistance, hindering the power capability. It will be better described in the degradation section of the thesis (see section 1.3.2).

Other types of commercially available anode materials include:

- **Graphite-Silicon mixtures (C-Si)**: small amount of silicon are now usually added to the the graphitic anode by manufacturers (up to 5% wt) [28]. SI has a very high gravimetric capacity, exceeding 3000 mAh/g. Hence, even some traces can bring the gravimetric capacity of graphite anode to 400-500 mAh/g, overcoming its theoretical limit. As drawback, the electrode voltage is in average higher;

- **Amorphous carbons (C)**: disordered carbon structures, as hard and soft carbon, represent a small market share of the commercial anode material (≈7%) [13]. Their structure is full of configurational defects in which lithium can intercalate, increasing the theoretical limit of 372 mAh/g, and they have a lower cost than graphite. Nevertheless, their high specific surface favours the formation of an high amount of SEI, limiting the cell available capacity;

- **Lithium Titanate (LTO)**: $Li_4Ti_5O_{12}$ is an anode material that is thermally stable, has zero volume change during cycling and a good volumetric capacity (≈600 mAh/cm^3). It has an exceptional coulombic efficiency, since the SEI is barely present in this kind of electrode. However, it shows an high electrode potential (1-2 V) that severely limits its specific capacity (175 mAh/g), and the cost of titanium is way higher than the one of graphite [11]. For these reasons, the use of LTO is limited to some high power application, with a very small 2% market share.

The anode materials are manufactured as a fine powder with an average radius in the order of micrometers. A binder agent [29, 30] is required to consolidate the porous electrode structure, counteracting to volume changes, and to bind the anode powder to the anode current collector, that it is usually made of copper [31]. Additional agents as carbon black can be added to the anode to improve electronic conductivity, but this is less important than in cathodes thanks to graphite good conductive properties.

Cathode

The cathode is the positive electrode of a lithium-ion battery. In this electrode, we observe a reduction reaction during discharge and an oxidation reaction during charge. The desirable characteristics for a LIB cathode are almost the same of the anode. The only difference is that cathodes require a high electrode potential, in order to obtain a high voltage battery. During the years, lots of cathode materials have been proposed and there is plenty of research in this field [12]. The ones that managed to get into the market belong to the categories of transition metal oxides and polyanion compounds. The commercially available cathode materials are:

- **LCO**: $LiCoO_2$ was the first metal oxide to be employed in commercial LIBs [32]. LCO has a layered structure with an high theoretical gravimetric capacity (274 mAh/g), very high theoretical volumetric capacity (1363 mAh/g) and an high electrode voltage (up to 4.5 V). However, its main limitation is that the voltage has to be capped to 4.2 V to avoid structural disordering due to deep delithiation, halving its capacity [33]. Moreover, it has a low thermal stability, and cobalt is an expensive and toxic material;

- **NCA**: cobalt can be effectively substituted by nickel, another transition metal which is much more cheaper and less toxic while retaining a high specific capacity. Still, nickel has the tendency of occupying the sites in the cathode structure available for lithium ions, hindering lithium diffusion [34]. Hence, the addition of a part of cobalt improves the stability of the material. Including also a fraction of aluminum can enhance the thermal stability and reduce the impedance rise due to the formation of an electrolyte interphase on the nickel-cobalt cathode [35]. As a matter of fact, layered $LiNi_{0.8}Co_{0.15}Al_{0.05}O_2$, or NCA, is now used in electric vehicle applications thanks to an high theoretical gravimetric capacity (279 mAh/g), high theoretical volumetric capacity (1284 mAh/g) and a wide voltage operating range. However, the interphase formation on the cathode is enhanced when exceeding 40°C, inducing severe capacity fade [36];

- **LMO**: pure manganese cathodes are commercially available as $LiMn_2O_4$, the three-dimensional spinel form of this transition metal oxide. It is a more stable structure compared to the two-dimensional layered form [37], but still LMO suffers from substantial degradation during lifecycle, and it has the lowest gravimetric capacity among commercial cathodes (148 mAh/g). Its main benefit is the very low cost of manganese if compared to the other commonly used elements;

- **NMC**: manganese is another cheap and environmentally friendly material that is suitable as a component of cathode electrodes. However, in layered $LiMnO_2$, manganese is prone to dissolve in the electrolyte, disordering the cathode structure and enhancing the graphite anode SEI formation [12]. Therefore, nickel and cobalt are added to highly improve the structural stability of the manganese compounds. Layered $LiNi_{0.33}Co_{0.33}Mn_{0.33}O_2$, or NMC 111, has found widespread application in lithium-ion batteries, due to its very high theoretical gravimetric and volumetric capacity (280 mAh/g and 1333 mAh/cm³) and the very high coulombic efficiency. The research efforts are going towards the increase of the nickel content in NMC, as NMC 632 or NMC 811 [38], to reduce the presence of toxic and expensive cobalt and increase the specific capacity by lowering the percentage of manganese;

- **LFP**: among polyanion compounds, $LiFePO_4$, or LFP, is the only one that is commercially available. It is a very thermally stable material, capable of sustaining well high current rates. It has a quite low theoretical gravimetric capacity (170 mAh/g), but, unlike transition oxide metal, the high LFP electrochemical stability allow the utilization of almost all this theoretical capacity [39]. As drawbacks, its average voltage is quite low, and the electronic conductivity and solid diffusivity of lithium are very limited. To overcome this disadvantage, LFP particles are manufactured to have the average radius in the order of nanometers, compared to transition metal oxides particles radius that is in the micrometers range.

In commercial batteries, it is possible to find cathodes formed by the blending of two intercalating materials With this technique, manufacturers try to adjust the advantages and disadvantages of two different materials, creating more balanced cathodes with mixed properties.

Transition metal oxides and polyanion compounds can show poor to very poor electronic conductivity due their semiconductor behaviour [40]. This fact can severely hinder the lithium redox reaction, which requires the presence of free electrons. Consequently, cathode materials are enhanced with electronically conductive particles, often made of carbon black, in order to overrun this drawback [41]. Hence, along with the required binder like in anodes, in porous positive electrodes there is this more additional electrochemically inert material due to their worst conductive properties. The cathodic current collector is made of aluminum, which it is not corroded at the high voltages of cathodes [31].

1.2.2 Electrolyte

The role of the liquid electrolyte solution in LIBs is the transport of lithium ions between the anode and the cathode during the charge/discharge process [42, 43]. Lithium ions can be transported by migration, i.e. by a potential difference, and by diffusion, i.e. by the driving force created by the lithium concentration gradients in the electrolyte.

An electrolyte solution is made up of three components:

- an **electrolyte salt**, that it is dissolved into Li^+ and an anion, thus providing the electrically conducting solution to the system. Lithium hexafluorophosphate ($LiPF_6$) is the dominant choice among electrolyte salts for LIBs. It is not so thermally stable, and it is very sensitive to water, making more difficult and costlier its manufacturing and handling. Nevertheless, other possible salts are even more limiting than $LiPF_6$ [43];

- an **electrolyte solvent**, that dissolves the electrolyte salt, allowing the formation of an ionic current. Liquid solvents can be aqueous, i.e. water, or non-aqueous, as organic molecules. In case of LIBs, the aqueous solvents have a much smaller potential stability window than non-aqueous one, and so the latter are the only one that are commercially employed. However, aqueous solvents are inherently safer, and they do not present flammability or toxicity problems, and research efforts are going towards the development of stable water-based electrolytes [44, 45];

- **electrolyte additives**, tailored on the specific chemistry and on the purposes of the LIB. They can made up to 5% wt of the electrolyte solution, and they can serve to several purposes, such as SEI controllers, electrolyte salt stabilizers, current collectors corrosion inhibitors, cathode protectors, safety enhancers and Li^+ deposition improvers [46];

The desirable characteristics for an electrolyte solution are:

- **high ionic conductivity**: the key property for an electrolyte, that quantifies how much ions are mobile in the solution, and hence their availability for the electrochemical reactions. To obtain an high ionic conductivity, it is needed that the solvent shows a high dielectric permittivity, to dissociate well the salt in cations and anions, and a low viscosity, to allow a smooth ion transport [42]. No single solvent has both these qualities, therefore commercial LIBs contain mixtures of solvents that are characterized by the first property, as ethylene carbonate (EC), and by the second property, as dimethyl carbonate (DMC), diethyl carbonate (DEC), and ethyl methyl carbonate (EMC) [47]. In commercial batteries, electrolyte salts are dissolved into solvents with concentrations ranging from 800 to 1500 mol/m^3, depending on the solvent mix, in order to optimize the value of ionic conductivity;

- **high lithium diffusion coefficient**: while conductivity is related to the ability of an ion to pass through a medium when there is an external electrical field, the diffusivity represents the ability to pass through a medium where there is a species concentration gradient. It can be demonstrated that ionic conductivity and diffusivity are the same property and that they are directly correlated [40]. Therefore, an high ionic conductivity will assure an high lithium diffusion coefficient;

- **high lithium transference number**: this number represents the amount of cations, i.e. lithium ions, that are transported by the ionic current with respect to the total migration flow of cations and anions. An high transference number is important because the current that matters is the cationic one, and the information given by the ionic conductivity is on the total ionic flow [47]. Usually, the transference number of commercial LIB electrolytes lies in the 0.2-0.4 range;

- **high thermal stability**: the electrolyte should be stable at high temperatures, without decomposing and generating dangerous products, as gases;

- **electrochemical stability**: the electrolyte should be stable in the whole voltage range in which the battery operates, so between 0.05-0.5 V for the anode and 3.8-4.5 V for the cathode. If not, the electrolyte can decompose and form solid electrolyte interphases (SEI) on the anode and/or on the cathode;
- **no toxicity and flammability**: these properties are fundamental for the safety of the lithium-ion battery in all the phases of its lifecycle;
- **low cost**

Solid state electrolytes could be one of the most interesting improvements of LIBs in the next future. Their higher thermal and (sometimes) electrochemical stability can greatly improve LIBs safety and widen the voltage and thermal operating range. Moreover, only lithium ions are transported with the ionic current, improving the power capabilities of batteries. However, they are still in a phase of research and development, and problems about interface kinetics with the electrodes needs to be solved [48].

1.2.3 Separator

The separator is a porous solid barrier which has the purpose to physically separate anode and cathode, preventing short-circuits, while allowing the flow of ions through the electrolyte. It also acts as a fuse in case of battery malfunctioning, since it can melt when critical temperatures are reached, closing its pores and hence cutting the ionic current between anode and cathode. The ideal properties for separators are high wettability, high mechanical and thermal stability, fusibility at determined temperatures, no electronic conductivity to avoid battery self-discharge, electrochemical stability and small thickness [49]. In commercial batteries, they are commonly made of polyolefins, often covered by a ceramic coating, with a thickness in the 10-20 μm range [13].

1.3 Lithium-ion batteries: degradation

Lithium-ion batteries are time-variant systems, since their performances depend on the actual state of its constituents, that varies in time. The electrodes and the electrolyte properties continuously change with respect to the battery beginning of life (BOL), due to unwanted side reactions that degrade in various ways these components.

This is the reason why LIBs have to be replaced after a certain time, since they can show both a capacity fade and a power fade caused by these degradation reactions. In the EV industry, the common threshold for the end of life (EOL) of a LIB is when it retains 80% of the initial capacity or of the initial power [50]. Even if this number is quite arbitrary [51] and not so usually reached in the eight-years long warranty period of EV lithium-ion batteries [52], the remaining available capacity and power could be more than enough for other less demanding applications. This concept is the foundation of the battery second use (B2U), which aims to increase the useful lifetime of EV lithium-ion batteries, obtaining several benefits.

Of course, for such an objective, it is of the foremost importance to understand how the components of the battery degrade, which are the effects of degradation and how to effectively detect them, predicting the future behaviour of the battery.

1.3.1 Circular economy of lithium-ion batteries

The destination of lithium-ion batteries after their end of life is quite an open issue. Until now, the low volumes of spent LIBs, mostly coming from consumer electronics, has not driven much innovation in the sector, due to the classic chicken-and-egg problem. However, the recent surge in electric vehicle sales and the spreading of energy storage systems will bring increasing quantities of LIBs at their EOL in the next years [53] (see figure 1.5).

The number of facilites that are able to recycle LIBs are increasing, and currently seems that they are able to process around 50-60% of the yearly disposed batteries [54]. The high-temperature pyrometallurgical and low-temperature hydrometallurgical processes recover pure materials, while the direct cathode recovery process is used to directly obtain a new positive electrode from the spent battery [55]. The available recycling processes are feasible from an economic and environmental point of view only if there are considerable percentages of precious and energy-intensive metals that can be recovered, i.e. cobalt and nickel in LCO and NMC batteries [56]. If not, LIB recycling plants have to be subsidised, and anyway their profitability is strongly linked to the quite volatile market prices of these metals. Moreover, the tendency is to lower the amount of cobalt in batteries due to the toxicity and the cost of this material, further hindering the economic viability of recycling.

The other option for the EOL management is the battery second use, or battery second life, which means the repurposing of aged batteries for uses that are

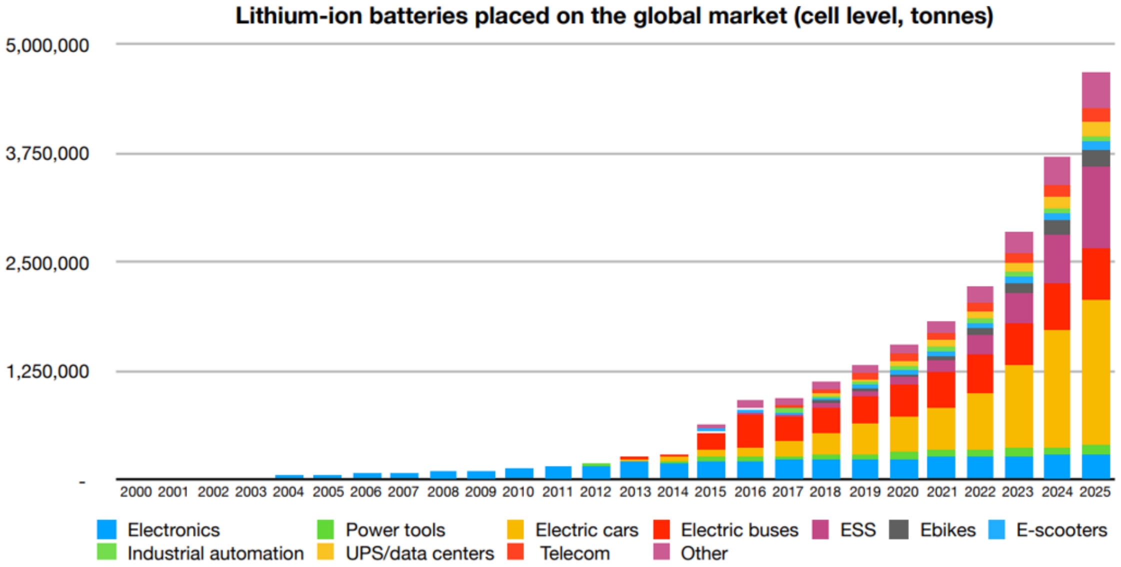

Figure 1.5: *Lithium-ion batteries placed on the market, in tonnes, with forecast to 2025 (Taken from [53])*

different from the original one. In a circular economy framework, reuse should be preferred to recycling, since it consumes much less energy and it directly provides a ready-to-use product instead of pure materials or single components [57].

Focusing on the electric vehicle case, we mentioned how retired EV batteries can retain 80% or more of their initial capacity or power. For electric vehicle users, it is fundamental to have maximum performances and autonomy throughout all the car lifetime, and the battery needs to maintain quite high specific energy and power, since it has to stay in the very limited space available in a road vehicle. This is why EV batteries have these strict EOL requirements. Instead, energy storage systems (ESS) are much less demanding, thanks to their modular structure, the removal of the available space limitation and the more [58]. Also, light-duty EVs such as e-scooters or e-bikes are more and more adopted in urban environments, and their capacity and power requisites are a fraction of cars' ones.

These two applications (especially the first one) can be the key for battery second use, with several benefits for the entire lithium-ion battery value chain:

- **reduction of environmental impact**: depending on the electric energy mix with which the EV is fueled, the LIB production phase can account for 10-20% of the life cycle GHG emissions and 20-50% of the toxicity indicators for the environment of an electric car [59]. These figures increase with cleaner energy mix as input for the vehicles. The extension of the battery lifetime by 10-20 years can reduce this impact by avoiding the production of new batteries for the systems in which second-life batteries are employed and delaying the recycling process;

- **decreased upfront cost of EV**: leasing is the commonly used business model for the battery pack of an electric vehicle, hence Original Equipment

Manufacturers (OEMs) retain the ownership of the battery after their retirement [60]. The revenue streams that come from B2U can be taken into account to reduce the leasing fee for customers (between 5 and 25%) [61], decreasing the overall EV cost;

- **lower investment costs for ESS**: in 2015, the potential difference of the cost between new and repurposed LIBs was estimated to be between 30 and 70%, depending on the first-life degradation rate and on the second-life use [62]. Therefore, the investment cost for energy storage systems in which second use batteries are employed can be quite reduced, with lower barriers for the implementation of such fundamental systems for the integration of renewable energy in the electric grid. All the pilot projects of B2U are directed towards ESS solutions, with car manufacturers as project sponsors [60];

Nevertheless, B2U faces several important challenges that needs to be solved for an economically viable and scaled implementation:

- **Degradation identification**: the value that can be extracted from second-life batteries strongly depends on their remaining lifetime and on the power performances. Without reliable data about the capacity and its future trend, it is quite hard to implement them in energy storage systems, since the ESS profitability and operation strategy (e.g. frequency regulation, behind-the-meter time of use, energy time shift) depend on the battery capabilities [62]. High uncertainties on the state of health can hinder the adoption of B2U. For this reason, it is of foremost importance to identify the degradation mechanisms that are affecting the battery and infer the future trend of the capacity and power fade. Ideally, this should be made at a cell level, since in battery modules the aging process is quite heterogeneous, and the worst performing cells limit the overall performances [63]. Enabling the possibility to rearrange battery packs and to group together cells with similar degradation characteristics will allow the creation of more homogeneous and reliable second-life batteries;

- **Battery handling and disassembly**: battery packs have to be disassembled in order to test and repurpose the cells for B2U. This phase can be quite dangerous, because of the safety hazards of handling lithium-ion batteries, such as short-circuits and thermal runaway [57]. Actually, the disassembling is performed manually by specialized operators, but with the forecasted high volumes of potential second-life batteries, the automation of the process has to be implemented [64] to avoid bottlenecks and high refurbishment costs. The absence of a standard for battery packs (different for every car manufacturer), cells (cylindrical, pouch, layered, coin) and support materials (glues, bolts, cases) implies a hard challenge for this delicate process. This fact shows the importance of the inclusion of circular economy principles in the design phase of lithium-ion batteries;

- **Diagnostic tests**: like the disassembly phase, also the diagnostic of cells lacks a standardized and automated procedure. A variety of techniques are studied and/or used [65], but only the most simple and less insightful ones have reached a quite widespread use. The normalization of this phase will decrease the refurbishment costs and will increase the reliability of the remaining lifetime prediction. Moreover, in a market logic, the full comparability of the diagnostic results will allow an unbiased choice of the best second-life product.

This thesis will deal with the first and the third problems, and hence in the next sections, before introducing the thesis specific objectives, we will briefly discuss about the state of LIB degradation identification and diagnostics.

1.3.2 Degradation mechanisms

The topic of lithium-ion batteries degradation has been thoroughly studied during the years [66–68], and there is a widespread accordance on the mechanisms and on the related causes of degradation.

As we already mentioned, degradation can affect both the energy and power capabilities of a LIB. For the first quantity, we observe a capacity fade, which corresponds to a decrease of the available lithium that can be cycled between the anode and the cathode (**loss of lithium inventory, LLI**) or to a reduction of electrochemically active material sites in both electrodes (**loss of active material, LAM**). For instance, in electric vehicles a capacity fade corresponds to a decrease of the available range. For the second quantity, we have a power fade, where there is an increase of the battery impedance due to the formation of additional resistive layers in the electrodes, a decrease of the conductivity of the existing ones and a decrease of the specific active area for the electrochemical reactions (**resistance increase, RI**). Power fade also occurs with the LAM, since this degradation mode reduces the amount of surface available for the electrochemical reactions, with an effect that is comparable to the decrease of specific active area [69]. Keeping the example of electric vehicles, a power fade corresponds to lower acceleration, maximum speed and drivability.

The mechanisms that induce this worsening of the overall performances of LIBs are (see figure 1.6):

- **SEI growth**: the solid electrolyte interphase, or SEI, is a layer that is generated on carbonaceous anodes after the first charge of the battery. Since the non-aqueous electrolyte is unstable at low potentials, at around 0.8 V it is reduced on the active carbon surface, forming an interface, i.e. the SEI, composed by inorganic and organic products of the salt and solvent degradation [70]. Its composition strongly depends on the electrolyte formulation, but generally it is made by C, Li and salt/solvent components, as P, F, or Br [71]. Its permeable structure allows the flow of lithium-ions, and it protects the anode from further contacts with the electrolyte. Therefore, after the first cycle, the SEI growth rate is strongly reduced thanks to the protective action of the SEI itself that separates the anode and the electrolyte The SEI consumes cyclable lithium, inducing a capacity fade, and it creates an additional layer that has to be crossed by the ionic current, hence increasing the overall cell resistance and causing a power fade. The SEI growth continues during the battery lifetime, and it is enhanced by high temperatures, high voltages and high current rates, all factors that favours the SEI formation reactions kinetics. An electrolyte interphase can be also present on the cathode side if the cathode voltage reaches high values that can favour the electrolyte oxidation. It is usually called Cathode Electrolyte Interphase (CEI), but its formation and growth is not generally limiting for LIBs performances [72];

- **SEI decomposition**: the SEI is not stable at high temperatures, and it can show a damage-reformation cycle that alters its structure and properties [73]. In particular, the SEI decomposition allows the contact between the anode and the electrolyte, inducing the formation of additional SEI and further capacity and power loss;

- **Electrolyte decomposition**: as we have seen describing the SEI, all the electrolyte components are involved in side reactions, and hence their concentrations in the solution is modified. Since the electrolyte salt concentration is optimized for maximum ionic conductivity, its variation induces a loss of conductivity, with the consequence of a resistance increase in the cell. Moreover, the electrolyte can degrade also because of high temperatures, forming dangerous gases [74];

- **Binder decomposition/loss of electric contact**: the binder and the conductive additive keep stable the anode/cathode structure, also ensuring that all the electrochemically active particles are connected together. High temperatures can induce binder decomposition reactions, and during cycling the volumetric expansion or/and the fracturing of electrode materials can also influence the binder-additive structure, isolating active particles from the whole electrode, i.e. a LAM [75];

- **Graphite exfoliation**: the layered structure of graphite is altered by the interaction with the electrolyte. The carbonate solvents can cointercalate with lithium in the interlayers, and the gases produced by the electrolyte decomposition reactions can exfoliate the anode structure [76]. Graphite exfoliation isolate active electrode particles, inducing a loss of active material;

- **Structural disordering**: both the electrode structures can suffer from high reaction rates, i.e. high currents, in particular lithiation states. For instance, highly lithiated LMO changes its cubic structure into a tetragonal one, with a phase change that causes binder decomposition and particle cracking [67]. Instead, the graphite anode should not be brought to its most delithiated states with high current loads in order to avoid the degradation of graphite into disordered carbons [77];

- **Lithium plating/dendrite formation**: in the negative electrode, overpotentials due to high charging currents can bring the overall electrode potential below 0 V. In this potential range, the deposition of lithium becomes thermodynamically allowed [78]. If the lithium ionic current is too high to be accepted by the graphite structure with the intercalation reaction, the plating reaction occurs, consuming cyclable lithium [79]. Metallic lithium can form a film on the graphitic anode, which increase the overall impedance of the cell by the removal of active sites, and also dendrites, whose needle-like structure can potentially pierce the separator and create short-circuits. Lithium deposition is enhanced by low temperatures, which decrease the solid diffusion coefficient of lithium in graphite;

- **Electrode particle cracking**: the fracture of electrode particles can happen both in anode [80] and cathode [81]. This phenomenon is caused by mechanical stresses, due to phase transitions and volume variations. Particle cracking expose active particles to the electrolyte, increasing the SEI or CEI formation, and it can isolate parts of the electrode;

- **Transition metal dissolution**: transition metal oxides cathodes can suffer from the dissolution of the transition metals embedded in their structure due to very low or very high voltages [82]. For instance, in LMO cathodes the manganese disproportionation reaction occurs at low potential, and it removes some Mn ions from the positive electrode structure, substituting them with Li ions. The Mn ions are transported by the electrolyte to the anode, where they enhance the SEI formation. Instead, at high potentials there are dissolution reactions both in LCO, for irreversible structural changes, and LMO cathodes, for the interaction with fluoridric acid (HF), which is formed by the electrolyte hydrolysis with water impurities due to the manufacturing process;

- **Corrosion of current collectors**: the copper (anode) and aluminum (cathode) current collectors can experience corrosion due to very high potentials for Al or very low potentials for Cu. Also, the effect of HF enhances Al degradation [31]. This mechanism increases the impedance of the cell, due to the lower amount of conductive material, and reduces the active sites for the lithium intercalation, since metallic ions can deposit on the electrodes surface.

1.3.3 Degradation diagnostics and identification

As we have seen, the causes of degradation are numerous, and most importantly they are strongly interdependent. Very different mechanisms can be due to the same stressors and they can bring to the same degradation modes, often disguising and/or enhancing each other.

For instance, in literature it is reported how lithium-ion cells exhibit a sudden exponential capacity decrease [62] (“ageing knee”) after a certain number of cycles that had a linear ageing trend, depending on the battery type and on the operative conditions. The identification of the onset of this phenomenon is very important for B2U, since after the ageing knee the battery capacity sharply reduces and they need to be substituted. This nonlinear behaviour has been attributed to the occurrence of lithium plating enhanced by other degradation mechanisms [83], to an exponential behaviour of LAM that is initially hidden by a linear behaviour of LLI [84, 85] and to the oversizing of negative electrode compared to positive electrode which postpones the effect of LLI and LAM [84, 86]. Each of

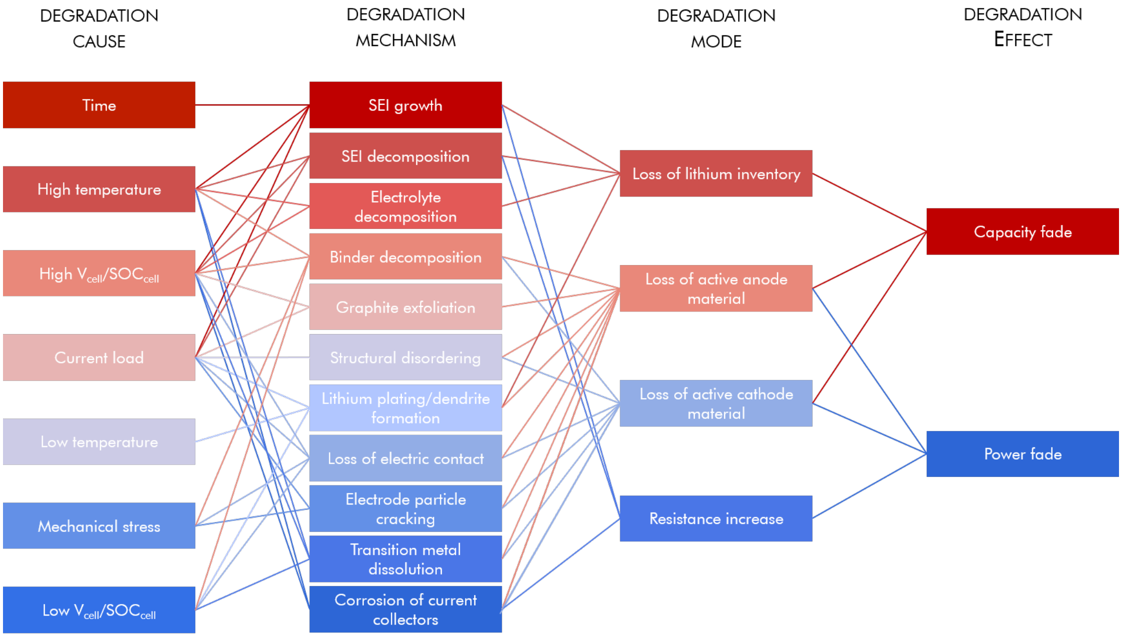

Figure 1.6: *Summary of degradation mechanisms with the related causes and effects in lithium-ion batteries. (Adapted from [69])*

these explanations are acceptable to elucidate the origin of the aging knee, and they can fit different used batteries according to their chemistry and first-life history.

The inherent complexity of the degradation phenomena is commonly summarized in a parameter called state of health (SOH). This indicator has not a standardized definition: the simplest one refers to the ratio between the actual maximum dischargeable capacity Q_{max} measured with the same conditions of the nominal capacity, and the nominal capacity Q_{nom} [87]:

$$SOH = \frac{Q_{max}}{Q_{nom}} \tag{1.18}$$

but it can also be related to the achievable peak power [88], to the DC [89] or AC [90] cell internal resistance or to more complex evaluations on the overall state of the cell [84]. The best representation of the battery state of health should comprehend different features of the battery itself, such as a combination of the listed parameters, in order to take into account all the aspects that contribute to degradation and to have a sound prediction of the remaining useful life (RUL) that considers also nonlinear and hidden effects.

The state of health determination stems from the execution of diagnostic tests, after which the SOH can be calculated or estimated with a variety of techniques [87] (e.g. direct measurement, model fitting, data filtering, data-driven approaches). There are different types of diagnostic tests too [65], that can give insights on certain characteristics of the LIB with varying degrees of accuracy and speed without altering the structure of the LIB itself (non-invasive tests). Some of them will be presented in the first part of chapter 2, since they have been employed during this thesis work.

In literature and in diagnostic standards, it is often used only one kind of test to characterize a LIB, usually the capacity test at different temperatures and current rates [91]. Nevertheless, it has also been shown how the use of more advanced techniques and the combination of them permit to understand much better the nature of a complex phenomenon such as degradation [65, 92]. In fact, the most insightful approach should be the one that exploits the strengths of each one of these tests, by combining them in an intelligent way that gives the maximum amount of useful data in a reasonable time frame.

Then, the information gathered during diagnostics should be analysed with a sound model that synthesizes the characteristics of the battery and how degradation occurred with some key parameters. In fact, we propose the use of a physically-derived model of lithium-ion batteries, adapted to the purpose of our work, in order to fit the experimental data coming from several techniques to a tool that can extend the outcome of the analysis to different conditions from the ones tested, thanks to the generality of the underlying equations of the model.

1.4 Thesis objectives

This master thesis is the context of the interdepartmental CIRC-EV project, which has the objective to enable the circular economy of lithium-ion batteries through the development of an automated and rapid disassembly, diagnostic and repurposing process of aged battery packs.
The MRT Fuel Cell & Battery Laboratory, where this thesis was developed, is working on the diagnostic part, with the objective of developing a sound and fast battery test procedure with the support of an electrochemical model of LIBs (see chapter 4) for the degradation identification.
A previous thesis work on the same project [93] dealt with the preparation of the test bench and the execution of an experimental campaign of battery stress tests at different current loads. It also verified the feasibility of the identification of degradation modes from battery experimental data with the electrochemical model.

The **research question** of this master thesis is: is it possible to estimate the lithium-ion battery defining parameters through a physical model, by using data coming from different diagnostic tests that give the maximum amount of insightful information on the battery with a limited duration of the experiments?

The steps with which we will try to answer this question are:

1. execution of an **experimental campaign** on commercial battery samples, to understand the information that are provided by three techniques in a variety of operative conditions: the capacity test, the relaxation test and the electrochemical impedance spectroscopy (EIS);

2. realization of a **sensitivity analysis** of the LIB physical model with respect to the battery parameters, simulating a wide operative condition matrix of the three diagnostic tests. Detection of the best conditions for the identification of the battery parameters through the results of the sensitivity analysis, and formulation of a test methodology;

3. implementation of the **proposed methodology** in a data fitting algorithm, making the calibration and the validation with the use of both simulated and experimental datasets.

The objective is to facilitate the development of a diagnostic test procedure for used LIBs that can readily detect the parameters that are linked to degradation effects [94], in order to understand its current state and infer about the remaining lifetime. Moreover, the sensitivity analysis can be a useful general tool to understand the behaviour of the LIB physical model in different operative conditions.

Chapter 2

Methodology

In this chapter, we will first describe the experimental techniques that are utilized in this work to test lithium-ion batteries (see Chapter 3). Then, we will present the LIB model that will be employed in the sensitivity analysis, with the improvements made to it. (see Chapter 4).

2.1 Experimental techniques

2.1.1 Capacity tests

The most widespread diagnostic technique for lithium-ion batteries is for sure the capacity test, that can be done both in charge and discharge. With this technique, it is possible to measure the voltage-capacity relationship of the battery, which depends on the C-rate and on the temperature at which the test is made. According to the international standards and the recent literature, capacity tests can have a current rate between 0.1C and 10C and an operating temperature between $-20°$C and 45°C [65].

The higher the C-rate of the test, the higher is the influence of the kinetic parameters of the battery that induce voltage losses, i.e. ohmic resistances, activation energies and diffusion, with a decrease of the discharged or charged capacity. For low C-rates, the voltage losses are much more limited, hence allowing the battery to receive or release more energy. In fact, the nominal capacity of the battery is commonly measured at a quite low C-rate, between 0.2C and 1C.

For the degradation diagnostics, this kind of test is useful to understand the remaining capacity of the LIB and estimate the impact of the resistances on the voltage curve. The choice of the test C-rate depends on the aspects that are investigated and on the desired duration of the test.

The capacity test procedure is the following:

1. Assuming that initially the battery is at a random state of charge, it has to be fully charged to 100% SOC in order to measure its whole available capacity. Therefore, the battery is charged in two steps. The first one is the **constant current (CC) step**, where the charging current I is kept constant, at a value specified by the manufacturer that usually is around 1C. This step ends

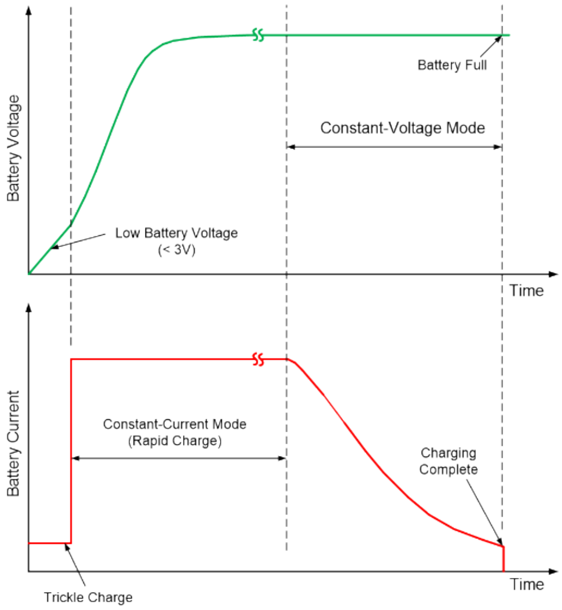

Figure 2.1: *Example of voltage and current trends in a CC-CV charge process*

when the battery voltage V reaches the upper voltage limit, a safety value specified by the manufacturer;

2. At this point, the battery is not fully charged yet. In case the circuit was opened, there would be a voltage drop equal to the overpotentials induced by the charging current (see Chapter 1.1.2). It is important to remind that we consider a battery at 100% SOC if its voltage at rest is equal to the upper limit voltage. Therefore, the second step of the charging process is a **constant voltage (CV) step**, where the current is gradually reduced to keep the voltage constant by reducing the overpotentials while continuing to charge the battery (see figure 2.1). The process stops when the current reaches the so-called termination current, usually 5-10% of the nominal one, when the battery is considered to be at equilibrium when the circuit is opened, i.e. the voltage remains at its upper limit value. In reality, there is still a drop due to residual overpotentials, in particular the one related to the concentration disequilibria. The species diffusion processes in the electrolyte and (mostly) in the electrodes are characterized by high time constants, and the strong concentration gradients caused by the high-current CC step can be still present after the end of the CV step. When the current is reduced and then removed, the gradients tends to zero, with a consequent change in the cell voltage. This mechanism will be better explained when describing the relaxation test in section 2.1.2.
   An even lower termination current would remove also this residual voltage drop, but the time required to complete the charge would become too high, so this approximation of a steady state is accepted.

3. when 100% SOC is finally reached, the battery can be **discharged** with a determined current rate down to the lower voltage limit, without a CV step. Manufacturers usually employ 0.5C or 1C to determine the nominal

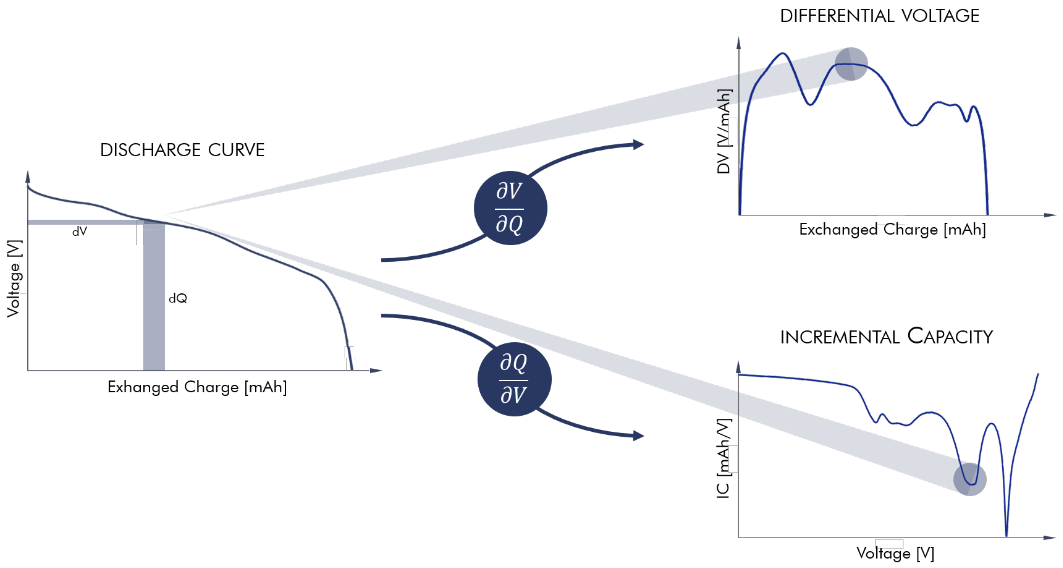

Figure 2.2: *Example of incremental capacitance and differential voltage, with their relations with the discharge curve*

capacity, while in research works also higher or lower C-rates are used for an in-depth study of the battery behavior. The voltage and eventually the surface temperature of the cell are registered as outputs. The capacity is commonly calculated with the coulomb-counting method, which practically is the integration of current in time seen in equation 1.1, discretized according to the data acquisition timestep.

If the current employed in capacity tests is very low (indicatively, less that 1/10C), the battery OCV curve of can be obtained with an acceptable degree of approximation, in a test that lasts at least 10 hours [95]. With this curve, it is possible to calculate the **incremental capacity (IC)** and the **differential voltage (DV)**, which are respectively the derivative of the capacity with respect to the voltage and vice versa:

$$IC = \frac{\partial Q}{\partial V} \tag{2.1}$$

$$DV = \frac{\partial V}{\partial Q} \tag{2.2}$$

At such low current rates, the IC and the DV represent the thermodynamic characteristic of the electrodes. These quantities permit an in-depth analysis of the state of the electrode materials and of the amount of lithium present in the battery [84]. In fact, phase transformations (see Chapter 1.1.1), which corresponds to flat voltage regions in the OCV curve, are enhanced by the derivatives and they are represented as peaks in the IC and plateaus in the DV (see figure 2.2). The change in the position and magnitude of these features can suggest the occurrence of loss of active material and loss of lithium inventory, with the possibility to attribute the degradation modes to the single electrodes [86, 96, 97]. These techniques were extensively analyzed in the previous thesis work on the same project [93].

2.1.2 Open circuit voltage tests

With capacity tests, even if the current rate is very small, the effects of kinetics is always present, and hence the real thermodynamic characteristic is not obtainable without approximations. However, OCV can be achieved by perturbing the battery and allowing it to relax with no current applied, measuring the value of the voltage after a certain time in which it is assumed that the battery reaches full equilibrium. This method is called **Galvanostatic Intermittent Titration Technique (GITT)**, and it allows to reconstruct the OCV curve with several points acquired by current pulses followed by relaxation. By increasing the number of measured points and the duration of the relaxation period, the accuracy of the OCV curve is increased too. However, the time needed for a GITT test, that can span from some hours to a couple of weeks [65], grows proportionally to the desired accuracy. Moreover, the OCV curve can be different whether the GITT is made in charge or in discharge due to the effect of phase transformations, a phenomenon called voltage hysteresis [98]. With a GITT test, we are able to determine the solid diffusion coefficient of lithium in an electrode material, in an half-cell configuration with lithium metal as anode. It is also possible to do it in commercial cells, whose anode and cathode are coupled, but it is not trivial to distinguish between the contributions of the single electrodes to the whole voltage response [99].
For the sake of degradation, a GITT test can be employed to track the variation of the OCV curve due to structural modifications of anode and cathode, or to observe change in the solid diffusion coefficient of lithium in the host materials of the electrodes [100].

Relaxation curve

In addition to the OCV that is reached at equilibrium conditions, also the **trend of voltage during relaxation** can give useful insights about the structure and the behavior of the lithium-ion battery. The voltage increases after the end of a discharge, while it decreases after the end of a charge, in both cases with a trend that resembles a decaying exponential (see figure 2.3).
During a current pulse, lithium concentration gradients easily develop in the electrolyte and in the solid particles of the two electrodes, due to the sluggish diffusion of lithium in these media. The higher the current and the pulse duration, the higher the magnitude of these concentration gradients.
The impact of the diffusion processes on the relaxation voltage trend can be explained by looking to their characteristic time τ_D, written as:

$$\tau_D \approx \frac{L_c^2}{D} \tag{2.3}$$

where L_c is the characteristic length of the diffusion, while D is the diffusion coefficient. The characteristic length of the diffusion in the electrolyte is the electrode length, in the order of $1 \cdot 10^{-4}$ m, while the one of the diffusion in the solid is the radius of the solid particle, in the order of $5 \cdot 10^{-6}$ m. The lithium diffusion coefficient in the electrolyte is in the order of $1 \cdot 10^{-10}$ m^2/s. Its value depends on the electrolyte chemical composition and on the concentration of lithium in this

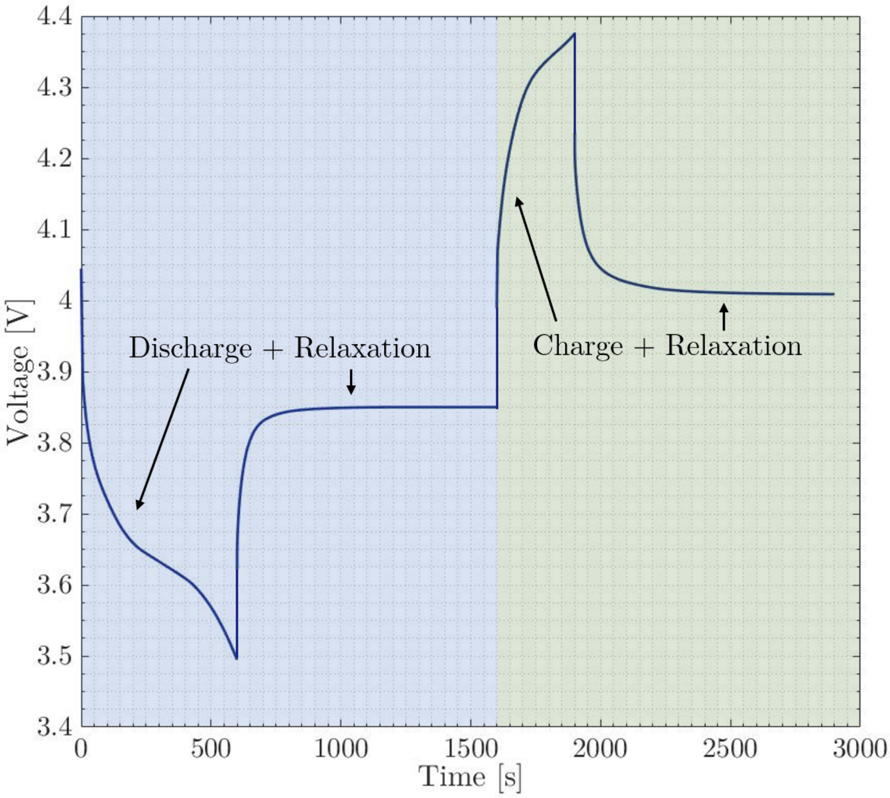

Figure 2.3: *Example of relaxation voltage profiles after a discharge and a charge*

liquid [40, 101].
Instead, the diffusion coefficient in the solid is in the $1{\cdot}10^{-13}$–$1{\cdot}10^{-18}$ m²/s range, according to the specific material and to the state of its crystalline structure [102]. Assuming a lithium diffusion coefficient in the solid of about $1{\cdot}10^{-14}$ m²/s, a value that is representative of many cathode materials, we get:

$$\begin{cases} \tau_{D,e} \approx \frac{(1\cdot10^{-4})^2}{1\cdot10^{-10}} = 100\, s \\ \\ \tau_{D,s} \approx \frac{(5\cdot10^{-6})^2}{1\cdot10^{-14}} = 2500\, s \end{cases}$$

In general the diffusion in the electrolyte is roughly one order of magnitude faster than the diffusion in the electrode. The former is in the 10^1–10^2 s range, while the latter belongs to the 10^2–10^3 s range. Thicker electrodes and bigger particles increase the characteristic time of these processes with a quadratic relationship. To make a comparison, in LIBs the ohmic overpotential is practically istantaneous, and the timescale of the charge transfer overpotential lies around 10^{-2} s [103]. Concentration gradients need a sufficently extended and intense current pulse to be developed, but their complete flattening can require a very long time (10^4–10^5 s), considering that the driving force of diffusion gradually decreases.

In addition to pure species diffusion, the relaxation of a LIB can also be driven by an **electrochemical reequilibration** process. To understand this phenomenon, it is useful to think to a discharge process [103]:

1. When the discharge current is applied, lithium deintercalates from the surface of the anode particles, flows in the electrolyte in its ionic form and reintercalates on the surface of the cathode particles. The shortest path between the negative and the positive electrode is the one that connects the faces of the electrodes that are in contact with the separator. Therefore, the deintercalation and intercalation processes are more intense near the separator, since the ionic lithium flow follows the path with the least resistance;

2. Consequently, the concentration of lithium on the surface of the electrodes particles is uneven along the electrode length. This phenomenon is enhanced by high current rates, which exacerbate species gradients, and by a low diffusion coefficient in the solid, which hinders an homogenization of the lithium concentration profile in the solid particles. Gradients of open circuit potential along the electrodes are then established by the said surface lithium concentration gradients. In fact, reminding from equation 1.15 that the electrode OCP is function of the electrode SOC on the surface of the particles, it is possible to notice that there is a potential difference between the part of the electrode near the separator and the one near the current collector;

3. When the applied current is set to zero, we still observe the presence of two reaction currents in the electrodes, independent of one another since the electric circuit that connects them is open. These reactions are due to the internal potential difference that was created during the pulse. This voltage acts as a driving force for an intercalation reaction inside of the electrodes. In particular, after a discharge the lithium deintercalates from the anode near the current collector and the cathode near the separator, and it intercalates in the anode near the separator and in the cathode near the current collector, until the surface concentration becomes homogeneous along the electrodes length.

This electrochemical reequilibration process is strongly linked to the shape of the open circuit potential curve of the electrodes, and of course it interacts with the lithium diffusion processes described above.

Therefore, the majority of the trend of voltage during relaxation is dictated by the geometry of the battery, the composition and the concentration of lithium in the electrolyte, and the structure and chemistry of the electrodes. These information can be very useful for the degradation detection, but the study of the relaxation curve with this purpose is seldom seen in literature [104].

2.1.3 Internal impedance tests

The internal resistance of a lithium-ion battery is not an univocal concept. Its value and its physical meaning depend on the nature of the current pulse with which it is measured, i.e. direct current (DC) or alternate current (AC). In the latter case it also depends on the frequency of the perturbing signal [105]. Temperature, SOC and internal concentration unbalances [106] in the cell have an influence on the value of the cell resistances too.

With DC signals, the resistance of the cell R_{DC} is measured by dividing the voltage drop ΔV at certain time (0.1-50 s) after the beginning of the pulse by the applied current I:

$$R_{DC} = \frac{\Delta V}{I} \tag{2.4}$$

Reminding the different overpotentials involved in the battery voltage drop (see chapter 1.1.2), according to the duration of the DC pulse, we will include different phenomena in the cell resistance, increasing it. The resistance value can also change in accordance with the direction of the pulse, since generally an higher electrode potential offers more resistance to the intercalation reactions. Therefore, during discharge the DC resistance will be slightly higher [105].

Electrochemical Impedance Spectroscopy

By using alternate current, the signal frequency ω determines the measured resistance, or impedance Z, which will be composed by a real part and by an imaginary part:

$$Z(\omega) = \frac{V(\omega)}{I(\omega)} = \frac{V_0 e^{i\varphi_1(\omega)}}{I_0 e^{i\varphi_2(\omega)}} = Z_0 e^{i(\varphi_1(\omega) - \varphi_2(\omega))} = Z_0(cos(\varphi(\omega)) + isin(\varphi(\omega)) \tag{2.5}$$

where Z_o is the module of the impedance, which represents the ratio between the amplitudes of voltage and current, while φ is the phase shift between the voltage and current sinusoids. Each frequency solicitates a phenomenon taking place inside the battery (e.g. ohmic drop, charge transfer, diffusion), therefore it is possible to obtain the resistance associated to each phenomena.

To obtain such a relationship between current and voltage, the system has to respect three criteria:

1. **Stability**: the voltage response of the battery should not diverge when the current input is applied. This condition is normally respected without particular conditions;

2. **Causality**: the voltage response of the battery should be caused only by the current input. Therefore, other factors that impact on the voltage should be avoided, as temperature variations or internal concentration unbalances;

3. **Linearity**: if a linear combination of current inputs is applied on the battery, the overall voltage response should be a linear combination of the voltage responses to the single current inputs, i.e. the lithium-ion battery is a linear system. In general, this statement is not true, and the battery voltage response is highly non-linear. Nevertheless, for a small amplitude of the voltage output (indicatively, under 10 mV), it is possible to assume that the battery is responding in a linear way to the current perturbation (first-order approximation). The validity of this assumption is usually controlled by employing the Kramers-Kronig analysis on experimental data [107].

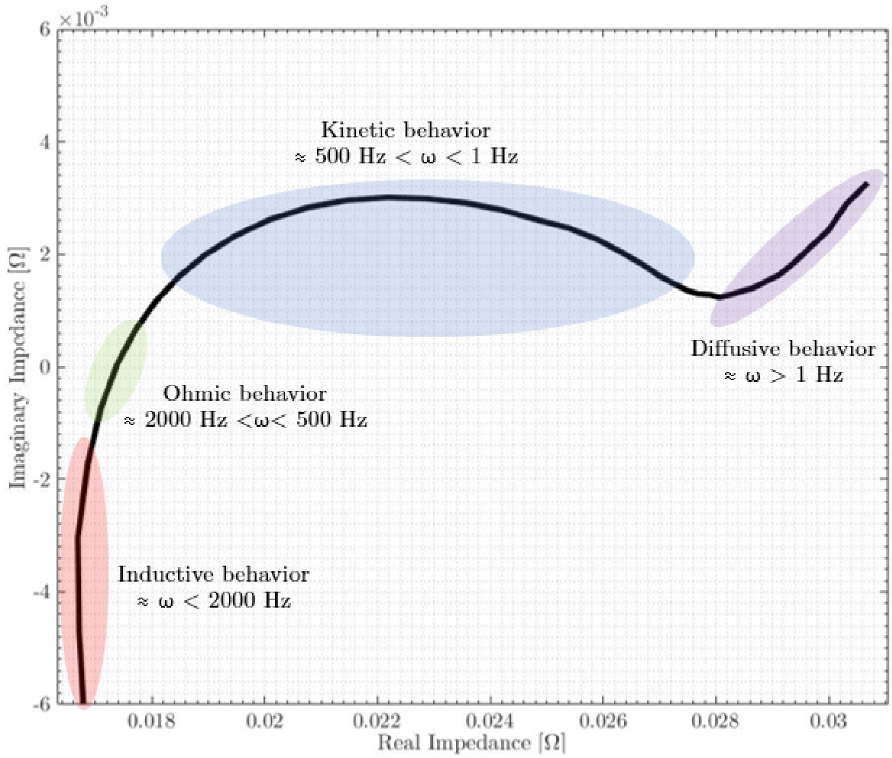

Figure 2.4: *Impedance spectrum obtained with the EIS, with the impedance regions that are commonly identified*

The AC impedance is commonly evaluated in diagnostic tests and by manufacturers with a single 1 kHz signal, that should correspond to the pure ohmic behaviour of the cell. Nevertheless, the frequency at which this behavior appears can widely change according to the test temperature and the type of cables with which the battery is tested, which add an inductive-ohmic impedance that influences the measured resistance.

Instead, the proper Electrochemical Impedance Spectroscopy (EIS) employs a wide range of frequencies to obtain a whole impedance spectrum, that can fully characterize the behaviour of the cell in all its mechanisms. Since a lithium-ion battery mainly shows a capacitive behavior, corresponding to a negative imaginary part, the ordinate axes of the EIS plot is usually reversed. According to the frequency range (see figure 2.4), we can indicatively classify the regions of the EIS as [108–110]:

- **Inductive behavior** (ω>2000 Hz): actually, a LIB does not have components related to an inductive impedance. Instead, the positive imaginary part at these high frequencies is caused by the battery wires induction. This purely imaginary contribution Z_w can be calculated as:

  $$Z_w(\omega) = i \cdot (2\pi\omega L_w) \tag{2.6}$$

  where L_w is the cables inductance. If L_w is known, the inductive part can be subtracted from the overall impedance of the battery;

- **Ohmic behavior** (2000 Hz<ω<500 Hz): in this frequency range, the imaginary part changes sign, shifting from an inductive to a capacitive behavior. At the frequency where the imaginary part is equal to zero, the overall impedance has only the real component, and it is called high frequency resistance (HFR). The HFR represents the purely ohmic behaviour of the battery, and it takes into account the electronic conductivity of the solid electrodes, the ionic conductivity of the electrolyte, the conductivity of the SEI/CEI film layers on the anode/cathode particles, and other external contributions, such as the ohmic resistance of the cables and contact resistances. The HFR characterize the istantaneous voltage drop/rise that we observe when applying a discharge/charge current to the battery;

- **Kinetic behavior ($\mathbf{R_{ct}}$)** (500 Hz<ω<0.5 Hz): at these intermediate frequencies, we observe the presence of one or more semicircle-like shapes in the battery impedance spectrum, with the real part which monotonously increases and the capacitive imaginary part which shows a maximum and a minimum. This frequency range is attributed to the charge transfer resistance ($\mathrm{R_{ct}}$) that characterize the interfacial reactions between the electrolyte and the electrodes, i.e. the kinetics of the intercalation reactions. Moreover, it is also present the double layer behavior of the said solid/liquid interfaces. In fact, the impedance of one electrode in this region is written as:

  $$Z_{ct}(\omega) = -\frac{1}{\frac{1}{R_{ct}} + i \cdot \omega C_{dl}} \tag{2.7}$$

  where C_{dl} is the double layer capacitance of the electrolyte/electrode interface. The charge transfer resistance R_{ct} can be modeled as:

  $$R_{ct} = \frac{RT}{i_0 F} \tag{2.8}$$

  where exchange current density i_o represents the kinetics of the lithium intercalation/deintercalation reaction in the Butler-Volmer equations (see section 2.2.2). The higher the value of the double layer capacitance, the lower the frequency at which the semicircle is present.
  Since in the battery there are two active electrodes, the impedance will be characterized by the sum of the charge transfer resistance of both electrodes.

- **Diffusive behavior** (ω>1 Hz): at such low frequencies, the concentration of lithium in the electrolyte and in the solid particles starts to be perturbed, since we reach the diffusion characteristic timescales (see section 2.1.2). The impedance in this region has approximately the shape of a finite-space Warburg element [111], which is associated to the diffusion of ions in a storage electrode. Many factors contributes to the low-frequency impedance: the porosity of the electrodes, the lithium diffusion coefficients in the anode and cathode, the diffusion coefficient in the electrolyte and the particle radii distribution in the electrode, the presence of a solid phase transition.
  The influence of the solid particles is particularly important, since the diffusion is much more limited in the electrodes if compared to the situation in the electrolyte.

The temperature at which the EIS is measured strongly influences the overall shape of the battery impedance spectrum [112]. The higher the temperature, the lower the module of the impedance, in particular at mid-low frequencies. In addition, the higher the temperature, the higher the frequency at which the described mechanisms display their features in the EIS.

Instead, the battery SOC impacts on the value of the AC impedance only if one of the electrodes is near its complete filling or depletion of lithium. In such a condition, the kinetics of the interfacial reaction in the said electrode is severely limited, and this effect is included in the definition of the exchange current density i_o in equation 2.16.

The EIS has the potential of being very useful for the detection of degradation since it can show the changes of the single components of the LIB resistance, and these changes could be related to different degradation modes [92]. However, it requires quite sophisticated and accurate test instruments for a reliable measurement.

2.1.4 Selection of the experimental techniques

The purpose of this thesis work is the formulation of a suitable experimental methodology for the parameter identification of aged lithium-ion batteries, and as remarked in section 1.3.3, the most insightful approach should be the one that combines different techniques, to obtain a complete dataset on the characteristics of the cell. For this reason, three experimental techniques are chosen and applied on commercial lithium-ion batteries, i.e. the capacity test, the relaxation test and the EIS. Each of these techniques should highlight different aspects of the tested battery, and they are explored in a wide number of operative conditions. In particular:

- the **capacity test** at high current rates should provide a general overview of the battery dynamic performances, with also the data on the exchanged capacity in each operative condition;
- the **relaxation test** should give information on the long-term diffusive processes happening in the battery after a current pulse. It could be useful to separate this aspect from the charge transfer and ohmic overpotentials;
- the **electrochemical impedance spectroscopy** should be useful to separate the resistances associated to each overpotential thanks to the broad range of frequencies involved in the impedance measurement. Also, the impact of the two electrodes on the overall charge transfer resistance could be separately assessed.

The results of the experimental campaign are reported and discussed in chapter 3.

2.2 Lithium-ion battery model

As will be seen in chapter 3, each of the diagnostic techniques enlighten the different characteristics of a lithium-ion battery. Also, the variability of the tests' results with operative conditions suggests that the effect of some key parameters that define the performance of the battery can be enhanced or weakened with specifically designed experiments. However, it is not evident nor the identity of these parameters nor the exact influence of the operative conditions on them.

The need for a model of the LIB stems from this point: by simulating the experimental tests with a battery mathematical model and observing the effect of the variation of the defining quantities of the model itself, it would be possible to understand the actual influence of these different quantities and hence give a sound explanation to the outcomes of the experiments. The parameters that are related to the aging process could be isolated by the others with selected experimental conditions and estimated with the interpretation of the diagnostic data by the battery model. For these reasons, we decided to select a suitable mathematical model of the LIB. The next sections will deal with the description of the chosen modelization, and the improvements made to it.

2.2.1 Model selection

In literature, it is possible to find three classes of lithium-ion battery models [87, 113]:

- **Equivalent Electric Circuit (EEC)**: Equivalent circuits are the most common kind of battery model, and they are structured as an electric circuit with an ohmic resistor and one or more RC circuits in series [114, 115]. Thanks to their simplicity and the very low computational effort needed, they are currently implemented as online battery management systems of consumer electronics and electric vehicles, where they are used to continuously monitor the state of charge and/or state of health through the measure of the battery output quantities.

  Basic EECs do not contain any physical background, and they act as lookup tables of the battery SOC/SOH with respect to voltage and sometimes temperature. The electrical components of the circuit are modeled by fitting experimental data to the response of the mathematical model of the EEC. This approach lacks the ability to extrapolate data from conditions that are not included in the fitted dataset, due to the absence of knowledge about the electrochemical behavior of the battery.

  More accurate representations are given when the circuit elements are related to electrochemical phenomena [5] and in this case, EIS is usually employed to assign to each element its physical meaning (see figure 2.5). Nevertheless, the mathematical formulation of these electric components is not trivial, and it requires some approximations to be practically implemented in EECs plus the introduction of more complex circuital elements, such as constant phase elements. Also, they are still a simplified approach if compared to full-scale electrochemical models;

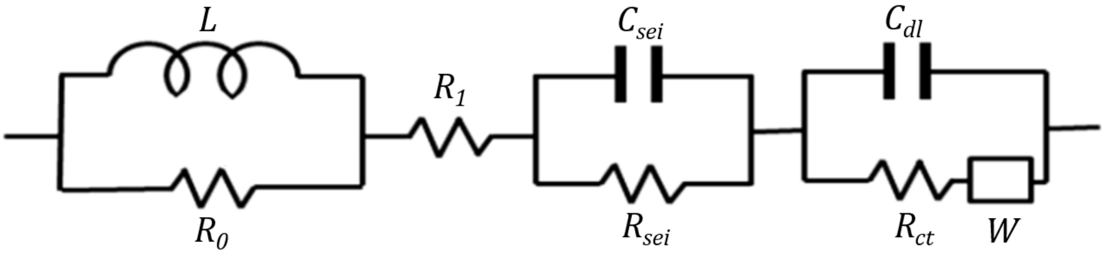

Figure 2.5: *Example of Equivalent Electric Circuit with electrochemically-based elements, used to fit EIS data (Taken from [116])*

- **Data-driven models**: Data-driven modeling is being studied for different kinds of applications in the lithium-ion battery field, thanks to the increasing availability of data and to the higher computational capabilities of battery management systems. The relation between the state of charge, the state of health and the battery output quantities (voltage, relaxation time, internal impedance, IC/DV, etc.) are learned by data-driven models with training on input-output data, and the obtained relations are tested and applied on new datasets. If these models are fully based on data, i.e. black-box models, some employed techniques are Support Vector Regression [117], Neural Networks [118] or Gaussian Process Regression [119]. They are mostly thought for on-board SOC/SOH monitoring, but a case of utilization of a black-box model for the offline prediction of remaining useful life has been reported [120]. Instead, we talk about grey-box models when data-driven approaches are coupled with EECs to improve prediction capabilities. For instance, the EEC identifies the SOC of the battery by modeling its dynamic behavior, avoiding the need for long resting periods for an accurate SOC estimate, and the data-driven part, such as a lookup table, predicts the SOH with the battery outputs and the SOC value [121].

  Both black-box and grey-box models can be very powerful since they do not need to know the physically exact relations between the battery parameters, but they can fail when going outside the training dataset. Moreover, due to their nature, it is not clear what are the relations that they build between inputs and outputs, and hence there is not a deep control over their behavior;

- **Mechanistic models**: Models that are based on the underlying physics of the lithium-ion battery aim to reproduce its behavior with the use of its geometrical, electrochemical and thermal properties coupled together in partial differential equations (PDE). A variety of phenomena can be accurately modeled in this way, such as heat transfer, SEI growth, lithium plating, and even microscale phase transformation [122]. Since the model parameters are based on measurable quantities, there is plenty of literature on the reasonable range in which their value lies, thanks to direct measurements. More general correlations can be obtained with mechanistic formulations, and they can be applied with a good degree of accuracy outside of the fitting dataset.

  Nevertheless, the computational burden of such models is quite high, since there are no closed-form expressions for these PDE and they have to be

> solved numerically. The number of needed parameters can easily reach very high numbers in complex models, with large differences in their value among the different battery chemistries. A full, faithful modelization of a LIB is unfeasible, and hence the employed model(s) should be tailored to the studied phenomena. For instance, if a mechanistic model is employed in on-board control systems, it is reduced to a simplified, analytical form to greatly reduce the computational time, with the cost of a reduced accuracy on the results [123, 124].

In this work, it was decided to use a mechanistic model. The objective is to develop a one-time diagnostic procedure of aged batteries, not a real-time, on-board control strategy. Hence, the drawback of the high calculation time is surely mitigated. In addition, the possibility to rely on a quite general formulation is a strong plus, due to the great variety of chemistries, shapes and past histories the tested batteries can have. The eventual optimization and implication of the model will be the objective of future activities, while in this work we concentrate on the correctness of the physical description the lithium-ion battery.
In particular, the chosen model is the Doyle-Fuller-Newman pseudo-two dimensional electrochemical model (P2D) [125]. The core of this model has been developed about thirty years ago, and it is still widely used in literature thanks to its good compromise between accuracy and computational cost. Starting from the P2D model, there has been the development of simpler formulations, like the single-particle model [126], and of more complex ones, like the electrochemical-electric-thermal 3D model [127], but the basis is still the Doyle-Fuller-Newman modelization of the battery. This model has been adapted and utilized in a previous thesis work [93] to replicate the aging process of cycled batteries, by simulating degradation modes. The author focused on thermodynamic aspects, ensuring that the OCV curves of the positive and negative electrodes and the overall capacity of the battery were well reproduced. For our scope, it has been necessary to improve the kinetic part of the model, as it will be explained in the next sections.

The model is implemented in COMSOL Multiphysics®, and the control of the simulations and the analysis of the outputs are done with MATLAB, with the support of COMSOL LiveLink™.

2.2.2 Model description

In this section, we will not describe the way in which the model's partial differential equations are obtained. The reader is referred to the original work of John Newman [10] and to the clear explanation of professor Gregory L. Plett [128] for the full derivation of the P2D model.

The parts of the battery that are modeled are the negative electrode, the separator and the positive electrode (see figure 2.6). Each of them has several nodes that form a 1D mesh, where the model's partial differential equations are applied and solved. The model is labeled as "pseudo-two dimensional" since the points in which the PDEs are solved are placed along a single dimension *x*. But, in every

Symbol	Description
Latin	
$a\ \left[m^{-1}\right]$	Specific active area
$A_{el}\ [m^2]$	Electrode area
$c\ [mol\, m^{-}]$	Lithium concentration
$C\ \left[J\, kg^{-1}\, K^{-1}\right]$	Specific heat
$C_{dl}\ \left[F\, m^{-2}\right]$	Double layer capacitance
$D\ \left[m^2\, s^{-1}\right]$	Lithium diffusion coefficient
$EA_k\ \left[J\, mol^{-1}\right]$	Rate constant activation energy
$EA_{D_s}\ \left[J\, mol^{-1}\right]$	Solid diffusion activation energy
$E_{ocp}\ [V]$	Electrode open circuit potential
$F\ \left[A\, s\, mol^{-1}\right]$	Faraday constant
$FCE\ [-]$	Ionic conductivity factor
$h\ \left[W\, m^{-2}\, K^{-1}\right]$	Heat transfer coefficient
$i\ \left[A\, m^{-2}\right]$	Current density
$i_0\ \left[A\, m^{-2}\right]$	Exchange current density
$I\ [A]$	Current
$j\ \left[mol\, m^{-2}\right]$	Lithium molar flux
$k\ \left[m\, s^{-1}\right]$	Rate constant
$k_T\ \left[\frac{W}{mK}\right]$	Thermal conductivity
$L\ [m]$	Cell component length
$n\ [-]$	Number of charges
$q\ \left[W\, m^{-3}\right]$	Volumetric heat flux
$Q\ [A\, s]$	Capacity
$r\ [m]$	Battery component radius
$R\ \left[J\, mol^{-1}\, K^{-1}\right]$	Gas constant
$R_b\ [m]$	Battery total radius
$R_{ext}\ [\Omega\, m^2]$	External resistance
$R_{film}\ [\Omega\, m^2]$	External resistance
$R_p\ [m]$	Particle radius
$SOC\ [-]$	State of charge
$t_0^+\ [-]$	Lithium transference number
$T\ [K]$	Battery temperature
$\Delta V\ [V]$	Cell voltage
Greek	
$\alpha\ [-]$	Transfer coefficient
$\varepsilon\ [-]$	Battery material fraction
$\eta\ [V]$	Overpotential
$\kappa_e\ \left[S\, m^{-1}\right]$	Electrolyte ionic conductivity
$\kappa_D\ \left[A\, m^{-1}\right]$	Electrolyte diffusional conductivity
$\varphi\ [V]$	Electric potential
$\rho\ \left[kg\, m^{-3}\right]$	Density

Symbol	Description
Subscript	
a	anodic
am	active material
ax	axial
c	cathodic
$conv$	convective
e	electrolyte
gen	generated
i	inactive material
man	mandrel
max	maximum
min	minimum
n	negative
nom	nominal
ohm	ohmic
p	positive
r	reaction
rad	radial
rev	reversible
s	solid
sep	separator
Superscript	
eff	effective
Coordinate	
r	radial coordinate
x	linear coordinate
z	axial coordinate
ϑ	angular coordinate
t	time

Table 2.1:
List of symbols, subscripts and superscripts used in the model description

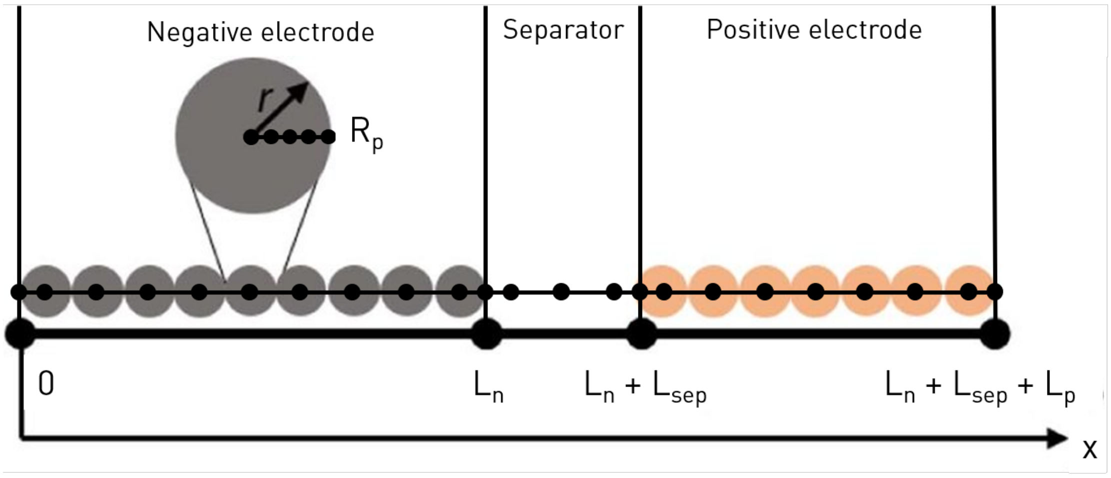

Figure 2.6: *Representation of the Fuller-Doyle-Newman P2D model domain*

point except for the separator, there is an additional radial dimension r which represents the solid particles of the electrodes. These particles are usually modeled as spheres, and the solid diffusion PDEs are solved in additional nodes along their radial dimension. All the quantities in the model's equations are reported in table 2.1.

The governing equations of the lithium-ion battery mathematical model are:

1. **Material balance in the electrolyte**
On the left-hand side of this PDE, there is the accumulation term of lithium in the electrolyte. On the right-hand side, there is the flow of lithium in the electrolyte, composed by the diffusion term, the migration term, and the source term. Since the lithium transference number $t_+{}^o$ is usually approximated as constant, the migration term is often neglected. In the separator, this equation holds true except for the source term, which is equal to zero due to the absence of reactions in the separator.

$$\varepsilon_e \frac{\partial c_e}{\partial t} = \frac{\partial}{\partial x}\left(\varepsilon_l D_e^{eff} \frac{\partial c_e}{\partial x}\right) - \frac{\mathbf{i}_e \frac{\partial t_+^0}{\partial x}}{nF} + a j_{\mathrm{r}}(1 - t_+^0) \tag{2.9}$$

The effective lithium diffusion coefficient in the electrolyte $D_e{}^{eff}$ accounts for the effect of the tortuosity of the porous electrode with the Bruggeman correlation:

$$D_e^{eff} = D_e \varepsilon_l^{1.5} \tag{2.10}$$

The boundary conditions for the balance in the electrolyte are:

$$\begin{cases} \left.\frac{\partial c_e}{\partial x}\right|_{x=0} = \left.\frac{\partial c_e}{\partial x}\right|_{x=L_n+L_{sep}+L_p} = 0 \\ \\ -\left.D_e^{eff} \frac{\partial c_e}{\partial x}\right|_{x=L_n^-} = -\left.D_e^{eff} \frac{\partial c_e}{\partial x}\right|_{x=L_n^+} \\ \\ -\left.D_e^{eff} \frac{\partial c_e}{\partial x}\right|_{x=L_n+L_{sep}^-} = -\left.D_e^{eff} \frac{\partial c_e}{\partial x}\right|_{x=L_n+L_{sep}^+} \end{cases} \tag{2.11}$$

where the first two conditions refer to the impermeable walls that contain the battery, with a null lithium flux, and the last two conditions refer to the continuity of lithium-ions transport at the interfaces between the two electrodes and the separator.

2. **Material balance in the solid particles**
   This partial differential equation models the diffusion of lithium in the solid particles, with spherical coordinates.

$$\frac{\partial c_s}{\partial t} = \frac{1}{r^2}\frac{\partial}{\partial r}\left(D_s r^2 \frac{\partial}{\partial r} c_s\right) \tag{2.12}$$

   The model simplifies the real characteristic of a battery electrode, where a complex distribution of particle radii is present. Here, R_p is a single radius that represents the average value of the said distribution.
   The equation has the boundary conditions of no flux in the center of the sphere, and of equivalence between the lithium flux at the surface of the particle and local reaction lithium flux:

$$\begin{cases} \left.\frac{\partial c_s}{\partial r}\right|_{r=R_p} = -\frac{j_{loc}}{D_s} \\ \\ \left.\frac{\partial c_s}{\partial r}\right|_{r=0} = 0 \end{cases} \tag{2.13}$$

3. **Electrochemical kinetics**
   The local reaction current density i_r generated by the electrode reaction is determined by the Butler-Volmer equation, which relates it to the overpotential η of the electrochemical reactions.

$$i_r = i_0\left[\exp\left(\frac{\alpha_a F}{RT}\eta\right) - \exp\left(-\frac{\alpha_c F}{RT}\eta\right)\right] \tag{2.14}$$

   The local reaction current density i_r is related to the local reaction lithium flux j_r through the Faraday's law:

$$i_r = nFj_r \tag{2.15}$$

   The exchange current density i_o, i.e. the bidirectional current between the electrode and the electrolyte that is present at equilibrium conditions, is expressed as:

$$i_o = F\left(k_c\right)^{\alpha_a}\left(k_a\right)^{\alpha_c}\left(c_{s,\max} - c_s\right)^{\alpha_a}\left(c_s\right)^{\alpha_c}\left(\frac{c_e}{c_{e,0}}\right)^{\alpha_a} \tag{2.16}$$

   where the concentration of lithium in the solid material is calculated on the external surface of the electrode particle.
   These concentration-related terms correct the exchange current density according to the availability of lithium in the electrode and in the electrolyte: the lower the amount of lithium in the electrolyte and the nearer to the lithium concentration limits of the electrode, the lower the exchange current density.

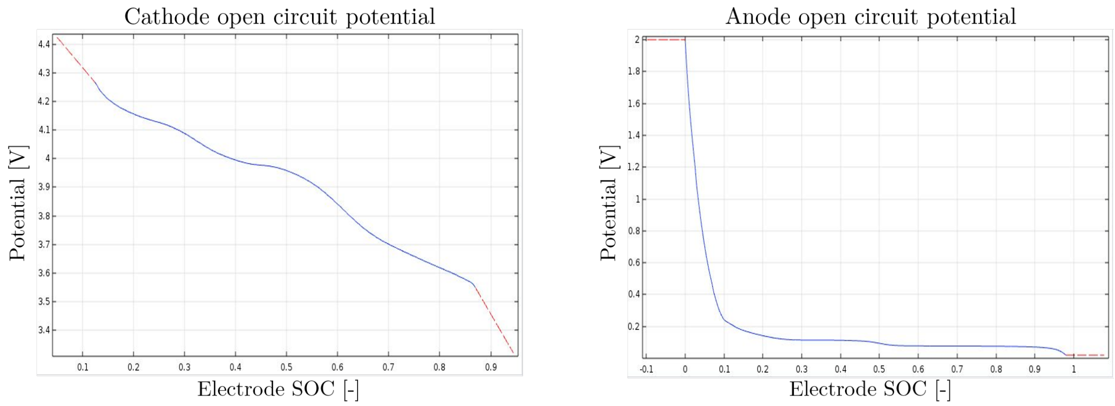

Figure 2.7: *Cathode and anode open circuit potentials profiles used in the model*

A low exchange current density corresponds to an high charge transfer resistance [108]. Since the α_a and α_c transfer coefficients are assumed to be equal to 0.5, and the cathodic k_c and anodic k_a reaction rates are considered equal to a generic electrode reaction constant k, the expression can be simplified to:

$$i_o = Fk\sqrt{(c_{s,\max} - c_s)\,(c_s)}\sqrt{\left(\frac{c_e}{c_{e,0}}\right)} \tag{2.17}$$

Instead, the overpotential is expressed as:

$$\eta = \varphi_s - \varphi_e - E_{ocp} - i_r R_{film} \tag{2.18}$$

where the R_{film} represents the resistance of SEI/CEI on the surface of the active electrode particles, simply modeled as a film with no thickness.
In this work, the battery thermodynamic characteristic is not fitted, and hence the open circuit potential curves E_{ocp} are calculated from lookup tables of the electrode potential as a function of the electrode state of charge 2.7. According to the methodology developed in the previous thesis work, the lookup tables are obtained from the experimental data of a slow 0.1C discharge on the battery samples (see section 3), which is considered as a good approximation of an equilibrium process [93]. The electrode state of charge SOC_{el} is calculated according to equation 1.15.

4. **Solid potential**
   The current density in the solid i_s is modeled with Ohm's law:

$$i_s = -\sigma_s^{eff}\frac{\partial \varphi_s}{\partial x} \tag{2.19}$$

The electrode electric conductivity $\sigma_s{}^{eff}$ is corrected for the tortuosity of the porous electrode with the Bruggeman correlation:

$$\sigma_s^{eff} = -\sigma_s \varepsilon_s^{1.5} \tag{2.20}$$

For what concerns boundary conditions, to have a reference point with which it is possible to measure the cell voltage, the potential of the solid φ_s is set to zero on the left boundary of the negative electrode. Also, since in the separator only the electrolyte is present, at the interfaces between the separator and electrodes, the current in the solid is equal to zero as well as the potential gradient.

$$\begin{cases} \varphi_s\big|_{x=0} = 0 \\ \frac{\partial \varphi_s}{\partial x}\Big|_{x=L_n^-} = \frac{\partial \varphi_s}{\partial x}\Big|_{x=L_n+L_{sep}^+} = 0 \\ \frac{\partial \varphi_s}{\partial x}\Big|_{x=L_n+L_{sep}+L_p} = -\frac{i_s}{\sigma_s^{eff}} \end{cases} \tag{2.21}$$

5. **Electrolyte potential**
The current density in the electrolyte i_e has a part that is due to Ohm's law and another one that accounts for the transport of ions by the concentrations gradients.

$$i_e = -\kappa_e^{eff}\frac{\partial \varphi_e}{\partial x} + \frac{2\kappa_e^{eff}RT}{F}\left(1+\frac{\partial \ln f_\pm}{\partial \ln c_e}\right)\left(1-t_+^0\right)\frac{\partial \ln c_e}{\partial x} \tag{2.22}$$

The second term on the right-hand side is often expressed as the diffusional conductivity ${\kappa_D}^{eff}$:

$$\kappa_D^{eff} = \frac{2\kappa_e^{eff}RT}{F}\left(1+\frac{\partial \ln f_\pm}{\partial \ln c_e}\right)\left(1-t_+^0\right) \tag{2.23}$$

The ionic conductivity of the electrolyte ${\kappa_e}^{eff}$ is corrected for the tortuosity of the porous electrode with the Bruggeman correlation:

$$\kappa_e^{eff} = \kappa_e \varepsilon_l^{1.5} \tag{2.24}$$

The boundary conditions on the electrolyte potential φ_e are:

$$\begin{cases} \frac{\partial \varphi_e}{\partial x}\Big|_{x=0} = \frac{\partial \varphi_e}{\partial x}\Big|_{x=L_n+L_{sep}+L_p} = 0 \\ \varphi_e\big|_{x=L_n^-} = \varphi_e\big|_{x=L_n^+} \\ \varphi_e\big|_{x=L_n+L_{sep}^-} = \varphi_e\big|_{x=L_n+L_{sep}^+} \end{cases} \tag{2.25}$$

where the first two conditions refer to the continuity of the potential at the interfaces between the electrodes and the separator, i.e. there is only flow of current in the electrolyte inside the separator. Instead, the last two conditions imply that there is only flow of current in the solid at the edges of the battery, where there are the metallic current collectors.

6. **Charge conservation**
The derivative of the current density in the electrolyte and in the solid are related by the equation:

$$\frac{\partial i_e}{\partial x} = -\frac{\partial i_s}{\partial x} = nFaj_r + aC_{dl}\frac{\partial\left(\Phi_e - \Phi_s\right)}{\partial t} \tag{2.26}$$

where the first term on the right-hand side of the equation is the reaction current density (also called faradaic current), while the second term accounts for the current density in the double layer (also called non-faradaic current). The active surface-to-volume ratio of spherical particles a is calculated as:

$$a = 3\frac{\varepsilon_{s,am}}{R_p} \tag{2.27}$$

Please note that the active surface-to-volume ratio is calculated with the active solid fraction $\varepsilon_{s,am}$. In each electrode and in the separator, the mass balance of the constituents gives:

$$\varepsilon_e + \varepsilon_s = \varepsilon_e + \varepsilon_{s,am} + \varepsilon_{s,i} = 1 \tag{2.28}$$

where $\varepsilon_{s,i}$ is the fraction of inactive solid material, i.e. the binder and the conductive additives. In the separator, $\varepsilon_{s,am}$ is equal to zero due to the absence of active material. The total current density i is given by the sum of the solid and electrolyte current densities:

$$i = i_e + i_s \tag{2.29}$$

The overall current I that is applied to the battery is related to the total current density through the relation:

$$I = A_{el} \cdot i \tag{2.30}$$

The cell voltage $\Delta\ V$ is measured by the model as the difference between the solid potentials at the edges of the battery plus the voltage drop over an external resistance referred to the electrodes' area R_{ext}, which accounts for current collectors and cables resistances:

$$\Delta V = \varphi_s|_{x=L_n+L_{sep}+L_p} - \varphi_s|_{x=0} - \frac{R_{ext}I}{A_{el}} \tag{2.31}$$

Lastly, the battery nominal capacity Q_{nom} is calculated as:

$$Q_{nom} = min\{Q_p, Q_n\} \tag{2.32}$$

The electrodes' capacities Q_p and Q_n are:

$$\begin{cases} Q_p = A_{el}\, L_p\, \varepsilon_{s,am,p}\, c_{s,max,p}(SOC_{max,p} - SOC_{min,p}) \\ \\ Q_n = A_{el}\, L_n\, \varepsilon_{s,am,n}\, c_{s,max,n}(SOC_{max,n} - SOC_{min,n}) \end{cases} \tag{2.33}$$

determined by the lengths of the electrodes L_p and L_n, by the fraction of active materials $\varepsilon_{s,am,p}$ and $\varepsilon_{s,am,n}$, by the maximum concentrations of lithium in the electrodes $c_{s,max,p}$ and $c_{s,max,n}$ and by the SOC limits of the electrodes (see Chapter 1.1.1).

The independent variables of the model are x, t, and r, while the dependent variables are c_e,c_s, φ_e, φ_s, i_e, and j_{loc}. The PDEs 2.9, 2.14, 2.19, 2.22 and 2.26 are solved in each one of the N nodes of the 1D mesh of the lithium-ion battery. The solid diffusion PDE 2.12 is solved in each of the M nodes inside each of the N-N$_{sep}$ electrode spherical particles, where N$_{sep}$ is the number of nodes in the separator, that has no particles inside. Therefore, in each timestep, 5N+(N-N$_{sep}$)·M partial differential equations are solved. The direct, fully coupled solver uses the nonlinear Newton's method, with the implicit backward differentiation formula for the time stepping.

2.2.3 Model improvements

In this work, the basic P2D model has been extended in order to include the heat transfer, and hence the influence of temperature on the simulations. Since the basic model formulation is isothermal and its physical parameters do not have a dependency on temperature, the outcomes of the simulation are not reliable when the ambient temperature is far from normal conditions. Also, when high current rates are employed for a prolonged time, it is experimentally observed an increase in the battery temperature. Therefore, a comprehensive simulation of such conditions has to include the effect of temperature on the model.

The LIBs that have been experimentally studied and modeled are cylindrical (see Chapter 3.1.1), hence the thermal model will be based on this geometry. The general 3D heat conduction equation in cylindrical coordinates is:

$$\frac{1}{r}\frac{\partial}{\partial r}\left(rk_T\frac{\partial T}{\partial r}\right)+\frac{1}{r^2}\frac{\partial}{\partial \vartheta}\left(k_T\frac{\partial T}{\partial \vartheta}\right)+\frac{\partial}{\partial z}\left(k_T\frac{\partial T}{\partial z}\right)+\overline{q_{gen}}=\rho C\frac{\partial T}{\partial t} \tag{2.34}$$

On the left-hand side, we have in succession the radial conduction term, the angular conduction term, and the axial conduction term, plus the internal heat generation. On the right-hand side, there is the heat accumulation term.

Cylindrical lithium-ion batteries are made by wrapping the compound active material around a central insulating mandrel, all enclosed by a steel can (*figure 2.8*). The number of windings is variable, but it usually lies between 15 and 30, according to the type of battery. Thanks to the high number of layers that compose the spiral, the angular heat conduction can be neglected without losing accuracy [129].

Therefore, the heat conduction equation reduces to:

$$\frac{1}{r}\frac{\partial}{\partial r}\left(rk_T\frac{\partial T}{\partial r}\right)+\frac{\partial}{\partial z}\left(k_T\frac{\partial T}{\partial z}\right)+\overline{q_{gen}}=\rho C\frac{\partial T}{\partial t} \tag{2.35}$$

Therefore, in COMSOL Multiphysics, the cylindrical battery is modeled as a 2D geometry with radial symmetry (*figure 2.9*), with three layers that represent the central mandrel, the active material, and the steel can. The heat transfer equation will be solved in each of these three regions, connected by the heat flux continuity boundary conditions. The heat generation term is present only in the active material layer, where the electrochemical reactions are taking place.

The boundary conditions are:

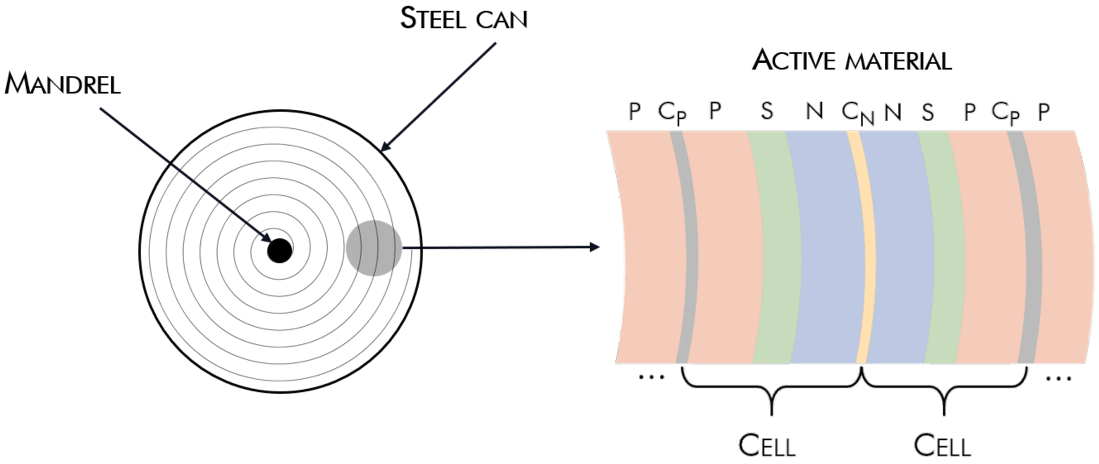

Figure 2.8: *Cross-section of a cylindrical lithium-ion battery, with a zoom on the structure of the active material. P: positive electrode; N: negative electrode; S: separator;* C_P*: positive current collector;* C_N*: negative current collector*

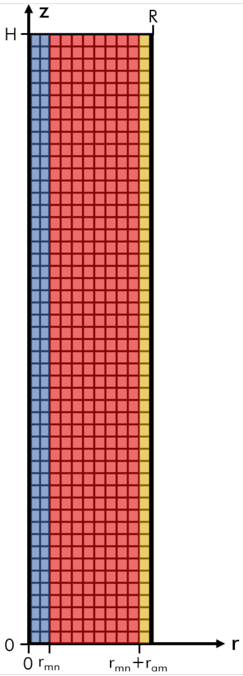

Figure 2.9: *Geometry of the 2D cylindrical LIB thermal model. Blue area: mandrel; Red area: active material; Yellow area: steel casing*

$$\begin{cases} \left.\frac{\partial T}{\partial r}\right|_{r=0,z\in[0,H]} = 0 \\ -k_T \left.\frac{\partial T}{\partial r}\right|_{r=r_{md}^-,z\in[0,H]} = k_T \left.\frac{\partial T}{\partial r}\right|_{r=r_{md}^+,z\in[0,H]} \\ -k_T \left.\frac{\partial T}{\partial r}\right|_{r=r_{md}+r_{am}^-,z\in[0,H]} = k_T \left.\frac{\partial T}{\partial r}\right|_{r=r_{md}+r_{am}^-,z\in[0,H]} \\ -k_T \left.\frac{\partial T}{\partial r}\right|_{r=R_b^-,z\in[0,H]} = h_{conv}(T - T_{amb})|_{r=R_b^+,z\in[0,H]} \\ -k_T \left.\frac{\partial T}{\partial z}\right|_{r\in[0,R_b],z=(0,H)^-} = h_{conv}^{'}(T - T_{amb})\Big|_{r\in[0,R_b],z=(0,H)^+} \end{cases} \tag{2.36}$$

Apart from the no flux condition at the center of the cylinder and the heat flux continuity between layers, the PDE has convective heat transfer conditions on the external surfaces, with a convective heat trasfer coefficient $h_{conv}{}'$ at the top and bottom surfaces which is assumed to be 25% of the one on the lateral surface $h_{conv}{}'$. These convective heat transfer boundary conditions are quite simplified with respect to the real situation [130], but this approximation is suitable for our purposes: we are not interested in the inhomogeneous temperature distribution inside the battery since this temperature distribution will be averaged, in order to have a single temperature value for the active material.

The thermal conductivity of the active material is strongly anisotropic. In fact, the radial thermal conductivity $k_{T,rad}$ is about two orders of magnitude lower than the axial thermal conductivity $k_{T,ax}$, mainly because of the contact resistance between all the layers [131]. The heat conduction equation is solved numerically in each of the nodes of a 2D mesh, generated by COMSOL.

The only unknown parameter of this thermal model is the volumetric heat generation term q_{gen}, which is determined by the electrochemical model. In fact, it is possible to express this term as:

$$q_{gen} = q_{ohm} + q_r + q_{rev} \tag{2.37}$$

The generated heat has three components:

- **Ohmic heat generation**: heat generated by the passage of current in the resistances of the battery, because of the Joule effect. It is calculated as:

  $$q_{ohm} = \sigma_s^{eff} \left(\frac{\partial \varphi_s}{\partial x}\right)^2 + \kappa_e^{eff} \left(\frac{\partial \varphi_e}{\partial x}\right)^2 + \kappa_D^{eff} \frac{\partial \ln(c_e)}{\partial x} \frac{\partial \varphi_e}{\partial x} \tag{2.38}$$

  where the three terms represent respectively the heat generation due to the passage of current in the solid, the heat generation due to the passage of current in the electrolyte and the heat generation due to the ionic migration;

- **Reaction heat generation**: heat generated by the irreversibilities of the electrochemical reaction, e.g. activation energy. It is calculated as:

  $$q_r = a i_r \eta \tag{2.39}$$

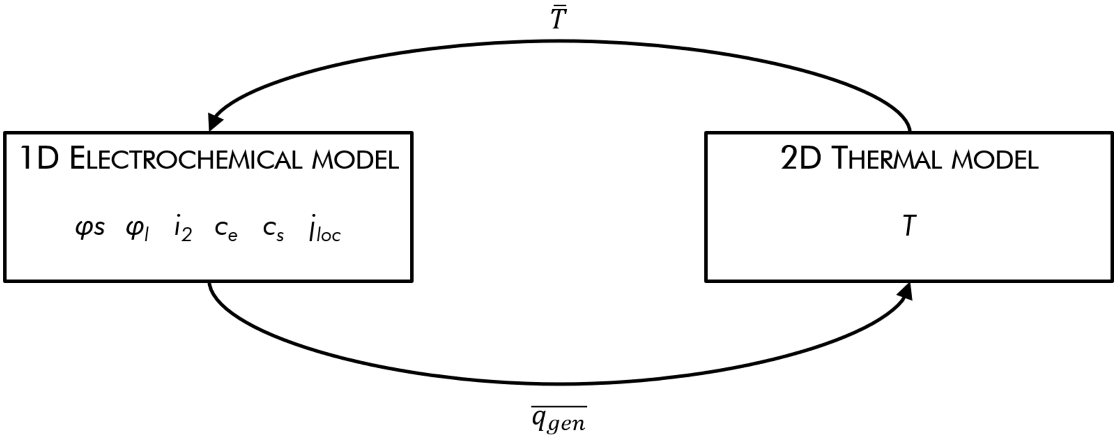

Figure 2.10: *Scheme of the coupling principle between the 1D electrochemical model and the 2D thermal model*

- **Reversible heat generation**: heat generated by the entropy change of the electrodes, expressed as:

  $$q_{rev} = ai_r T \frac{\partial E_{ocp}}{\partial T} \tag{2.40}$$

  The derivative of the open circuit potential with respect to the temperature of each electrode is a SOC-dependent quantity, taken as a lookup table from the COMSOL material library. The accuracy of this term is quite low, but the reversible heat generation is not so relevant in the overall heat generation, in particular at mid-high current rates.

The volumetric heat generation is calculated in each node of the 1D battery mesh, but the 2D thermal model can only accept a single volumetric heat generation term. Therefore, on each timestep, the average heat generation in the battery is calculated as:

$$\overline{q_{gen}} = \frac{1}{L}\int_0^L q_{gen} dx \tag{2.41}$$

where L is the overall length of the battery.
On the other hand, each timestep the 1D battery model takes only a single temperature as an input for the whole domain, being the model isothermal. Hence, the temperature distribution in the active material calculated by the 2D thermal model is averaged as:

$$\overline{T} = \frac{1}{A_{am}}\int_{A_{am}} T dA \tag{2.42}$$

where A_{am} is the area of the active material in the red section of figure 2.9.

Summing up, in each timestep the battery model takes as input the average temperature calculated by the thermal model while giving to it the average volumetric heat generation term (*figure 2.10*).

Since the temperature is now a variable quantity in the electrochemical model, we implemented a temperature dependence for the physical quantities that are more influenced by this parameter and that have more impact on the simulation output:

- **Open circuit potential**: each electrode open circuit potential has an additional term function of temperature, which is exactly the one included in the reversible heat generation. This term derives from the thermodynamic definition of open circuit potential:

$$E_{ocp} = E_{ocp,0} + T\frac{\partial E_{ocp}}{\partial T} \tag{2.43}$$

- **Ionic conductivity**: for the electrolyte ionic conductivity, it is used an empirical correlation of temperature and lithium concentration in the electrolyte, obtained from experimental data on $LiPF_6$-based electrolytes [101]:

$$\begin{aligned}\kappa_e =& FCE \cdot c_e(-10.5 + 0.0740T - 6.96 \cdot 10^{-5} + 0.668c_e - 0.0178c_eT \\ &+ 2.8 \cdot 10^{-5}c_eT^2 + 0.494c_e^2 - 8.86 \cdot 10^{-4}c_e^2T)^2\end{aligned} \tag{2.44}$$

  The trend of the ionic conductivity with temperature and concentration can be visualized in figure **??**.
  FCE is a constant that multiplies the ionic conductivity obtained from the correlation, in order to scale it during the data fitting process, adapting it to the specific battery.

- **Lithium diffusion in the electrolyte**: for what concerns the lithium diffusion coefficient in the electrolyte, it is possible to demonstrate that it is directly correlated with the ionic conductivity through the Nernst-Planck relationship [40]:

$$D_e = \frac{\kappa_e RT}{F^2 c_e} \tag{2.45}$$

- **Activity coefficient**: the activity coefficient, contained in the ${\kappa_D}^{eff}$ expression, corrects this quantity according to the deviation from the dilute solution condition. It is expressed as an empirical correlation of temperature and lithium concentration in the electrolyte, obtained from experimental data on $LiPF_6$-based electrolytes [101]:

$$\left(1 + \frac{\partial \ln f_\pm}{\partial \ln c_e}\right) = 1 + \frac{c_e}{c_{e,ref}}\left[\frac{-1.0189}{21 + 0.9831\sqrt{c_e}}\left(\frac{1}{\sqrt{c_e}} - \frac{0.9831}{1 + 0.9831\sqrt{c_e}}\right) + 1.5842\right] \tag{2.46}$$

- **Rate constant**: the rate constant k, which is contained in the definition of the exchange current density, has an Arrenhius-type dependence with the temperature. Each of the two electrodes' rate constant will be coupled to an activation energy EA_k, with the reference rate constant k_o measured at T_o:

$$k = k_0 \exp\left\{\frac{EA_k}{R}\left(\frac{1}{T_0} - \frac{1}{T}\right)\right\} \tag{2.47}$$

- **Solid diffusivity**: also the lithium diffusion coefficient in the solid material D_s presents an Arrenhius-type dependence with temperature [23], alike the rate constant, with the activation energy EA_D. The reference solid diffusivity $D_{s,o}$ is measured at T_o:

$$D_s = D_{s,0} \exp\left\{\frac{EA_D}{R}\left(\frac{1}{T_0} - \frac{1}{T}\right)\right\} \tag{2.48}$$

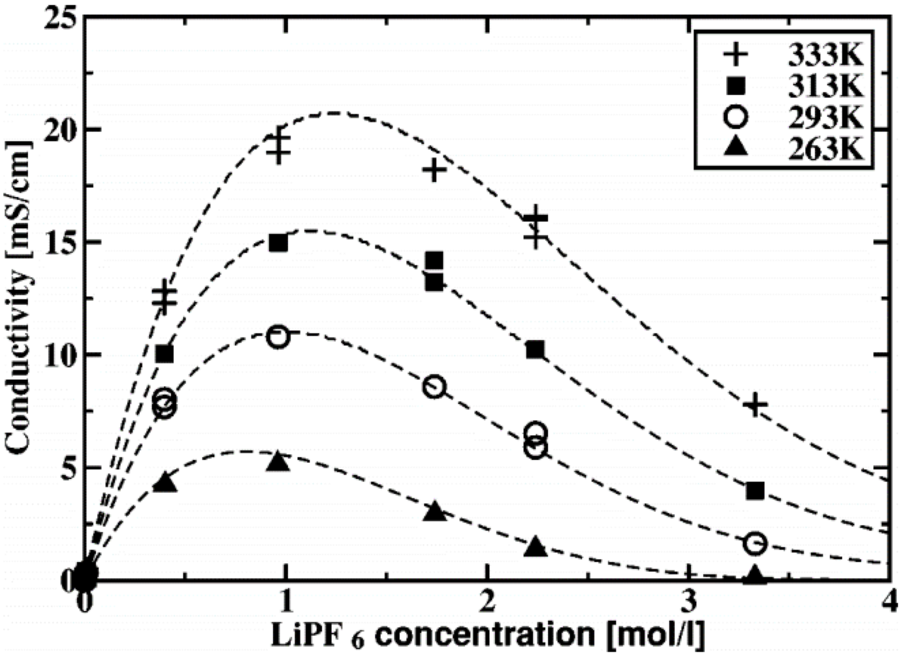

Figure 2.11: *Trend of the electrolyte ionic conductivity with concentration and temperature given by the correlation of equation 2.44 (taken from [101])*

The dependence of the electrical resistances with temperature were not added, due to the lack of data about these relationships in lithium-ion battery literature. Moreover, their impacts on the simulation output are considered negligible if compared to the ones of the parameters listed above.

Finally, the integration of COMSOL with MATLAB has been improved, allowing the users to give complex combinations of inputs to the model from the MATLAB IDE, and to easily export and store the desired simulation data for subsequent analyses.

Chapter 3

Experimental campaign

3.1 Experimental bench

The core of the test bench was designed and built in the context of the previous thesis on the same project [93]. During this work, we improved and rationalized the system's wiring, and we eliminated a source of electromagnetic noise that decreased the accuracy of the electrochemical impedance spectroscopy.
The test bench (see figure 3.1) has been developed with a modular structure, that allows the testing of batteries in a flexible way in four independent channels, each equipped with a Chroma UM 63640-80-80 electronic load. A NI DAQ USB 6218 acquisition board is used to measure voltage oscillations during EIS and to check the battery voltage read by the electronic loads, while the power supply NI RMX-4124 acts as battery charger. The batteries are placed in a Binder KT 53 climatic chamber, that controls and adjusts the operative temperature in the $4°C - 100°C$ range. The individual surface temperature of each LIB is measured through four RS PRO type K thermocouples, with a NI CDAQ 9211 as temperature acquisition board.
In addition to this fixed setup, an Autolab PGSTAT30 with a FRA2 module is employed to perform high-precision electrochemical impedance spectroscopies on the batteries. The list of all the components is reported in the table 3.1 below.

Instrument	**Scope**	**Measured quantity**	**Measurement uncertainty**
NI RMX-4124	Power supply	Current	$\pm 0.5\% \pm 0.1\%$f.s.[b]
Chroma UM 63640-80-80	Electronic load	Voltage Current	$\pm 0.025\% \pm 0.01\%$f.s.[b] $\pm 0.1\% \pm 0.1\%$f.s.[b]
NI DAQ USB 6128	Voltage acquisition	Voltage	$\pm 0.0085\% \pm 0.002\%$f.s.[b]
Binder KT 53	Temperature control	Temperature	±0.3 K[b]
NI CDAQ 9211 w/ K-TC	Temperature measurement	Temperature	±3 K[b]
Autolab PGSTAT30+FRA2	Impedance measurement	Impedance	variable [a]

[a] Measurement uncertainty type A
[b] Measurement uncertainty type B, see table 3.3

Table 3.1: *Instruments used in the lithium-ion batteries experimental bench*

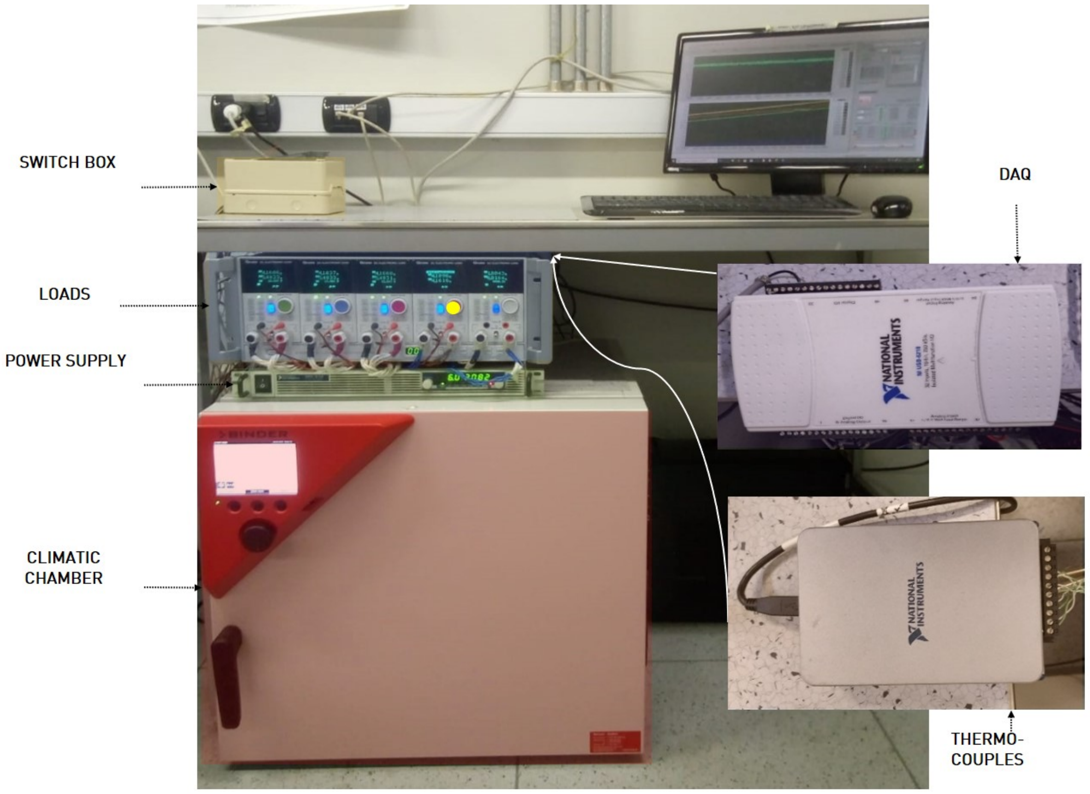

Figure 3.1: *Photo of the laboratory test bench, with the core components highlighted*

In figure 3.2 it is represented the electric circuit that connects each battery to the respective electronic load and to the power supply. Each battery is coupled to a switch, that allows to pass from the discharge mode (position *a*, open) to the charge mode (position *b*, closed) and vice versa. The standard position is *a*, where the battery is disconnected from the circuit.
The load has the possibility to drain a variable current from the battery, while the power supply applies a fixed current, according to its selected range. If the switch is in position *a*, the battery can be only discharged by the electronic load. If the switch is in position *b*, the battery can be charged by the power supply. In this case, due to the fixed applied current of the power supply, the charging current of each battery is regulated by the respective the electronic load, that subtracts a specified amount of current according to the desired C-rate on the battery. A fifth electronic load acts as a fixed resistance of $0.3\ \Omega$ that checks the value of the current in the main electric circuit
With this configuration, the batteries are completely independent from one another and they can operate in different modes without affecting the others. Moreover, a single power supply is sufficient to charge all of them. When the Autolab station is needed for the electrochemical impedance spectroscopy, its power cables are connected to the load corresponding to the tested battery, while the sensor cables are connected to the corresponding channel in the voltage acquisition board.

The test bench is connected to a computer and controlled with the software

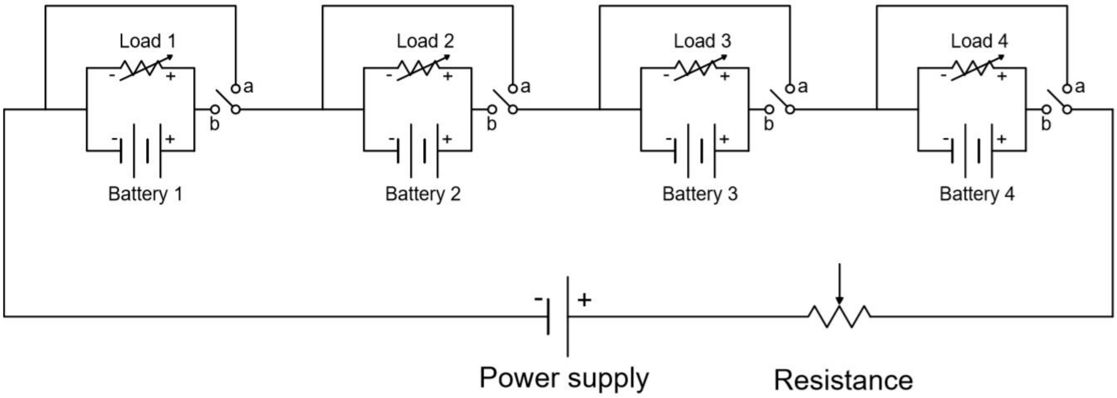

Figure 3.2: *Electric circuit of the laboratory test bench*

LabView©. The data about voltage, current and temperature are collected by the instruments, and monitored and saved by the test bench control system. The control system also checks that the batteries operative conditions are among the safety limits, in order to avoid overcharges, overdischarges and excessive temperatures. These conditions can not only be detrimental for the battery health, but they can also be dangerous for the safety of the test bench itself, due to the problem of thermal runaway [90].
The safety limits of the test bench are:

- **Maximum current**: I<20 A (limit on the switches maximum load, fixed);
- **Maximum voltage**: $V < V_{max}$ (limit on the batteries maximum voltage, adjustable);
- **Minimum voltage**: $V > V_{min}$ (limit on the batteries minimum voltage, adjustable);
- **Maximum temperature**: T<50°C (limit on the batteries maximum temperature, fixed);

If one of these limits is met, the switches and the resistance on the main circuit are opened, and the batteries are disconnected from the power supply. Moreover, the electronic loads have an internal lower voltage limit, that can be manually set and that can act as a redundancy in case of a failure of the control system.
The limits on the maximum and minimum voltage can be adjusted according the specific battery that is being tested, since different chemistries can have different voltage limits.

3.1.1 Battery samples

The tested lithium-ion batteries are commercially available products, in accordance to the scope of the thesis project, directed towards the second use of commercial batteries. Apart from some basic data about the nominal voltage and capacity, the safety limits and the chemistry of the electrodes, there are no information regarding the parameters that would be important for the model, such

Characteristic	**US**26650**VT**	**US**18650**V**3
Cathode chemistry	NMC+LMO	NMC
Anode chemistry	Graphite	Graphite
Nominal capacity	2600 mAh	2250 mAh
Maximum charge current	2.6 A	2.25 A
Maximum discharge current	26 A	10 A
Nominal voltage	3.7 V	3.7 V
Maximum voltage	4.2 V	4.2 V
Minimum voltage	2.8 V	2.5 V
Temperature range (charge)	0 – 40° C	0 – 45° C
Temperature range (discharge)	−10 – 45° C	−20 – 60° C
Weight	85 g	44 g
Dimensions (D x H)	26 mm x 65 mm	18 mm x 65 mm

Table 3.2: *Characteristics of the tested battery samples*

as the internal geometry, the particles average radius in the anode and the cathode or the type of electrolyte. This is a common situation in the LIB sector, where a wide application of the industrial secret causes a lack of information on the composition and structure of the batteries.

Before reporting the known specifics of the batteries, it is important to describe the differences between the two main types of commercial lithium-ion batteries that are currently employed [132]:

- **high-power batteries**: these batteries are designed for high current drain applications, where it is more important the peak power performance than the autonomy. To obtain this characteristic, the battery resistance has to be minimized. The available active area in the anode and in the cathode is maximized by using a low average active particle size, offering an high amount of sites for the electrochemical reactions. Then, the electrodes are made thin, in order to reduce their resistance and to minimize the electrolyte concentration unbalance across the cell after a strong charge/discharge, lowering the resulting overpotential. Finally, the porosity of the electrodes is quite high, in order to make available an high quantity of electrolyte to the active materials when high current rates are achieved;

- **high-energy batteries**: this kind of battery is employed in applications where an high autonomy is desired, and the battery capacity is the key parameter. An high capacity is obtained by storing an high amount of lithium in the electrodes. To do so, the electrodes are made thick and less porous, increasing the amount of active material that can accept lithium. The drawback is an increased resistance of the cell, that limits its maximum current rates;

According to these general characteristics of the two battery types and to the existing literature, it is possible to assign sound values to the geometrical and thermodynamic parameters of the tested batteries, in order to consider them fixed during the sensitivity analysis (see chapter 4.1).

In total, four lithium ion batteries are tested in the experimental campaign: two Sony US26650VT and two Sony US18650V3 (*figure* **??**). The former belong to the high-power category, while the latter have more high-energy characteristics. Each group of two batteries is composed by a new and an aged sample. The aging has been performed in laboratory during the previous thesis work [93] in case of the high-power battery, while the aged high-energy battery was used in electric bikes. Their specifics are reported in the table 3.2.

3.1.2 Measurement uncertainty

Uncertainty on voltage measurement

For what concerns the voltage, the electronic load has 6 V as full-scale value. According to the accuracy band reported by the manufacturer, the uncertainty on the voltage output σ_V will be:

$$\sigma_V = (0.025\% \cdot +0.01\% \cdot 6\,V) = 0.085\%$$

Uncertainty on current measurement

The accuracy on the load current σ_I is reported by the manufacturer of the electronic load (*table 3.1*). Since the full-scale value of the current in the electronic load is 8 A, we get:

$$\sigma_I = (0.1\% \cdot +0.1\% \cdot 8\,A) = 0.9\%$$

Uncertainty on the ambient temperature

The temperature that is set by the climatic chamber, i.e. the battery operative temperature, has an absolute error u_T declared by the manufacturer, that is:

$$u_T = \pm 0.3\,K$$

Uncertainty on the initial OCV

When the battery is brought through a charge or a discharge to the desired SOC, there is always a small error that makes the actual SOC different from the target one. In our case, the most common condition is reaching SOC equal to 100% with a charge before starting a discharge. This SOC should correspond to 4.2 V, nevertheless it is always observed a small deviation from this value, that depends on the current rate at which the charge is made, on the time waited after the charge before starting the discharge and on the termination current used during the CV section of the charge. This little offset causes a vertical shift of the whole discharge curve with respect to the "ideal" discharge curve that starts from exactly 4.2 V. This uncertainty on the initial OCV is quantified by analysing the experimental data of the discharge curves that started from 100% SOC that we performed during the experimental campaign and calculating the mean and the double of the standard deviation of the voltage value of the initial points of such discharge curves, assuming a normal distribution of the errors. The result of this analysis is:

$$u_{OCV} = \pm 0.0045\,V$$

Uncertainty on the exchanged capacity

Regarding the exchanged capacity, its uncertainty is based on the one of the current drained by the load during the discharge. The formula that calculates the exchanged capacity Q_{exc} is:

$$Q_{exc} = I_{dis} \cdot t_{dis} \tag{3.1}$$

where I_{dis} is the applied discharge current and t_{dis} is the duration of the discharge. Theoretically, t_{dis} could be calculated according to the discharge operative parameters as:

$$t_{dis} = \frac{DOD \cdot 3600 \left[\frac{s}{h}\right]}{C} \tag{3.2}$$

Nevertheless, this formula gives only a rough estimate of the duration of the discharge, since it is based on the nominal capacity of the battery. For currents higher than the nominal one, the real duration will be lower, vice versa for currents lower than the nominal one. Moreover, here the aging of the cell is not considered, and the lower available capacity caused by degradation phenomena make the discharge duration decrease even more.

The uncertainty on Q_{exh} is the cumulative sum of the uncertainty on the applied current. Therefore, σ_Q is based on the accuracy on the load current σ_I reported by the manufacturer of the electronic load (*table 3.1*) and on the duration of the capacity test. Being a cumulative sum of the normal probability distributions of the current uncertainty u_I (multiplied a constant timestep), u_Q has a normal distribution too. To obtain the trend of the uncertainty on the exchanged charge during a discharge with our experimental bench, we simulate the sum of normal probability distributions using a full discharge from SOC 100% to SOC 0% in a battery with a nominal capacity of 2600 mAh, such as the US26650VT, dividing the discharge curve in . In each point n we run 100000 simulations on the possible outcome of the uncertainty $u_{Q,n}$:

$$u_{Q,n} = \sum_{i=1}^{n} randn(\mu = 0,\, \sigma = 0.0045) \cdot I \cdot \Delta t$$

where the current I is taken equal to 1.3 A, 2.6 A, 5.2 A and 7.8 A, corresponding respectively to 0.5C, 1C, 2C and 3C, and $randn(\mu = 0, \sigma = 0.0045)$ is a random number in a normal distribution with mean (μ) equal to zero and standard deviation (σ) equal to half the uncertainty on the current, assuming that this uncertainty corresponds to a 95% level of confidence.

Therefore, for each point n we obtain a probability distribution of the uncertainty on the exchanged charge. The double of the standard deviation of each probability distribution is then calculated (95% level of confidence), obtaining the trend of the uncertainty on the exchanged charge u_Q during the discharge of figure 3.3.

Combined uncertainty on the cell voltage

By combining all the previous data, it is possible to estimate the uncertainty on the measured voltage by taking into account all the possible sources of error. The

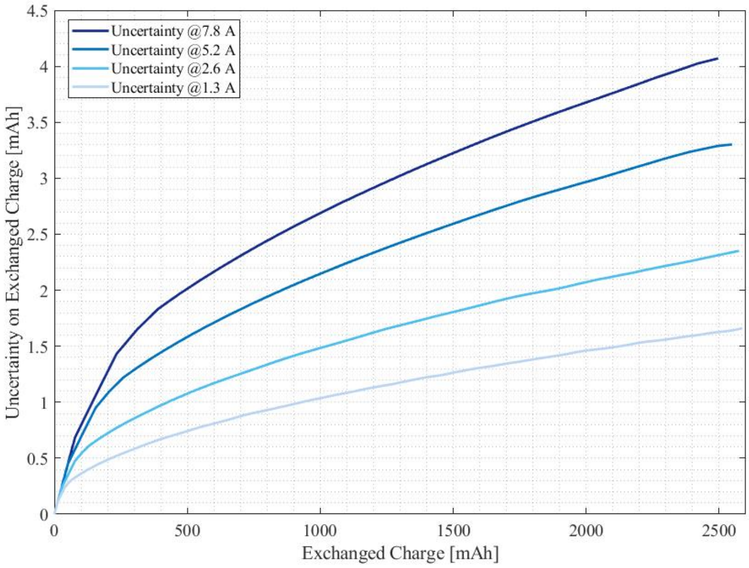

Figure 3.3: *Trend of the error on the exchanged charge*

combined uncertainty on the cell voltage V is expressed as:

$$u_V = \sqrt{(\sigma_V \cdot V)^2 + \left(\frac{\Delta V}{\Delta I} \cdot u_I\right)^2 + \left(\frac{\Delta V}{\Delta T} \cdot u_T\right)^2 + u_{OCV}^2 + \left(\frac{\Delta V}{\Delta Q} \cdot u_Q\right)^2} \tag{3.3}$$

where $\Delta V / \Delta I$ is the variation of voltage caused by a variation of the current, $\Delta V / \Delta T$ is the variation of voltage caused by a variation of the temperature and $\Delta V / \Delta Q$ is the variation of voltage caused by a variation of the exchanged charge. Each of these three terms is dependent on the current rate, on the operative temperature and on the state of charge. Therefore, it is not possible to give an exact, fixed value for every discharge curve, but they will be calculated in each specific operative condition.

Here, we give an example on a full discharge curve starting from 100% SOC, with current rate equal to 3 and ambient temperature equal to 25°C. By analyzing the experimental data, we can calculate approximated values for the variation of the voltage with current and temperature:

$$\begin{cases} \frac{\Delta V}{\Delta I} = 35\,\frac{mV}{A} \\ \\ \frac{\Delta V}{\Delta T} = 8\,\frac{mV}{K} \end{cases}$$

It is not possible to approximate the variation of the voltage with the charge to a single value without introducing a significant error.

The resulting uncertainty on the cell voltage of the considered discharge curve is shown in figure 3.4. For most of the duration of the discharge the voltage error stays around ±7 mV, while it raises up to ±14 mV in the final part of the curve, where the slope of the voltage is higher and the uncertainty on the exchanged charge has more weight.

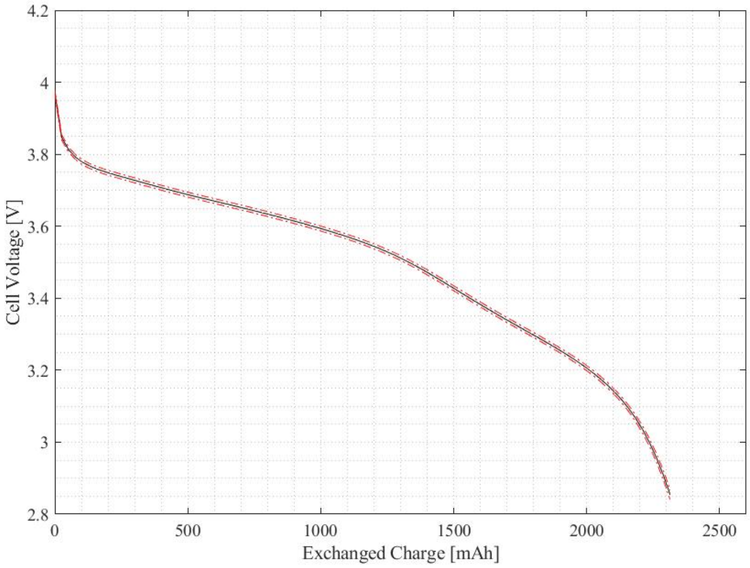

Figure 3.4: *Error bands (in red) on the measured voltage during a full discharge from* 100% *SOC, at* $3C$ *and* $25°C$

Uncertainty on the battery surface temperature

The temperature is the measured quantity on which there is the highest uncertainty, due to the low accuracy of the used instruments, on the non-optimal contact between the battery and the thermocouple, and the absence of insulation from the ambient air of the thermocouples. The manufacturer of the temperature acquisition board reports a maximum error $\sigma_{T,tc}$ of ±2 K with K-type thermocouples in the temperature range employed in our tests. Nevertheless, we observed from experimental data that the dispersion of the temperature among the four thermocouples employed in our setup was much more limited than the range reported by the manufacturers. By analyzing the data of temperature acquisitions during a whole day where the temperature of the batteries and the temperature of the chamber was not changed, we calculated the mean and the double of the standard deviation of the temperature data, assuming a normal distribution of the errors. The resulting uncertainty on the measured battery surface temperature is equal to ±0.18 K. However, due to the poor quality of the battery-thermocouple contact and to the exposition to ambient air, it was decided that the measured temperature was not a reliable indicator of the actual battery surface temperature. Therefore, this temperature acquisition is only used as a control to avoid excessive battery heating and to check the ambient temperature set by the climatic chamber.

Uncertainty on impedance

For the measurement of the battery impedance, the employed instrument is the Autolab PGSTAT30 with the FRA2 module. The manufacturer does not provide an accuracy band on the impedance value, but he reports the uncertainty on the measured voltage and on the applied current. Nevertheless, the band for the impedance cannot be calculated as the compound uncertainty since the analytical

	High Frequency		Mid Frequency		Low frequency	
Temperature	u_{Z_R} [µΩ]	u_{Z_I} [µΩ]	u_{Z_R} [µΩ]	u_{Z_I} [µΩ]	u_{Z_R} [µΩ]	u_{Z_I} [µΩ]
10° C	±18.0	±13.5	±590	±216	±197	±238
25° C	±12.2	±11.1	±208	±93.6	±168	±114
40° C	±10.9	±7.88	±238	±76.3	±81.0	±99.6

Table 3.3: *Results of the uncertainty analysis on the battery impedance with Autolab PGSTAT30*

relationship between the impedance and these two quantities is very complex, and hence the partial derivatives contained in the compound uncertainty formula are not easily computable.

Due to this fact, the accuracy on the battery impedance is computed based on repeated measurements, as a type A uncertainty. It is evaluated on the new US26650VT battery at 100% SOC and with ambient temperature equal to 10° C, 25° C and 40° C. In each of these three conditions, 20 impedance measurement are performed in succession in the frequency range 4000-0.05 Hz, with 25 logarithmically spaced points. In this way, we include the uncertainties on the other quantities, e.g. temperature, frequency.

The uncertainty is calculated as the double of the standard deviation of the measurements in each frequency point (2σ confidence interval assuming a normal distribution of the errors), separately for the real part (u_{Z_R}) and for the imaginary part (u_{Z_I}):

$$\begin{aligned} u_{Z_R} &= 2 \cdot \sqrt{\tfrac{1}{20} \sum_{n=1}^{20} (\overline{Z_R} - Z_{R,n})^2} \\ u_{Z_I} &= 2 \cdot \sqrt{\tfrac{1}{20} \sum_{n=1}^{20} (\overline{Z_I} - Z_{I,n})^2} \end{aligned} \tag{3.4}$$

In table 3.3. the results of the uncertainty analysis are reported, while in figures 3.5, 3.6 and 3.7 the real and imaginary impedance error bars in each frequency point and in each temperature are shown. The average impedance value is indicated as a red dot. The axes ranges are different in the three charts, in order to better visualize the error bars.

In order to provided more compact information in the table 3.3, an average of the uncertainties is calculated according to the frequency range. In particular, high frequency includes the points between 4000 Hz and 100 Hz, mid frequency includes the points between 100 Hz and 1 Hz, and low frequency includes the points between 1 Hz and 0.05 Hz.

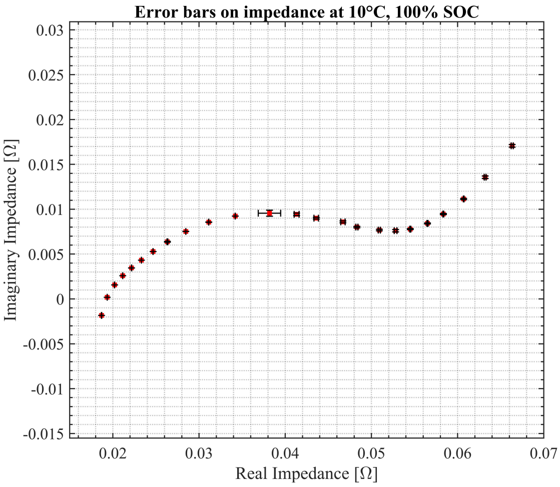

Figure 3.5: *Error bars for the impedance measurement in an EIS at* 100*% SOC,* 10° *C*

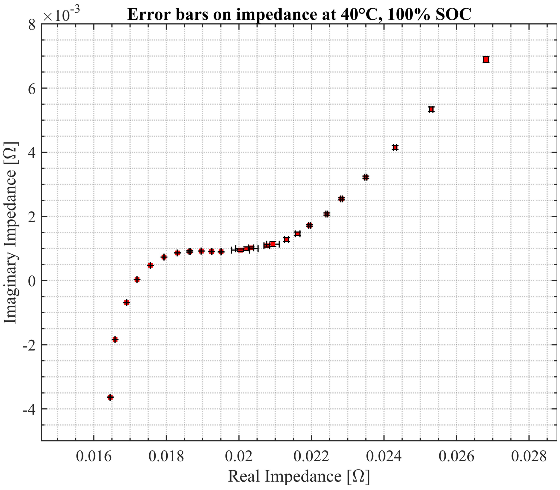

Figure 3.6: *Error bars for the impedance measurement in an EIS at* 100*% SOC,* 25° *C*

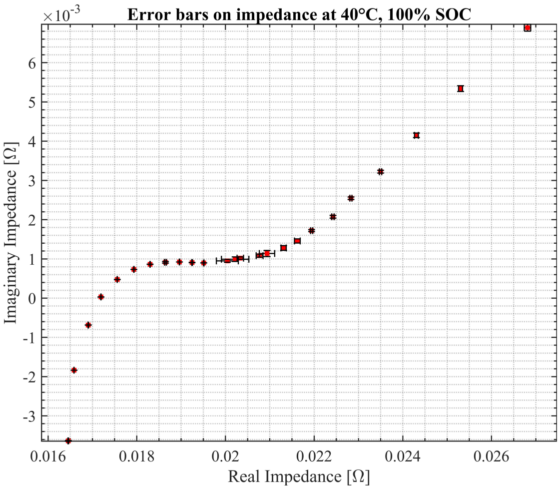

Figure 3.7: *Error bars for the impedance measurement in an EIS at* 100*% SOC,* 40° *C*

3.2 Results

In the following section, we will present and discuss the results of the performed tests on the samples, i.e. the capacity tests (Chapter 3.2.1), the relaxation tests (Chapter 3.2.2) and the electrochemical impedance spectroscopies (Chapter 3.2.3), with the objective of understanding the information on the batteries provided by each technique.

3.2.1 Capacity test

The capacity tests are executed according to the methodology reported in section 2.1.1, with a CC-CV charge with 0.05 A as CV termination current followed by a discharge down to the lower voltage limit of the battery. When the climatic chamber temperature is modified, the batteries are left at rest for at least 4 hours, in order to obtain a homogeneous battery temperature profile.
The experimental matrix for the capacity tests is composed by:

- three values of ambient temperature: T_{amb} ∈{10°C, 25°C, 40°C};
- four values of current rate: C ∈{0.5C, 1C, 2C, 3C};

The combinations of current rates and ambient temperatures have the purpose of exploring the impact of these two operative parameters on the results of the diagnostic procedure. The figures shown in this chapter are obtained from capacity tests on the new US26650VT battery, plus a couple of examples from the aged US26650VT and the new US18650V3 in order to make comparisons with the new US26650VT.

Effect of current rate

In figure 3.8.a, it is shown the variation of the discharge curve of the pristine US26650VT at 25° C with the C-rate. It is possible to see that an increase of the C-rate corresponds to a lower exchanged capacity, and in general this is true for all the tested batteries and for all the employed ambient temperatures. For instance, the pristine US26650VT passes from 2501 mAh at 0.5C to 2357 mAh at 3C.
The reasons for this effect are:

- an higher C-rate implies an larger reaction current i_r, which increases the activation overpotential according to the Butler-Volmer kinetics (equation 2.14). Moreover, the electronic ohmic losses in the solid are enhanced, since they are proportional to the current in the solid i_s itself (equation 2.19). Finally, the higher current in the electrolyte i_e leads to an increase of the ionic ohmic losses and of the electrolyte concentration overpotential, according to equation 2.22. The increase of the activation and ohmic losses can be noticed by the higher initial voltage drop, since at the beginning of every discharge the battery has the same equilibrium conditions (100% SOC, at 4.2 V);
- an higher C-rate induces a higher lithium concentration disequilibrium in the particles of both the electrodes, due to the higher molar flow rate of

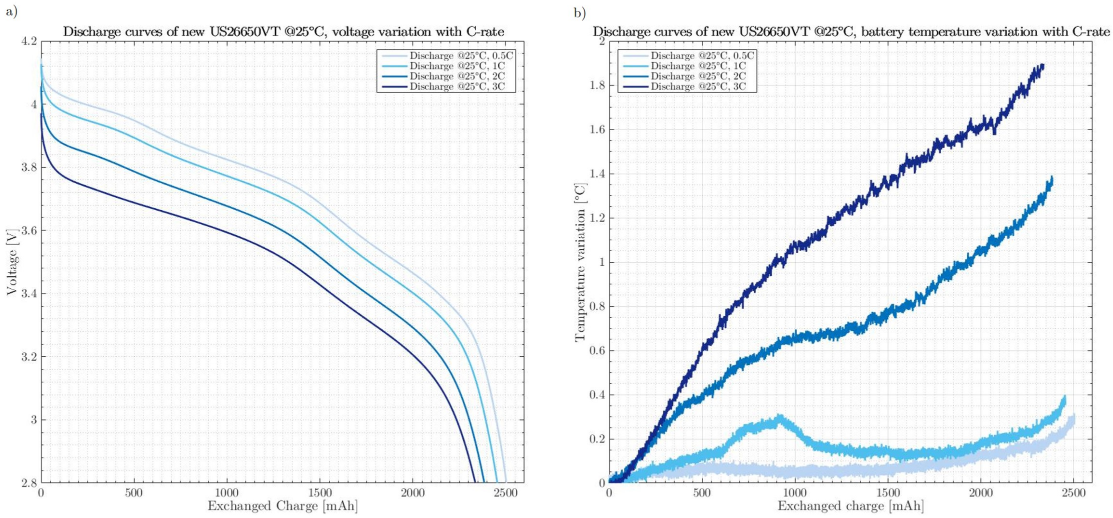

Figure 3.8: *On the left: Discharge curves of new US26650 VT, @25° C, voltage variation with C-rate. On the right: Discharge curves of new US26650 VT, @25° C, battery temperature variation with C-rate*

lithium transported in the cell. According to the mechanism described in section 1.1.2, the difference in concentration between the electrode particle surface and the bulk of the electrode particle itself implies a lower/higher open circuit potential of the cathode/anode if compared to a situation where the discharge does not create an inhomogeneous lithium concentration profile in the particles.

In addition, an higher C-rate has the effect of enhancing the difference between the surface lithium concentration of the electrode particles near the current collector and the ones near the separator. The electrochemical reaction is more concentrated in the points that are nearer to the other electrode, i.e. in proximity of the separator [103]. This uneven reaction profile further limits the amount of lithium accessible during the reaction, decreasing the exchanged capacity during the discharge.

The effects of the unbalances in the concentration of lithium in the solid in the capacity tests are observable from the contraction of the discharge curve towards lower exchanged capacities, without taking into account the vertical shift due to the ohmic and activation losses.

The increased overpotential is also consistent with the trend of the surface temperature with the C-rate, in figure 3.8.b. Higher voltage losses cause a higher heat generation, as shown by equation 2.37.

Effect of ambient temperature

The effect of the ambient temperature on the discharge curves can be observed in figures 3.9 and 3.10. The former figure shows tests at 0.5C while the latter figure shows test at 3C. We choose to report these two conditions in order to help to understand the impact of a temperature variation with different battery loads.

The lower the ambient temperature at which the battery operates, the lower the exchanged capacity, and this effect is enhanced at higher current rates. For example, in the pristine US26650VT the capacity in a discharge curve at 0.5C passes from 2503 mAh at 40°C to 2377 mAh at 10°C, with a difference of 126 mAh. Instead, the capacity in a discharge curve at 3C changes from 2406 mAh at 40°C to 2146 mAh at 10°C, a delta of 260 mAh.
The explanations for this phenomenon are:

- the lower operating temperature has the effect of slowing the kinetics of the electrochemical reactions, as indicated by the Arrhenius-type relation of the rate constants k with the temperature (equation 2.47), leading to an higher activation overpotential. Moreover, the temperature affects also the electrolyte ionic conductivity κ_e, making it decrease, as seen in figure 2.11. Therefore, the ohmic losses increase;

- the equivalent ionic conductivity κ_D is directly proportional to the ionic conductivity κ_e and to the temperature. Therefore, with a temperature decrease, κ_D decreases too. According to equation 2.22, to maintain the same electrolyte current the concentration gradient in the electrolyte has to increase. This increased concentration gradient makes the whole electrode less accessible for the electrochemical reaction, which consequently concentrates near the separator, giving the same effect described when discussing about the variation of the current rate. The steeper concentration gradient is also implied by the lower lithium diffusion coefficient in the electrolyte D_e, determined by equation 2.45. D_e decreases if the ionic conductivity κ_e and the temperature decrease too;

- the lithium diffusion coefficient in the solid electrode D_s has an Arrhenius-type dependence with temperature, according to equation 2.48. The lower the temperature, the lower this diffusion coefficient. Therefore, the obtained effect is analogous to the one described in the section about the current rate variation, with the difference that the increased concentration gradients in the electrode are caused by a more sluggish diffusion of the lithium and not by an higher lithium molar flow. This effect is particularly evident at higher current rates, as in figure 3.9.a. In fact, with the low current rate of figure 3.10.a, we notice only a vertical shift of the voltage, while in figure 3.9.a a contraction of the curves is evident at 10°C.

The variation of the battery surface temperature of figure 3.9.b validates the explanation of higher overpotentials induced by the lower temperature.

Effect of battery aging

In figure 3.11.a, it is possible to see how the capacity tests change according to the battery aging, with a discharge at 0.5C and 40°C, and one at 3C and 10°C. Comparing the capacity tests of the pristine and the aged US26650VT, we have

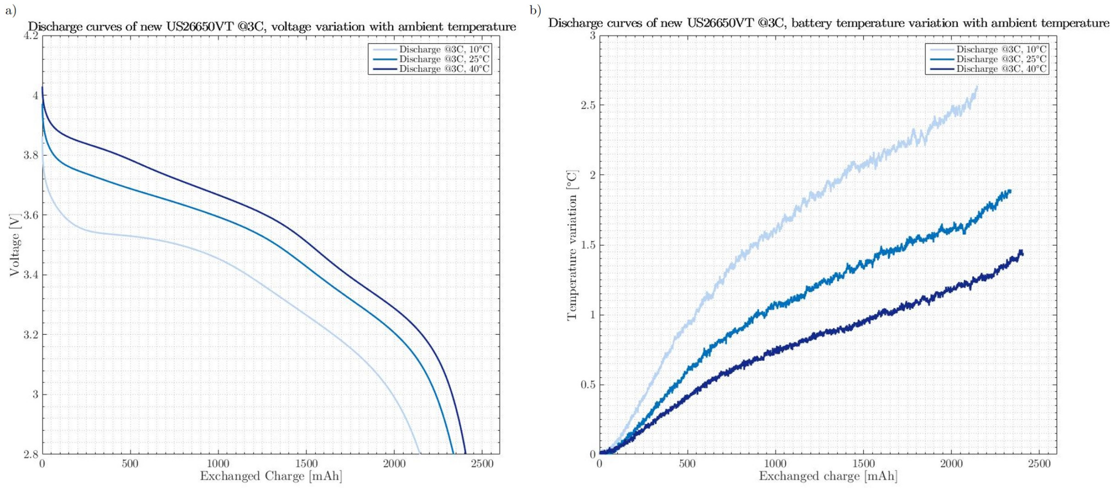

Figure 3.9: *On the left: Discharge curves of new US26650VT, @3C, voltage variation with ambient temperature. On the right: Discharge curves of new US26650VT, @3C, battery temperature variation with ambient temperature*

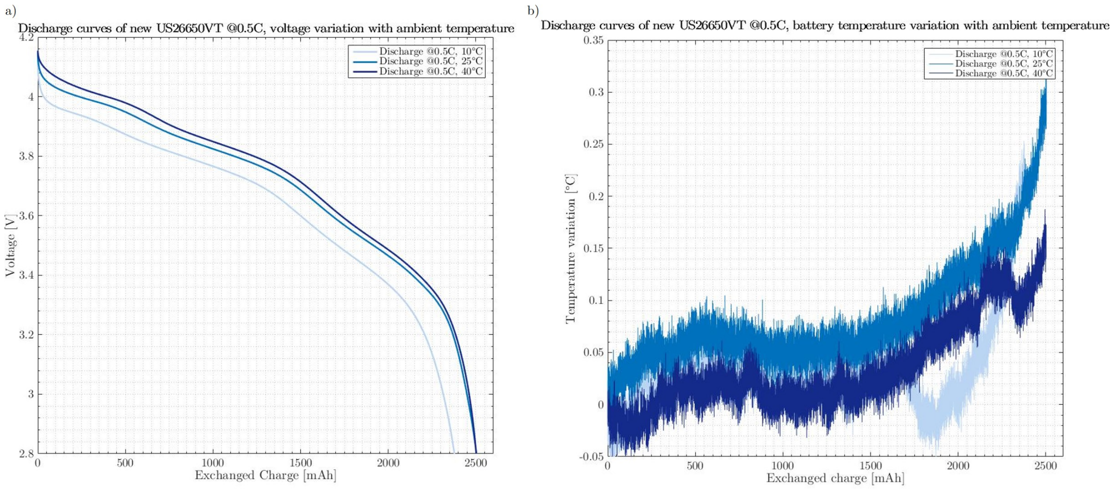

Figure 3.10: *On the left: Discharge curves of new US26650VT, @0.5C, voltage variation with ambient temperature. On the right: Discharge curves of new US26650VT, @0.5C, battery temperature variation with ambient temperature*

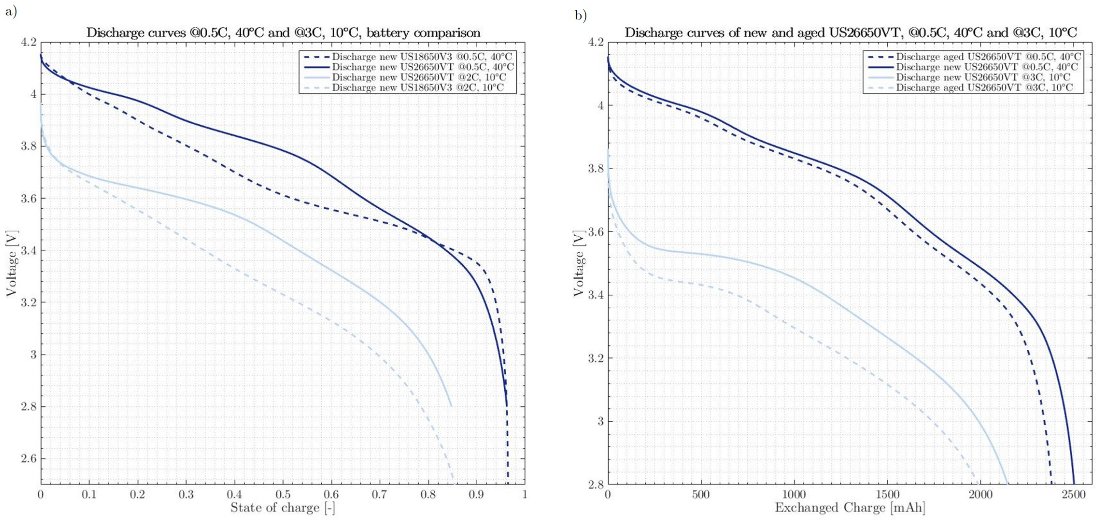

Figure 3.11: *On the left: Discharge curves @*$0.5C$*,* $40°C$ *and* $3C$*,* $10°C$*, battery comparison. On the right: Discharge curves of new and aged* $US26650VT$*, @*$0.5C$*,* $40°C$ *and @*$3C$*,* $10°C$

2503 mAh against 2381 mAh at 0.5C and 40°C, and 2146 mAh against 1989 mAh at 3C and 10°C.
The reasons for this effect are:

- the aged US26650VT battery has a lower available capacity than the new US26650VT battery, due to the degradation effects that induce a capacity fade. The discharge curve made at 0.5C and 40°C shows this fact, since the overpotentials and the concentration gradient are very low with this current rate, and the difference between the new and the aged voltage curve can be only explained by a difference in the capacity;

- the aged battery shows higher ohmic and activation losses, as noticeable from the difference between the new and the aged voltage curve at 3C and 10°C. This characteristic reflects a power fade in the aged battery, probably due to the additional resistance created by the SEI layer, by the lower ionic conductivity caused by the electrolyte degradation, and by the lower specific active area in the electrodes due to particle cracking, structural disordering, etc. (see Chapter 1.3.2);

- from these curves it is not clear if there are differences in the diffusion processes between the two batteries;

Effect of battery type

Figure 3.11.b show the comparison between the discharge curve of the new US26650VT and the one of the new US18650V3, still with a discharge at 0.5C and 40°C, and one at 3C and 10°C. As x-axis, the state of charge is used instead of the exchanged capacity, due to the unequal nominal capacity of the two batteries. The most evident feature are:

- the difference in the open circuit voltage, as it is clear from the shape of the 0.5C and 40°C discharges. Since the anode material is graphite in both cases, the variation of open circuit voltage is due to the distinct cathode materials of the two batteries: LMO+NMC for the US26650VT, NMC for the US18650V3. Also, the second chemistry allows a lower cut-off voltage to the US18650V3 battery (2.5 V vs 2.8 V);

- from the curves of figure 3.11.b it seems that there are no major differences in the ohmic and activation losses, but we have to remind that the actual current at which the tests are made is not the same for the two batteries. In fact, 3C for the US26650VT is equal to 7.8A, while 3C for the US18650V3 is equal to 6.75A. Since the voltage losses are proportional to the current, actually the US26650VT has lower ohmic and activation overpotentials than the US18650V3 at the same current, since these losses are equal in figure 3.11.b.

3.2.2 Relaxation test

The relaxation voltage profile is obtained after a current pulse that discharges the battery with a depth of discharge (DOD) of 20%. The depth of discharge is the percentage of nominal capacity that is exchanged during a current pulse. After the pulse, the battery is allowed to relax for at least three days, in order to be sure to measure the whole voltage recovery after the end of discharge. In fact, a full equilibrium can be reached only after hours or days after a current pulse, according to the magnitude of the current pulse itself [106, 133, 134]. Then, the subsequent pulse is applied. The starting point for each battery is 100% SOC, and theoretically there could be five pulses with 20% DOD. Nevertheless, the last pulse is always stopped before reaching the desired depth of discharge because of the lower voltage limit. Since we want to have the same exchanged capacity for all the pulses, the relaxation tests are stopped when 20% SOC is reached. Therefore, the reached states of charge are 80% SOC, 60% SOC, 40% SOC and 20% SOC.
The experimental matrix for the relaxation tests is composed of:

- three values of ambient temperature: $T_{amb} \in$ {10°C, 25°C, 40°C};

- two values of current rate in the pulse: $C \in$ {0.2C, 3C};

In the figures, the quantity with which the relaxation curve is shown as the voltage recovery after the end of discharge, taking as reference the first point measured with current equal to zero ($t \approx 0.5$ s), and subtracting this reference value to all the subsequent points. This quantity allows to easily compare the trends of the tests that have a different end of discharge voltage. Since the relaxation curves start from approximately 0.5 seconds after the end of discharge, the ohmic and activation overpotentials considered recovered, as well as the discharge of the double layers capacity is considered complete, thanks to the very low characteristic times that are associated to these phenomena ($\approx$ 0.01 − 0.001 s) [103, 125]. Therefore, the trend of the relaxation curve is practically determined by the reequilibration of the lithium concentration gradients in the electrolyte and in the solid materials.

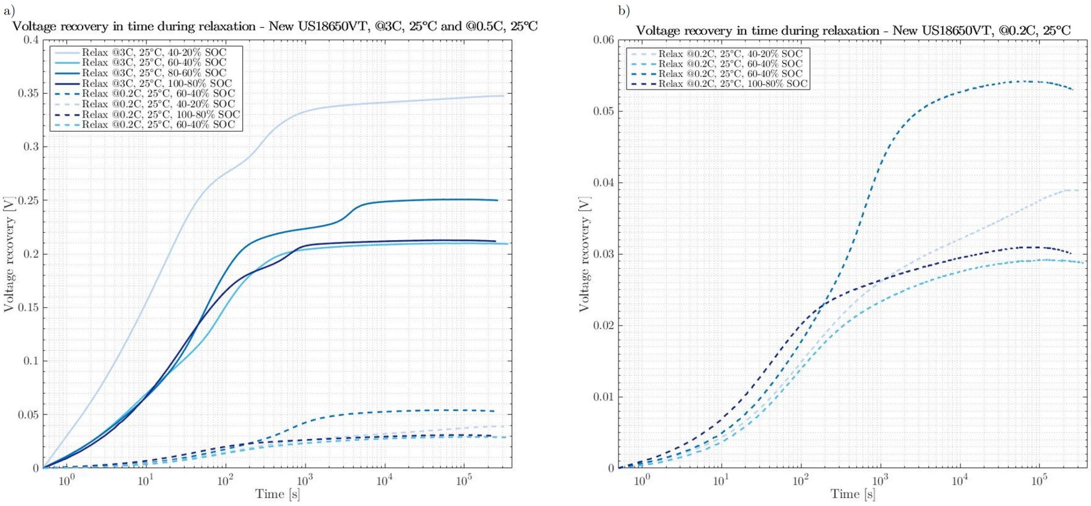

Figure 3.12: *On the left: Voltage recovery in time during relaxation, logarithmic time scale - New* $US18650V3$*, @*$3C$*,* $25°C$ *and* $0.5C$*,* $25°C$*. On the right: zoom on the voltage recovery* $0.5C$*,* $25°C$ *(different voltage scale)*

The battery surface temperature is not reported, since its trend is only determined by the preceding discharge pulse and by the convective heat transfer coefficient in the climatic chamber, that cools the battery down to the ambient temperature. The relaxation process does not affect the battery temperature per se, since in this phase there are no reaction currents that are so relevant that they can induce heat generation. The figures report the tests on the new US18650V3 high-energy battery, with a comparison with the aged US18650V3 and with the new US26650VT high-power battery. We chose to report the data about the high-energy batteries since the voltage recovery during the relaxation is larger than the one of the high-power batteries, and then it is easier to understand the effect of the variation of the operative conditions.

Effect of pulse current rate

In figure 3.12.a, it is shown the voltage recovery in the new US18650V3 after all the 20% DOD discharge pulses at 25°C, with two different current rates. Figure 3.12.b is a zoom on the relaxation voltage after the pulses at 0.2C, to better appreciate the difference between the reached states of charge. The main trends in these plots are:

- the magnitude of the voltage recovery is strongly affected by the current rate at which the previous discharge is performed. The voltage recovery for the 3C pulse is 5 times higher than the 0.2C pulse for the discharge from 80% to 60% SOC, while it is 10 times higher in case of the discharge from 40% to 20% SOC. The explanation for this behavior can be found in the much higher concentration disequilibria caused by the high current, which corresponds to higher voltage losses according to the mechanisms described in section 1.1.2;
- it is interesting to notice how in both cases the voltage profiles reach an almost stable value in the $5 \cdot 10^4 - 10^5$ s range, which correspond to about $12 - 24$ h.

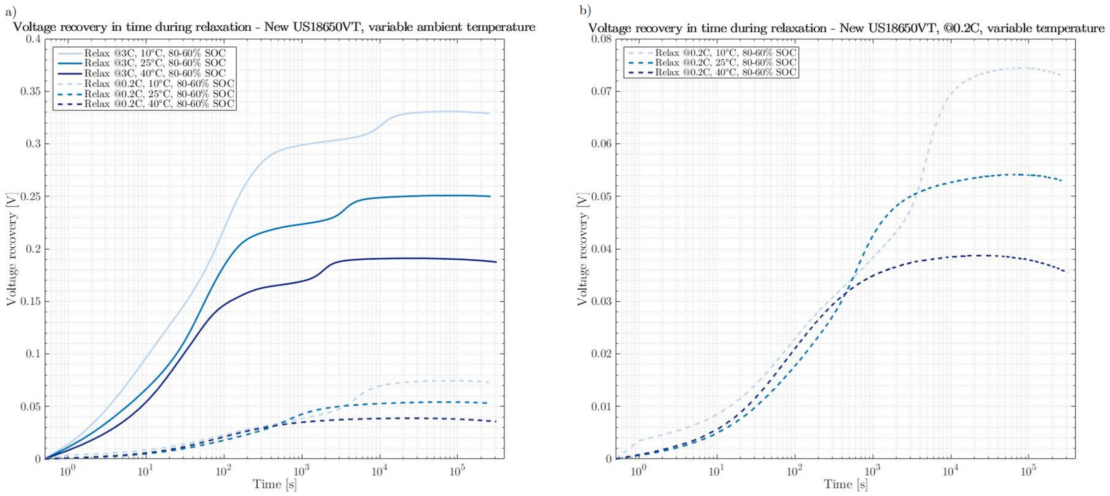

Figure 3.13: *On the left: Voltage recovery in time during relaxation, logarithmic time scale - New* $US18650V3$*, @*$3C$ *and* $0.5C$*, variable ambient temperature. On the right: zoom on the voltage recovery @*$0.5C$ *(different voltage scale)*

This similarity in the time needed to reach the peak value of voltage recovery can be explained by the fact that the rate at which a concentration gradient is flattened is proportional to the concentration gradient itself (see equation 2.12). Therefore, the reequilibration process progressively slows down with time. In case of the high current pulses, at the beginning of the relaxation the concentration gradients are very steep, in fact the voltage recovery is quite high and fast in this zone. Instead, from $10^3 - 10^4$ s the voltage recovery is much more gradual, with a trend comparable to the one of the low current pulses;

- another reason of the very slow voltage recovery can be found in the shape of the open circuit potential of the graphitic anode (see figure 1.4 of Chapter 1.2.1). If the lithium concentration in the anode corresponds to an almost constant potential region in the OCP curve, the electrochemical reequilibration process that balances the surface concentration of lithium on the electrode particles has practically no driving potential. This is due to the fact that even if two particles in the anode have two different lithium concentrations on their surfaces, the corresponding open circuit potentials are almost equal [133]. Therefore, the lithium cannot easily pass from a particle to the another through the electrolyte, causing a severe slowing of the relaxation process in anode. Nevertheless, the voltage recovery due to the graphite is much lower than the one due to the cathode material, due to the much narrower range of the anodic OCP [103];

- this last consideration is not entirely valid when the battery gets near low states of charge. In fact, the slope of the graphite OCP is high in this region, and therefore the voltage recovery is impacted by the reequilibration in the anode material too. This fact can be seen in figure 3.12.a, where the voltage recovery after the 3C current pulse from 40% SOC to 20% SOC is about 50% higher than the ones of the other 3C pulses. For the pulses at 0.2C

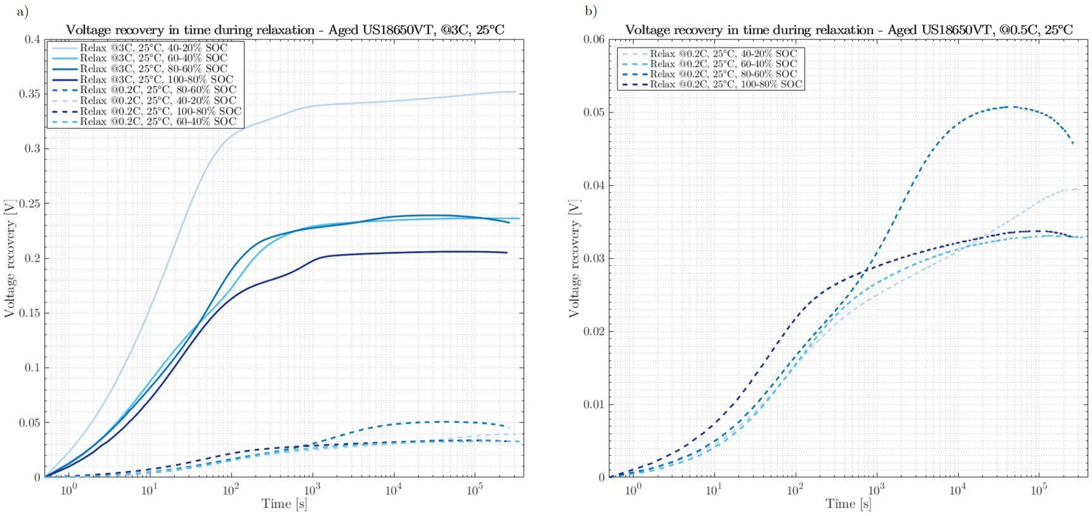

Figure 3.14: *On the left: Voltage recovery in time during relaxation, logarithmic time scale - Aged* $US18650V3$*, @*$3C$*,* $25^\circ C$ *and @*$0.5C$*,* $25^\circ C$*. On the right: zoom on the voltage recovery @*$0.5C$*,* $25^\circ C$ *(different voltage scale)*

of figure 3.12.b, this phenomenon is much less present, probably because the disequilibrium induced by the very low current is not enough strong to effectively deplete the negative electrode. Nevertheless, both the relaxation processes need an higher time to reach a peak value ($t > 10^5$);

- each voltage recovery reaches a peak value, after which it slowly starts to decrease (please note the logarithmic scale of the time axis). The magnitude of this decrease is compatible with the self-discharge phenomena that affect lithium-ion batteries [135], which lead to a 2%-10% reversible SOC loss per month, according to the ambient temperature and to the SOC itself (the higher the temperature and the SOC, the higher the self-discharge). The causes are the side reactions in the battery, such as the leakage of electrons from the anode to the cathode through the electrolyte, and an imperfectly open battery electric circuit, which creates a closed circuit between the electrodes. The voltage decrease is much more evident with the low current pulses, because the magnitude of the voltage recovery is comparable to the one of self-discharge voltage loss. Nevertheless, they are present after the high current pulses, too;

Effect of ambient temperature

In figure 3.13.a, the effect of the ambient temperature on the relaxation profiles with the two current rates is shown, keeping constant the SOC value after the discharge. Figure 3.13.b is a zoom of the low current pulses. The features of these curves are:

- an ambient temperature decrease corresponds to an increase in the voltage recovery. This phenomenon is caused by the higher concentration gradients that are established during the discharge pulse, because of the lower lithium diffusion coefficient in the electrolyte D_e and in the solid material D_s;

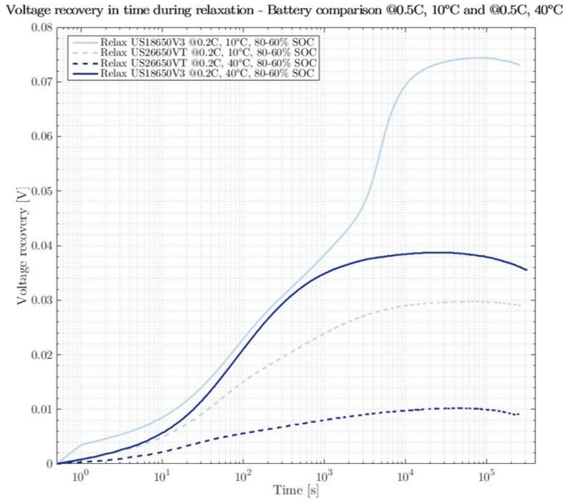

Figure 3.15: *Voltage recovery in time during relaxation, logarithmic time scale - Battery comparison @0.5C, $10° C$ and @0.5C, $40° C$*

- the ambient temperature affects the speed of the voltage recovery, too. This fact can be seen both for the low current and for the high current pulses. The peak point of the voltage recovery shifts toward higher times when the ambient temperature decreases, since the diffusion is more sluggish, and the trend of the relaxation profile is mostly determined by diffusion in this region.

Effect of battery aging

A comparison between the relaxation profiles of the aged and of the pristine US18650V3 at 0.2C/3C and 25°C can be made by comparing the figures 3.14.a and 3.12.a. Figure 3.14.b shows a zoom on the low current pulse relaxations of the aged battery. Comparing these tests, we see that all the low and the high current pulse relaxations show a quite small difference in the final value of voltage recovery, except for the 3C pulse between 60% and 40% SOC. The voltage recovery of this pulse passes from 0.21 V in the new battery to 0.24 V in the aged battery, and the difference between the two values, 0.03 V, is almost equal to the potential difference between the stage 1 and the stage 2 of lithiated graphite (see Chapter **??**). If the cathode-related voltage recovery is the same, this fact implies that at equilibrium conditions, the 40% SOC point of the new US18650V3 battery lies in the stage 1 region of the graphitic anode, while the 40% SOC point of the aged US18650V3 is in stage 2. Hence, the shape of the OCV curve of the aged US18650V3 battery is probably different from the one of the new US18650V3 battery, due to the effect of a loss of lithium inventory (LLI, see Chapter 1.3.2). Since the NMC cathode open circuit potential curve has a quite constant slope and does not show voltage plateaus [12], this hypothesis is reasonable.

Effect of battery type

Finally, in figure 3.15 we compare the voltage recovery of the new US18650V3 high-energy battery with the one new US26650VT high-power battery, at 0.2C and two ambient temperatures, 10°C and 40°C. The high-power battery shows both a lower voltage recovery and a lower time to reach the voltage recovery peak, in particular at low temperature. High-power batteries are made with thinner electrodes and with smaller electrode particles to enhance the specific active area and decrease the battery resistance (see Chapter 3.1.1). Therefore, the characteristic time of diffusion in the electrolyte and in the electrode τ_D is smaller in the US26650VT, since it depends on the square of the characteristic diffusion length (see equation 2.3). In general, high-power battery concentration gradients are smaller than the ones of high-energy batteries, and the diffusion process is faster too, at same operative conditions.

3.2.3 Electrochemical Impedance Spectroscopy

The impedance spectra obtained with the EIS are measured at steady state, in the 10000-0.05 Hz frequency range and 40 logarithmically spaced points, and a 0.15 A amplitude of the current sinusoid. The experimental matrix is:

- three values of ambient temperature: $T_{amb} \in \{10°\text{C}, 25°\text{C}, 40°\text{C}\}$;
- five values of state of charge: $SOC \in \{100\%, 80\%, 60\%, 40\%, 20\%\}$;

The combinations of state of charge and temperature are thought with the purpose of fully characterizing the battery impedance in many different operative conditions. Starting from 100% SOC, the impedance spectrum is measured and then the battery is discharged with a 0.2% pulse and 20% DOD. The battery is left at rest for 24 hours before performing the next EIS and repeating the cycle down to 20% SOC, since it is known that the impedance spectrum is sensitive to internal concentration unbalances [106, 134]. The test could not provide the steady-state impedance values if made shortly after the battery is perturbed.

The EIS is made on the pristine and aged high-power US26650VT batteries. For the pristine and aged high-energy US18650V3, only some specific conditions are investigated in this work. For the indication of the frequency on the plots, please refer to figure 2.4 of Chapter 2.

Effect of state of charge

Figure 3.16. shows the impedance spectra of the pristine US26650VT at 25°C and at all the states of charge included in the experimental matrix. For what concerns this trend, we can say that:

- the high frequency resistance is practically equal for all the SOC values (around 17.5 mΩ), while the real and imaginary impedance related to the charge transfer are very similar only up to the $20-5$ Hz frequency range. After these values, a dependency of the impedance with the SOC is evident;
- at 100% SOC, the impedance shows a relevant linear branch at low frequency, whose shape can be linked to limitations in the lithium diffusion due to phase transformations [136, 137] and to the slope of the open circuit potential [108]. The higher the slope, the higher the diffusion impedance, while a phase

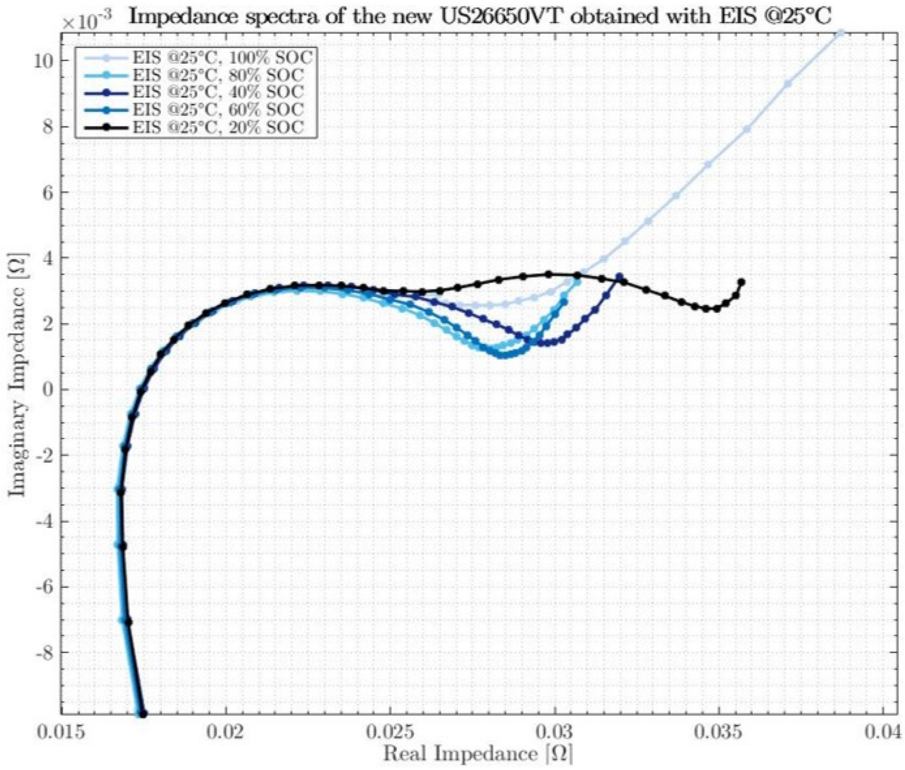

Figure 3.16: *Impedance spectra of the new US26650VT obtained with EIS @25° C, state of charge variation*

transformation leads to a slope in the Nyquist plot lower than 45°. Moreover, phase transformations also cause locally lower diffusion coefficients D_s [138], leading to an higher diffusion impedance. Hence, the presence of a phase transformation at 100% SOC in our battery seems to be the case that explains the experimental data, due to the higher diffusion impedance and to the lower slope of the linear branch if compared to the other SOCs;

- at SOC equal to 80% and 60%, the impedance spectra are quite similar, with a much smaller diffusion impedance if compared to the 100% case. The impedance starts to grow in the mid-low frequency range, below 20 − 5 Hz. Theoretically, the exchange current density i_0 has a inverted parabolic shape trend with the electrode state of charge, with a maximum at 50% SOC. Since the charge transfer resistance is inversely proportional to the exchange current density (see equation 2.8), the impedance should have a minimum around 50% SOC. Our data seem to show this trend, but only for mid-low frequencies;

- at 20% SOC, a second semicircle appears at low frequency, which overlaps with the diffusion impedance. The theoretical exchange current density relation with SOC does not explain this trend, since this impedance growth appears to be quite abrupt, while the exchange current density has a much more gradual decrease with the SOC that approaches zero or one. An explanation could be given by the behavior of layered cathode materials when near to the fully lithiated state, i.e. when the battery SOC is going towards zero.

When approaching this region, the lithium intercalation makes the layered material shift from a semi-metal behavior to a semi-conductor behavior [110, 136]. The latter has a much more limited kinetics, which could explain the sudden impedance increase.

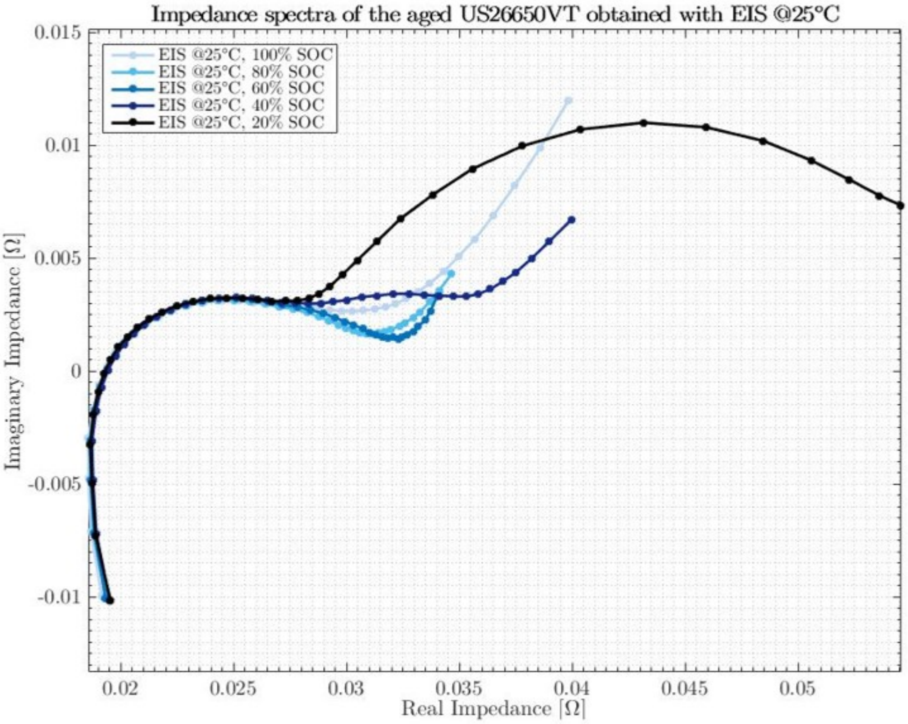

Figure 3.17: *Impedance spectra of the aged US26650VT obtained with EIS @25° C, state of charge variation*

Effect of battery aging

In figure 3.17, it is possible to see the impedance spectra of the aged US26650VT, in the same operative conditions of the pristine battery, at 25°C and at all the states of charge. The differences between the two impedance spectra are:

- the aged battery shows an HFR equal to 19 mΩ, while the HFR of the pristine one is 17.5 mΩ. The high frequency resistance increase with aging is due to the formation of the SEI, which creates an additional resistive layer R_{film} around the graphitic anode particles. Also, a small contribution can to the HFR increase can come from the electrolyte decomposition. In fact, the electrolyte concentration $c_{e,0}$ in new batteries is commonly calibrated by manufacturers to have the maximum ionic conductivity (see equation 2.44). If the electrolyte decomposes, the concentration of the lithium salts decreases, with a consequent decrease of the ionic conductivity. This effect is in accordance with the increase in the initial voltage drop observed comparing the discharge curves of the aged and pristine US26650VT batteries. With the EIS, we see how it is possible to understand that the increased voltage drop is due to an increase in the ohmic overpotential, thanks to the separation of the limiting phenomena of the battery in the impedance spectrum;

- at 20% SOC, the aged battery has a second semicircle in the low frequency region which is about 7 times bigger than the second semicircle of the new battery. Also, the impedance spectrum at 40% SOC is larger than the correspondent in the new battery too. This relevant increase at 20% SOC could be explained by the fact that the aged battery is actually "smaller" than the new one in terms of available capacity, due to the degradation effects that induce a capacity fade. Therefore, a theoretical 20% SOC in the aged battery (based on the nominal capacity at the beginning of life) is actually much more close to an actual 0% SOC, due to the lower capacity of the aged battery. Therefore, the positive electrode of the aged battery should be more lithiated than the positive electrode of the new one, with a sharp increase of the related impedance due to the enhanced semi-conductor behavior.

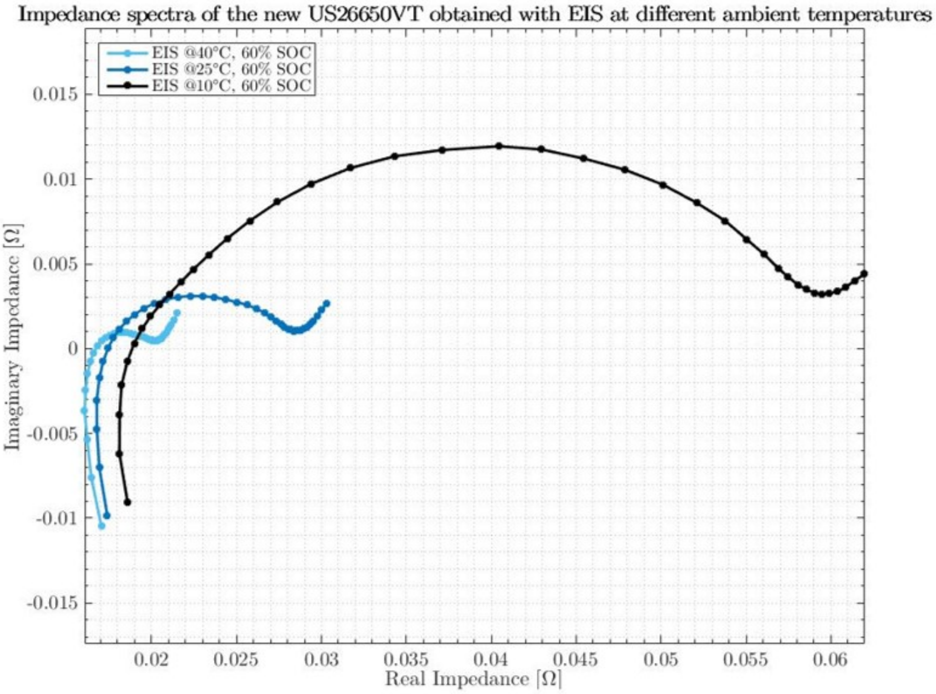

Figure 3.18: *Impedance spectra of the new US*26650*VT obtained with EIS at* 60% *SOC, ambient temperature variation*

Effect of ambient temperature

The variation with the ambient temperature of the impedance spectrum of the new US26650VT is reported in figure 3.18, with a fixed SOC at 60%. The main trends in this chart are:

- the HFR increases as the ambient temperature decreases. The main component of this resistance increase is the decrease of ionic conductivity of the electrolyte κ_e with the temperature, as it is possible to see in figure 2.11 and from the equation 2.44 of the previous chapter.

- the charge transfer resistance semicircle has a strong growth when temperature decreases. The Arrhenius-type dependence of the kinetic rate constants k of the electrodes' reactions with temperature explains this trend (see Chapter 2.2.3), since the kinetics of the electrochemical reactions is enhanced at high temperatures and hindered at low temperatures.

3.3 Final remarks

In this chapter, we explored three different experimental techniques for the battery diagnostics, and we observed how they can provide data on all the main characteristics of the lithium-ion battery. Also, aged batteries can be distinguished from new batteries in each of these techniques. Hence, all of them have proven to be valid tools for the battery parameter identification, in particular if used together.

As far as the author's knowledge, the combination of the information given by capacity tests, relaxation tests and EIS to reproduce the lithium-ion battery behavior is not present in literature. Nevertheless, an optimal diagnostic procedure should not take into account only the quantity of provided information on the studied system, since each experiment requires time for its execution. It is not realistic to perform on aged commercial battery that have to be characterized all the experiments that we made on our battery samples, in particular in the scenario in which high volumes of spent batteries will be available for the second-use market in the next future.

Therefore, it is important to understand the conditions in which these techniques can give the higher amount of insights on the battery, in order to exploit these conditions to design a diagnostic procedure that combines the quantity and quality of provided information with a low experimental time.

Chapter 4

Sensitivity analysis

In this chapter, we describe the sensitivity analysis made with the P2D model on the experimental techniques studied, analyzed and applied during the first part of this work, reported in chapter 3. The objectives of the proposed sensitivity analysis are:

- to **understand the effect of the variation of the model parameters** when simulating the same set of tests performed in the experimental campaigns, i.e. voltage or temperature variations during discharge and relaxations, and impedance change during the EIS. Usually, the influence of a parameter is qualitatively known, but the actual magnitude of this influence among different diagnostic tests and operative conditions are not straightforward, due to the strongly nonlinear behavior of the P2D model. For some physical quantities, the range of sensible values can span among two orders of magnitudes, while others exist in a narrow interval, according to the uncertainty in the literature on their actual value and on the battery characteristics. The sensitivity analysis helps to quantitatively understand the impact of the battery defining parameters in their validity range on the model's results;
- to **identify the operating conditions and the measurements where each parameter shows the highest sensitivity value** (or a group of them) by assessing their effect on the test outputs, for the sake of the fitting of experimental data (see Chapter 5). For instance, a parameter can impact more on the trend in time of the voltage during relaxation than on other conditions, or/and it can be the only one that defines that relaxation voltage trend. Therefore, the fitting of that parameter will be based on a relaxation test. Having analyzed 28 parameters of the P2D model, it would be unfeasible to run a different test for each of them, and hence it will be necessary to select conditions that result to be the best compromise for the good identification of groups of parameters.

First, we will describe the structure of our sensitivity analysis, starting with a brief literature review (Chapter 4.1.1) and explaining its mathematical formulation 4.1.2. Then, we will present the most relevant results of the sensitivity analysis (Chapter 4.2), with the formulation of an optimized experimental protocol that is able to provide data for the fitting of the lithium-ion battery physical model (Chapter 4.3).

4.1 Sensitivity analysis: structure

4.1.1 Literature review

There are many tools to understand the sensitivity of a model to its parameters, but in general the most adopted methodologies are [139]:

- **One-Factor-At-Time (OFAT)**: in the OFAT analysis, the model parameters are set to nominal values, and they are varied one at a time while keeping the others fixed. The variations of the output with respect the variations of a single input are calculated, and the results are analyzed to understand the sensitivity of the model to that input. Each parameter has a validity range, and the simulations are performed by assigning to the parameter several values within its own range. This procedure is repeated for every parameter. If the range in which the values of the parameter are chosen is wide, the analysis allows to explore well the relationship between the output and the input, revealing nonlinear behaviors or tipping points. Instead, if the range is small, the result of the sensitivity analysis resembles more a partial derivative of the model output with respect to the selected input, calculated in the point where the input assumes its nominal value.
  The advantages of the OFAT analysis are its simplicity, its relatively low computational cost and its ability to well understand the mechanistic relations among the model output and the inputs. The drawbacks are that interactions among different inputs are not explored (i.e. the parameters are not varied simultaneoulsy) and that the information that the OFAT analysis give are quite qualitative;

- **Global Sensitivity Analysis (GSA)**: in a GSA, a more rigorous statistical approach is used, since it is based on the variance of the model output with respect to a great number of combinations that the model parameters can assume. The contribution of each parameter to the total variance of the output can be assessed with various techniques, for instance with regression models or Sobol' indices. GSA can unveil the effect of interactions among the model parameters, and it is able to give a statistically sound quantitative information on the sensitivity of each of them, assigning an index based on variance analysis. Nevertheless, GSA requires a great amount of model runs in order to get a suitable sample of model outputs, with the use of Monte Carlo simulations or analogous methods. Also, the effects of poorly-sensitive parameters might be lost since they are hidden by more sensitive parameters [140].

In literature, it is possible to find several examples of sensitivity analyses on lithium-ion battery models: on electric equivalent circuits [141–143], on the single-particle model [144–146], on the proper P2D model [147, 148] and also on the coupled electrochemical-electrical-thermal model [140]. The use of GSA is possible only for EECs and for simplified versions of physical models, due to the high computational time required. The battery model is usually linearized or expressed in an approximated polynomial form, in order to be solved much faster than its partial-differential equation form, with the consequence of a lower accuracy of the results. Instead, the OFAT analysis is performed both on simplified models and on the full-scale P2D model. It is important to notice that the reported sensitivity analyses of the battery models have been performed only on discharge curves or on more complex combinations of current inputs, such as driving cycles. As far as the author's knows, there are no papers that focus on the combined sensitivity of capacity tests, relaxation tests, and EIS tests in order to obtain an optimized experimental methodology.

In the work of Schmidt et. al [144], they analyzed five specific experiments, which comprehended pulse tests and discharges with a simultaneous ambient temperature variation. The sensitivity analysis was coupled with the parameter identification process, in order to understand which parameters could be fitted to each experiment in a better way. The results were satisfactory, but they did not report the performance of the model in other conditions than the fitting experiments.

Lin et. al. [140] performed a global sensitivity analysis on the coupled electrochemical-electrical-thermal model, using Sobol' indices with several simplifications to the battery model, which were necessary for a reasonable computational time. The limits of a GSA are evident in this work: the most sensitive parameters had to be excluded from the analysis in order to get a meaningful sensitivity index on the other parameters. Moreover, it is hard to get physical insights from this approach. For instance, Lin et. al. noticed a very high influence of the solid diffusivity of the cathode on the maximum temperature reached by a battery after a discharge. They justified it with the high impact of the concentration overpotential on the overall one, an impact that was reflected on the heat generation from irreversibilities (Chapter 2.2.3, eq. 2.39). However, as we reminded in chapter 1.1.2, the effect of inequality between the surface and bulk concentration of lithium on the electrode material is related to a variation of the open circuit potential of the electrode itself, and not to the development of a proper overpotential like the ohmic and kinetic ones. Therefore, a variation of the solid diffusion coefficient is not directly related to a temperature variation. What Lin et. al. observed is probably due to the fact that if the solid diffusivity is low, the battery voltage reaches the lower cutoff voltage limit faster than if the solid diffusivity is high. Consequently, the battery has less time to heat up and hence the maximum temperature is lower. Therefore, the influence of solid diffusivity on the temperature is correct, but it is indirect, and not linked to a proper overpotential that generates heat.

Murbach and Schwartz [149] created a large database of EIS simulated with the P2D model, with the purpose of using it as a fitting tool for experimental data, but they did not analyze the sensitivity of the EIS with respect to the model parameters.

The sensitivity analysis methodology that is chosen in this work is similar to the one of Zhang et. al. [147] and of Edouard et. al. [145]. They both performed an OFAT analysis, the former on an LFP battery simulated with the full-scale P2D-thermal model, the latter on an LFP battery simulated with the single-particle model coupled to a thermal model. They took 10 different values for each model parameter, and they simulated a wide matrix of possible operative conditions for a

Table 4.1: *P2D model parameters involved in the sensitivity analysis*

	Anode		Separator/Electrolyte/Cell		Cathode	
Parameter	**Nominal**	**Range**	**Nominal**	**Range**	**Nominal**	**Range**
$C_{dk}\,[F\,m^{-2}]$	1	$0.02 - 50$	-	-	1	$0.02 - 50$
$k[m\,s^{-1}]$	$1 \cdot 10^{-9}$	$1 \cdot 10^{-10} - 1 \cdot 10^{-8}$	-	-	$1 \cdot 10^{-9}$	$1 \cdot 10^{-10} - 1 \cdot 10^{-8}$
$c_{e,0}\,[mol\,m^{-3}]$	-	-	1200	$800 - 1600$	-	-
$FCE\,[-]$	-	-	0.387	$0.100 - 1.500$	-	-
$t_0^+\,[-]$	-	-	0.350	$0.300 - 0.400$	-	-
$\sigma_s\,[S\,m^{-1}]$	316	$10 - 10000$	-	-	3.16	$0.1 - 100$
$R_p\,[m^1]$	$6.75 \cdot 10^{-6}$	$1 \cdot 10^{-6} - 12.5 \cdot 10^{-6}$	-	-	$6.75 \cdot 10^{-6}$	$1 \cdot 10^{-6} - 12.5 \cdot 10^{-6}$
$D_s\,[m\,s^{-1}]$	$1.58 \cdot 10^{-13}$	$5 \cdot 10^{-14} - 5 \cdot 10^{-13}$	-	-	$3.16 \cdot 10^{-14}$	$1 \cdot 10^{-14} - 1 \cdot 10^{-13}$
$R_{film}\,[\Omega\,m^2]$	$3.16 \cdot 10^{-3}$	$1 \cdot 10^{-3} - 1 \cdot 10^{-2}$	-	-	$3.16 \cdot 10^{-4}$	$1 \cdot 10^{-4} - 1 \cdot 10^{-3}$
$\varepsilon_e\,[-]$	0.375	$0.325 - 0.425$	0.600	$0.550 - 0.650$	0.375	$0.325 - 0.425$
$EA_k\,[J\,mol^{-1}]$	$4 \cdot 10^4$	$2 \cdot 10^4 - 6 \cdot 10^4$	-	-	$4 \cdot 10^4$	$2 \cdot 10^4 - 6 \cdot 10^4$
$EA_{D_s}\,[J\,mol^{-1}]$	$4 \cdot 10^4$	$2 \cdot 10^4 - 6 \cdot 10^4$	-	-	$4 \cdot 10^4$	$2 \cdot 10^4 - 6 \cdot 10^4$
$\rho_{am}\,[kg\,m^{-3}]$	-	-	2500	$2250 - 2750$	-	-
$C_{am}\,[J\,kg^{-1}\,K^{-1}]$	-	-	1250	$1000 - 1500$	-	-
$k_{T,rad,am}\,[W\,m^{-1}\,K^{-1}]$	-	-	0.550	$0.100 - 1.000$	-	-
$k_{T,ax,am}\,[W\,m^{-1}\,K^{-1}]$	-	-	30.00	$10.00 - 50.00$	-	-
$h_conv\,[W\,m^{-2}\,K^{-1}]$	-	-	30.00	$5.000 - 55.00$	-	-
$R_{ext}\,[\Omega\,m^2]$	-	-	0.003	$0.001 - 0.005$	-	-

discharge curve. The standard deviation of voltage and surface temperature was used as a descriptor of the sensitivity of the output with respect to the varied parameter. Then, the parameters were classified according to their mean sensitivity values and a cluster analysis was performed, in order to find the experimental conditions that enhanced the identification of the model parameters. Lastly, the parameter identification was performed on a simulated dataset in [147] and on an experimental dataset in [145], with a stepwise methodology that firstly fitted the most sensitive parameters and then all the others. They both found good accordance between the simulation output and the dataset created with their methodology. Nevertheless, they focused only on a simple discharge test as an experimental technique, and their results should be taken as valid only for LFP batteries, which show quite different values for the physical parameters with respect to the other chemistries.

In this thesis, the sensitivity analysis methodology is the OFAT, through which it is possible to get insights on the underlying mechanistic processes of the lithium-ion battery that are influenced by the model parameters. Also, its lower computational burden is helpful to reduce the time needed to perform the analysis on the very wide matrix of operative conditions and experimental techniques that will be described below. The 28 LIB parameters on which the sensitivity analysis is performed are reported in table 4.1, with the associated validity range, defined after a thorough literature review [132, 150–163]. Five values for each parameter are used in the simulations, which explore the whole available range. The five parameter values are linearly or logarithmically spaced, according to the distance between the minimum and maximum values of the range: linear if the minimum and the maximum have the same order of magnitude, otherwise logarithmic.

It has been chosen to not take into account all the parameters that are related to the thermodynamic and geometric characteristics of a lithium-ion battery, i.e. all the parameters that define its capacity ($\varepsilon_{s,a,p}$, $\varepsilon_{s,a,n}$, $SOC_{min,p}$, $SOC_{min,n}$, $SOC_{max,p}$, $SOC_{max,n}$, L_p, L_n, A_{el}, $\mathrm{c_{s,max,p}}$, $\mathrm{c_{s,max,n}}$). The reason behind this choice is that the thermodynamic parameters require slow experimental techniques in order

Table 4.2: *Fixed P2D model parameters*

Parameter	Anode	Separator/Electrolyte/Cell	Cathode
$L\,[m]$	$40.0 \cdot 10^{-6}$	$22.5 \cdot 10^{-6}$	$40.0 \cdot 10^{-6}$
$SOC_{min}\,[-]$	0.049	-	0.125
$SOC_{max}\,[-]$	0.850	-	0.870
$c_{s,max}\,[mol\,m^{-3}]$	31000	-	37035
$\varepsilon_{s,a}\,[-]$	0.500	-	0.450
$A_{el}\,[m^2]$	-	0.19534	-
$Q_{nom}\,[mAh]$	-	2600	-
$\alpha_c\,[-]$	0.5	-	0.5
$\alpha_a\,[-]$	0.5	-	0.5
$T_{ref}\,[K]$	298.15	298.15	298.15
$H\,[m]$	-	$65.00 \cdot 10^{-3}$	-
$r_{am}\,[m]$	-	$10.75 \cdot 10^{-3}$	-
$r_{man}\,[m]$	-	$2.000 \cdot 10^{-3}$	-
$t_{st}\,[m]$	-	$0.250 \cdot 10^{-3}$	-
$C_{man}\,[J\,kg^{-1}\,K^{-1}]$	-	1700	-
$C_{st}\,[J\,kg^{-1}\,K^{-1}]$	-	475	-
$\rho_{man}\,[kg\,m^{-3}]$	-	1150	-
$\rho_{st}\,[kg\,m^{-3}]$	-	7850	-
$k_{T,man}\,[W\,m^{-1}\,K^{-1}]$	-	0.26	-
$k_{T,st}\,[W\,m^{-1}\,K^{-1}]$	-	44.5	-

to be properly evaluated, such as incremental capacity and differential voltage, which were investigated the previous work [93]. In this thesis, we concentrate on faster techniques that enhance the dynamic behavior of lithium-ion batteries, away from equilibrium conditions. Instead, the geometric parameters can be evaluated quite accurately by comparing the type of battery that is being analyzed with the data that are available in literature [132, 150–152], thanks to some design standards that are present in the lithium-ion battery manufacturing. Therefore, the thermodynamic and geometric parameters are fixed and taken from experimental tests and literature, as well as other secondary parameters (*table 4.2*).

The battery modeled in the sensitivity analysis is based on the pristine SONY US26650VT (section 3.1.1), an NMC/LMO high power battery, with a nominal capacity of 2600 mAh. Therefore, the benchmark of all the model parameters stems from this type of battery. It is important to remind that this sensitivity analysis should be considered completely valid only for the batteries that are similar to the one on which the benchmark parameter set is based on. Nevertheless, general implications are obtained from the study, applicable to the specific cases with some modifications.

The sensitivity analysis is performed in the subsequent conditions:

- **Capacity test**: the discharge simulation matrix is made of four ambient temperatures ($T_{amb} \in \{-5°C, 10°C, 25°C, 40°C\}$), four starting states of charge ($SOC_{in} \in \{100\%, 75\%, 50\%, 25\%\}$), four depths of discharge ($DOD \in \{100\%, 75\%, 50\%, 25\%\}$) and four current rates ($C \in \{0.5, 1, 2, 3\}$). Obviously, in every simulation, the depth of discharge has to be equal or lower the starting state of charge. Therefore, we obtain 160 operating conditions for the capacity test in which the outputs are cell voltage and cell surface temperature. The battery model is initialized with the selected starting SOC and ambient temperatures, then the current is applied for a certain amount of time according to the selected C-rate and depth of discharge.

The number of registered data points is 100, and hence the timestep Δt of each discharge simulation will be:

$$\Delta t = \frac{DOD \cdot 3600 \left[\frac{s}{h}\right]}{100 \cdot C} \tag{4.1}$$

The simulation can end before its expected duration, due to the fact that the model has a stop condition if the cell voltage gets lower than the cutoff voltage provided by the manufacturer limit for the simulated battery. In this case, the output will have a lower number of data points;

- **Relaxation test**: the relaxation simulation matrix is the direct consequence of the discharge simulations and it has exactly the same operative conditions. In fact, after every discharge, the current is set to zero in the model, allowing the battery to restore an equilibrium condition starting from the unbalanced lithium concentrations in the electrolyte and in the electrodes.
  It is important to underline that for the sake of the sensitivity analysis, the trends of voltage and temperature during relaxation are fully comparable only if there has been exactly the same DOD before the end of discharge. This is because the differences among the internal disequilibria in the battery have to be caused only by the varied physical parameter, and not by inequalities in the operative conditions of the discharges that generate those disequilibria. In this way, it is possible to appreciate the influence of the varied parameter on the voltage and temperature trends separated by other effects. Therefore, the simulations of relaxation processes where the starting SOC is equal to the DOD in the preceding discharges will be discarded, since this combination always meets the lower cutoff voltage stop condition that ends the discharge before the prefixed duration, creating differences among the tests. As a consequence of this fact, 96 operative conditions are modeled for the relaxation tests.
  The timestep of the simulation is equal for every simulation, logarithmically spaced, with 34 points for each decade between 10^{-1} s and 10^{3} s and a total of 133 data points of cell voltage and surface temperature. The choice of a logarithmic timestep is due to the dominance of diffusion during relaxation, and as a first approximation, the lithium diffusion processes in the cell follow an exponential decay trend. Hence, to capture the behavior of the first moment of relaxation, a very small timestep is needed, while a much larger one is sufficient for the final part of the test.
  The simulation ends after 1000 seconds due to the inability of the employed P2D model to replicate the long-term voltage behavior experimentally seen in Chapter 3, as in figure 3.12. This trend is probably caused by temperature and concentration disequilibria along the length of the battery spiral [164, 165], which are very slow to reequilibrate with respect to the disequilibria along the electrochemical cell. The difference in the length scale of the two geometries (10^{-1} m for the spiral vs. $10^{-4} - 10^{-5}$ m for the cell), which determines the characteristic time of diffusion, explains this phenomenon. Since the P2D model simulates only a single cell and not the whole battery, we only take into account the first part of the relaxation process, the one dominated by the cell re-equilibration;

- **Electrochemical Impedance Spectroscopy**: the EIS is simulated at equilibrium, at four ambient temperatures ($T_{amb}\in$\{-5°C, 10°C, 25°C, 40°C\}) and at five states of charge values ($SOC_{in}\in$\{100%, 75%, 50%, 25%, 0%\}), with a total of 20 operative conditions. The frequency range in which the EIS is performed is between 4000 Hz and 0.005 Hz, with 30 logarithmically spaced data points where the real and imaginary impedances are calculated. The amplitude of the sinusoidal current input is 0.15 A, similar to the one employed in experimental tests, with 16 sampled points for each sinusoid.
  The EIS is simulated in the time domain, by applying the alternating current to the battery model and registering the consequent voltage output. Two complete sinusoids are applied, and only the output of the second one is used, in order to remove the effect of an initial transient voltage response. Then, the Fast Fourier Transform (FFT) [166] is employed in MATLAB to calculate the impedance value. The inductive trait at high frequency, typical of experimental EIS because of the cables inductance, is added to the impedance after the FFT with a correction that has the formula:

$$Z_{corr}(\omega) = Z(\omega) + 2 \cdot \pi l \omega \tag{4.2}$$

  where l is the cable inductance, equal to $1.07 \cdot 10^{-6}\,H$, estimated from our experimental data.
  It is important to remark that in the EIS sensitivity analysis, the five parameters that are related to a temperature variation in the battery (ρ_{am}, C_{am}, $k_{T,rad,am}$, $k_{T,ax,am}$ and h_{conv}) can be excluded. This is because the EIS is made as a steady state measurement and the alternating current employed is very small, and hence the temperature variations due to an heat generation in the battery are neglegible. Therefore, the EIS sensivivity analysis is made on 23 parameters.

In total, the sensitivity analysis is based on 38140 simulated conditions, which took a total of 42 full days of computations on two desktop PCs of the laboratory.

4.1.2 Mathematical formulation

The large amount of information that is generated by this wide simulation matrix needs to be summarized with few key indicators. These indicators will enable a simpler and more insightful analysis of the sensitivity results, allowing us to compare together the outcomes coming from different operative conditions and from different parameters.

Following the works of Zhang et al.[147] and Edouard et al.[145], the indicator that was chosen to understand the impact of the variation of a parameter on the model outputs is the standard deviation *SD*. This quantity represents the variability of the n^{th} of the N_d data points of a model output y (tension, temperature or impedance) considering the five x values of the j^{th} physical parameter, in the i^{th} of the N_o operative conditions related to an experimental technique. The coordinate i is linked to a specific combination of temperature, starting SOC, DOD and current

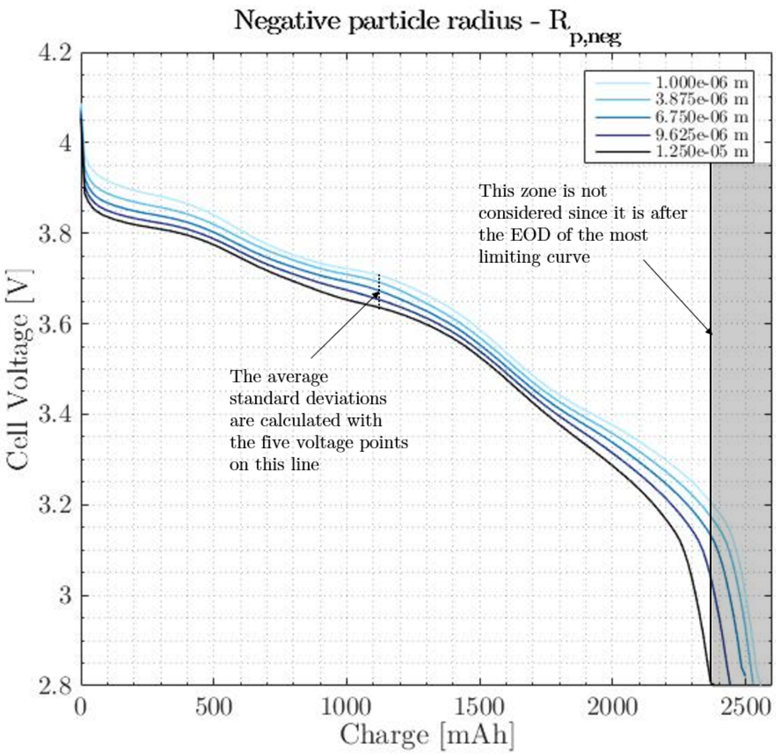

Figure 4.1: *Explanation of the computation of the SD values in a set of discharge curves*

rate (only temperature and SOC in case of the EIS).
Therefore, the formula for the standard deviation is:

$$SD^n_{y,j,i} = \sqrt{\frac{\sum_{x=1}^{5}\left(y^n_{j,i,x} - \overline{y}^n_{j,i}\right)^2}{5}} \tag{4.3}$$

where $\overline{y}^n_{j,i}$ is the mean of the five values of the output $y^n_{j,i,x}$ for the j^{th} physical parameter in the i^{th} operative condition, calculated as:

$$\overline{y}^n_{j,i} = \frac{\sum_{x=1}^{5}\left(y^n_{j,i,x}\right)}{5} \tag{4.4}$$

Then, the standard deviation of the output is averaged in different ways, according to the specific experimental technique. This averaging is made to condense the information about the variability of the output given in every point for each operative condition in a simple number, greatly reducing the number of handled data:

- for the **discharge curve**, we calculate the average of the standard deviation considering all the data points of the curves. If one of the curves has a smaller amount of points (since it reaches the cutoff voltage before the others), we only consider the points in common to all the curves, since *SD* can be calculated only if the data of all the five curves are available. In figure 4.1, this process

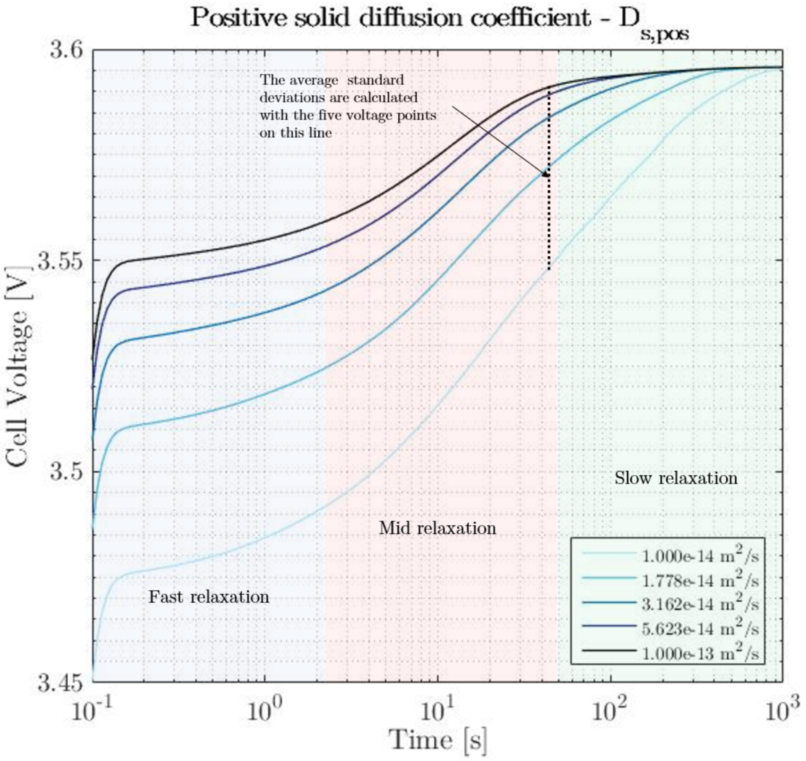

Figure 4.2: *Explanation of the computation of the SD values in a set of relaxation curves*

is explained graphically. Hence, we obtain:

$$\overline{SD}^{D}_{y,j,i} = \frac{\sum_{n=1}^{N_{d,min}} \left(SD^{n}_{y,j,i} \right)}{N_{d,min}} \tag{4.5}$$

where $N_{d,min}$ is:

$$N_{d,min} = min\{N_{d,x_1}, N_{d,x_2}, N_{d,x_3}, N_{d,x_4}, N_{d,x_5}\} \tag{4.6}$$

This formula is applied both for tension and temperature, obtaining only two values of SD per parameter in each operative condition;

- for the **relaxation test**, we divide the time vector of the voltage and the temperature curves in three regions with an equal number of logarithmically spaced data points:
  - **Fast Relaxation (FR)** ($1 \leq n \leq 44$, $0.1\,s \leq t \leq 1.7\,s$)
  - **Mid Relaxation (MR)** ($45 \leq n \leq 88$, $1.8\,s \leq t \leq 31\,s$)
  - **Slow Relaxation (SR)** ($89 \leq n \leq 133$, $32.6\,s \leq t \leq 1000\,s$)

  This division is made to understand if there are some physical parameters that are influential only on a certain timescale of the relaxation process. For instance, it is expected that the diffusion of lithium in the solid will be more impactful on the output voltage over longer timescales if compared to the diffusion of lithium in the liquid [125].

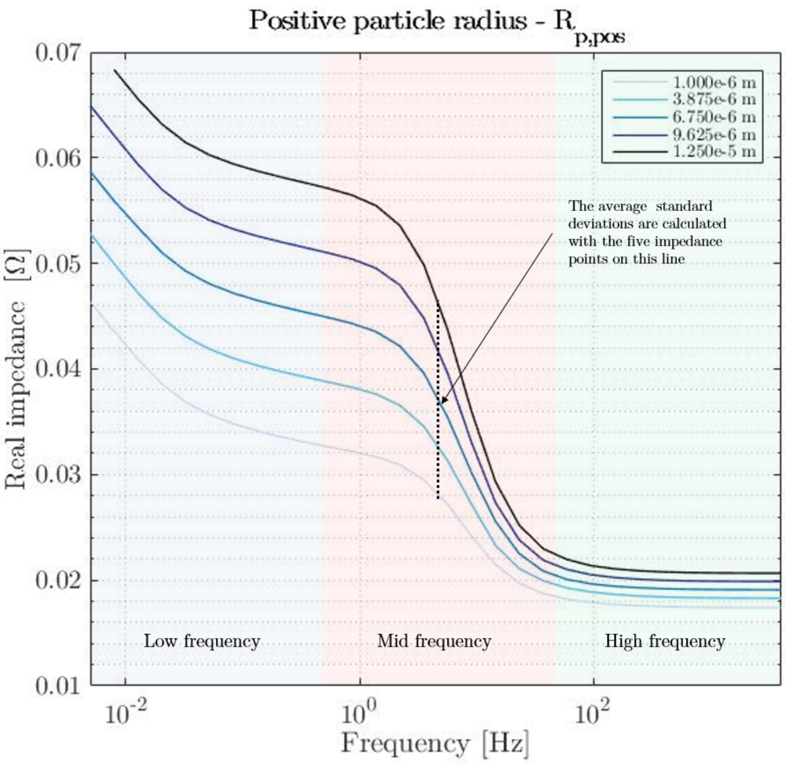

Figure 4.3: *Explanation of the computation of the SD values in a set of Bode plots*

Therefore, the formulas will be:

$$\begin{cases} \overline{SD}^{SR}_{y,j,i} = \dfrac{\sum\limits_{n=1}^{44} \left(SD^{n}_{y,j,i} \right)}{44} \\[2em] \overline{SD}^{MR}_{y,j,i} = \dfrac{\sum\limits_{n=45}^{88} \left(SD^{n}_{y,j,i} \right)}{44} \\[2em] \overline{SD}^{FR}_{y,j,i} = \dfrac{\sum\limits_{n=89}^{133} \left(SD^{n}_{y,j,i} \right)}{45} \end{cases} \tag{4.7}$$

The graphical explanation is found in figure 4.2;

- in the **EIS**, each data point with the respective real and imaginary impedances is associated to a certain frequency. These logarithmically spaced frequencies are divided in three sections:
  - **High Frequency (HF)** ($1 \leq n \leq 10$, $4000\, Hz \leq f \leq 59\, Hz$)
  - **Mid frequency (MF)** ($11 \leq n \leq 20$, $37\, Hz \leq f \leq 0.54\, Hz$)
  - **Low frequency (LF)** ($21 \leq n \leq 30$, $0.34\, Hz \leq f \leq 0.005\, Hz$)

  Similarly to the case of relaxation, the EIS is divided in regions in order to find differences in the sensitivity of the physical parameters if more timescales are considered.

Hence, we get:

$$\begin{cases} \overline{SD}^{HF}_{y,j,i} = \dfrac{\sum\limits_{n=1}^{10}\left(SD^{n}_{y,j,i}\right)}{10} \\ \\ \overline{SD}^{MF}_{y,j,i} = \dfrac{\sum\limits_{n=11}^{20}\left(SD^{n}_{y,j,i}\right)}{10} \\ \\ \overline{SD}^{LF}_{y,j,i} = \dfrac{\sum\limits_{n=21}^{30}\left(SD^{n}_{y,j,i}\right)}{10} \end{cases} \tag{4.8}$$

Once again, there is a graphic explanation of this concept in figure 4.3, where a Bode plot of the real impedance is used to visualize the frequencies on the x-axis.

Classification

To summarize these information and to get a qualitative synthesis of the results of the sensitivity analysis, for each parameter j and for each output y we calculate the mean of the average standard deviations $\overline{\overline{SD}}_{y,j}$ among all the operative conditions, and we report the maximum value of the average standard deviation $\overline{SD}_{y,j,max}$, as well as the operative condition where maximum value is located.

$$\begin{cases} \overline{\overline{SD}}_{y,j} = \dfrac{\sum\limits_{i=1}^{N_o}\left(\overline{SD}_{y,j,i}\right)}{N_o} \\ \\ \overline{SD}_{y,j,max} = max\{\overline{SD}_{y,j,i}\} \end{cases} \tag{4.9}$$

Moreover, a first classification of the physical parameter is made according to the comparison with a minimum limit value $SD_{y,lim}$. The standard deviations are compared with these reference values in order to define whether they are significant or negligible. The limit values for voltage, real and imaginary impedance are based on the experimental uncertainty analysis of chapter 3, according to this line of reasoning: if the dispersion of an output caused by the variation of a parameter (i.e. its standard deviation) is smaller than the experimental uncertainty on that output, it is not correct to fit that parameter with experimental data, because its effect on the output is lower than the uncertainty in the measuring process.
Therefore, the parameters are classified according to these criteria:

- **insensitive** if $\overline{SD}_{y,j,max} < SD_{y,lim}$
- **low sensitive** if $\overline{\overline{SD}}_{y,j} < SD_{y,lim}$ and $\overline{SD}_{y,j,max} > SD_{y,lim}$
- **mid sensitive** if $\overline{\overline{SD}}_{y,j} > SD_{y,lim}$ and $\overline{\overline{SD}}_{y,j} < 2SD_{y,lim}$;
- **high sensitive** if $\overline{\overline{SD}}_{y,j} > 2SD_{y,lim}$

where the minimum limit values $SD_{y,lim}$ are:

$$\begin{cases} SD_{V,lim} = 0.004\,V \\ SD_{T,lim} = 0.1\,K \\ SD_{Z_R,lim} = 0.0001\,\Omega \\ SD_{Z_I,lim} = 0.0001\,\Omega \end{cases}$$

Clustering

The last step of the sensitivity analysis is the clustering of all the results, in order to analyze them together, see the trends that emerge from the variation of the operative condition and of the diagnostic technique, and refine the concept of sensitivity of a parameter (see section 4.2.2).
For every combination of operating condition and diagnostic technique, a clustering algorithm divides the standard deviations of the parameters into three classes: low sensitive, mid sensitive and high sensitive. The classes are adaptive, in the sense that they are relative to the values of the standard deviation $\overline{SD}_{y,j,i}$ of all the parameters in that operative condition. Therefore, the membership of a parameter to a certain class depends not only on the value of its own standard deviation, but also on the values of the standard deviation of the other parameters. For instance, a standard deviation equal to $\mathrm{SD_x}$ can indicate a low sensitivity in the operative condition where the average standard deviation among the parameters is $10 \cdot \mathrm{SD_x}$, but it is surely connected to a high sensitivity if the average standard deviation in another operative condition is $0.1 \cdot \mathrm{SD_x}$.

The employed algorithm is the Fuzzy C-Means clustering, implemented in the software MATLAB, based on the minimization of the cost function:

$$CF = \sum_{i=1}^{D} \sum_{j=1}^{N} \mu_{ij}^{m} \left\| x_i - c_j \right\|^2 \tag{4.10}$$

where D is the number of values that have to be clustered, N is the number of clusters in which the dataset is divided, μ_{ij} is the degree of membership of a value x_i to the cluster j. $\mathrm{c_j}$ is the center of the cluster j, calculated as:

$$c_j = \frac{\sum\limits_{i=1}^{D} \mu_{ij}^{m} x_i}{\sum\limits_{i=1}^{D} \mu_{ij}^{m}} \tag{4.11}$$

Instead, the degree of membership is calculated as:

$$\mu_{ij} = \frac{1}{\sum\limits_{k=1}^{N} \left(\frac{\|x_i - c_j\|}{\|x_i - c_k\|} \right)^{\frac{2}{m-1}}} \tag{4.12}$$

where c_k are exactly the same cluster centers indicated in the previous equation as c_j, but with a different index k for the summation, since in this formula the index j is fixed. The parameter m is an exponent that defines the degree of overlap between

the clusters. It has to be greater that 1, and the higher its value, the fuzzier is the membership of a value x_i to the cluster, i.e. the said value has a more distributed membership to the clusters. The sum of all the degrees of membership for a given value is always 1. Then, the highest of the values of μ_{ij} is selected and the point x_i is assigned to the cluster j.
In this work, D is equal to 28, the number of model parameters on which the sensitivity analysis is performed (23 for the EIS sensitivity analysis, since the five parameters related the battery thermal model are not considered), whose value of average standard deviation $\overline{SD}_{y,i,j}$ is x_i. As already noted, the number of clusters N is equal to 3, in order to have a cluster that groups together the parameters with a low SD value in that operative condition (low sensitivity cluster), a cluster that does the same with the parameters with a medium SD value (mid sensitivity cluster), and a cluster for the high SD values (high sensitivity cluster).

Before performing the clustering, the average standard deviation values of the parameters are normalized with respect to the reported minimum limit values $SD_{y,lim}$. In this way, the sensitivity of the parameters on the different model outputs can be easily compared by means of their ratio with the minimum value at which they are considered detectable. The normalization formula is:

$$\overline{SD}'_{y,j,i} = \frac{\overline{SD}_{y,j,i}}{SD_{y,lim}} \tag{4.13}$$

where at each output y is associated its own minimum value.

The whole scheme of the sensitivity analysis is summarized in figure 4.4.

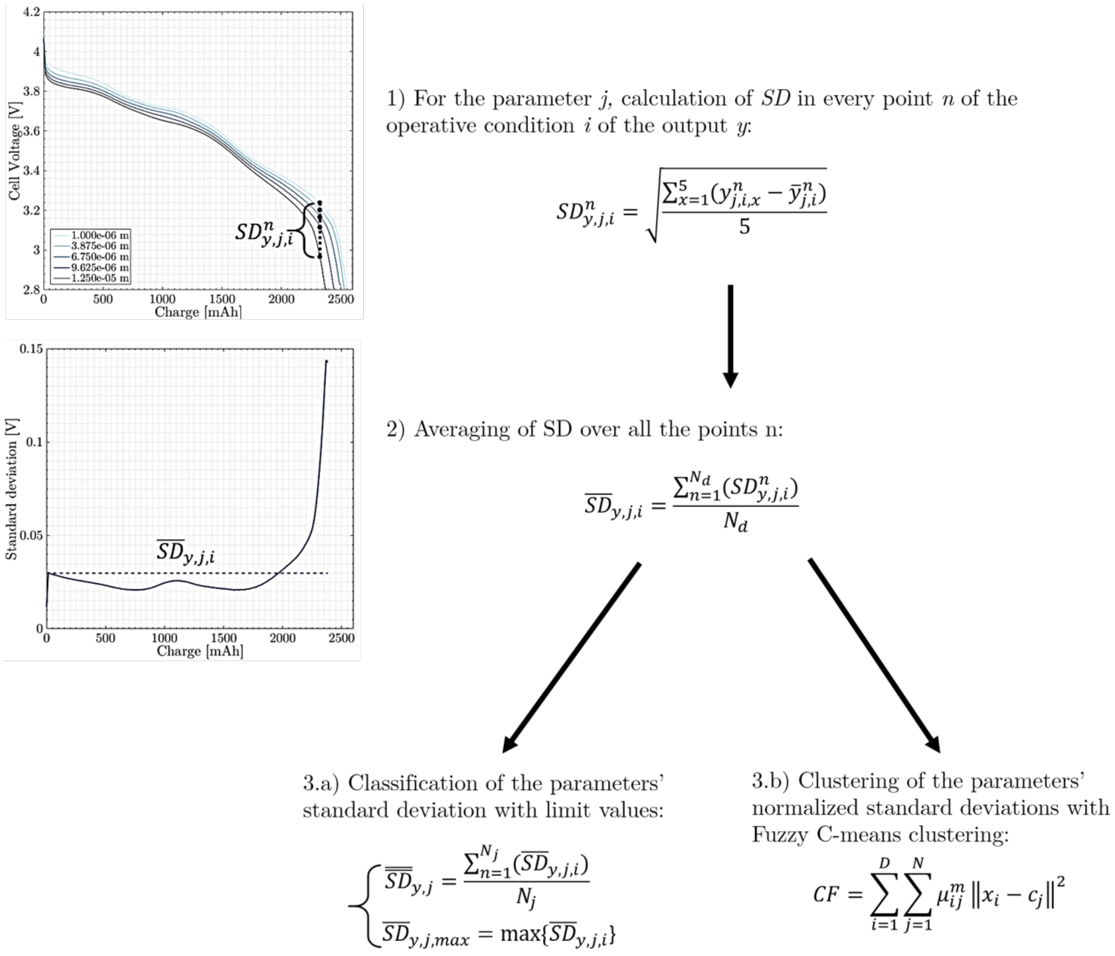

1) For the parameter *j*, calculation of *SD* in every point *n* of the operative condition *i* of the output *y*:

$$SD^n_{y,j,i} = \sqrt{\frac{\sum_{x=1}^{5}(y^n_{j,i,x} - \bar{y}^n_{j,i})}{5}}$$

2) Averaging of SD over all the points n:

$$\overline{SD}_{y,j,i} = \frac{\sum_{n=1}^{N_d}(SD^n_{y,j,i})}{N_d}$$

3.a) Classification of the parameters' standard deviation with limit values:

$$\begin{cases} \overline{\overline{SD}}_{y,j} = \dfrac{\sum_{n=1}^{N_j}(\overline{SD}_{y,j,i})}{N_j} \\ \overline{SD}_{y,j,max} = \max\{\overline{SD}_{y,j,i}\} \end{cases}$$

3.b) Clustering of the parameters' normalized standard deviations with Fuzzy C-means clustering:

$$CF = \sum_{i=1}^{D}\sum_{j=1}^{N}\mu_{ij}^{m}\left\|x_i - c_j\right\|^2$$

Figure 4.4: *Summary of the sensitivity analysis process*

4.2 Sensitivity analysis: results

4.2.1 Output variation with operative conditions

First, we describe how the model reproduces in a satisfactory way some trends observed during the experimental campaign of Chapter 3. It indicates that the model is reliable on its interpretation of the lithium-ion battery behavior.

Capacity test

Figure 4.5 shows the effect of ambient temperature and current rate on battery temperature and voltage profiles during some discharges. All the trends resemble the ones of figures 3.8, 3.9 and 3.10 of Chapter 3, where the influence of these operative parameters on the measured discharge curves was reported. The increased ohmic and activation losses are noticeable, as well as the impact of the more sluggish lithium diffusion at high current rates and, in particular, at low temperatures. The temperature profiles confirm these reasonings.

Relaxation test

In figure 4.6, we report the effects of the current rate and of the depth of discharge on the voltage and temperature values during relaxation. Also in this case, the trends resemble the ones of figures 3.12 and 3.13 of Chapter 3. An higher C-rate at fixed DOD increases the overall variation of the voltage during the relaxation process as well as its duration, while maintaining the same OCV as final voltage value.

The effect of the DOD variation on the left of figure 4.6 is shown as the voltage recovery during relaxation. The resemblance with the experimental results is clear: the trend is mainly guided by the OCP curves of the electrodes, therefore we have a non-linear variation of the voltage recovery with the depth of discharge. Even though it is not used in the sensitivity analysis, the relaxation trend after a 100% DOD is shown. The much higher variation of voltage during relaxation is due to the high slope of the OCP of the graphite in the region near the end of discharge, as hypothesized while discussing the results of the experimental campaign.

EIS

The impact of the variation of the ambient temperature and of the SOC on the EIS is shown in figure 4.7. The temperature decrease results in an increase of all the resistances, in particular the charge transfer one, as seen in the experiments from figure 3.18 of Chapter 3. The trend of the HFR is shown in a inset in the figure 4.7: its increase with the temperature decrease is evident, and it is comparable with the experimental results.

The effect of the SOC variation on the EIS shows a non-linear behavior, and it is observable both on the charge transfer resistance and on the diffusion resistance. The former changes due to the trend of the exchange current density with the electrode state of charge (equation 2.17), which shows a maximum for 50% SOC and decreases towards 100% SOC and 0% SOC. The latter is proportional to the

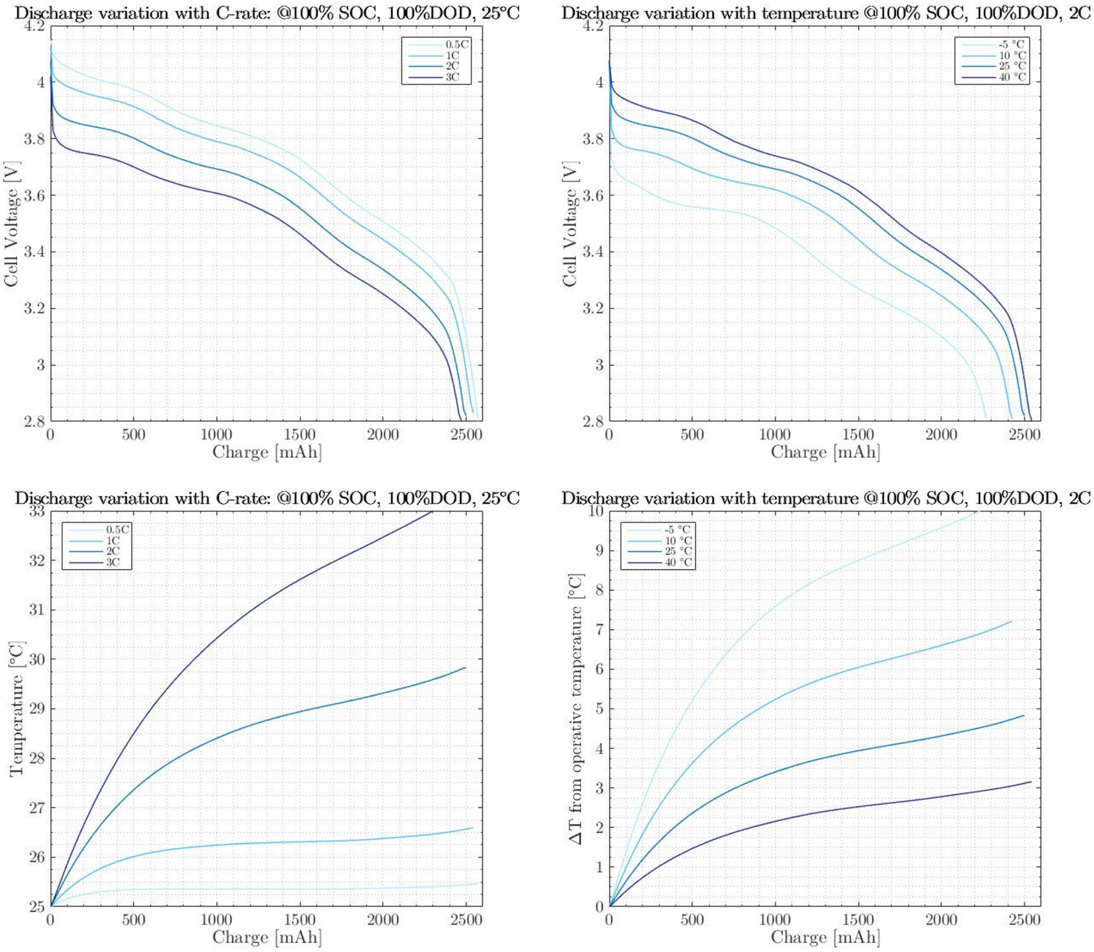

Figure 4.5: *On the left, effect of the C-rate variation on the voltage and temperature profiles simulated by the model in a discharge curve. On the right, effect of the ambient temperature variation on the same quantities*

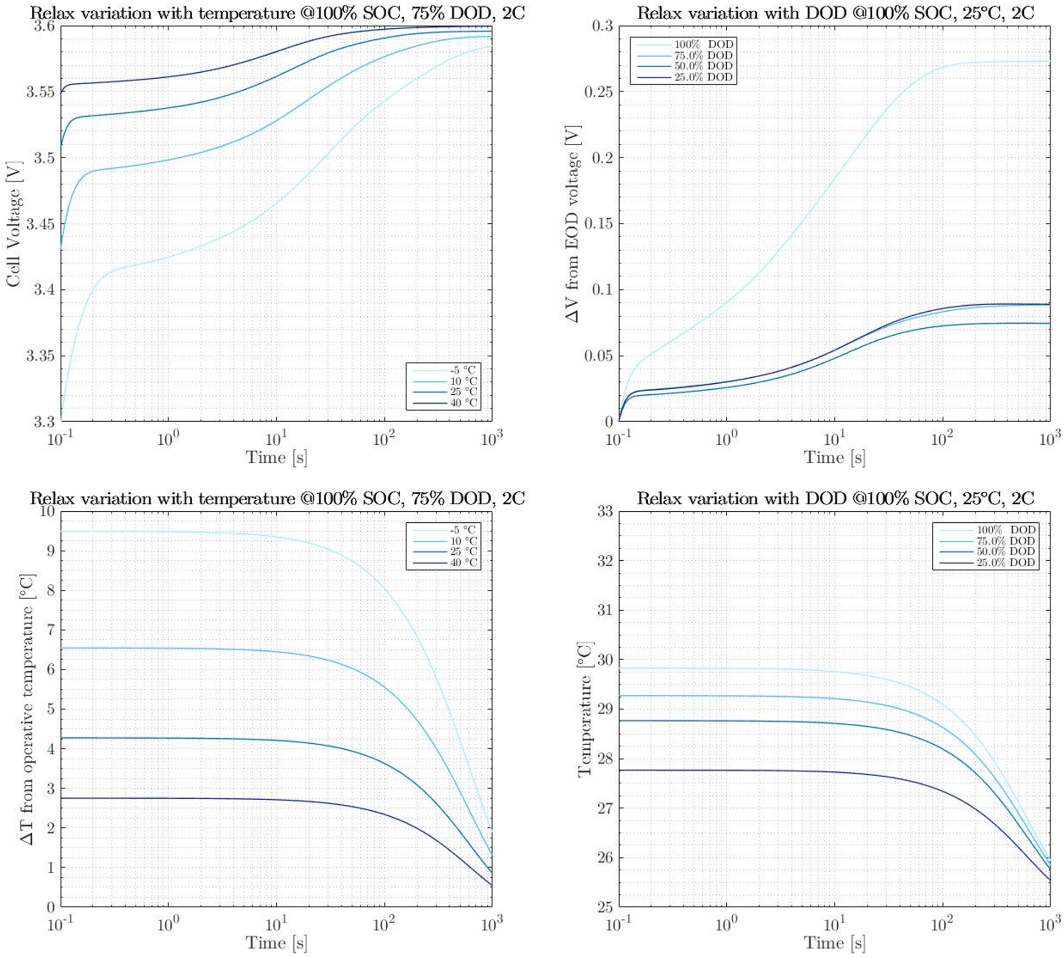

Figure 4.6: *On the left, effect of the ambient temperature variation on the voltage and temperature profiles simulated by the model in a relaxation curve. On the right, effect of the DOD variation on the same quantities*

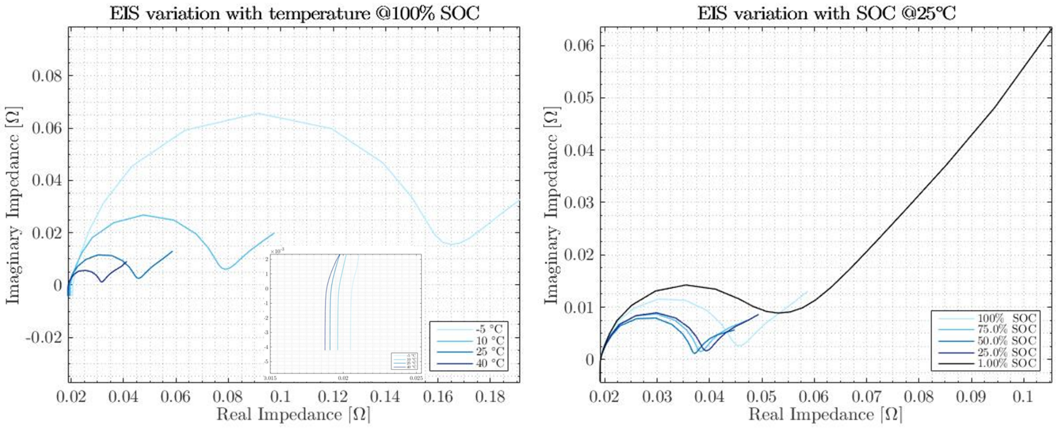

Figure 4.7: *On the left, effect of the ambient temperature variation on the real and imaginary impedance simulated by the model in a EIS, with a zoom on the HFR zone. On the right, effect of the SOC variation on the same quantities*

slope of the open circuit potentials of the anode and cathode [108], which is higher at the extreme values of the state of charge. The EIS at 1% SOC has not been experimentally observed, so we are not able to confirm the model behavior at this value of SOC, while the trend of the EIS with the other values of SOC are similar the ones seen in figure 3.16.

Nevertheless, the second circle that appears experimentally at low SOC is not seen in figure 4.7. This can be due to the benchmark set that is used for the sensitivity analysis, that is not meant to perfectly fit the experimental behavior of the battery samples. Also, the capability of the P2D model of reproducing the EIS of a complex electrochemical system as a commercial lithium-ion battery in all its characteristics has been questioned in literature [151], in particular in its simplification of the particle size distribution in the electrodes as a single particle radius and in the shape of the diffusion impedance.

External parameters

Lastly, in figure 4.8 we show on the left the effect of the variation of the external resistance R_{ext} on the voltage in a discharge curve, and on the right the one of the variation of the convective heat transfer coefficient h_{conv} on the surface temperature during another discharge curve. These plots highlight the importance of knowing the value of these two quantities, whose extent is not due to the lithium-ion battery. Instead, it comes from the instruments and the components that are employed in the lithium-ion battery diagnostics, in particular the wiring and the connections for the external resistance, and the climatic chamber for the convective heat transfer coefficient. In fact, during the subsequent fitting of the battery, they are kept constant at a reasonable value according to our experimental conditions. An error in the evaluation of one of them could lead to considerable errors in the identification of the battery parameters, since their effects on the output are of the same order of magnitude of the effects of the other parameters, if not higher in some

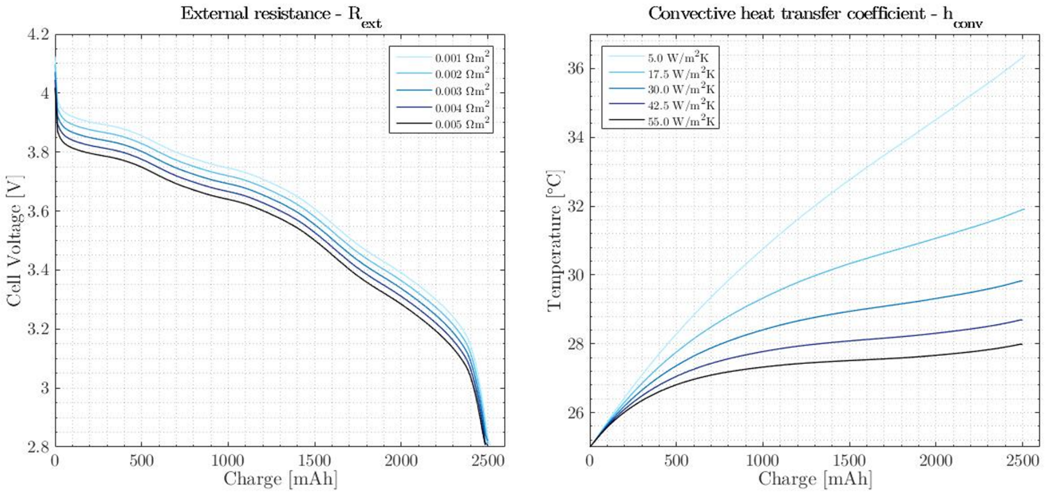

Figure 4.8: *On the left, effect of the variation of the external resistance on the voltage simulated by the model in a discharge curve. On the right, effect of the variation of the convective heat transfer coefficient on the battery surface temperature simulated by the model in a discharge curve*

cases. Therefore, when the diagnostic of a battery is made to try to evaluate its parameters, a careful calculation of the cables and contact resistances and of the heat transfer coefficient should be made in order to avoid considerable errors [167].

4.2.2 Output variation with model parameters

In the next pages, an example of the effects of the variation of a sample of eight parameters (FCE, $R_{film,n}$, $R_{p,n}$, $C_{dl,p}$, k_p, $D_{s,p}$, $\varepsilon_{e,sep}$ and $k_{T,rad,am}$) in some different experimental conditions are shown (figures 4.9, 4.10, 4.11, 4.12 and 4.13). We chose these parameters because with them it is possible to understand all the main trends that emerge from the sensitivity analysis. From the analysis of these parameters and of the other ones not shown here for reasons related to the available space, some general considerations can be made:

- some parameters have a negligible impact in certain techniques and/or in certain operative conditions, while they are very important in others. The parameters that belong to this **mixed impact** category show a mean of the average standard deviations

$\overline{\mathrm{SD}_{y,j}}$ that is much lower than the maximum of the average standard deviations $\overline{SD_{y,j,max}}$, and/or they are among the most sensitive ones only in one or two of the three diagnostic techniques. This characteristic is very interesting for the purpose of our analysis, since it implies the possibility to exclude or isolate the effect of a parameter in some conditions.
For instance, the variation of the double layer capacity of the positive electrode (as well as the one of double layer capacity of the negative electrode, not shown in the figures) has not an appreciable effect on the discharge curve voltage and temperature

(figures 4.9 and 4.10), in any operative condition. In the relaxation test, a difference in the voltage in the first fractions of second after the beginning of the relaxation can be seen in figure 4.11, but such a rapid variation is not detectable from our voltage acquisition system, as well as from common battery cyclers. Instead, the EIS impedance shows a great sensitivity to a variation of the double layer, since this parameter defines the frequency at which the charge transfer effects occur. The higher the double layer capacitance, the lower the range of frequencies of the charge transfer semicircle, since this capacitance delays and smooths the onset of the faradaic current.
Another example is the effect of the lithium solid diffusion coefficient in the positive electrode. In most conditions, it is one of the most sensitive parameters on the voltage value of discharge and relaxation curves, since it has a strong influence on the lithium concentration unbalance between the surface and the bulk of the cathode particles. Lowering the current rate, decreasing the depth of discharge and increasing the ambient temperature, the effect of this parameter declines, because the diffusion is favored at higher temperatures and smaller current pulses imply a lower concentration disequilibrium in the cathode due to the lower quantity of transported lithium. Moreover, the effect of a variation of the diffusion coefficient on the temperature is negligible, since the concentration unbalances in the solid do not induce a proper overpotential 1.1.2;

- some parameters show an **uniform impact** in almost all the explored conditions. These parameters have an the mean of the average standard deviation

  $\mathrm{SD}_{y,j}$ in the same order of magnitude of maximum standard deviation $\overline{SD}_{y,j,max}$. This characteristic is not desirable for the parameter identification, since there are no conditions where they can be effectively isolated.
  A notable example is the effect of the positive particle radius (as well as effect of the negative one, not shown in the figures). A variation of this parameter leads to high dispersions in all the outputs of the capacity test, of the relaxation curve and of the EIS (figures 4.9, 4.10, 4.11, 4.12 and 4.13). The positive particle radius has a linear impact on the charge transfer resistance of the positive electrode, since it is contained in the expression of the specific active electrode area (equation 2.27). Also, its squared value is in the expression of the characteristic time of diffusion in the solid particle (equation 2.3). Therefore, the particle radius of the cathode material has a direct and high influence on the main phenomena that dictate the trend of the battery voltage, temperature and impedance;

- finally, some parameters have a **negligible impact** in every simulated condition. Their mean of the average standard deviations

  $\mathrm{SD}_{y,j}$ and their maximum standard deviation $\overline{SD}_{y,j,max}$ are below the chosen minimum limits $SD_{y,lim}$, and hence their fitting do not lead to sound parameter values. Therefore, these parameters can be excluded from the parameter identification process and kept constant equal to a reasonable value taken from literature.
  For instance, the electrolyte volume fraction in the separator shows a very little influence on all the outputs of all the simulated experimental conditions (figures 4.9, 4.10, 4.11, 4.12 and 4.13). The reasons of this behavior are that the range in which it can vary is very narrow, due to the manufacturing standards of the battery

separators [49], and that in the P2D model it is only present in the formulation of the equivalent ionic conductivity in the separator (equation 2.23).

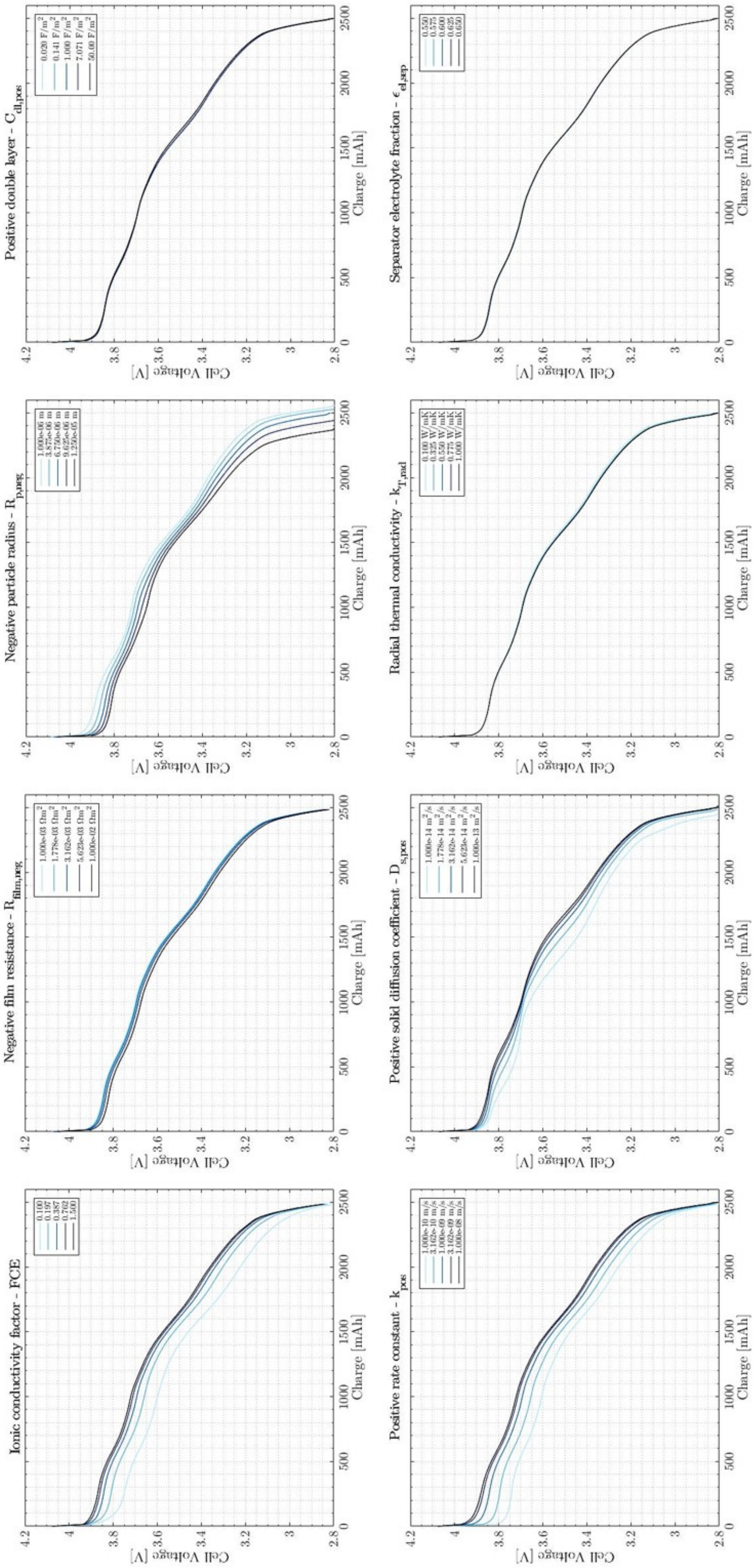

Figure 4.9: *Sensitivity on the discharge curve voltage with respect to eight relevant physical parameters at* $25^\circ C$, 100% SOC, 100% DOD, $2C$

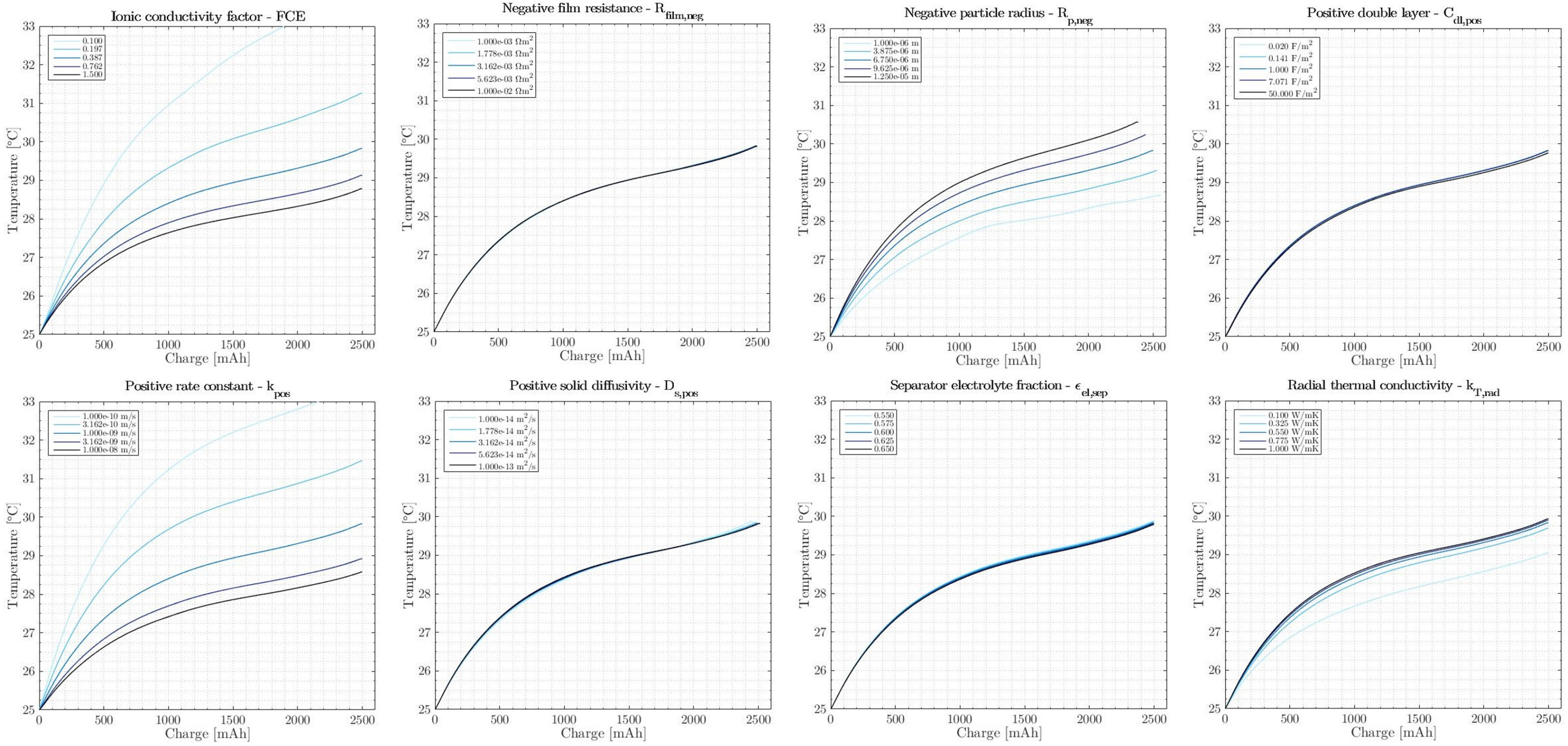

Figure 4.10: *Sensitivity on the discharge curve temperature with respect to eight relevant physical parameters at 25° C, 100% SOC, 100% DOD, 2C*

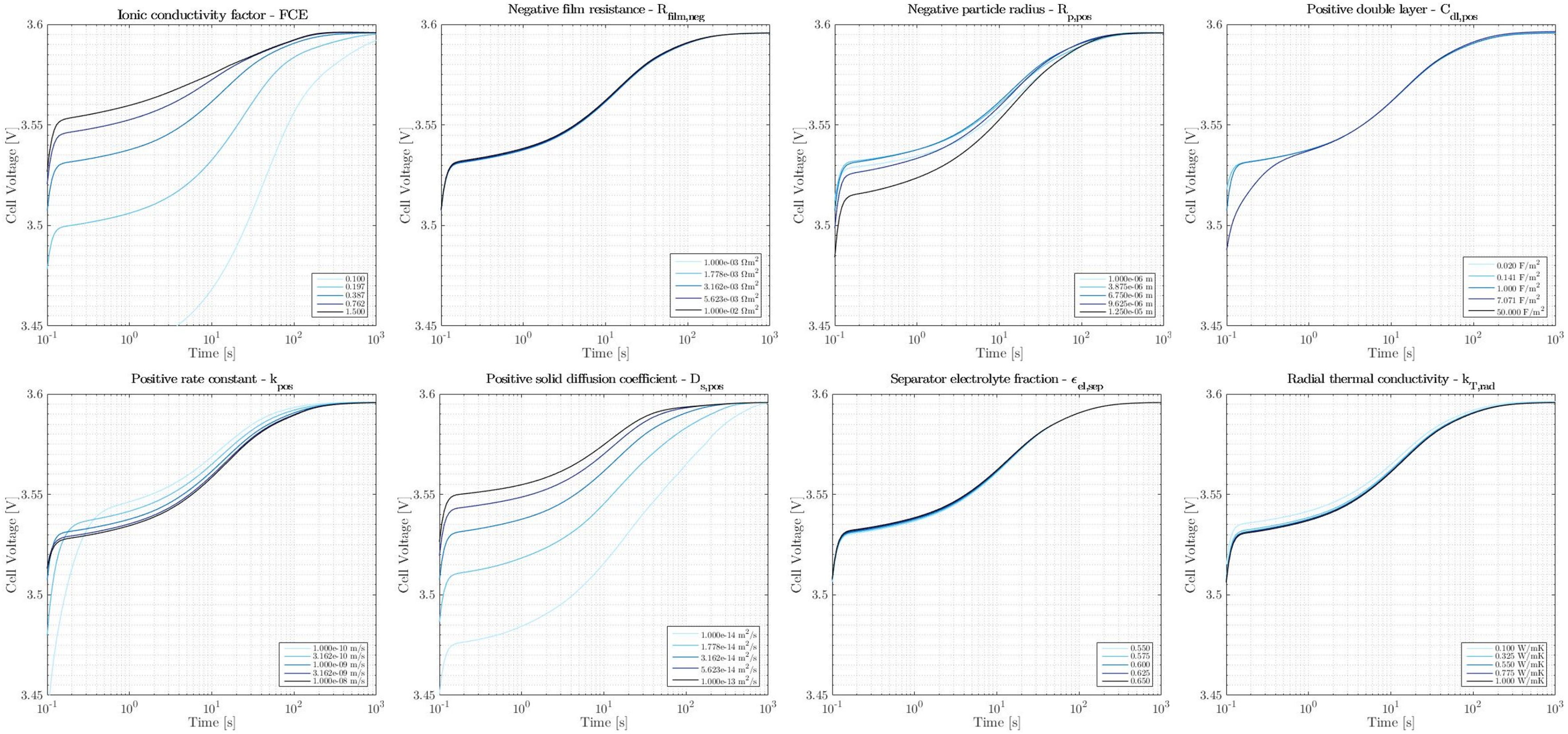

Figure 4.11: *Sensitivity on the relaxation curve voltage with respect to eight relevant physical parameters at* 25° *C*, 100% *SOC*, 75% *DOD*, 2*C*

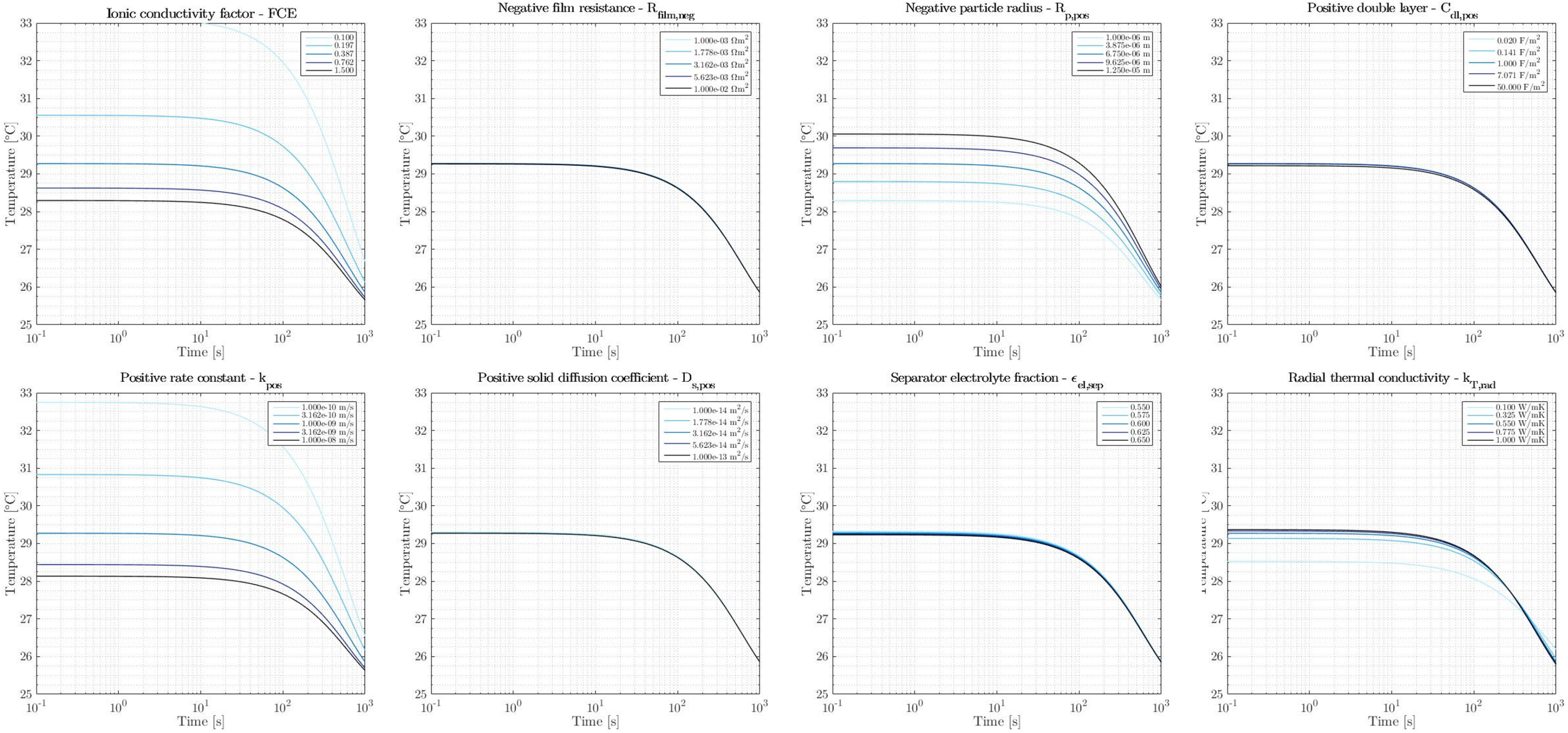

Figure 4.12: *Sensitivity on the relaxation curve temperature with respect to eight relevant physical parameters at 25° C, 100% SOC, 75% DOD, 2C*

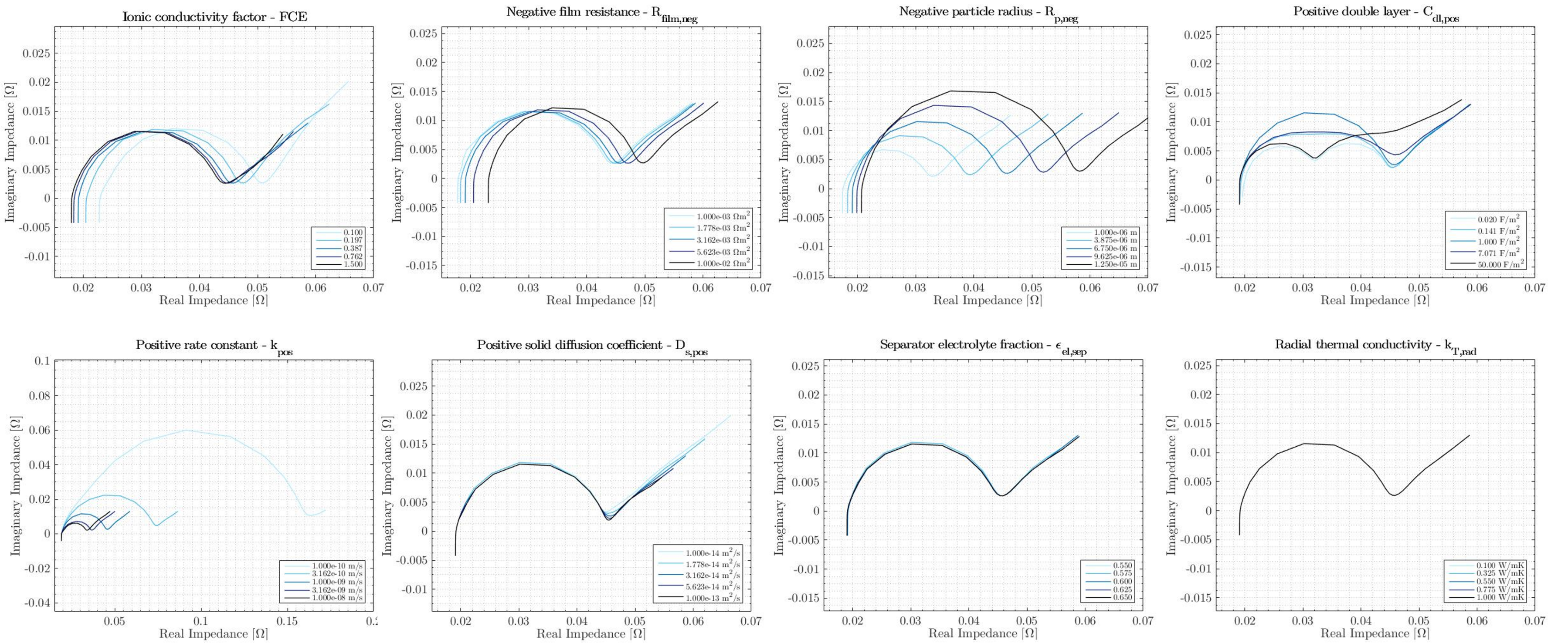

Figure 4.13: *Sensitivity on the EIS impedance with respect to eight relevant physical parameters at 25° C, 100% SOC*

All the results of the sensitivity analysis are summarized in the tables 4.3, 4.4, 4.5, 4.6, 4.7 and 4.8. For each parameter, it is reported the mean of the average sensitivites of all the operative conditions $\overline{\overline{SD}}_{y,j}$, the maximum value of average sensitivity $\overline{SD}_{y,j,max}$ with the related operative condition at which we observe this maximum value, and the class which the parameter belongs to, according to the criteria reported in the previous section.
However, this level of analysis is not sufficient to understand in depth the impact of each parameter in the different operative conditions and experimental techniques. With these tables, we are able to qualitatively assess which is the degree of sensitivity of the outputs to the model parameters.
Instead, the objective is to understand if it is possible to find a combination of tests that maximizes the useful information obtainable from the battery diagnostics, to allow a comprehensive parameter identification. In literature, the battery P2D model fitting is often made with only charge/discharge curves, and the electrochemical impedance spectroscopy is employed only with electric equivalent circuit models (see Chapter 2). The combination of capacity tests, relaxation curves and EIS made in several operative conditions should provide a full characterization of the lithium-ion battery, since the fitting dataset would include very different behaviors, with a variety of characteristic timescales included.

The ideal parametrization process should include a specific test for each model parameter according to its maximum sensitivity conditions reported in the tables, i.e. its best condition for identification. Actually, this approach is for sure excessively complicate and time consuming, due to the high number of experiments required (at least one per parameter). Therefore, it is important to select a reasonable number of experiments, each of which is sufficiently near to the best conditions for identification of a group of parameters, and far from the the ones of all the other parameters. In this way, each chosen experiment should be used to effectively fit the group of parameters that impact the most in that condition, while keeping low/very low the sensitivity to all the other parameters.
At the end, the desired outcome is a set of few experiments that together are able to fully characterize the battery, while minimizing the time needed for their execution.

	Discharge curve - Voltage			
Parameter	$\overline{\overline{SD}}^D_{V,j}$ [mV]	$\overline{SD}^D_{V,j,max}$ [mV]	**Operative condition**	**Class**
$C_{dl,pos}$	2.1	9.2	−5°C, 25% SOC, 25% DOD, 3C	Low Sensitivity
$C_{dl,neg}$	2.1	9.2	−5°C, 25% SOC, 25% DOD, 3C	Low Sensitivity
k_p	42.2	67.7	−5°C, 25% SOC, 25% DOD, 3C	High Sensitivity
k_n	42.2	67.9	−5°C, 25% SOC, 25% DOD, 3C	High Sensitivity
$c_{e,0}$	3.5	6.9	−5°C, 50% SOC, 25% DOD, 3C	Low Sensitivity
FCE	39.4	90.0	−5°C, 50% SOC, 50% DOD, 3C	High Sensitivity
t_0^+	2.6	6.8	−5°C, 100% SOC, 25% DOD, 3C	High Sensitivity
σ_p	3.0	6.9	−5°C, 25% SOC, 50% DOD, 3C	High Sensitivity
σ_n	0.04	0.45	−5°C, 25% SOC, 25% DOD, 2C	Insensitivity
$R_{p,p}$	62.5	157.7	−5°C, 100% SOC, 75% DOD, 3C	High Sensitivity
$R_{p,n}$	31.3	73.5	−5°C, 25% SOC, 25% DOD, 1C	High Sensitivity
$D_{s,p}$	36.8	112.6	−5°C, 100% SOC, 100% DOD, 3C	High Sensitivity
$D_{s,n}$	9.3	40.4	−5°C, 25% SOC, 25% DOD, 0.5C	High Sensitivity
$R_{film,n}$	7.9	15.3	−5°C, 75% SOC, 25% DOD, 3C	Mid Sensitivity
$R_{film,p}$	0.8	1.8	−5°C, 25% SOC, 25% DOD, 3C	Insensitivity
R_{ext}	30.6	56.5	10°C, 75% SOC, 50% DOD, 3C	High Sensitivity
$\varepsilon_{e,p}$	1.7	5.2	−5°C, 50% SOC, 25% DOD, 3C	Low Sensitivity
$\varepsilon_{e,sep}$	0.8	2.2	−5°C, 100% SOC, 25% DOD, 3C	Insensitivity
$\varepsilon_{e,neg}$	1.6	4.1	−5°C, 25% SOC, 25% DOD, 3C	Low Sensitivity
C_{am}	1.1	7.2	−5°C, 75% SOC, 75% DOD, 3C	Low Sensitivity
$k_{T,rad,am}$	2.1	14.9	−5°C, 100% SOC, 100% DOD, 3C	Low Sensitivity
$k_{T,ax,am}$	0.01	0.08	−5°C, 50% SOC, 50% DOD, 3C	Insensitivity
ρ_{am}	1.6	4.1	−5°C, 25% SOC, 25% DOD, 3C	Low Sensitivity
h_{conv}	5.3	34.2	−5°C, 100% SOC, 100% DOD, 3C	Mid Sensitivity
EA_{k_p}	7.6	26.0	−5°C, 25% SOC, 25% DOD, 3C	Mid Sensitivity
EA_{k_n}	7.6	25.9	−5°C, 25% SOC, 25% DOD, 3C	Mid Sensitivity
$EA_{D_{s,p}}$	14.5	65.2	−5°C, 75% SOC, 25% DOD, 3C	High Sensitivity
$EA_{D_{s,n}}$	7.1	45.6	−5°C, 75% SOC, 25% DOD, 0.5C	High Sensitivity

Table 4.3: *Sensitivity analysis: Voltage output, discharge curve*

Discharge curve - Temperature

Parameter	$\overline{\overline{SD}}^{D}_{T,j}$ [°C]	$\overline{SD}^{D}_{T,j,max}$ [°C]	Operative condition	Class
$C_{dl,pos}$	0.014	0.053	−5°C, 50% SOC, 25% DOD, 3C	Insensitivity
$C_{dl,neg}$	0.005	0.032	−5°C, 25% SOC, 25% DOD, 3C	Insensitivity
k_p	0.749	1.930	10°C, 100% SOC, 100% DOD, 3C	High Sensitivity
k_n	0.745	1.868	10°C, 100% SOC, 100% DOD, 3C	High Sensitivity
$c_{e,0}$	0.056	0.194	−5°C, 100% SOC, 100% DOD, 3C	Low Sensitivity
FCE	0.663	2.754	−5°C, 100% SOC, 100% DOD, 3C	High Sensitivity
t_0^+	0.049	0.205	−5°C, 100% SOC, 25% DOD, 3C	Low Sensitivity
σ_p	0.062	0.222	40°C, 25% SOC, 50% DOD, 3C	Low Sensitivity
σ_n	0.001	0.007	10°C, 100% SOC, 50% DOD, 3C	Insensitivity
$R_{p,p}$	0.300	0.884	10°C, 100% SOC, 75% DOD, 3C	High Sensitivity
$R_{p,n}$	0.299	0.915	−5°C, 100% SOC, 75% DOD, 3C	High Sensitivity
$D_{s,p}$	0.013	0.049	−5°C, 100% SOC, 100% DOD, 3C	Insensitivity
$D_{s,n}$	0.011	0.059	−5°C, 75% SOC, 50% DOD, 3C	Insensitivity
$R_{film,n}$	0.002	0.015	−5°C, 100% SOC, 100% DOD, 3C	Insensitivity
$R_{film,p}$	0.001	0.006	10°C, 100% SOC, 50% DOD, 3C	Insensitivity
R_{ext}	0.001	0.002	−5°C, 75% SOC, 75% DOD, 2C	Insensitivity
$\varepsilon_{e,p}$	0.029	0.135	−5°C, 100% SOC, 100% DOD, 3C	Low Sensitivity
$\varepsilon_{e,sep}$	0.016	0.065	−5°C, 100% SOC, 100% DOD, 3C	Insensitivity
$\varepsilon_{e,neg}$	0.031	0.116	−5°C, 100% SOC, 100% DOD, 3C	Low Sensitivity
C_{am}	0.080	0.300	−5°C, 75% SOC, 75% DOD, 3C	Low Sensitivity
$k_{T,rad,am}$	0.202	1.007	−5°C, 100% SOC, 100% DOD, 3C	High Sensitivity
$k_{T,ax,am}$	0.002	0.011	−5°C, 100% SOC, 100% DOD, 3C	Insensitivity
ρ_{am}	0.080	0.300	−5°C, 75% SOC, 75% DOD, 3C	Low Sensitivity
h_{conv}	0.721	2.892	−5°C, 100% SOC, 100% DOD, 3C	High Sensitivity
EA_{k_p}	0.134	0.493	−5°C, 100% SOC, 100% DOD, 3C	Mid Sensitivity
EA_{k_n}	0.133	0.488	−5°C, 100% SOC, 100% DOD, 3C	Mid Sensitivity
$EA_{D_{s,p}}$	0.006	0.042	−5°C, 75% SOC, 50% DOD, 3C	Insensitivity
$EA_{D_{s,n}}$	0.009	0.072	−5°C, 75% SOC, 25% DOD, 3C	Insensitivity

Table 4.4: *Sensitivity analysis: Temperature output, discharge curve*

Relaxation curve - Voltage

Parameter	$\overline{\overline{SD}}^R_{V,j}$ [mV]	$\overline{SD}^R_{V,j,max}$ [mV]	Operative condition	Class
$C_{dl,pos}$	6.3	44.3	−5°C, 50% SOC, 25% DOD, 2C, FR	Mid Sensitivity
$C_{dl,neg}$	5.7	39.9	−5°C, 50% SOC, 25% DOD, 3C, FR	Mid Sensitivity
k_p	5.7	36.4	−5°C, 100% SOC, 50% DOD, 3C, FR	Mid Sensitivity
k_n	6.0	35.3	−5°C, 100% SOC, 50% DOD, 3C, FR	Mid Sensitivity
$c_{e,0}$	4.1	20.7	−5°C, 50% SOC, 25% DOD, MR 3C	Mid Sensitivity
FCE	22.8	83.0	−5°C, 100% SOC, 75% DOD, 3C, FR	High Sensitivity
t_0^+	1.4	7.5	−5°C, 100% SOC, 25% DOD, 3C, FR	Low Sensitivity
σ_p	0.392	4.1	−5°C, 100% SOC, 50% DOD, 3C, FR	Low Sensitivity
σ_n	0.014	0.139	−5°C, 100% SOC, 50% DOD, 3C, SR	Insensitivity
$R_{p,p}$	36.2	171.7	−5°C, 100% SOC, 50% DOD, 3C, FR	High Sensitivity
$R_{p,n}$	7.4	85.8	−5°C, 100% SOC, 75% DOD, 1C, FR	Mid Sensitivity
$D_{s,p}$	32.1	153.3	−5°C, 100% SOC, 50% DOD, 3C, MR	High Sensitivity
$D_{s,n}$	7.2	102.0	−5°C, 100% SOC, 75% DOD, 2C, FR	Mid Sensitivity
$R_{film,n}$	0.146	0.829	−5°C, 100% SOC, 25% DOD, 3C, MR	Insensitivity
$R_{film,p}$	0.018	0.168	−5°C, 100% SOC, 25% DOD, 3C, MR	Insensitivity
R_{ext}	0.001	0.104	−5°C, 100% SOC, 75% DOD, 2C, MR	Insensitivity
$\varepsilon_{e,p}$	0.907	4.8	−5°C, 100% SOC, 25% DOD, 3C, FR	Low Sensitivity
$\varepsilon_{e,sep}$	0.341	1.5	−5°C, 100% SOC, 25% DOD, 3C, FR	Insensitivity
$\varepsilon_{e,neg}$	0.499	2.9	−5°C, 100% SOC, 25% DOD, 3C, FR	Insensitivity
C_{am}	0.548	7.9	−5°C, 50% SOC, 25% DOD, 3C, FR	Low Sensitivity
$k_{T,rad,am}$	1.5	15.9	−5°C, 100% SOC, 75% DOD, 3C, FR	Low Sensitivity
$k_{T,ax,am}$	0.004	0.137	−5°C, 100% SOC, 50% DOD, 3C, LR	Insensitivity
ρ_{am}	0.548	7.9	−5°C, 50% SOC, 25% DOD, 3C, FR	Low Sensitivity
h_{conv}	4.0	41.6	−5°C, 100% SOC, 75% DOD, 3C, FR	Mid Sensitivity
EA_{k_p}	1.2	10.1	−5°C, 100% SOC, 50% DOD, 3C, FR	Low Sensitivity
EA_{k_n}	1.2	9.9	−5°C, 100% SOC, 50% DOD, 3C, FR	Low Sensitivity
$EA_{D_{s,p}}$	11.9	84.6	−5°C, 50% SOC, 25% DOD, 2C, MR	High Sensitivity
$EA_{D_{s,n}}$	6.5	123.9	−5°C, 75% SOC, 50% DOD, 1C, MR	Mid Sensitivity

Table 4.5: *Sensitivity analysis: Voltage output, relaxation curve*

Relaxation curve - Temperature

Parameter	$\overline{\overline{SD}}^{R}_{T,j}$ [°C]	$\overline{SD}^{R}_{T,j,max}$ [°C]	Operative condition	Class
$C_{dl,pos}$	0.011	0.041	−5°C, 75% SOC, 25% DOD, 3C, FR	Insensitivity
$C_{dl,neg}$	0.003	0.029	−5°C, 50% SOC, 25% DOD, 3C, FR	Insensitivity
k_p	0.965	2.657	−5°C, 100% SOC, 75% DOD, 3C, FR	High Sensitivity
k_n	0.954	2.563	−5°C, 100% SOC, 75% DOD, 3C, FR	High Sensitivity
$c_{e,0}$	0.070	0.310	−5°C, 100% SOC, 75% DOD, Fr 3C	Low Sensitivity
FCE	0.980	4.701	−5°C, 100% SOC, 75% DOD, 3C, FR	High Sensitivity
t_0^+	0.067	0.283	−5°C, 100% SOC, 75% DOD, 3C, FR	Low Sensitivity
σ_p	0.082	0.300	40°C, 100% SOC, 75% DOD, 3C, FR	Low Sensitivity
σ_n	0.001	0.009	10°C, 100% SOC, 50% DOD, 3C, FR	Insensitivity
$R_{p,p}$	0.423	1.539	−5°C, 50% SOC, 25% DOD, 3C, FR	High Sensitivity
$R_{p,n}$	0.405	1.291	−5°C, 100% SOC, 75% DOD, 3C, FR	Mid Sensitivity
$D_{s,p}$	0.054	1.652	−5°C, 50% SOC, 25% DOD, 3C, FR	Low Sensitivity
$D_{s,n}$	0.035	1.265	−5°C, 50% SOC, 25% DOD, 2C, FR	Low Sensitivity
$R_{film,n}$	0.003	0.017	−5°C, 100% SOC, 75% DOD, 3C, FR	Insensitivity
$R_{film,p}$	0.001	0.007	−5°C, 100% SOC, 50% DOD, 3C, FR	Insensitivity
R_{ext}	0.063	0.008	−5°C, 100% SOC, 50% DOD, 3C, LR	Insensitivity
$\varepsilon_{e,p}$	0.042	0.205	−5°C, 100% SOC, 75% DOD, 3C, FR	Low Sensitivity
$\varepsilon_{e,sep}$	0.022	0.088	−5°C, 100% SOC, 75% DOD, 3C, FR	Insensitivity
$\varepsilon_{e,neg}$	0.041	0.157	−5°C, 100% SOC, 75% DOD, 3C, FR	Low Sensitivity
C_{am}	0.077	0.371	−5°C, 50% SOC, 25% DOD, 3C, FR	Low Sensitivity
$k_{T,rad,am}$	0.258	1.443	−5°C, 100% SOC, 75% DOD, 3C, FR	High Sensitivity
$k_{T,ax,am}$	0.003	0.016	−5°C, 100% SOC, 75% DOD, 3C, FR	Insensitivity
ρ_{am}	0.077	0.371	−5°C, 50% SOC, 25% DOD, 3C, FR	Low Sensitivity
h_{conv}	1.448	6.467	−5°C, 100% SOC, 75% DOD, 3C, LR	High Sensitivity
EA_{k_p}	0.165	0.598	−5°C, 100% SOC, 50% DOD, 3C, FR	Mid Sensitivity
EA_{k_n}	0.163	0.591	−5°C, 100% SOC, 50% DOD, 3C, FR	Mid Sensitivity
$EA_{D_{s,p}}$	0.015	0.726	−5°C, 50% SOC, 25% DOD, 3C, FR	Low Sensitivity
$EA_{D_{s,n}}$	0.031	1.437	−5°C, 50% SOC, 25% DOD, 3C, FR	Low Sensitivity

Table 4.6: *Sensitivity analysis: Temperature output, relaxation curve*

EIS - Real impedance

Parameter	$\overline{\overline{SD}}^{E}_{Z',j}$ [mΩ]	$\overline{SD}^{E}_{Z',j,max}$ [mΩ]	Operative condition	Class
$C_{dl,pos}$	5.7	27.8	−5°C, 100% SOC, MF	High Sensitivity
$C_{dl,neg}$	7.1	48.4	−5°C, 1% SOC, LF	High Sensitivity
k_p	25.9	169.0	−5°C, 100% SOC, LF	High Sensitivity
k_n	27.9	200.6	−5°C, 1% SOC, LF	High Sensitivity
$c_{e,0}$	2.7	19.5	−5°C, 1% SOC, LF	High Sensitivity
FCE	2.8	4.8	−5°C, 1% SOC, LF	High Sensitivity
t_0^+	0.056	0.215	25°C, 100% SOC, LF	Low Sensitivity
σ_p	0.823	0.892	−5°C, 100% SOC, HF	High Sensitivity
σ_n	0.009	0.057	25°C, 100% SOC, LF	Insensitivity
$R_{p,p}$	7.5	45.7	−5°C, 100% SOC, LF	High Sensitivity
$R_{p,n}$	9.7	83.1	−5°C, 1% SOC, LF	High Sensitivity
$D_{s,p}$	0.422	3.4	−5°C, 100% SOC, LF	High Sensitivity
$D_{s,n}$	0.724	15.7	−5°C, 1% SOC, LF	High Sensitivity
$R_{film,n}$	1.8	1.9	−5°C, 75% SOC, HF	High Sensitivity
$R_{film,p}$	0.022	0.035	−5°C, 1% SOC, HF	Insensitivity
R_{ext}	7.2	7.2	−5°C, 100% SOC, HF	High Sensitivity
$\varepsilon_{e,p}$	0.135	0.257	−5°C, 25% SOC, LF	Mid Sensitivity
$\varepsilon_{e,sep}$	0.066	0.095	−5°C, 25% SOC, LF	Insensitivity
$\varepsilon_{e,neg}$	0.125	0.257	−5°C, 1% SOC, LF	Mid Sensitivity
EA_{k_p}	4.6	47.1	−5°C, 100% SOC, LF	High Sensitivity
EA_{k_n}	5.1	64.1	−5°C, 1% SOC, LF	High Sensitivity
$EA_{D_{s,p}}$	0.189	2.7	−5°C, 100% SOC, LF	Mid Sensitivity
$EA_{D_{s,n}}$	0.565	19.1	−5°C, 1% SOC, LF	High Sensitivity

Table 4.7: *Sensitivity analysis: Real impedance output, EIS*

EIS - Imaginary impedance

Parameter	$\overline{\overline{SD}}^{E}_{Z'',j}$ [mΩ]	$\overline{SD}^{E}_{Z'',j,max}$ [mΩ]	Operative condition	Class
$C_{dl,pos}$	2.9	10.6	−5°C, 100% SOC, MF	High Sensitivity
$C_{dl,neg}$	3.3	16.2	−5°C, 1% SOC, MF	High Sensitivity
k_p	9.0	56.3	−5°C, 100% SOC, LF	High Sensitivity
k_n	10.5	83.6	−5°C, 1% SOC, LF	High Sensitivity
$c_{e,0}$	0.764	3.5	−5°C, 100% SOC, MF	High Sensitivity
FCE	0.447	0.990	10°C, 100% SOC, LF	High Sensitivity
t_0^+	0.062	0.247	25°C, 100% SOC, LF	Low Sensitivity
σ_p	0.0222	0.062	−5°C, 100% SOC, HF	Insensitivity
σ_n	0.001	0.043	25°C, 100% SOC, HF	Insensitivity
$R_{p,p}$	2.2	10.8	−5°C, 100% SOC, MF	High Sensitivity
$R_{p,n}$	2.9	34.0	−5°C, 1% SOC, LF	High Sensitivity
$D_{s,p}$	0.504	4.9	−5°C, 100% SOC, LF	High Sensitivity
$D_{s,n}$	0.804	20.0	−5°C, 1% SOC, LF	High Sensitivity
$R_{film,n}$	0.095	0.529	−5°C, 100% SOC, HF	Low Sensitivity
$R_{film,p}$	0.016	0.098	−5°C, 25% SOC, HF	Insensitivity
R_{ext}	0	0	-	Insensitivity
$\varepsilon_{e,p}$	0.031	0.108	−5°C, 100% SOC, LF	Low Sensitivity
$\varepsilon_{e,sep}$	0.012	0.060	25°C, 100% SOC, MF	Insensitivity
$\varepsilon_{e,neg}$	0.036	0.109	−5°C, 100% SOC, LF	Low Sensitivity
EA_{k_p}	1.3	9.0	−5°C, 100% SOC, MF	High Sensitivity
EA_{k_n}	1.6	15.9	−5°C, 1% SOC, LF	High Sensitivity
$EA_{D_{s,p}}$	0.236	3.8	−5°C, 100% SOC, LF	High Sensitivity
$EA_{D_{s,n}}$	0.680	25.1	−5°C, 1% SOC, LF	High Sensitivity

Table 4.8: *Sensitivity analysis: Imaginary impedance output, EIS*

4.2.3 Clustering of the results

The clustering of the results of the sensitivity analysis is performed to enable the comparison of the average standard deviations caused by the parameters' variations on the model outputs. With this technique, it is possible to evaluate the trend of their sensitivity while varying the operative conditions, and eventually select experiments where one or more parameters are much more relevant than the others in defining the cell voltage, the surface temperature or the impedance.

Firstly, the average standard deviations $\overline{SD}_{y,j,i}$ are normalized with respect to the minimum border value of the output $SD_{y,lim}$, according to equation 4.13. The nondimensionalization of the standard deviations has the purpose of comparing in a more direct way the sensitivities of voltage, temperature and impedance to the model parameters. The nondimensionalized value can be read as the how many times larger the variation of an output caused by a change of a parameter is than the minimum detectable variation of the output itself.
Then, the clustering algorithm described in the section 4.1.2 is separately applied to each operative condition in each experimental technique. Three clusters are created, and in the subsequent figures they are indicated as **red**, **yellow** and **green**, which are respectively the **low sensitivity cluster**, the **mid sensitivity cluster** and the **high sensitivity cluster**. Their shape changes according to the operative condition, since they are based on the values of the standard deviation in that operative condition.
In each point, the normalized average standard deviations of the parameters $\overline{SD}'_{y,j,i}$ will belong to one of the three clusters, but they can change cluster in the other points according to the sensitivity of the model output in the other operative conditions.

In figures 4.14, 4.15, 4.16, 4.17, 4.18, 4.19, 4.20, 4.21, 4.22, 4.23 and 4.24, some of the most relevant trends obtained from the clustering analysis are reported. In particular, the trend of the normalized average standard deviation $\overline{SD}'_{y,j,i}$ is shown for the parameters already used in the previous section to show the variation of the model outputs (FCE, $R_{film,n}$, $R_{p,n}$, $C_{dl,p}$, k_p, $D_{s,p}$, $\varepsilon_{e,sep}$ and $k_{T,rad,am}$). For the sake of brevity, not all the operative conditions are shown.

The main considerations that we can make from the clustering of the sensitivity analysis are:

- in the **discharge curve**, a low ambient temperature generally increases the sensitivity of the model outputs to the parameters, in particular the cell voltage. The diffusion-related parameters as the ionic conductivity factor and the solid diffusion coefficients are very impactful, since the diffusion process tends to become very sluggish at low temperatures. As this variable increases, the relative influence of the charge transfer-related parameters as the rate constants increases, too.
  The effect of the current rate variation is very high: the influence of a parameter on the cell voltage in a discharge at 3C is as much as 3-4 times

larger than its influence in a discharge at 0.5C, and up to 10 times higher if we consider the battery temperature. Even the generally less impactful parameters as the ones related to the thermal behavior of the battery are more important with high current rates. The reason of this trend can be found in the higher reaction rate required in case of high current, which exasperates all the battery irreversibilites, with a substantial increase of the ohmic, activation and concentration overpotentials and of the heat generation. Therefore, the values of the parameters that define these irreversibilites have much more impact on the resulting cell voltage and temperature.
A decrease of the depth of discharge affects mostly the diffusion process and the parameters related to it, as it is possible to see in top figure 4.15 for the solid diffusion coefficient in the positive electrode. With a lower DOD at the same current rate, there is less time for the establishment of concentration gradients and hence the model sensitivity to the diffusion decreases. Also, a lower DOD implies a lower duration of the heat generation in the battery, and hence a general reduction in the sensitivity of the battery temperature to the parameters. The effect of the initial state of charge is not shown, since it is quite similar to the effect of the depth of discharge;

- in the **relaxation curve**, the differentiation among the three time regions of the relaxation process reveals that in the first instants (fast relaxation, $0.1\,s \leq t \leq 1.7\,s$) the double layer capacitances and the rate constants have a certain influence on the cell voltage, but they are almost not relevant in the other timescales.
  As expected, the parameters that dictate the trend of the voltage and that remain influential in all the timescales are the diffusion-related parameters, i.e. the solid diffusion coefficients and the ionic conductivity factor. The former has a much higher normalized sensitivity in case of high current rates and low temperatures, while the latter has a more homogeneous trend with respect to these two operative conditions. The higher the DOD, the higher the overall sensitivity of both voltage and temperature, since there has been more time in the discharge to establish concentration gradients and to heat up the battery.
  The "spikes" that are seen in the top of figures 4.19, 4.20 and 4.21 for the lowest ambient temperature are due to the very limited diffusion in this condition, which induces a high variability in the final point of the discharge that precedes the relaxation;

- for the **EIS impedance**, from the figures 4.22, 4.23 and 4.24 it is actually possible to observe all the operative conditions in which the EIS has been simulated, thanks to the much lower number of possible combinations among the said operative conditions.
  The sensitivity of the real and imaginary impedance to the value of the double layer capacitances is quite important at high and medium frequencies, while it decreases sharply at low frequencies. This is because the double layer influences the dynamics of the charge transfer process, that is commonly found at high-mid frequencies.

The real impedance at high frequency, i.e. the HFR, is mostly determined by ionic conductivity factor, the negative film resistance (and hence also from the negative particle radius), the solid conductivity of the positive electrode and the double layer capacitances. In addition, a variation of external resistance can change the value of the HFR considerably, and this fact strengthen the reasoning made in section 4.2.1 about the necessity of an accurate evaluation of this parameter before the fitting process.

The mid-low frequency impedance is practically determined by the rate constants and the particle radii, which determine the value of the charge transfer resistance. The effect of a variation in diffusion-related parameters in the very low frequencies is not as evident as a variation of the charge transfer-related parameters in the mid-low frequencies. The solid diffusion coefficients become more important at the extremes of the state of charge, where both the electrode are nearer to their maximum/minimum concentration of lithium allowed by the material. The solid particles are rapidly filled/depleted by the low frequency AC signals, and hence the particles show a capacitor-like behavior [108]. In general, all the parameters are more influential at very low or very high SOC, even in the charge transfer region, because of the parabola-shaped exchange current density formulation from equation 2.17.

As seen for the other experimental techniques, a lower ambient temperature increases the sensitivity of the real and imaginary impedance to all the model parameters.

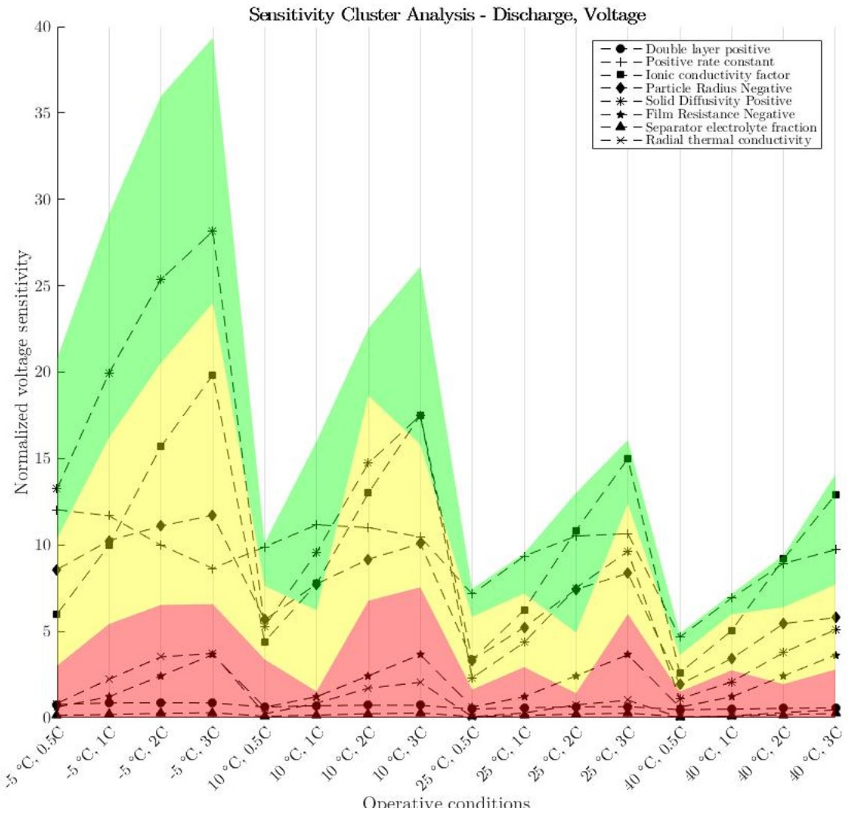

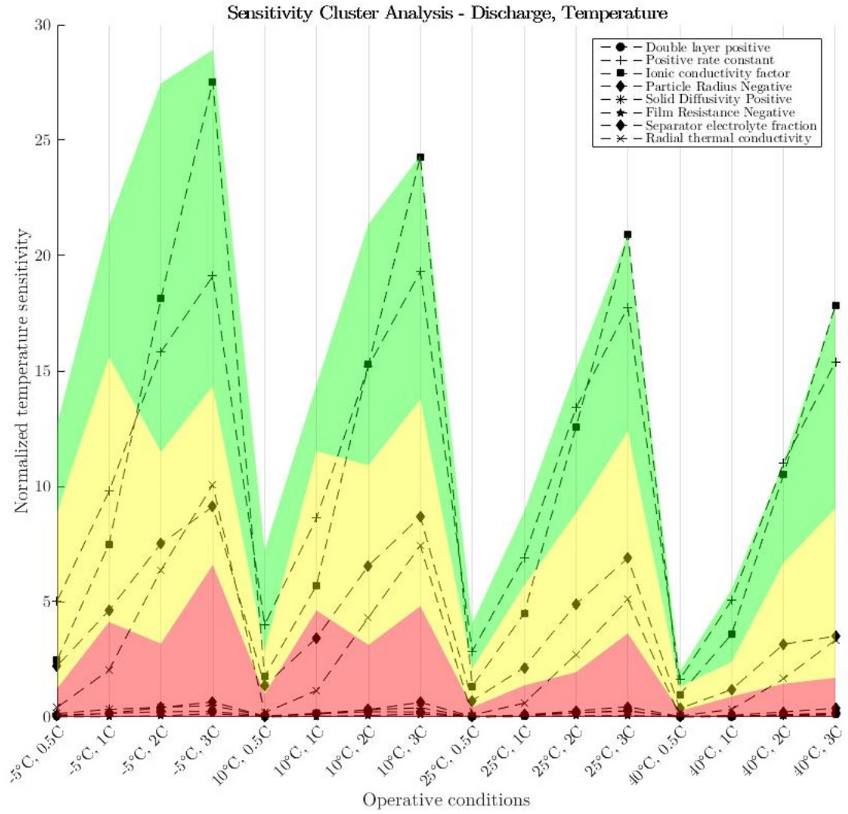

Figure 4.14: *Trend of* $\overline{SD}'_{y,j,i}$ *for the voltage and temperature outputs from the discharge curve at* 100% *SOC and* 100% *DOD, varying the ambient temperature and the current rate*

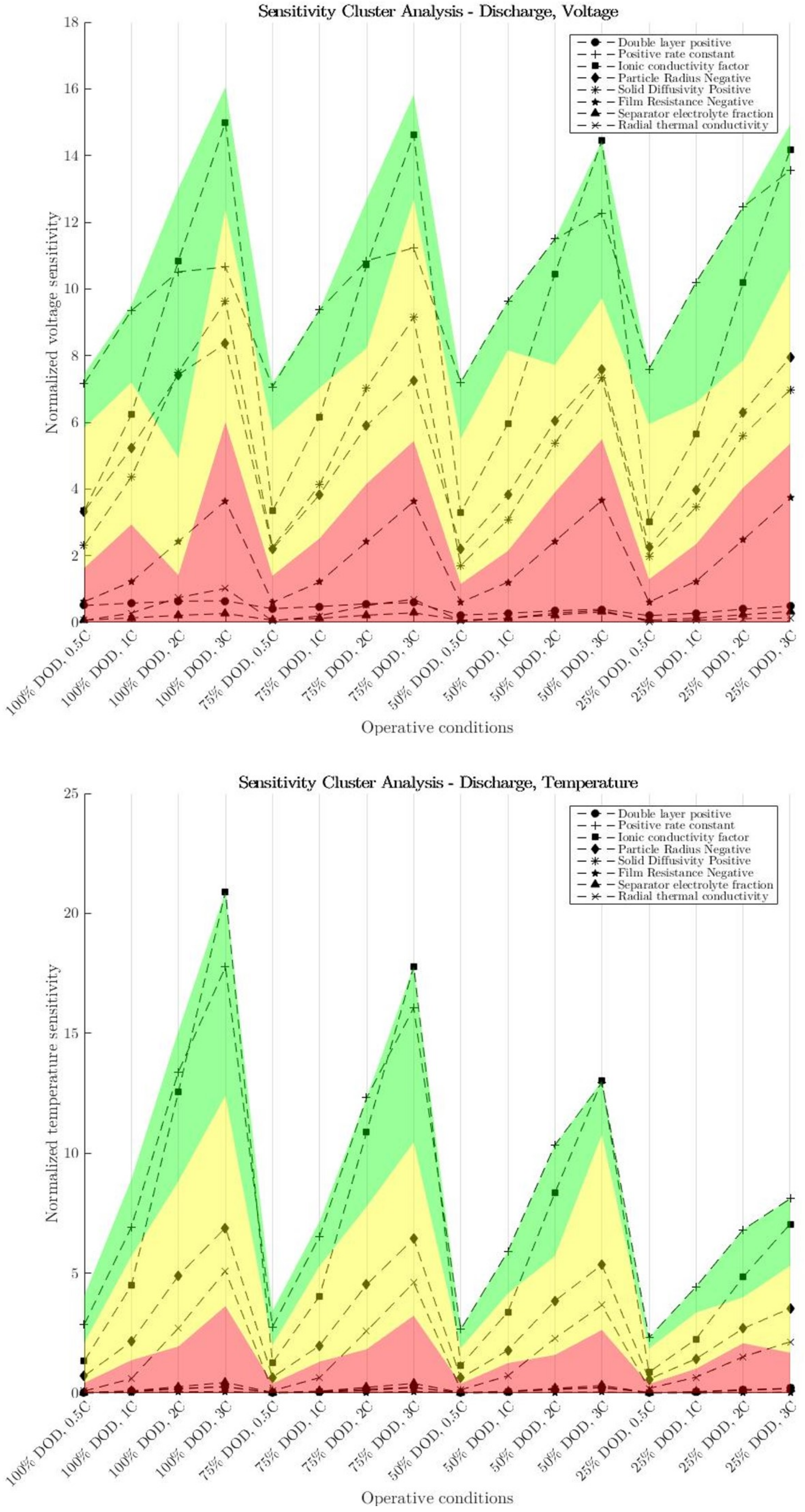

Figure 4.15: *Trend of* $\overline{SD}'_{y,j,i}$ *for the voltage and temperature outputs from the discharge curve at* 100% *SOC and* 25° *C, varying the depth of discharge and the current rate*

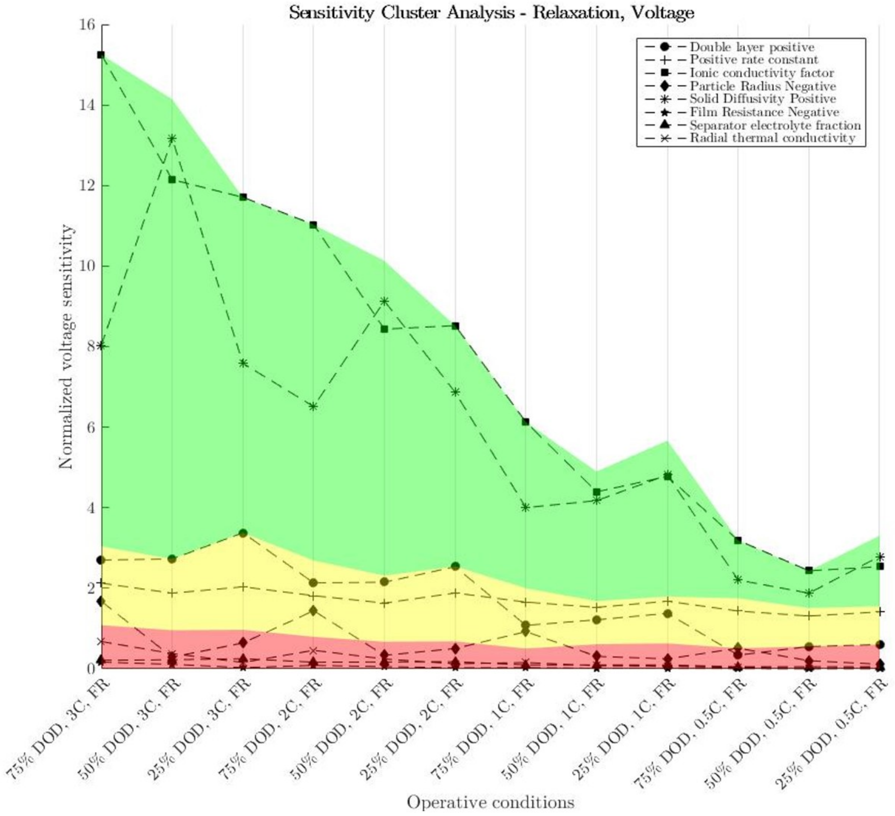

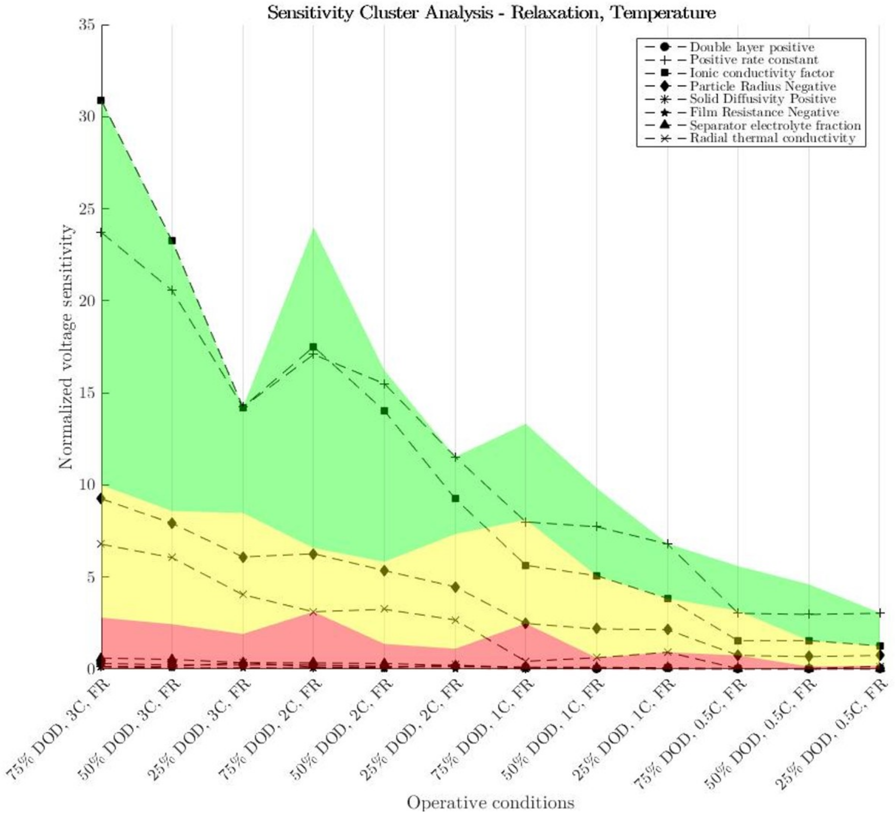

Figure 4.16: *Trend of* $\overline{SD}'_{y,j,i}$ *for the voltage and temperature outputs from the relaxation curve at* 100% SOC *and* $25°\,C$*, varying the depth of discharge and the current rate (fast relaxation)*

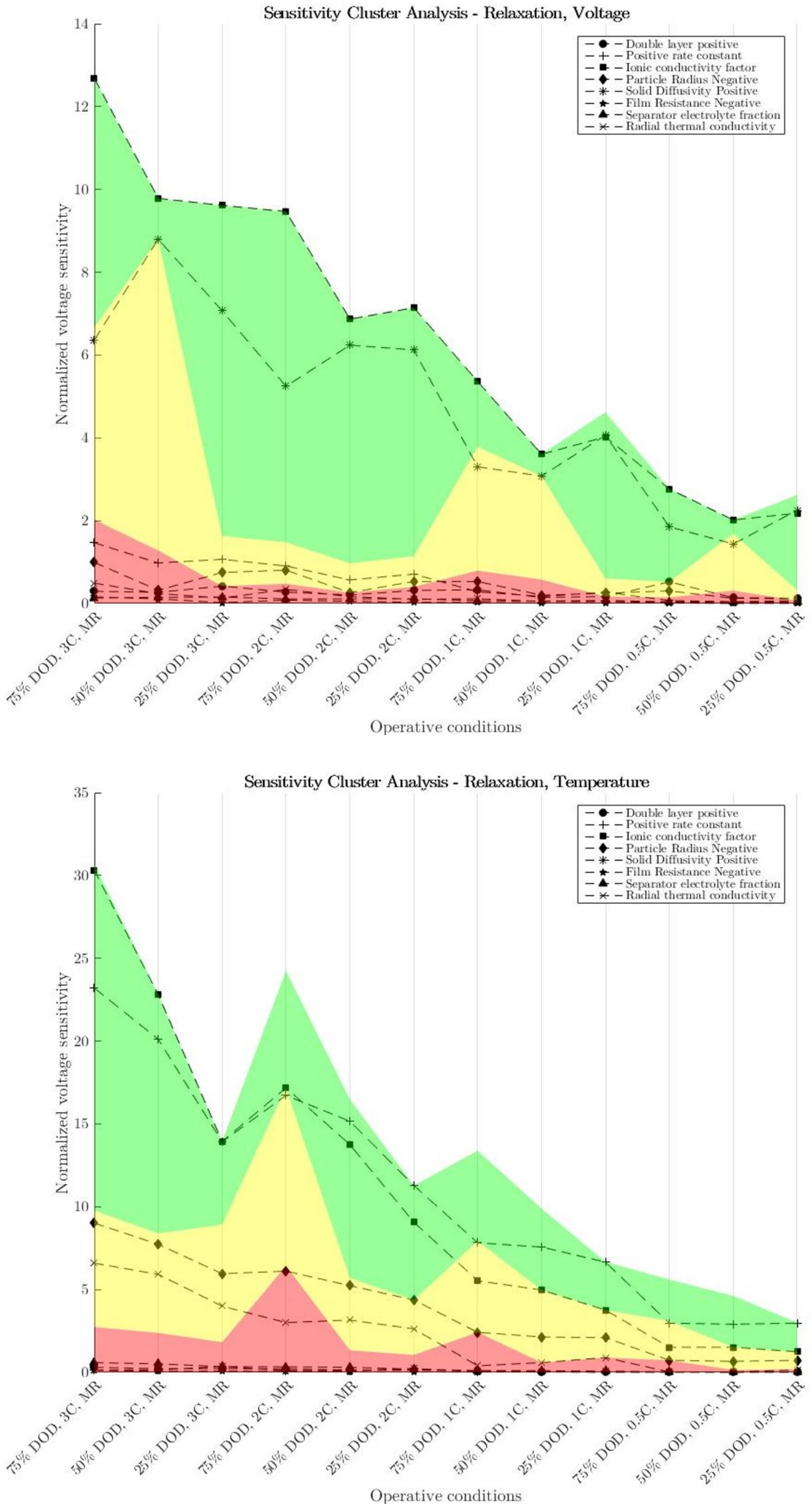

Figure 4.17: *Trend of* $\overline{SD}'_{y,j,i}$ *for the voltage and temperature outputs from the relaxation curve at* 100% *SOC and* 25° *C, varying the depth of discharge and the current rate (mid relaxation)*

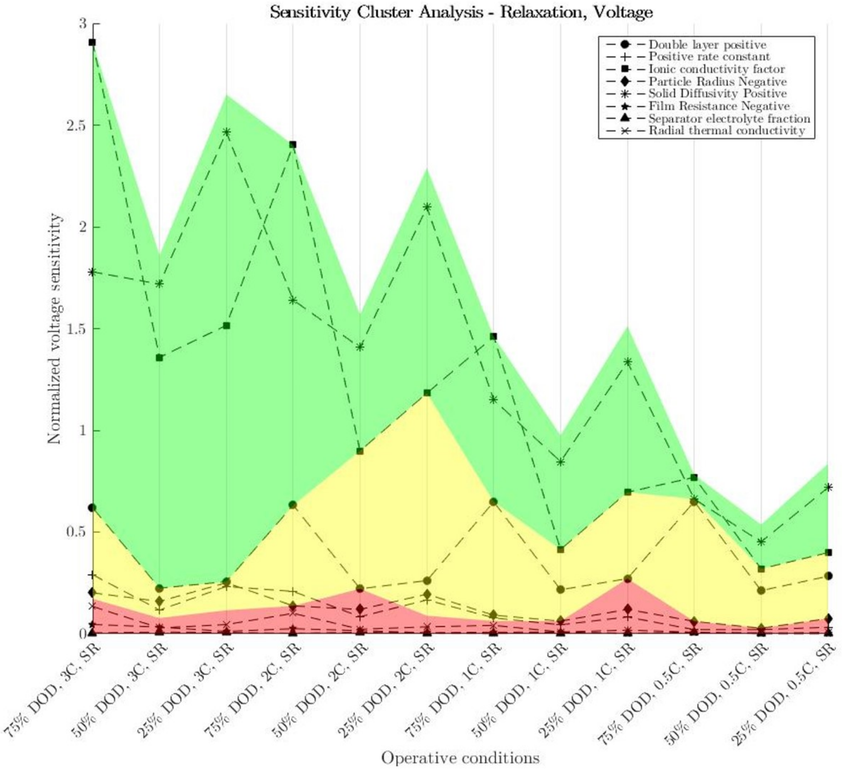

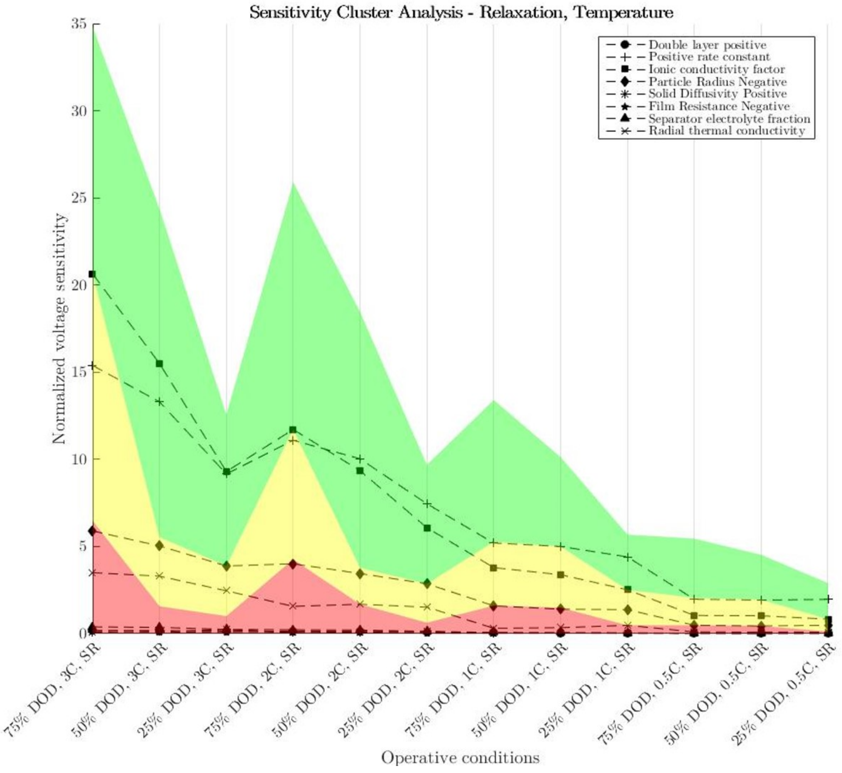

Figure 4.18: *Trend of* $\overline{SD}'_{y,j,i}$ *for the voltage and temperature outputs from the relaxation curve at* 100% *SOC and* 25° *C, varying the depth of discharge and the current rate (slow relaxation)*

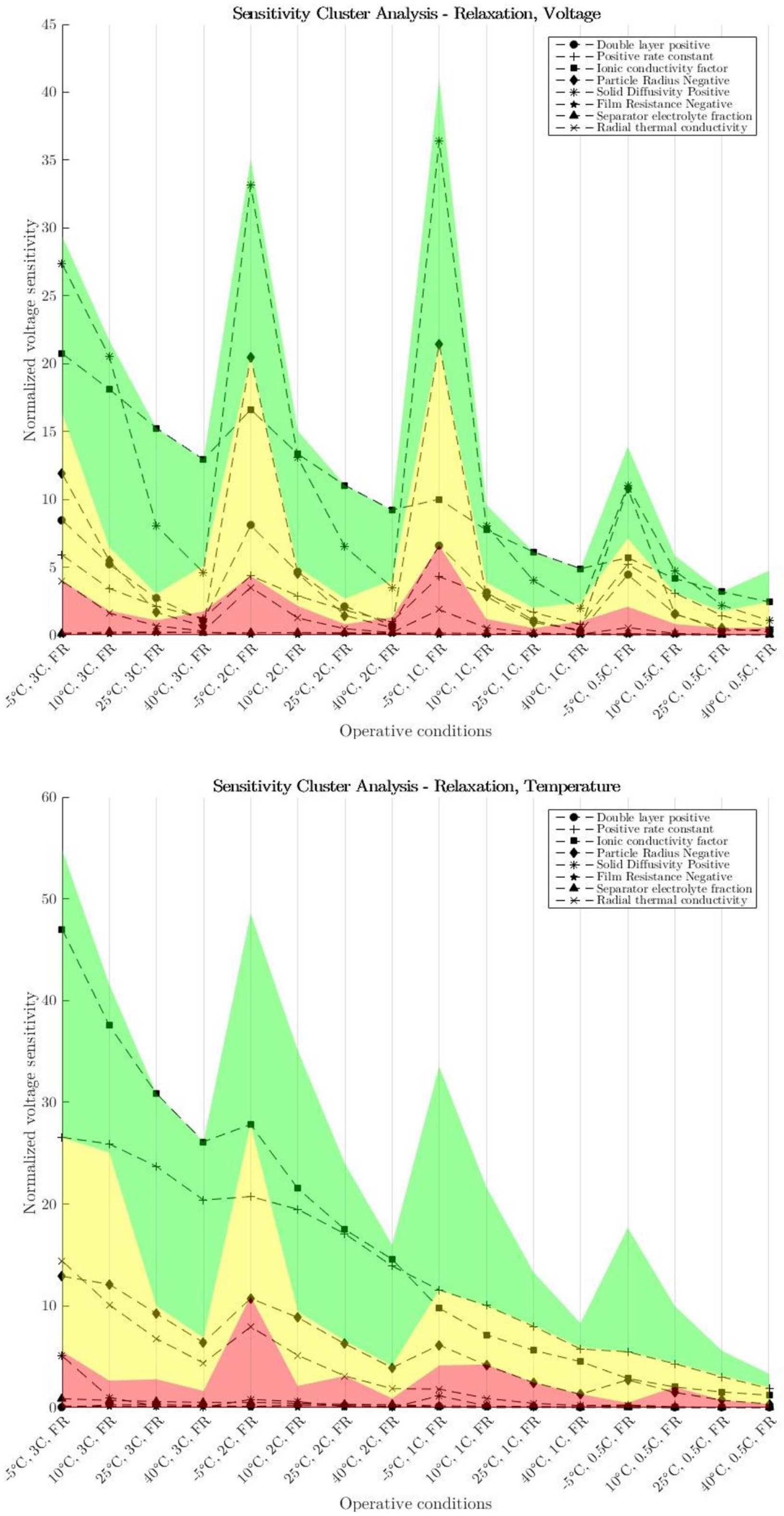

Figure 4.19: *Trend of* $\overline{SD}'_{y,j,i}$ *for the voltage and temperature outputs from the relaxation curve at* 100% *SOC and* 75° *C, varying the ambient temperature and the current rate (fast relaxation)*

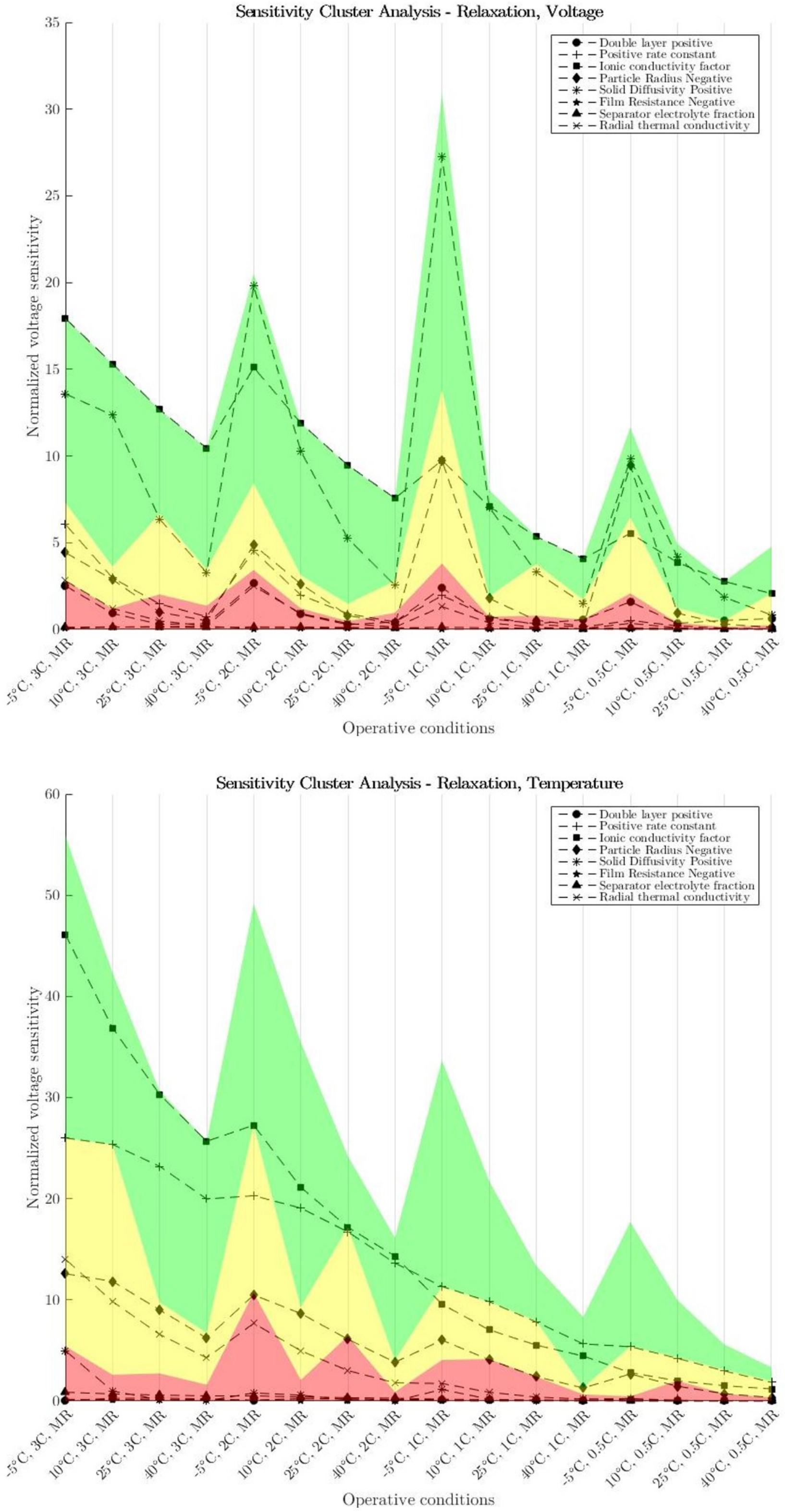

Figure 4.20: *Trend of* $\overline{SD}'_{y,j,i}$ *for the voltage and temperature outputs from the relaxation curve at* 100% SOC *and* $75°C$*, varying the ambient temperature and the current rate (mid relaxation)*

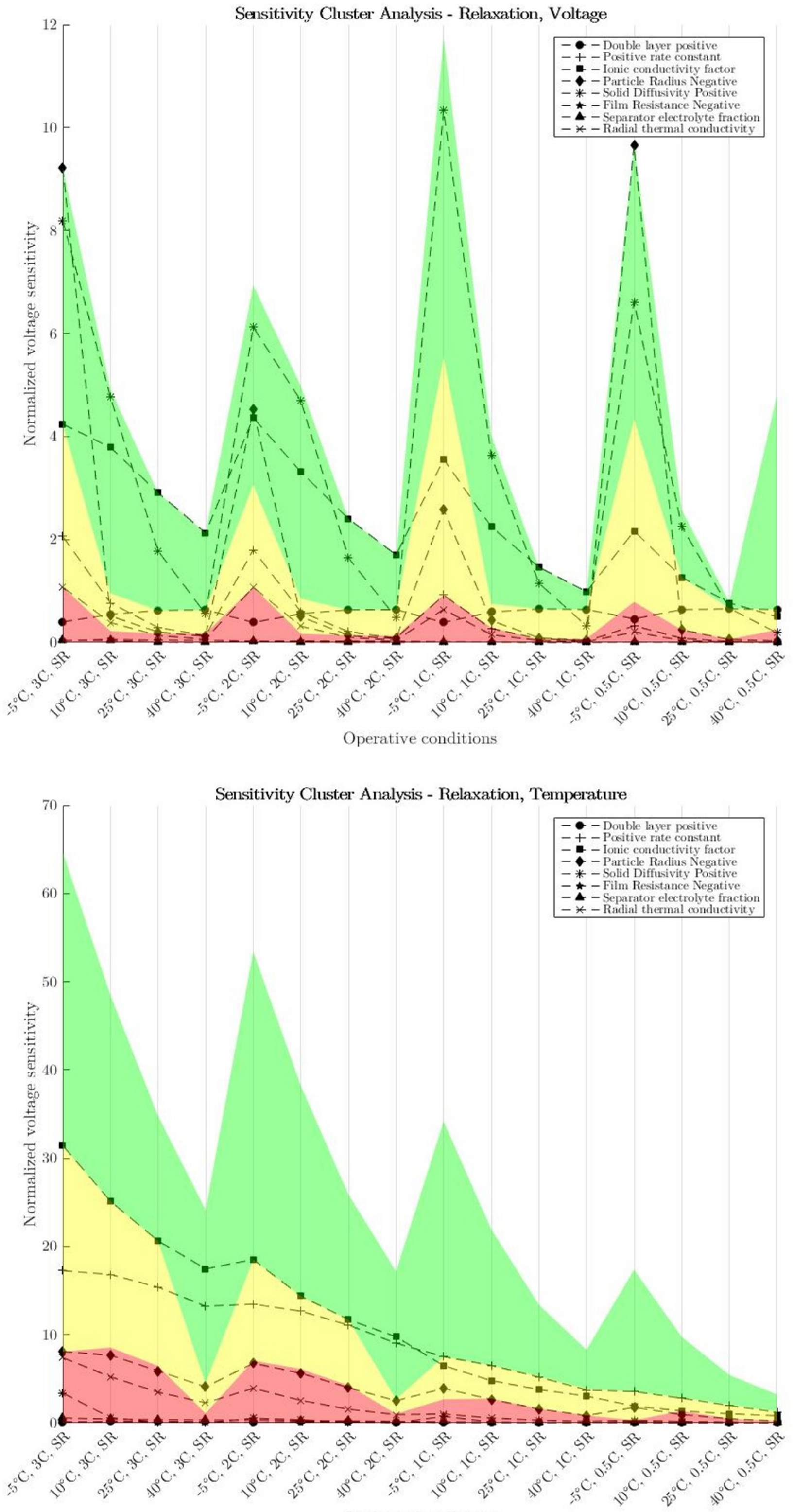

Figure 4.21: *Trend of* $\overline{SD}'_{y,j,i}$ *for the voltage and temperature outputs from the relaxation curve at* 100% *SOC and* 75° *C, varying the ambient temperature and the current rate (slow relaxation)*

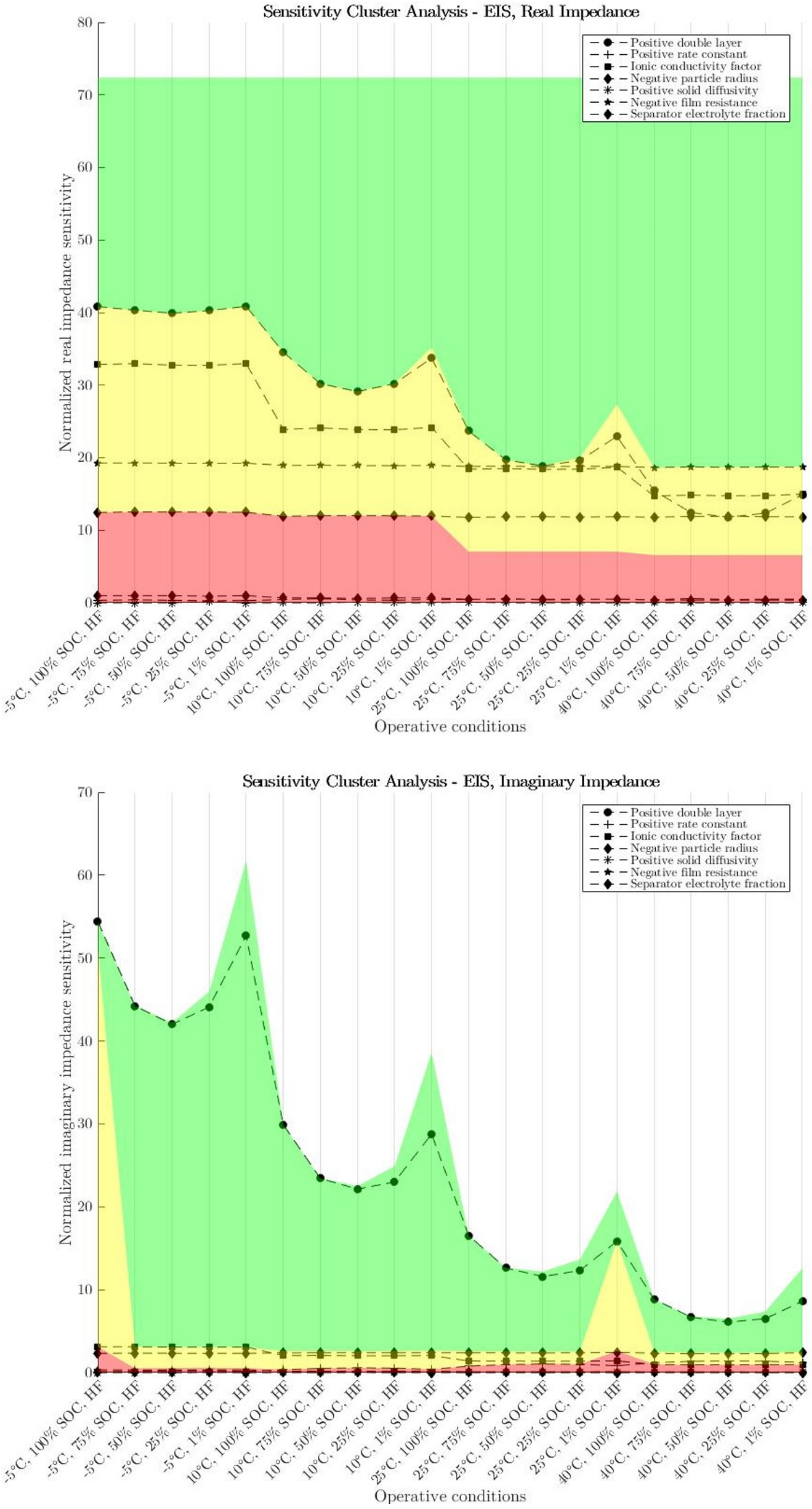

Figure 4.22: *Trend of* $\overline{SD}'_{y,j,i}$ *for the real and imaginary impedance outputs from the EIS, varying the ambient temperature and the state of charge (high frequency)*

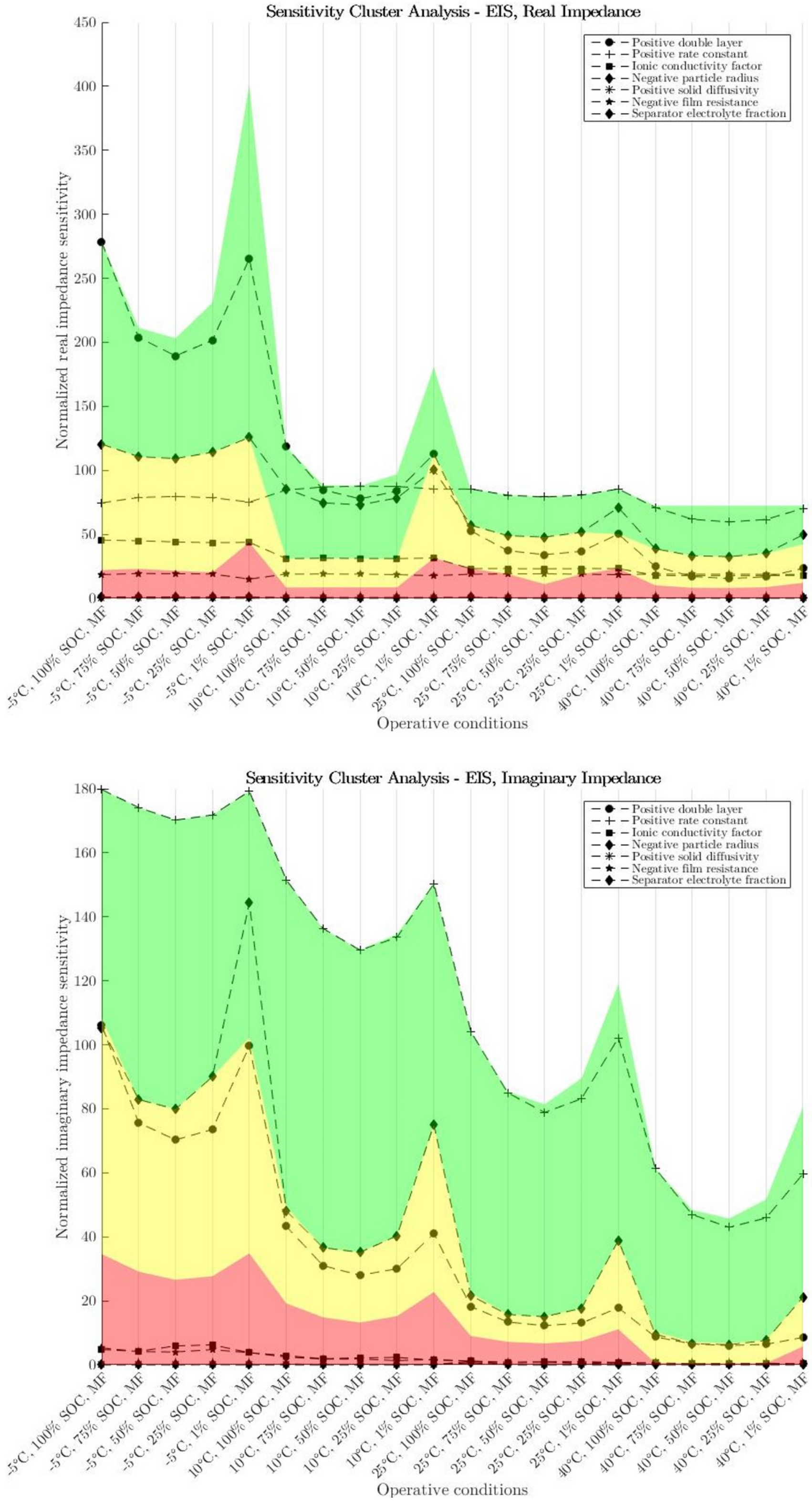

Figure 4.23: *Trend of* $\overline{SD}'_{y,j,i}$ *for the real and imaginary impedance outputs from the EIS, varying the ambient temperature and the state of charge (mid frequency)*

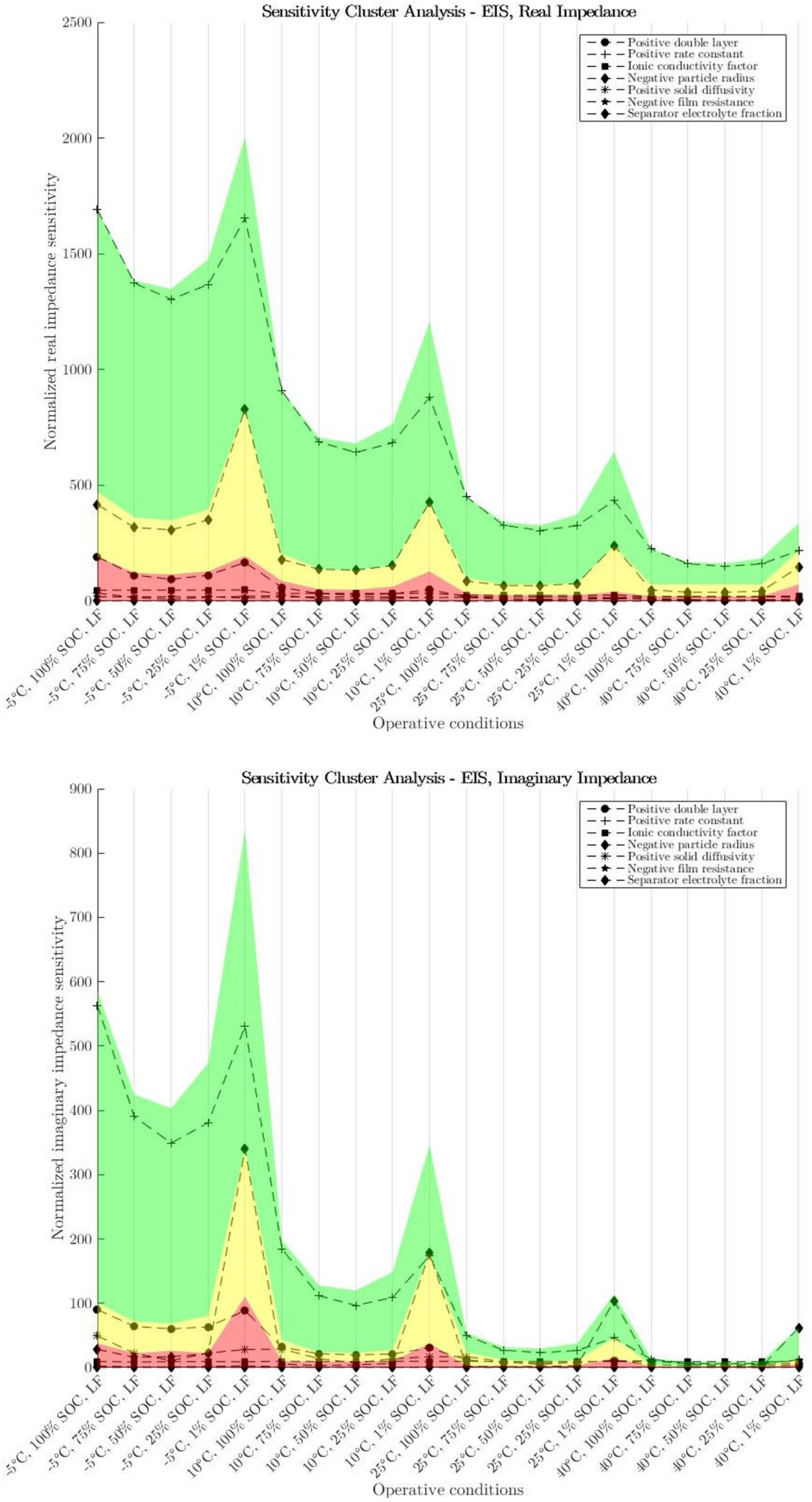

Figure 4.24: *Trend of* $\overline{SD}'_{y,j,i}$ *for the real and imaginary impedance outputs from the EIS, varying the ambient temperature and the state of charge (low frequency)*

4.3 Methodology formulation

By analyzing all the information obtained from the sensitivity analysis, it is possible to propose a diagnostic methodology that satisfies the requirements of completeness with respect to the identification of the model parameters and of low experimental time.

Our proposal is (figure 4.25):

1. after a sufficient rest time to ensure steady state, the impedance spectrum is measured with an **EIS** at 10°C and 100% SOC, in the 4000-1 Hz range with 20 logarithmically spaced frequencies and two sinusoids per frequency (time employed: around 2 minutes);

2. then, the battery is **discharged** for three quarters of its nominal capacity (75% DOD) with a current rate equal to $3C$ (time employed: around 15 minutes). The cell voltage and battery surface temperature are registered;

3. the current is set to zero and the battery **relaxation** process starts. The cell voltage and the battery surface temperature are measured for 1000 s, and then the ambient temperature is modified to 25°C. A certain amount of time has to be waited to allow the heating of the battery and to obtain a sufficiently homogeneous temperature profile. With the battery samples employed in this work, half an hour is sufficient for this purpose (time employed: around 45 minutes);

4. a second **EIS** is performed, at 25°C and 25% SOC, with the same frequency range and spacing of the first one (time employed: around 2 minutes);

5. the battery is **discharged** down to the minimum voltage limit with a 1C current rate and a theoretical 25% DOD, at 25°C and starting from 25% SOC (time employed: around 15 minutes).

The reasons that motivates this particular choice are:

- the EIS are meant to provide information about the parameters that define the vast majority of the ohmic and charge transfer overpotentials. Since the EIS separates the former from the latter, unlike the discharge curve, it is convenient to use this technique to efficiently obtain the maximum amount of useful information for the parameter identification. The EIS is stopped at 1 Hz, since around this frequency the diffusive processes start to influence the impedance spectrum. The impact of the diffusion on the impedance is quite small and not so accurately modeled, hence it is excluded from the methodology.
  For the ohmic overpotential, we include the negative film resistance R_{film}, the ionic conductivity factor FCE, and the positive solid conductivity σ_{pos} (high frequency). For the charge transfer overpotential, we have the rate constants k_p and k_n, and the particle radii $R_{p,p}$ and $R_{p,n}$ (mid frequency). The double layer capacitances $C_{dl,p}$ and $C_{dl,n}$ influences both the phenomena, by changing

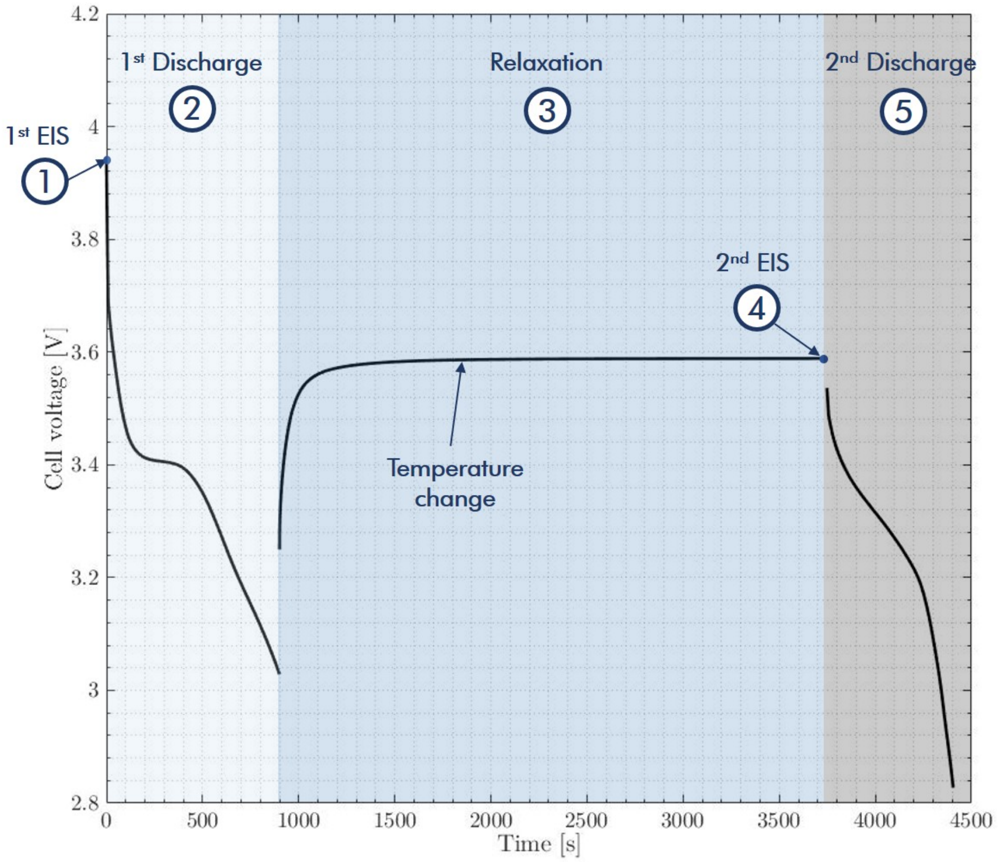

Figure 4.25: *Explanation of the proposed methodology, with the trend of the cell voltage in time*

the frequencies at which they occur.
The use of two ambient temperatures (10°C and 25°C) and two states of charge (100% SOC and 25% SOC) allow to include in the parameter identification process two very different operative conditions for the same output, i.e. the real and imaginary impedance of the battery. The variation of ambient temperature is useful to obtain the value of the positive and negative rate constant activation energies EA_{k_p} and EA_{k_n}, since they are the parameters that control the variation of the charge transfer resistance with the temperature. Then, as it was seen in chapter 3, differences in the impedance spectra can emerge at two distant state of charges, since the electrode are nearer to their concentration limits;

- the relaxation curve is measured for the fitting of the diffusion-related parameters, i.e. the lithium solid diffusion coefficient $D_{s,p}$ and $D_{s,n}$, the ionic conductivity factor FCE, and the particle radii R_p and R_n. Since we want to isolate as much as possible the effect of these parameters, only the slow relaxation part ($32.6\,s \leq t \leq 1000\,s$) of the cell voltage is used as fitting data, since only the diffusion processes are relevant in this part of the relaxation curve;

- the discharge curves are meant to be used in the fitting dataset as a way to fit all the model parameters, since with this technique is not trivial to separate their different effects on the battery voltage and temperature. Nevertheless, the two operative conditions in which the discharge curves are measured aim to maximize the information that are obtained. The one at 25°C, 25% SOC, 25% DOD and 1C is designed to limit the overpotentials, thanks to the low duration and to the relatively low employed current. Nevertheless, the low SOC region is approached, and the lithium solid diffusion coefficient in the negative electrode $D_{s,n}$ strongly influences the cell voltage, because of the high slope of the anode open circuit potential (see figure 1.4). Since in the relaxation curve most of the trend is dictated by the lithium solid diffusion coefficient in the cathode, this capacity test is a way to obtain useful data for the negative one. The discharge curve at 10°C, 100% SOC, 75% DOD and 3C has the purpose of fitting all the remaining parameters (ρ_{am}, C_{am}, $\varepsilon_{e,p}$, $\varepsilon_{e,n}$, $c_{e,0}$, t_0^+), since the sensitivities of the outputs are highly enhanced in this condition thanks to the low temperature, the high depth of discharge and the high current rate. Also, it serves as additional dataset for ones that already have a dedicated experiment. The two ambient temperatures are also useful to obtain the information about the positive and negative solid diffusion coefficient activation energies $EA_{D_{s,p}}$ and $EA_{D_{s,n}}$, which determine the variation of the solid diffusion coefficients with temperatures;

- the separator electrolyte fraction $\varepsilon_{e,sep}$, the positive film resistance $R_{film,p}$, the axial thermal conductivity $k_{T,ax,rad}$ and the negative solid conductivity $\sigma_{s,n}$ are not included in the analysis since the model outputs are found to be insensitive to a variation of the said parameters, as it can be read in the tables 4.3, 4.4, 4.5, 4.6, 4.7 and 4.8. Instead, as already explained the convective heat transfer coefficient h_{conv} and the external resistance R_{ext} are not fitted with these experimental data, but they are measured or estimated in other manners and fixed to the obtained value before the fitting process;

- it is important to notice that in the the proposed methodology we tried to minimize the required time for the experiments, by avoiding erratic conditions and by choosing tests that can be easily concatenated.

In the next chapter, we will use the data obtained from the described experimental methodology applied to one of the battery samples to fit the battery P2D model, by employing an optimization algorithm. In total, 22 model parameters will be considered in the fitting process.

Chapter 5

Calibration and validation

In this chapter, we will present the algorithm with which the fitting of experimental data was performed. Then, we will briefly discuss about the calibration of the algorithm for our specific problem. Finally, we will show the results of the fitting of the training experimental data obtained with the methodology defined in the previous chapter on the validation dataset.

5.1 Data fitting algorithm

The fitting of the results of a model to experimental data is an optimization problem, where the cost function is usually expressed as the sum of the squared difference between the corresponding points in the experimental data and in the model results. The minimum of the said function can be found with an optimization algorithm, which is chosen in accordance to the nature and the complexity of the considered model.
Being a mechanistic formulation, the P2D lithium-ion battery model has complex non-linear relations between the outputs (voltage, temperature and impedance) and the inputs (the model parameters). Moreover, it is not easy to guess an initial point that can be near to the cost function minimum, due to the high number of parameters and to the uncertainty about their actual value, that can span order of magnitudes in some cases.

By analyzing the literature that concerns the parameter identification of lithium-ion batteries, we see that the most commonly employed algorithms are the Levenberg–Marquardt Algorithm (LMA) [146, 148, 168], the Genetic Algorithm (GA) [147, 169, 170], and the Particle Swarm Optimization (PSO) [171–173]. The first one requires the gradient calculation, while the second and the third one are gradient-free techniques.
In this work, it was chosen to use the Particle Swarm Optimization algorithm, due to its simplicity of implementation and to its robustness with respect to the nature of the cost function. Nevertheless, the PSO does not assure that the global optimum is obtained, since it can also stop on a local optimum. The principle of this metaheuristic algorithm is based on the collaborative search of the function minimum by a set of possible inputs, i.e. the swarm.

Considering the iteration i of the algorithm, each input, i.e. the particle, is represented as a vector that contains all the model parameters, also called position P_i. Each component of the particle position $P_{i,k}$ is one of the model parameters. The particle position is given as input to the cost function, which is evaluated and its output is assigned to the particle. The particle position changes according to its velocity S_i, which is calculated as:

$$S_i = w \cdot S_{i-1} + c_1 \cdot rand(0,1) \cdot (P_i - P_{i,lb}) + c_2 \cdot rand(0,1) \cdot (P_i - P_{gb}) \tag{5.1}$$

where the parameters are:

- w is called inertia coefficient, and it multiplies the velocity of the previous iteration S_{i-1}. This parameter has the purpose of keeping the information about the previous iterations through the use of the damped preceding velocity;
- c_1 is the competitive velocity coefficient, multiplied by the difference between the current position P_i and the best local position $P_{i,lb}$, i.e. the position where the lowest output of the cost function for the considered particle was calculated. The velocity term linked to c_1 enhances the exploration of the solution space, by making the particles stay near the minimum they have found;
- c_2 is the collaborative velocity coefficient, multiplied by the difference between the current position P_i and the best global position P_{gb}, i.e. the position where the lowest output of the cost function among all the particles was calculated. The velocity term linked to c_2 enhances the exploitation of the best found position, by making the particles move towards the optimum.

The velocity S_i is then summed to the current position P_i to obtain the position of the subsequent iteration:

$$P_{i+1} = P_i + S_i \tag{5.2}$$

The velocity and the position are subject to limits, in order to avoid that the particle exits the valid solution space:

$$\begin{cases} if\ S_i < S_{min},\ S_i = S_{min} \\ if\ S_i > S_{max},\ S_i = S_{max} \end{cases} \begin{cases} if\ P_{i,k} < P_{k,min},\ P_{i,k} = P_{k,min} \\ if\ P_{i,k} > P_{k,max},\ P_{i,k} = P_{k,max} \end{cases}$$

At the first iteration, each particle is initialized with a random position and a random velocity, with which the cost function is evaluated to initialize the local and global best positions too.

The algorithm uses a certain number of particles N_p in each iteration: the higher this value, the better the exploration of the solution space, but the higher the number of needed cost function evaluation. Indicatively, 10 particles are needed for each component $P_{i,k}$ of the position, since by increasing the length of the input vector from n to $n+1$, the solution space changes from R^n to R^{n+1}.

The algorithm stops when a maximum number of iteration I_{max} is reached or when the value of the cost function is below a certain threshold E_{min}. The result of the PSO is the position of the particle with which the lowest output of the cost function

Table 5.1: *Range of the model parameters included in the fitting process*

Parameter	Anode	Separator/Electrolyte/Cell	Cathode
$C_{dl}\,[F\,m^{-2}]$	$0.02-50$	-	$0.02-50$
$k\,[m\,s^{-1}]$	$1\cdot10^{-10}-1\cdot10^{-8}$	-	$1\cdot10^{-10}-1\cdot10^{-8}$
$c_{e,0}\,[mol\,m^{-3}]$	-	$1000-1500$	-
$FCE\,[-]$	-	$0.1-1.5$	-
$t_0^+\,[-]$	-	$0.3-0.4$	-
$\sigma_s\,[S\,m^{-1}]$	1000 (assumed)	-	$1-10$
$R_p\,[m]$	$3\cdot10^{-6}-12.5\cdot10^{-6}$	-	$3\cdot10^{-6}-12.5\cdot10^{-6}$
$D_s\,[m^2\,s^{-1}]$	$5\cdot10^{-15}-5\cdot10^{-13}$	-	$1\cdot10^{-15}-1\cdot10^{-13}$
$R_{film}\,[\Omega\,m^2]$	$0.001-0.05$	-	0.0001 (assumed)
$\varepsilon_e\,[-]$	$0.325-0.425$	0.575 (assumed)	$0.325-0.425$
$EA_k\,[J\,mol^{-1}]$	$20000-80000$	-	$20000-80000$
$EA_D\,[J\,mol^{-1}]$	$20000-80000$	-	$20000-80000$
$\rho_{am}\,[kg\,m^{-3}]$	-	$2000-2750$	-
$C_{am}\,[J\,kg^{-1}\,K^{-1}]$	-	$800-1200$	-
$k_{T,rad,am}\,[W\,m^{-1}\,K^{-1}]$	-	$0.1-1$	-
$k_{T,ax,am}\,[W\,m^{-1}\,K^{-1}]$	-	30 (assumed)	-
$h_{conv}\,[W\,m^{-2}\,K^{-1}]$	-	17.5 (estimated)	-
$R_{ext}\,[\Omega\,m^2]$	-	$6.87\cdot10^{-4}$ (estimated)	-

was calculated. For what concerns this work, the shape of the cost function is described in section 5.1.1, while the validity range given to the model parameters included in the optimization is shown in table 5.1. Actually, these values are the ones that limit the position of the components of the input vector $P_{i,k}$.

The fixed model parameters are the same of the sensitivity analysis, and they can be found in table 4.2. In addition, five parameters that were included in the sensitivity analysis are considered constant in the fitting process, due to their irrelevance for the model outputs as observed from the sensitivity analysis ($\sigma_{s,n}$, $\varepsilon_{e,sep}$ and $k_{T,ax,am}$) or because they are external parameters that do not depend on the lithium-ion battery nature (R_{ext} and h_{conv}). Their value is taken from literature or estimated.

Finally, the PSO algorithm parameters are initialized with these values, based on the literature [174] and on the observed behavior of the algorithm with this specific problem:

- $w = 0.721$
- $c_1 = 1.665$
- $c_2 = 1.665$
- $N_p = 200$
- $I_{max} = 20$
- $E_{min} = 1\cdot10^{-4}$
- $S_{max} = 0.05\cdot(P_{k,max} - P_{k,min})$
- $S_{min} = -0.05\cdot(P_{k,max} - P_{k,min})$

Note that the maximum number of iterations is very low for a PSO algorithm, since this parameter is commonly two orders of magnitude higher than the one used in this work. This limit had to be set to obtain a reasonable computational time. Every simulation of the five experiments of the methodology takes $200 - 225$ s, and every iteration requires N_p simulations. Therefore, about nine days are needed for 20 full iterations. For sure, one of the future developments of this work will be the decrease of the computational time, by implementing a model order reduction and/or parallel computing.

5.1.1 Cost function

The cost function that we have to set in this optimization problem has to consider the difference between the experimental data that are used for the fitting process and the result that the model gives with the set of parameters corresponding to the position of the particle. In particular, the chosen measure is the root-mean-square error (RMSE) between the experimental data and the model data. Therefore, the cost function is expressed as:

$$CF = \sum_{j=1}^{N_f} \left(f_j \cdot \sqrt{\frac{1}{N_{d,j}} \cdot \sum_{i=1}^{N_{d,j}} \frac{(x_{i,j}^e - x_{i,j}^m)^2}{\overline{x}_j^e}} \right) \tag{5.3}$$

where:

- N_f is the number of experimental outputs used in the cost function, each one with an associated sub-cost function. Reminding the methodology defined in chapter 4, in our case we have five different experimental test, two discharge curves, a relaxation curve and two EIS. From the relaxation curve and the discharge curves we only use the measured cell voltage as experimental output. The reason behind the choice of not considering the battery surface temperature is that these data could have a quite low reliability, due to the contact resistance between the thermocouples and the batteries, and the exposure of the non-insulated thermocouples to the ambient air (see section 3.1.2). From each EIS we obtain the real and the imaginary impedance. Therefore, the number of experimental outputs is equal to 7;
- $N_{d,j}$ is the number of data points associated to the j^{th} output. The discharge curves are divided into 100 points, the relaxation curve has 45 points, while for the two EIS we take only 8 points for the real and the imaginary impedance. The reason behind this low number of used points is the high amount of time needed by the model to simulate the EIS, which is the bottleneck of the overall simulation time. Since the outputs have a different number of data points, the sub-cost function are divided by $N_{d,j}$ to avoid a bias towards the sub-cost functions with an higher number of data points;
- f_j is a weight factor for the sub-cost function of the j^{th} output. These weights are empirically determined, and they have the purpose of giving the same relative weight to all the sub-cost functions, avoiding a bias due to the typical values of the j^{th} experimental data;

- $x^e_{i,j}$ and $x^m_{i,j}$ are respectively the i^{th} data point of the experimental data and of the model data of the j^{th} output;

- $\overline{x}^e_j$ is the mean of the experimental data vector of the j^{th} output. Not all the sub-cost function have the same unit of measure, since they are related to different outputs, and they could not be summed together. Therefore, the mean value of the j^{th} experimental data vector (equal in every algorithm iteration) is used to nondimensionalize the j^{th} sub-cost function.

5.2 Simulated datasets

Prior to the fitting of experimental data, we perform the tuning of the data fitting algorithm, to confirm the capability of the said algorithm of obtaining an accurate result for what concerns the values of the model parameters. For this purpose, we use two simulated training datasets with two different sets of model parameters. Each set of parameters is given as input to the model, and the five experimental tests of the formulated methodology are simulated. Then, the outputs of the simulation of these tests are used as fictitious experimental data in the cost function, and the PSO is employed to obtain a set of parameters that can reproduce the said dataset.
The main objective of these algorithm tests is to understand whether it is possible to find a set of parameters that not only reproduces well the experimental dataset, but that represents the correct values of the model parameters too. This aspect is very important for the purpose of this work: a wrong set of parameters could bring to a satisfactory experimental data fitting thanks to the particular combination of the said wrong parameters, that at the end has the same effects on the model outputs of the correct set of parameters.

The results of the fitting of the simulated datasets are shown in table 5.2, where the real values of the parameters are contrasted with the values obtained with the fitting by the algorithm. The important things to notice are that:

- the values of the particle radii $R_{p,p}$ and $R_{p,n}$ during the two fitting processes are fixed to the correct numbers. The reason for this choice is that, without using the right values for the particle radii, the experimental data are fitted with a wrong parameter set. In fact, the particle radius is a parameter that in the P2D model is linked to all the overpotentials of the lithium-ion battery, because it defines the specific active area of the battery (see equation 2.27) determining the charge transfer overpotential, and it has quadratic relationship with the characteristic diffusion time in the solid (see equation 2.3). Moreover, the presence of a significant film resistance $R_{film,n}$ on the negative electrode means that the negative particle radius $R_{p,n}$ influences the ohmic overpotential, too. During the fitting process, all the combinations between the values of the other parameters that are included in the definition of these overpotentials, such as the rate constants k and the lithium diffusion coefficients in the solid D_s, and the particle radii that give a satisfactory fit of the experimental data are considered as good "candidates" for the parameter

	Simulated dataset 1			**Simulated dataset 2**		
Parameter	Real value	Fitted value	Difference	Real value	Fitted value	Difference
$C_{dl,p}\,[F\,m^{-2}]$	2.000	2.016	0.79%	0.800	1.604	100.49%
$C_{dl,n}\,[F\,m^{-2}]$	0.25	0.2503	0.10%	1.2	0.5426	54.79%
$k_p\,[m\,s^{-1}]$	$8.25 \cdot 10^{-10}$	$7.72 \cdot 10^{-10}$	6.42%	$5.25 \cdot 10^{-9}$	$7.50 \cdot 10^{-9}$	42.95%
$k_n\,[m\,s^{-1}]$	$1.50 \cdot 10^{-9}$	$1.38 \cdot 10^{-9}$	7.92%	$3.50 \cdot 10^{-9}$	$2.52 \cdot 10^{-9}$	42.95%
$c_{e,0}\,[mol\,m^{-3}]$	1150	1310	13.91%	1350	1285	4.81%
$FCE\,[-]$	1.150	0.891	22.51%	0.550	0.639	16.17%
$t_0^+\,[-]$	0.325	0.347	6.73%	0.39	0.300	23.04%
$\sigma_p\,[S\,m^{-1}]$	2.5	1.371	45.17%	9.5	9.783	2.98%
$R_{p,p}\,[m]$	9.25	9.25[a]	-	5.7	5.7[a]	-
$R_{p,n}\,[m]$	4.5	4.5[a]	-	4.2	4.2[a]	-
$D_{s,p}\,[m^2\,s]$	$2.56 \cdot 10^{-14}$	$2.94 \cdot 10^{-14}$	14.89%	$8.50 \cdot 10^{-15}$	$7.26 \cdot 10^{-15}$	10.26%
$D_{s,n}\,[m^2\,s]$	$1.60 \cdot 10^{-13}$	$9.40 \cdot 10^{-14}$	41.26%	$7.00 \cdot 10^{-14}$	$3.71 \cdot 10^{-13}$	430.29%
$R_{film,n}\,[\Omega\,m^2]$	$6.75 \cdot 10^{-3}$	$5.224 \cdot 10^{-3}$	22.61%	$3.25 \cdot 10^{-3}$	$5.21 \cdot 10^{-3}$	60.30%
$\varepsilon_{e,p}\,[-]$	0.390	0.332	14.99%	0.360	0.373	3.52%
$\varepsilon_{e,neg}\,[-]$	0.360	0.353	1.96%	0.32	0.411	28.54%
$EA_{k_p}\,[J\,mol^{-1}]$	53500	37716	29.50%	53000	59572	12.40%
$EA_{k_n}\,[J\,mol^{-1}]$	55500	58049	4.59%	47000	33314	29.12%
$EA_{D_{s,p}}\,[J\,mol^{-1}]$	28900	31922	10.46%	41500	35078	15.47%
$EA_{D_{s,n}}\,[J\,mol^{-1}]$	35600	47116	32.35%	33300	46572	39.86%
$\rho_{am}\,[kg\,m^{-3}]$	2130	2334	9.58%	2120	2488	17.36%
$C_{am}\,[J\,kg^{-1}\,K^{-1}]$	1120	1180	5.36%	930	886	4.73%
$k_{T,rad,am}\,[W\,m^{-1}\,K^{-1}]$	0.165	0.250	51.58%	0.125	0.103	23.04%

[a] fixed value

Table 5.2: *Results of the fitting of the simulated datasets*

set that minimizes the cost function. Therefore, it is likely that the parameter set obtained at the end of the PSO does not represent the real value of the battery parameters, but it is only a combination that gives the same outputs. To solve this problem, it was chosen to fix the values of the particle radii, because they are quantities that govern to all the phenomena of the battery. Also, they are a geometric measurable quantity with appropriate techniques as laser diffraction [150], or they can be provided by the battery manufacturer;

- both the sets of parameters found by the algorithm fit well the simulated datasets, but only the one associated to the simulated dataset 1 is similar to the real model parameters.
  The simulated dataset 1 represents a battery whose electrodes have very different properties, with the positive one that has a charge transfer resistance about four times higher than the negative one, and the frequency range in which the charge transfer resistance is present in the impedance spectrum is lower for the positive electrode, due to the much higher double layer capacitance C_{dl}.
  Instead, the simulated dataset 2 represents a battery whose electrodes show similar properties, with almost equal double layer capacitances. In this situation, the fitting parameter set does not represent the real one in a satisfactory way.
  The better performance of the fitting algorithm with the simulated dataset 1 can be explained by the great difference between the properties of the anode and of the cathode, which implies that it is hard to find a combination

of wrong model parameters that can fit well the dataset. On the contrary, the fitting algorithm performed worse on the simulated dataset 2, probably because of the similarity between the electrodes;

- the parameters that are linked to the high frequency resistance of the battery, i.e. the ionic factor conductivity FCE, the positive solid conductivity $\sigma_{s,p}$ and the negative film resistance $R_{film,n}$ show differences between the real values and the fitted values in the $20-60\%$ range. These moderate/high differences are due to the fact that their overall effect on the HFR can be obtained with a variety of combinations of these three parameters, which can bring to wrong estimate. Since the negative film resistance is an important parameter for the degradation identification, linked to the SEI growth, it is necessary to have a quite accurate estimate. Possible solutions are the fitting of all the coefficients of the ionic conductivity correlation with concentration and temperature (see equation 2.44), and the use of a correlation also for the positive solid conductivity [175], in order to improve the quality of the estimate of these two parameters;

- the lithium diffusion coefficient in the negative electrode $D_{s,n}$ and its related activation energy $EA_{D_{s,n}}$ are not fitted well in both the simulated datasets probably because the diffusion in the anode is not a limiting condition for the battery with these sets of parameters, and hence the output of the model are not affected in a significant way by these parameters. By comparing the characteristic times of diffusion in the electrodes, we can see how the diffusion in the cathode is much more limiting, determining the trend of the cell voltage. In fact, $D_{s,p}$ and $EA_{D_{s,p}}$ are fitted in a satisfactory way.

$$\begin{cases} \tau_{D_{s,p,1}} = \frac{(9.25\cdot 10^{-6})^2}{2.56\cdot 10^{-14}} = 3342\,s \\ \\ \tau_{D_{s,n,1}} = \frac{(4.5\cdot 10^{-6})^2}{1.60\cdot 10^{-13}} = 126\,s \end{cases} \quad \begin{cases} \tau_{D_{s,p,2}} = \frac{(5.7\cdot 10^{-6})^2}{8.50\cdot 10^{-15}} = 3822\,s \\ \\ \tau_{D_{s,n,2}} = \frac{(4.2\cdot 10^{-6})^2}{7.00\cdot 10^{-14}} = 252\,s \end{cases}$$

- the parameters that were classified as "low sensitive" in the sensitivity analysis (t_0^+, $c_{e,0}$, $\varepsilon_{e,p}$, $\varepsilon_{e,n}$, ρ_{am}, C_{am} and $k_{T,rad,am}$) can have a quite high difference between the fitted value and the real value, because the lower sensitivity of the model output to the value of the said parameters.

The information obtained by this calibration step will be very useful to critically analyze the results of the fitting of the real experimental data, and for the future development of the battery diagnostic procedure.

5.3 Experimental dataset

The final step of this work is the use of an experimental dataset in the fitting algorithm as training dataset, to understand if it is possible to find a set of parameters that reproduces the behavior of the battery only using the data obtained with the proposed methodology.

The five tests (see Chapter 4.3) are performed on the new high-power US26650VT battery. Because of extraordinary reasons, it was not possible to make the second discharge curve from 25% SOC at 1C and 25°C, as well as the EIS at 25% SOC and 25°C. Therefore, the experimental dataset is completed with a discharge curve from 25% SOC at 0.5C and 40°C, and a EIS at 25% SOC and 40°C. They were performed on the same battery few days before the other three tests (EIS at 100% SOC and 10°C, discharge curve from 100% SOC to 25% SOC at $3C$ and 10°C, and relaxation test for 1000 s after the discharge), and they are quite similar to the tests planned in the methodology, although not so optimal.

Instead, the validation dataset includes:

- four complete discharge curves from 100% to the lower voltage limit at 25°C, with four current rates: 0.5C, 1C, 2C and 3C;
- three complete discharge curves from 100% to the lower voltage limit at 0.5C, with three ambient temperatures: 10°C, 25°C and 40°C;
- three complete discharge curves from 100% to the lower voltage limit at 3C, with three ambient temperatures: 10°C, 25°C and 40°C;
- four relaxation curves from 0.5 s to 1000 s, after four concatenated discharge pulses at 0.2C, 10°C and 20% DOD: $100-80\%$ SOC, $80-60\%$ SOC, $60-40\%$ SOC and $40-20\%$ SOC;
- four relaxation curves from 0.5 s to 1000 s, after four concatenated discharge pulses at 3C, 40°C and 20% DOD: $100-80\%$ SOC, $80-60\%$ SOC, $60-40\%$ SOC and $40-20\%$ SOC;
- three impedance spectra from 10000 Hz to 0.05 Hz with 40 logarithmically spaced points, at 25°C and three states of charge: 100% SOC, 60% SOC, 20% SOC;
- three impedance spectra from 10000 Hz to 0.05 Hz with 40 logarithmically spaced points, at 60% SOC and ambient temperatures: 10°C, 25°C and 40°C.

These experimental data on the new US26650VT battery were collected during the experimental campaign described in Chapter 3. We choose these tests because they show different operative conditions from the ones of the training dataset, and they can highlight both the strengths and the limits of the obtained set of model parameters.

5.3.1 Results

The set of fitted parameters is reported in table 5.3. The comparison between the experiments and the model on training dataset, with the tests of the proposed methodology, is shown from figure 5.1 to 5.5. Instead, it is possible to see the comparison between the experiments and the model in the validation dataset from figure 5.6 to 5.12. The root mean square error is used as a measure of the average

Table 5.3: *Set of parameters obtained from the fitting of experimental data*

Parameter	Anode	Separator/Electrolyte/Cell	Cathode
$C_{dl}\,[F\,m^{-2}]$	0.244	-	1.536
$k\,[m\,s^{-1}]$	$9.793 \cdot 10^{-10}$	-	$5.985 \cdot 10^{-10}$
$c_{e,0}\,[mol\,m^{-3}]$	-	1302	-
$FCE\,[-]$	-	0.167	-
$t_0^+\,[-]$	-	0.365	-
$\sigma_s\,[S\,m^{-1}]$	1000 (assumed)	-	2.669
$R_p\,[m]$	$10.67 \cdot 10^{-6}$	-	$5.753 \cdot 10^{-6}$
$D_s\,[m]$	$1.624 \cdot 10^{-14}$	-	$3.717 \cdot 10^{-15}$
$R_{film}\,[\Omega\,m^2]$	$7.808 \cdot 10^{-3}$	-	0.0001 (assumed)
$\varepsilon_e\,[-]$	0.361	0.575 (assumed)	0.3714
$EA_k\,[J\,mol^{-1}]$	56213	-	41182
$EA_{D_s}\,[J\,mol^{-1}]$	38521	-	32251
$\rho_{am}\,[kg\,m^{-3}]$	-	2225	-
$C_{am}\,[J\,kg^{-1}\,K^{-1}]$	-	886.5	-
$k_{T,rad,am}\,[W\,m^{-1}\,K^{-1}]$	-	0.1762	-
$k_{T,ax,am}\,[W\,m^{-1}\,K^{-1}]$	-	30 (assumed)	-
$h_{conv}\,[W\,m^{-2}\,K^{-1}]$	-	17.5 (estimated)	-
$R_{ext}\,[\Omega\,m^2]$	-	$6.87 \cdot 10^{-4}$ (estimated)	-

distance between the results of the model and the real data. The root mean square error $RMSE_j$ between the two curves of each output j is calculated as:

$$RMSE_j = \sqrt{\frac{1}{N_{d,j}} \sum_{i=1}^{N_{d,j}} \left(x_{i,j}^{e} - x_{i,j}^{m} \right)^2} \tag{5.4}$$

As far as the author's knowledge, in the literature concerning the parameter identification made with the P2D physical model, the reported root-mean-square errors are only related to discharge curves. In the works on the EIS impedance spectra, only equivalent circuits are employed, while we have not found papers that focus on the relaxation curves.

Zhang et al. [147] reported RMSEs between 8 and 24 mV for discharge curves between 0.5C and $2C$ at 30°C, and between 20 and 37 mV for discharge curves between 0.5C and $2C$ at 15°C, on $LiCoO_2$ batteries. Park et al. [168] obtained RMSEs of 11.8 mV and 25.5 mV, respectively for a 0.5C and 1C discharge at 25°C, with a NCA battery. Li et al. [169] worked on a LMO battery, achieving RMSEs between 6.4 mV and 12.9 mV for discharge curves between 0.5C and 3C, at 25°C. Yang et al. [173] reported RMSEs of 15.6 mV and 21.6 mV, respectively for a 1C and a 2C discharge curve, at 25°C, with a NMC battery.

For what concerns the training dataset, we can observe that:

- there is a good accordance between experiments and model for the 3C, 10°C discharge of figure 5.1, with a RMSE of 36.7 mV. The voltage plateau of the curve between 200 and 600 mAh is due to the progressive heating of the battery, that locally benefits from the higher temperature in terms of lower overpotentials. The model reproduces well this complex behavior, thanks to the introduced coupling between the electrochemical and the thermal behaviors;

- the discharge curve at 0.5C, 40°C shows a quite high RMSE (44.0 mV) for such a low current test. Since the model and the experiment curves of figure 5.2 seems to be vertically shifted, we suppose that their difference is due to a non-optimal thermodynamic fitting, i.e. the open circuit potential curves of the electrodes implemented in the model could be improved. This part of the model is based on experimental data, but it has not been fitted like the parameters that determine the dynamic behavior, hence it shows a lower accuracy;

- the relaxation curve of figure 5.3, made after the discharge of figure 5.1, has an RMSE of 40.1 mV, mostly due to the difference in the reached OCV between the experiment and the model, a fact that can be attributed again to the non-optimal thermodynamic behavior. Nevertheless, the dynamics of the relaxation is reproduced well in the considered time frame, which suggest a correct estimation of the diffusion-related phenomena;

- the EIS impedance spectrum of figure 5.4 is performed at 10°C and 100% SOC. The RMSE of the real impedance is 5.61 mΩ, while the one of the imaginary impedance is 1.91 mΩ. At high frequency, on the left part of the chart, the experimental curve shows a lower slope than the model one. This almost 45° linear slope on the experimental data is attributed to the presence of a distribution of particle sizes in the electrodes [108], instead of a single characteristic particle size like in our model. In fact, the model is not able to reproduce such a low slope in any combination, and hence the best approximation is a more circular shape of this trait. This mismatching and an overall higher frequency of the model impedance lead to a moderate RMSE of the real part, while the imaginary part shows a good accordance;

- lastly, the impedance spectrum of figure 5.5, made at 40°C and 25% SOC, has a real impedance RMSE of 0.712 mΩ, and an imaginary impedance RMSE of 0.470 mΩ. The shift in the HFR is probably due to the non-optimal correlation between the ionic conductivity and the battery temperature. With such a low FCE parameter, (see table 5.3), the relative impact of the the ionic conductivity on the HFR is quite high, and the variation of this model parameter with temperature is not a fitted characteristic, but it is obtained from an empirical correlation (see equation 2.44). At low frequency, the experimental data show higher value of real and imaginary impedance, due to the occurrence of the second semicircle at low SOC that was described in Chapter 3.2.3 [110, 136]. This complex behavior is not well reproduced by the model, partly because of the non-optimal thermodynamic behavior, but mostly because the exchange current density relation with the SOC of equation 2.17, which does not take into account such a non-linear behavior of the cathode material.

The performance on the validation dataset is summarized in table 5.4, where the

Technique	Operative condition	RMSE
Discharge curve	0.5C, 25°C, 100 – 0% SOC	20.6 mV
	1C, 25°C, 100 – 0% SOC	20.3 mV
	2C, 25°C, 100 – 0% SOC	18.3 mV
	3C, 25°C, 100 – 0% SOC	26.6 mV
	0.5C, 10°C, 100 – 0% SOC	37.8 mV
	0.5C, 40°C, 100 – 0% SOC	22.9 mV
	3C, 10°C, 100 – 0% SOC	60.5 mV
	3C, 40°C, 100 – 0% SOC	30.9 mV
Relaxation test	0.2C, 10°C, 100 – 80% SOC	6.5 mV
	0.2C, 10°C, 80 – 60% SOC	12.0 mV
	0.2C, 10°C, 60 – 40% SOC	17.1 mV
	0.2C, 10°C, 40 – 20% SOC	11.6 mV
	3C, 40°C, 100 – 80% SOC	18.6 mV
	3C, 40°C, 80 – 60% SOC	28.8 mV
	3C, 40°C, 60 – 40% SOC	35.7 mV
	3C, 40°C, 40 – 20% SOC	38.8 mV
EIS	25°C, 100% SOC	Z_R: 1.28 mΩ Z_I: 1.43 mΩ
	25°C, 60% SOC	Z_R: 1.27 mΩ Z_I: 0.606 mΩ
	25°C, 20% SOC	Z_R: 2.69 mΩ Z_I: 1.00 mΩ
	40°C, 60% SOC	Z_R: 0.501 mΩ Z_I: 0.313 mΩ
	10°C, 60% SOC	Z_R: 8.54 mΩ Z_I: 1.95 mΩ

Table 5.4: *Summary of the RMSE between the model data and the experimental data in the validation dataset*

RMSEs of all the comparisons between model and experiments are reported. Some general consideration that can be made are:

- the results on the discharge curves (figures 5.6, 5.7 and 5.8) are satisfying, with RMSEs on the voltage that are aligned with the literature values. The best performances are shown at 25°C, a temperature that is not included in the provided training dataset. This fact shows the reliability of the model in a wide range of conditions, thanks to the generality of most of the underlying mechanistic correlations.
  The higher RMSE among these tests belongs to the 3C, 10°C discharge (figure 5.7), which shows a mismatching between model and experiment at low voltage. This behavior is probably due to the moderately high activation energies of the solid diffusion coefficients $EA_{D_{s,p}}$ and $EA_{D_{s,n}}$, which overestimate the effect of the battery heating on the lithium diffusion in the electrode, leading to progressively lower voltage losses due to concentration disequilibria (see Chapter 1.1.2);

- both the sets of relaxation curves show good results, in particular the one with low current pulses (figure 5.9). The curves at high current of figure 5.10

show larger RMSEs probably because of the higher disequilibrium caused by such an higher current, that can lead to the temperature and concentration inhomogeneities along the battery spiral described in Chapter 4.2.2 [164, 165]. Such inhomogeneities lead to much higher relaxation times ($10^4 - 10^5$ s), that our model is not able to predict;

- the results of the EIS are particularly good for high-mid SOC at 25°C of figure 5.11, where the behavior of the experimental data is well reproduced, with a slightly higher RMSE at high SOC. The model EIS at 20% SOC does not show the second semicircle at low frequency, for the same reason explained in the training dataset observations. The variation of the model impedance with temperature of figure 5.12 is good going towards higher temperatures, while the experimental low temperature spectrum is underestimated by the model.
- for what concerns the experimental uncertainty, the results obtained in the related Chapter 3.1.2 suggest an average error on the voltage measurement in the order of $5 - 10$ mV, depending on the operative condition. Instead, the average uncertainty on the impedance measurement is in the order of $0.02-0.5$ mΩ, strongly varying with the frequency range. Comparing these values with the RMSEs of table 5.4, we see how the in certain conditions, as the high-temperature EIS and the low current pulse relaxations, the average difference between model and experimental data is comparable with the measurement uncertainty. Nevertheless, many other conditions show an RMSE much higher than the related uncertainty, suggesting that the quality of the fitting has still room for improvement even considering the errors on the measurement process.

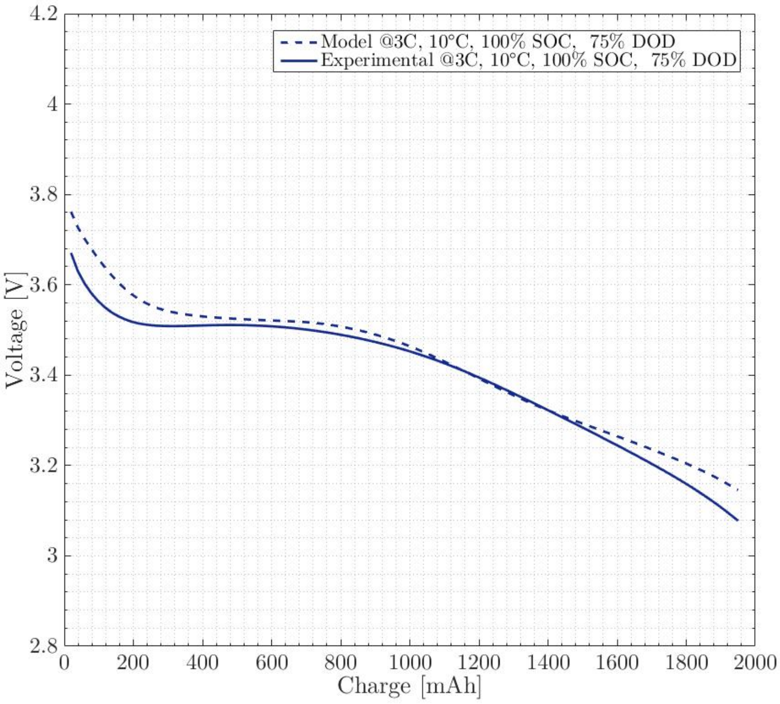

Figure 5.1: *Training dataset: Discharge curve at* $3C$*,* $10° C$*, from* 100% *SOC to* 25% *SOC. RMSE:* $36.7\ mV$

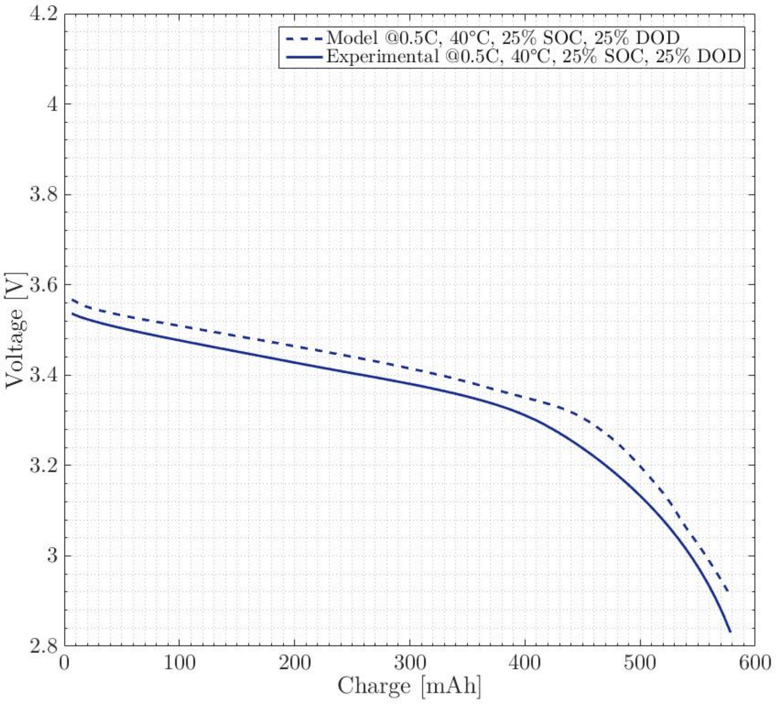

Figure 5.2: *Training dataset: Discharge curve at* $0.5C$*,* $40° C$*, from* 25% *SOC to* 0% *SOC. RMSE:* $44.0\ mV$

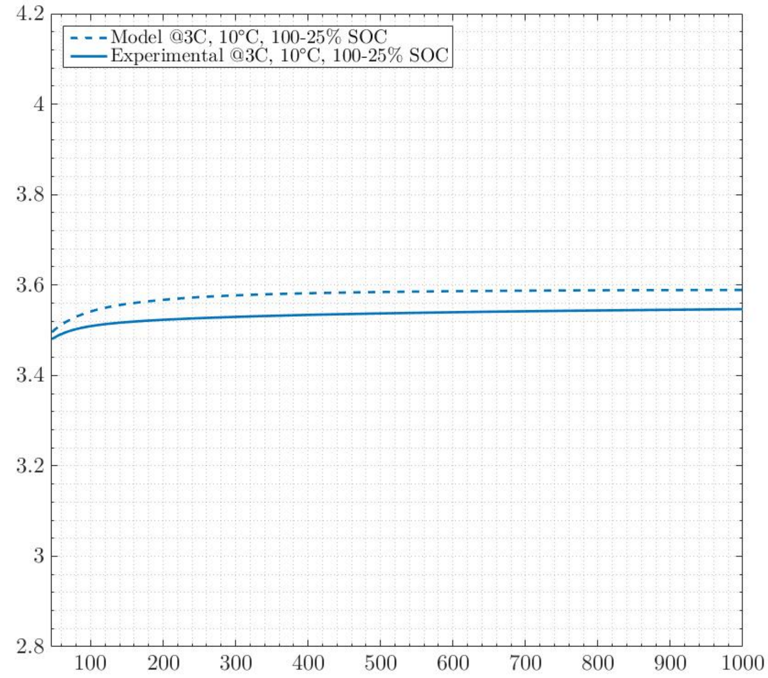

Figure 5.3: *Training dataset: Relaxation curve after discharge at* $3C$*,* $10°C$*, from* 100% *SOC to* 25% *SOC. RMSE:* 40.1 mV

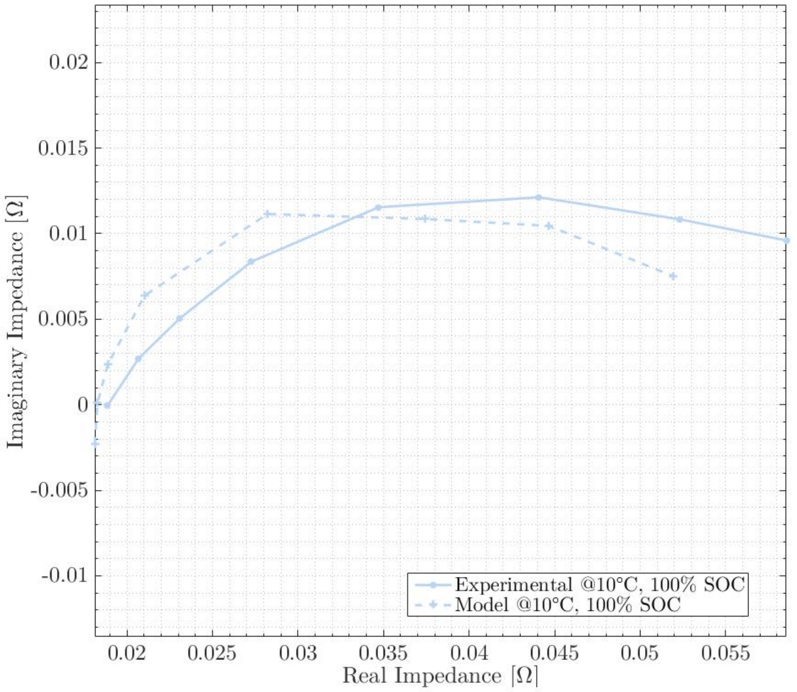

Figure 5.4: *Training dataset: Impedance spectrum at* $10°C$*,* 100% *SOC. RMSE real impedance:* 5.61 $m\Omega$*, RMSE imaginary impedance:* 1.91 $m\Omega$

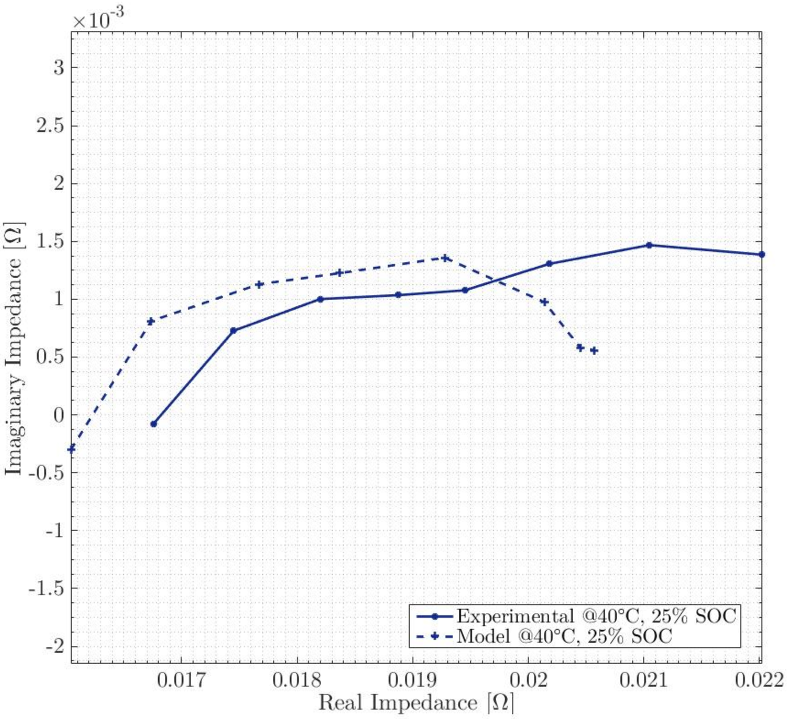

Figure 5.5: *Training dataset: Impedance spectrum at* $40°C$*,* 25% *SOC. RMSE real impedance:* 0.712 *m*Ω*, RMSE imaginary impedance:* 0.470 *m*Ω

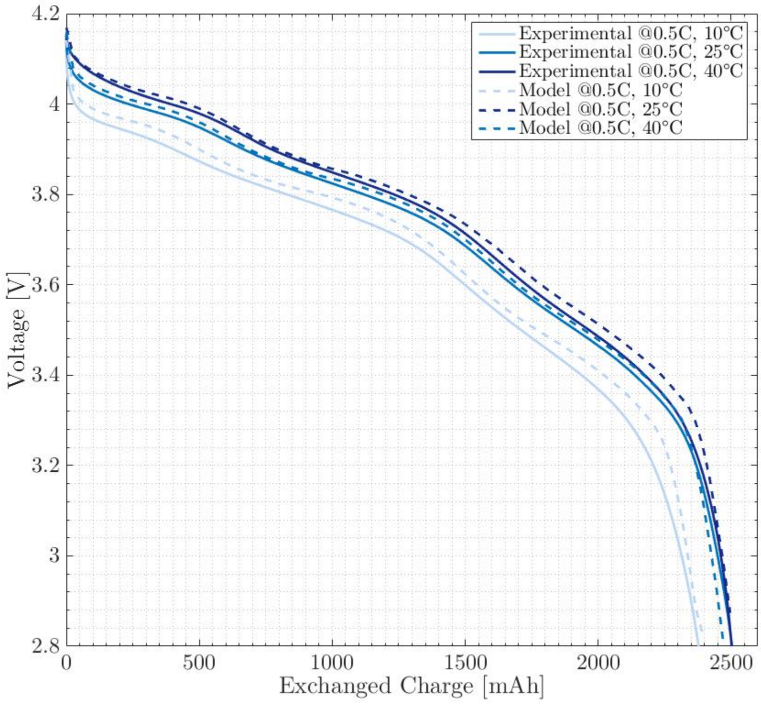

Figure 5.6: *Validation dataset: Discharge curves at* 0.5*C, from* 100% *SOC to* 0% *SOC, temperature variation. RMSE* 10°*:* 37.8 *mV, RMSE* 25°*:* 20.6 *mV, RMSE* 40°*:* 22.9 *mV*

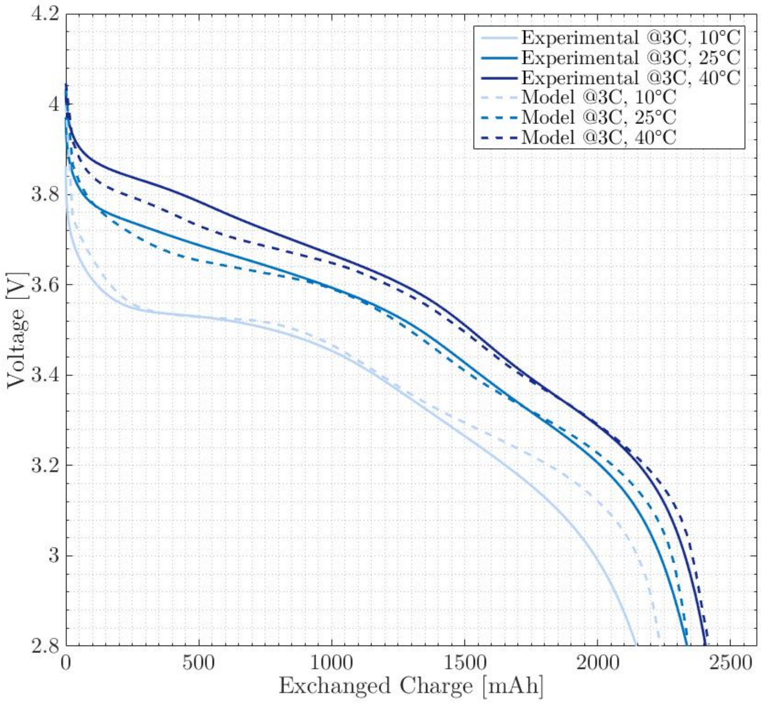

Figure 5.7: *Validation dataset: Discharge curves at* $3C$*, from* 100% *SOC to* 0% *SOC, temperature variation*

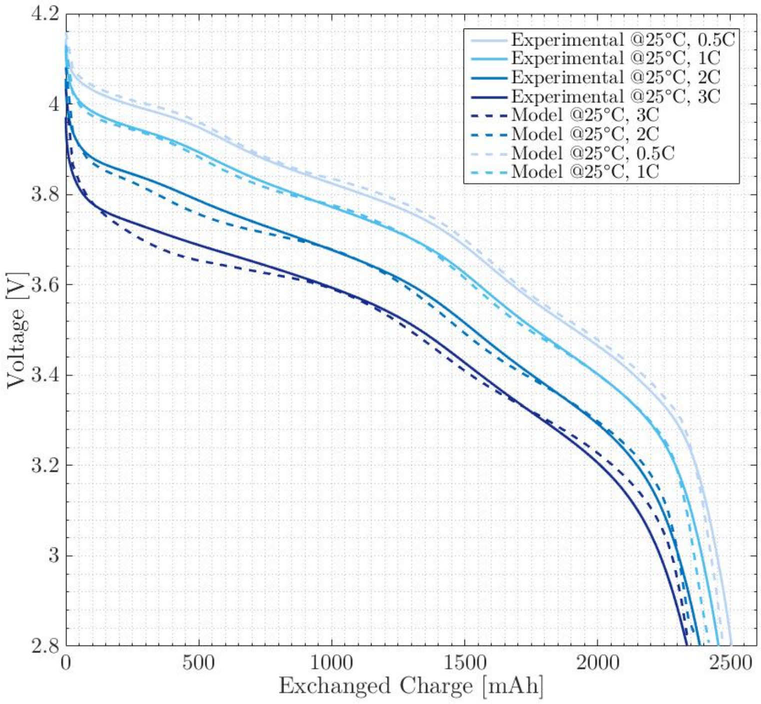

Figure 5.8: *Validation dataset: Discharge curves at* $25° C$*, from* 100% *SOC to* 0% *SOC, current rate variation*

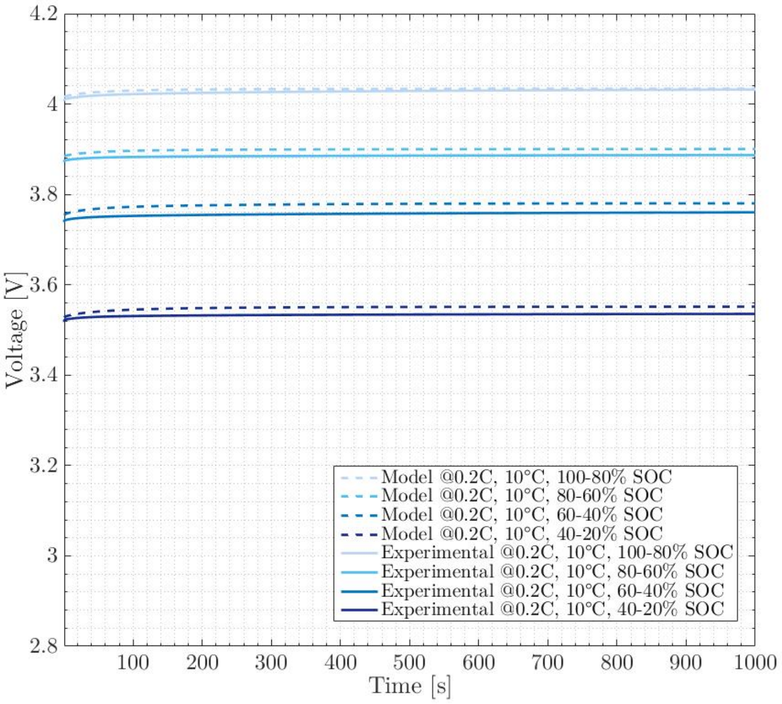

Figure 5.9: *Validation dataset: Relaxation curves after discharges at* $0.2C$*,* $10°C$*, with* 20% *DOD, starting SOC variation*

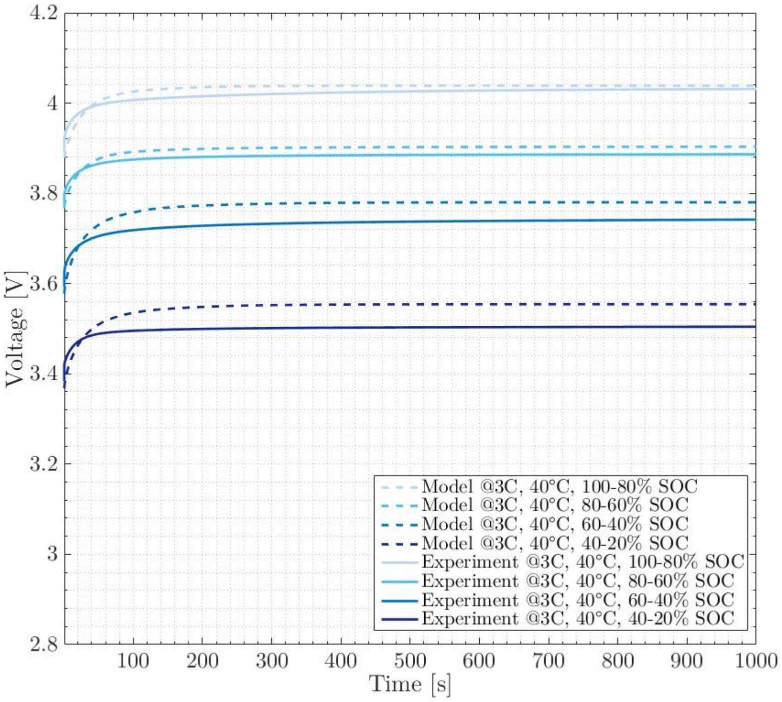

Figure 5.10: *Validation dataset: Relaxation curves after discharges at* $3C$*,* $40°C$*, with* 20% *DOD, starting SOC variation*

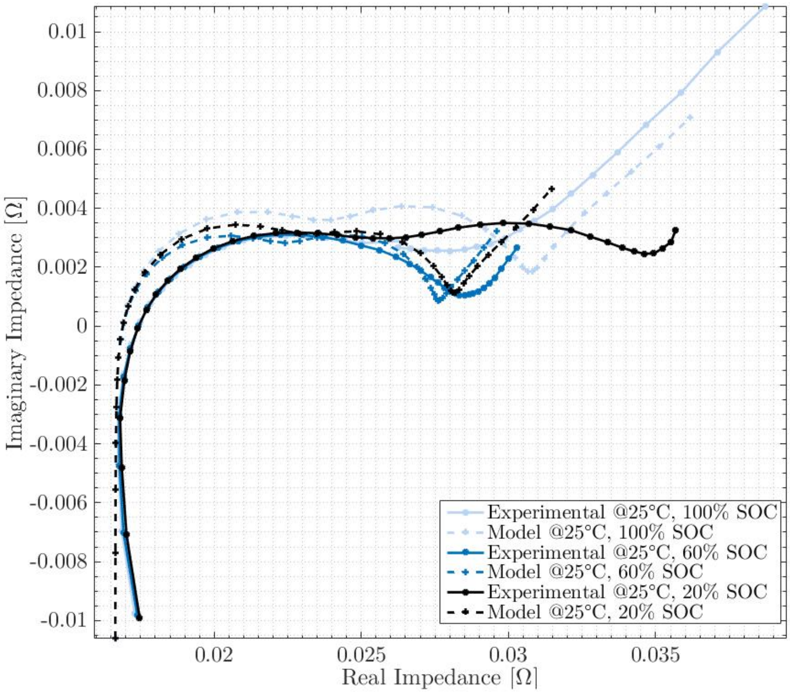

Figure 5.11: *Validation dataset: Impedance spectra at* 25° *C, SOC variation*

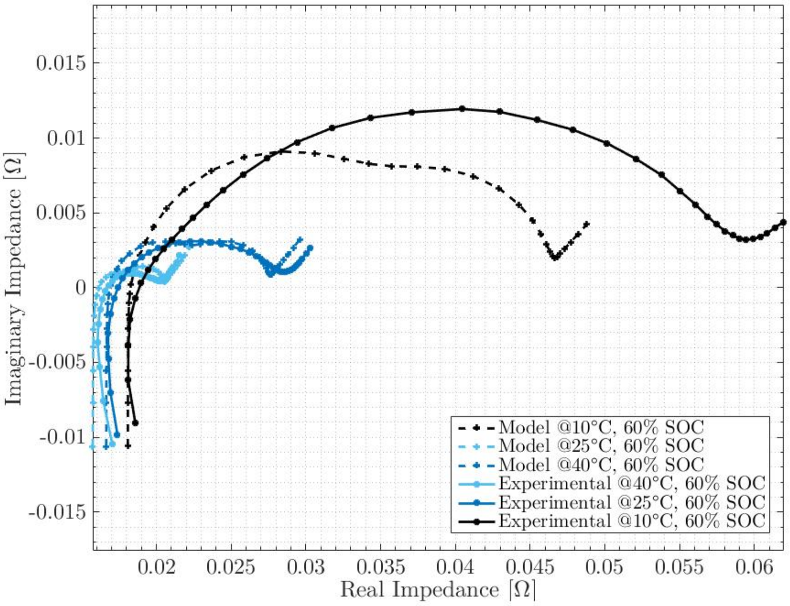

Figure 5.12: *Validation dataset: Impedance spectra at* 60% *SOC, temperature variation*

5.3.2 Final remarks

The results obtained with the application of the proposed experimental methodology suggest that the combination of discharge curves, relaxation tests and EIS can be a powerful tool for the parameter estimation of a lithium-ion battery in a physical model. We obtained a good results on a wide range of conditions that were not included in the training dataset, and considering a much wider range of operative conditions and techniques than the literature. This novel and comprehensive approach to battery characterization can be a stepping stone in the definition of a complete diagnostic procedure of aged lithium-ion batteries. The open issues that have to be addressed are:

- the set of parameters of table 5.3, obtained by the algorithm with the fitting of experimental data, could suffer from the issue highlighted in Chapter 5.2, where it was shown how a wrong set can still reproduce a training dataset. The proposed solutions to this problem at the end of Chapter 5.2 should be applied. Also, a post-mortem investigation of the value of the parameters could be performed with appropriate techniques, to check the validity of the set with direct measurements;

- the computational time required by the model is quite high, allowing only a really low number of iterations of the fitting algorithm. An improvement in this direction, for instance with model order reductions and parallelization, could improve further the quality of the data fitting and of the parameter estimation process;

- in the validation dataset, the regions where the model performed less well were the ones of low/very low state of charge, probably due to a lack of a proper thermodynamic fitting and of poor correlations not suitable for highly non-linear effects. The thermodynamic characteristics of the battery could be fitted with a process analogous to the one designed in this work for the dynamic characteristics.

Conclusions

This master's thesis fits into the context of the circular economy of lithium-ion batteries, acknowledging the fact that in the near future there will be a continuously increasing number of aged LIBs retired after their end of life in electric vehicles and that these used batteries can be employed in less demanding applications. One of the enabling factors of this circular framework is a reliable and standardized measurement procedure of the aged batteries state of health and the remaining useful lifetime. The objective of this work is the definition of a novel experimental methodology to estimate the physical parameters that determine the battery behavior in a mechanistic model. The values of these parameters can be then related to the effects of aging, for the evaluation of the state of health.

- Reviewing the literature on diagnostic procedures of lithium-ion batteries, we understood how only capacity tests have a widespread use. Instead, it is suggested that the most insightful approach should be the one that combines different techniques, to obtain a complete dataset on the cell behavior in a variety of operative conditions. For this reason, three techniques were chosen and applied in the experimental campaign, i.e. the capacity test, the relaxation test and the electrochemical impedance spectroscopy. For what concerns the modeling part, the electrochemical pseudo two-dimensional Doyle-Fuller-Newman model was integrated with a two-dimensional thermal model of a cylindrical battery, and the effect of temperature variations on the battery physical parameters was implemented.

- The experimental campaign was performed on four batteries, with pristine and aged commercial samples with different cathode chemistries. We understood how each technique can highlight different effects of the degradation on LIBs, with important variations according to the operative conditions of the test. Therefore, the effectiveness of the combination of capacity tests, relaxation tests and EIS was proven.

- To define the methodology, a sensitivity analysis of the LIB physical model was designed and carried out, where the three diagnostic techniques were simulated and 28 model parameters were varied within a range defined by the literature review. We obtained a quantitative classification of the model parameters according to the sensitivity of the model outputs to their variations. From these results, we designed an experimental methodology that balanced the trade off between the amount of information obtainable from the experimental techniques for the parameter estimation phase and the tests' duration. In particular, the methodology consists of two discharge curves, a relaxation curve and two impedance spectra from the EIS.

- Finally, the methodology was implemented and tested in a parameter estimation process, where a metaheuristic Particle Swarm Optimization algorithm was chosen and adapted to our problem and used to fit the model results to the training dataset. Two simulated datasets and one experimental dataset obtained from a pristine 2.6 Ah high-power commercial battery were used for the calibration and validation of the methodology. It was possible to exclude some physical parameters from the parameter estimation process thanks to the insights obtained by the sensitivity analysis.

- For what concerns the experimental dataset, the results on the validation data show how the estimated parameters reproduce well the battery behavior in the majority of the conditions not included in the training data, obtaining RMSEs that are aligned with the relevant literature on the topic. Moreover, we included in our validation three different experimental techniques and a wide range of operative conditions, a feature that is not present in literature and that indicates the generality of our approach;

The proposed methodology has shown promising results, and it confirmed how the combination of different experimental techniques and of a physical model can be a powerful tool for a comprehensive battery characterization. The main follow up activities that should be performed in the next future for the definition of a complete diagnostic procedure are:

- the proper fitting of the thermodynamic characteristic of the battery. In the validation, some limitations emerged in the operative conditions where the battery SOC is low. It was highlighted the necessity more accurate thermodynamic characteristic to obtain a fully reliable set of parameters. This fitting could be following the same path of this thesis, applied to the thermodynamic-related model parameters;

- the reduction of computational time required by the model simulation, to allow an higher number of iterations of the fitting algorithm. With this improvement, for instance with model order reductions and parallelization of the operations, it would be possible to further improve the quality of the obtained set of physical parameters from the fitting process;

- the definition of the correlations between the values of the physical parameters and the degradation modes sustained by the aged lithium-ion battery.

Acronyms

AC	Alternate current
B2U	Battery second use
BOL	Beginning of life
CEI	Cathode electrolyte interphase
DC	Direct current
DEC	Diethyl carbonate
DMC	Dimethyl carbonate
DV	Differential voltage
EC	Ethylene Carbonate
EEC	Equivalent electric circuit
EIS	Electrochemical impedance spectroscopy
EMC	Ethyl methyl carbonate
EOL	End of life
ESS	Energy storage system
EV	Electric vehicle
FFT	Fast Fourier transform
FR	Fast relaxation
GHG	Greenhouse gas
GITT	Galvanostati Intermitten Titration Technique
GSA	Global sensitivity analysis
HF	High frequency
IC	Incremental capacity
LAM	Loss of active material

LCO	Lithium cobalt oxide battery
LF	Low frequency
LFP	Lithium iron phosphate battery
LIB	Lithium-ion battery
LLI	Loss of lithium inventory
LMO	Lithium manganese oxide battery
LTO	Lithium titanate battery
MF	Mid frequency
MR	Mid relaxation
NCA	Nickel cobalt aluminum battery
NMC	Nickel manganese cobalt battery
OCP	Open circuit potential
OCV	Open circuit voltage
OEM	Original equipment manufacturer
OFAT	One factor at time
P2D	Pseudo two-dimensional
PDE	Partial differential equation
RI	Resistance increase
RMSE	Root mean square error
RUL	Remaining useful lifetime
SEI	Solid electrolyte interphase
SHE	Standard hydrogen electrode
SOC	State of charge
SOH	State of health
SR	Slow relaxation

Bibliography

[1] *CAIT Climate Data Explorer. https://www.climatewatchdata.org/ghg- emissions.* 2019 (cit. on p. 1).

[2] Rogelj, J., D. Shindell, K. Jiang, S. Fifita, P. Forster, V. Ginzburg, C. Handa, H. Kheshgi, S. Kobayashi, E. Kriegler, L. Mundaca, R. Séférian, and M.V. Vilariño. "Mitigation Pathways Compatible with 1.5°C in the Context of Sustainable Development". en. In: *Global Warming of 1.5°C: An IPCC Special Report on the Impacts of Global Warming of 1.5°C Above Pre-industrial Levels and Related Global Greenhouse Gas Emission Pathways, in the Context of Strengthening the Global Response to the Threat of Climate Change, Sustainable Development, and Efforts to Eradicate Poverty.* Intergovernmental Panel on Climate Change, 2018 (cit. on p. 1).

[3] Hannah Ritchie and Max Roser. "Renewable Energy". In: *Our World in Data* (Dec. 2017) (cit. on p. 1).

[4] *IEA - Tracking Energy Integration. https://www.iea.org/reports/tracking-energy-integration.* 2019 (cit. on p. 1).

[5] K Hampshire et al. "Electric vehicles from life cycle and circular economy perspectives". In: *Version* 2 (2018), p. 25 (cit. on p. 1).

[6] John T Warner. *The Handbook of Lithium-Ion Battery Pack Design: Chemistry, Components, Types and Terminology.* en. Elsevier, May 2015 (cit. on p. 2).

[7] *The Nobel Prize in Chemistry 2019. https://www.nobelprize.org/prizes/chemistry/2019/press-release/.* 2019 (cit. on pp. 3, 4).

[8] Petr Vanysek. "Electrochemical series". In: *CRC handbook of chemistry and physics* 8 (2000) (cit. on p. 3).

[9] International Organization for Standardization (ISO). *Electrically propelled road vehicles — Test specification for lithium-ion traction battery packs and systems.* Tech. rep. 12405-4. 2018 (cit. on p. 4).

[10] John Newman and Karen E Thomas-Alyea. *Electrochemical Systems.* en. John Wiley & Sons, Nov. 2012 (cit. on pp. 5, 7, 41).

[11] K Li and K J Tseng. "Energy efficiency of lithium-ion battery used as energy storage devices in micro-grid". In: *IECON 2015 - 41st Annual Conference of the IEEE Industrial Electronics Society.* Nov. 2015, pp. 005235–005240 (cit. on p. 6).

[12] Naoki Nitta et al. “Li-ion battery materials: present and future”. In: *Materials Today* 18.5 (June 2015), pp. 252–264 (cit. on pp. 7, 16, 74).

[13] Richard Schmuch et al. “Performance and cost of materials for lithium-based rechargeable automotive batteries”. In: *Nature Energy* 3.4 (Apr. 2018), pp. 267–278 (cit. on pp. 7, 13, 15, 19).

[14] Robert D Minter et al. “Three-electrode Coin Cell Preparation and Electrodeposition Analytics for Lithium-ion Batteries”. en. In: *Journal of visualized experiments: JoVE* 135 (May 2018) (cit. on p. 8).

[15] Anton Van der Ven et al. “Understanding Li Diffusion in Li-Intercalation Compounds”. In: *Accounts of Chemical Research* 46.5 (2013), pp. 1216–1225 (cit. on p. 7).

[16] J Gao, S Q Shi, and H Li. “Brief overview of electrochemical potential in lithium ion batteries”. In: *Chinese Physics B* (2015) (cit. on p. 10).

[17] Wladislaw Waag, Stefan Käbitz, and Dirk Uwe Sauer. “Experimental investigation of the lithium-ion battery impedance characteristic at various conditions and aging states and its influence on the application”. In: *Applied energy* 102 (Feb. 2013), pp. 885–897 (cit. on p. 11).

[18] Jessica Lück and Arnulf Latz. “The electrochemical double layer and its impedance behavior in lithium-ion batteries”. en. In: *Physical chemistry chemical physics: PCCP* 21.27 (July 2019), pp. 14753–14765 (cit. on p. 11).

[19] Irene J Ong. “Double-Layer Capacitance in a Dual Lithium Ion Insertion Cell”. In: *Journal of The Electrochemical Society* 146.12 (1999), p. 4360 (cit. on p. 11).

[20] Wu Xu et al. “Lithium metal anodes for rechargeable batteries”. en. In: *Energy & environmental science* 7.2 (2014), pp. 513–537 (cit. on p. 13).

[21] Chengcheng Fang, Xuefeng Wang, and Ying Shirley Meng. “Key Issues Hindering a Practical Lithium-Metal Anode”. en. In: *Trends in Chemistry* 1.2 (May 2019), pp. 152–158 (cit. on p. 13).

[22] Nitin A Kaskhedikar and Joachim Maier. “Lithium Storage in Carbon Nanostructures”. In: *Advanced materials* 21.25-26 (July 2009), pp. 2664–2680 (cit. on p. 13).

[23] J R Dahn, Rosamaria Fong, and M J Spoon. “Suppression of staging in lithium-intercalated carbon by disorder in the host”. In: *Physical Review B* 42.10 (1990), pp. 6424–6432 (cit. on pp. 14, 15).

[24] J R Dahn. “Phase diagram of LixC6”. en. In: *Physical review. B, Condensed matter* 44.17 (Nov. 1991), pp. 9170–9177 (cit. on pp. 13, 15).

[25] Martin Winter et al. “Insertion electrode materials for rechargeable lithium batteries”. In: *Advanced materials* 10.10 (1998), pp. 725–763 (cit. on p. 13).

[26] Tsutomu Ohzuku, Yasunobu Iwakoshi, and Keijiro Sawai. “Formation of lithium-graphite intercalation compounds in nonaqueous electrolytes and their application as a negative electrode for a lithium ion (shuttlecock) cell”. In: *Journal of the Electrochemical Society* 140.9 (1993), p. 2490 (cit. on p. 14).

[27] Michael Hess. “Kinetics and stage transitions of graphite for lithium-ion batteries”. PhD thesis. ETH Zurich, 2013 (cit. on p. 14).

[28] George E Blomgren. “The Development and Future of Lithium Ion Batteries”. en. In: *Journal of the Electrochemical Society* 164.1 (Dec. 2016), A5019 (cit. on p. 15).

[29] L Fransson et al. “Influence of carbon black and binder on Li-ion batteries”. In: *Journal of power sources* 101.1 (Oct. 2001), pp. 1–9 (cit. on p. 15).

[30] S F Lux et al. “Low Cost, Environmentally Benign Binders for Lithium-Ion Batteries”. In: *Journal of the Electrochemical Society* 157.3 (Mar. 2010), A320–A325 (cit. on p. 15).

[31] Seung-Taek Myung, Yashiro Hitoshi, and Yang-Kook Sun. “Electrochemical behavior and passivation of current collectors in lithium-ion batteries”. en. In: *Journal of materials chemistry* 21.27 (2011), pp. 9891–9911 (cit. on pp. 15, 17, 25).

[32] K Mizushima et al. “LixCoO2 (0<x<-1): A new cathode material for batteries of high energy density”. In: *Materials Research Bulletin* 15.6 (1980), pp. 783–789 (cit. on p. 16).

[33] Aurelien Du Pasquier et al. “A comparative study of Li-ion battery, supercapacitor and nonaqueous asymmetric hybrid devices for automotive applications”. In: *Journal of power sources* 115.1 (Mar. 2003), pp. 171–178 (cit. on p. 16).

[34] A Rougier, P Gravereau, and C Delmas. “Optimization of the Composition of the Li1- z Ni1+ z O 2 Electrode Materials: Structural, Magnetic, and Electrochemical Studies”. In: *Journal of the Electrochemical Society* 143.4 (1996), pp. 1168–1175 (cit. on p. 16).

[35] C H Chen et al. “Aluminum-doped lithium nickel cobalt oxide electrodes for high-power lithium-ion batteries”. In: *Journal of power sources* 128.2 (Apr. 2004), pp. 278–285 (cit. on p. 16).

[36] Ira Bloom et al. “Effect of cathode composition on capacity fade, impedance rise and power fade in high-power, lithium-ion cells”. In: *Journal of power sources* 124.2 (Nov. 2003), pp. 538–550 (cit. on p. 16).

[37] Michael M Thackeray. “Manganese oxides for lithium batteries”. In: *Progress in Solid State Chemistry* 25.1 (Jan. 1997), pp. 1–71 (cit. on p. 16).

[38] Gaurav Assat and Jean-Marie Tarascon. “Fundamental understanding and practical challenges of anionic redox activity in Li-ion batteries”. In: *Nature Energy* 3.5 (May 2018), pp. 373–386 (cit. on p. 17).

[39] A Yamada, S C Chung, and K Hinokuma. “Optimized LiFePO4 for Lithium Battery Cathodes”. In: *Journal of the Electrochemical Society* 148.3 (Mar. 2001), A224–A229 (cit. on p. 17).

[40] Myounggu Park et al. “A review of conduction phenomena in Li-ion batteries”. In: *Journal of Power Sources* 195.24 (2010), pp. 7904–7929 (cit. on pp. 17, 18, 33, 52).

[41] S L Bewlay et al. “Conductivity improvements to spray-produced LiFePO4 by addition of a carbon source”. In: *Materials letters* 58.11 (Apr. 2004), pp. 1788–1791 (cit. on p. 17).

[42] Kang Xu. “Electrolytes and interphases in Li-ion batteries and beyond”. en. In: *Chemical reviews* 114.23 (Dec. 2014), pp. 11503–11618 (cit. on pp. 17, 18).

[43] Raphael W Schmitz et al. “Investigations on novel electrolytes, solvents and SEI additives for use in lithium-ion batteries: Systematic electrochemical characterization and detailed analysis by spectroscopic methods”. In: *Progress in Solid State Chemistry* 42.4 (2014), pp. 65–84 (cit. on p. 17).

[44] Chongyin Yang et al. “4.0 V aqueous Li-ion batteries”. In: *Joule* 1.1 (2017), pp. 122–132 (cit. on p. 18).

[45] Nurhaswani Alias and Ahmad Azmin Mohamad. “Advances of aqueous rechargeable lithium-ion battery: A review”. In: *Journal of power sources* 274 (Jan. 2015), pp. 237–251 (cit. on p. 18).

[46] Sheng Shui Zhang. “A review on electrolyte additives for lithium-ion batteries”. In: *Journal of power sources* 162.2 (Nov. 2006), pp. 1379–1394 (cit. on p. 18).

[47] Kang Xu. “Nonaqueous liquid electrolytes for lithium-based rechargeable batteries”. en. In: *Chemical reviews* 104.10 (Oct. 2004), pp. 4303–4417 (cit. on p. 18).

[48] Jürgen Janek and Wolfgang G Zeier. “A solid future for battery development”. In: *Nature Energy* 1.9 (Sept. 2016), p. 16141 (cit. on p. 19).

[49] Hun Lee et al. “A review of recent developments in membrane separators for rechargeable lithium-ion batteries”. en. In: *Energy & environmental science* 7.12 (2014), pp. 3857–3886 (cit. on pp. 19, 101).

[50] Lockheed Idaho Technologies Co. *USABC electric vehicle Battery Test Procedures Manual. Revision 2*. 1996 (cit. on p. 20).

[51] Samveg Saxena et al. “Quantifying EV battery end-of-life through analysis of travel needs with vehicle powertrain models”. In: *Journal of power sources* 282 (May 2015), pp. 265–276 (cit. on p. 20).

[52] *What can 6,000 electric vehicles tell us about EV battery health? | Geotab*. *https://www.geotab.com/blog/ev-battery-health/*. Accessed: 2020-2-8 (cit. on p. 20).

[53] H E Melin. “The Lithium-Ion Battery End-of-Life Market—A Baseline Study”. In: *World Economic Forum: Cologny, Switzerland*. 2018, pp. 1–11 (cit. on pp. 20, 21).

[54] Mario Pagliaro and Francesco Meneguzzo. “Lithium battery reusing and recycling: A circular economy insight”. en. In: *Heliyon* 5.6 (June 2019), e01866 (cit. on p. 20).

[55] Linda Gaines. “Lithium-ion battery recycling processes: Research towards a sustainable course”. In: *Sustainable Materials and Technologies* 17 (Sept. 2018), e00068 (cit. on p. 20).

[56] Rebecca E Ciez and J F Whitacre. "Examining different recycling processes for lithium-ion batteries". In: *Nature Sustainability* 2.2 (Feb. 2019), pp. 148–156 (cit. on p. 20).

[57] Gavin Harper et al. "Recycling lithium-ion batteries from electric vehicles". en. In: *Nature* 575.7781 (Nov. 2019), pp. 75–86 (cit. on pp. 21, 22).

[58] Bruce Dunn, Haresh Kamath, and Jean-Marie Tarascon. "Electrical energy storage for the grid: a battery of choices". en. In: *Science* 334.6058 (Nov. 2011), pp. 928–935 (cit. on p. 21).

[59] Troy R Hawkins et al. "Comparative Environmental Life Cycle Assessment of Conventional and Electric Vehicles". In: *Journal of Industrial Ecology* 17.1 (Feb. 2013), pp. 53–64 (cit. on p. 21).

[60] Robert Reinhardt et al. "Towards sustainable business models for electric vehicle battery second use: A critical review". en. In: *Journal of environmental management* 245 (Sept. 2019), pp. 432–446 (cit. on p. 22).

[61] Jeremy Neubauer et al. *Identifying and overcoming critical barriers to widespread second use of PEV batteries.* Tech. rep. National Renewable Energy Lab.(NREL), Golden, CO (United States), 2015 (cit. on p. 22).

[62] E Martinez-Laserna et al. "Battery second life: Hype, hope or reality? A critical review of the state of the art". In: *Renewable and Sustainable Energy Reviews* 93 (Oct. 2018), pp. 701–718 (cit. on pp. 22, 25).

[63] S Rohr et al. "Quantifying Uncertainties in Reusing Lithium-Ion Batteries from Electric Vehicles". In: *Procedia Manufacturing* 8 (2017), pp. 603–610 (cit. on p. 22).

[64] Kathrin Wegener et al. "Robot assisted disassembly for the recycling of electric vehicle batteries". In: *Procedia Cirp* 29 (2015), pp. 716–721 (cit. on p. 22).

[65] Anup Barai et al. "A comparison of methodologies for the non-invasive characterisation of commercial Li-ion cells". In: *Progress in Energy and Combustion Science* 72 (2019), pp. 1–31 (cit. on pp. 22, 26, 27, 29, 32).

[66] Pankaj Arora, Ralph E White, and Marc Doyle. "Capacity Fade Mechanisms and Side Reactions in Lithium-Ion Batteries". In: *Journal of the Electrochemical Society* 145.10 (Oct. 1998), pp. 3647–3667 (cit. on p. 23).

[67] J Vetter et al. "Ageing mechanisms in lithium-ion batteries". In: *Journal of power sources* 147.1 (Sept. 2005), pp. 269–281 (cit. on pp. 23, 24).

[68] Anthony Barré et al. "A review on lithium-ion battery ageing mechanisms and estimations for automotive applications". In: *Journal of power sources* 241 (Nov. 2013), pp. 680–689 (cit. on p. 23).

[69] Christoph R Birkl et al. "Degradation diagnostics for lithium ion cells". In: *Journal of power sources* 341 (Feb. 2017), pp. 373–386 (cit. on pp. 23, 26).

[70] Kristina Edström, Marie Herstedt, and Daniel P Abraham. "A new look at the solid electrolyte interphase on graphite anodes in Li-ion batteries". In: *Journal of power sources* 153.2 (Feb. 2006), pp. 380–384 (cit. on p. 23).

[71] Pallavi Verma, Pascal Maire, and Petr Novák. “A review of the features and analyses of the solid electrolyte interphase in Li-ion batteries”. In: *Electrochimica acta* 55.22 (Sept. 2010), pp. 6332–6341 (cit. on p. 23).

[72] K Edström, T Gustafsson, and J O Thomas. “The cathode–electrolyte interface in the Li-ion battery”. In: *Electrochimica acta* 50.2 (Nov. 2004), pp. 397–403 (cit. on p. 24).

[73] H H Lee, C C Wan, and Y Y Wang. “Thermal Stability of the Solid Electrolyte Interface on Carbon Electrodes of Lithium Batteries”. In: *Journal of the Electrochemical Society* 151.4 (Apr. 2004), A542–A547 (cit. on p. 24).

[74] Najmus Saqib et al. “On the Decomposition of Carbonate-Based Lithium-Ion Battery Electrolytes Studied Using Operando Infrared Spectroscopy”. en. In: *Journal of the Electrochemical Society* 165.16 (Dec. 2018), A4051 (cit. on p. 24).

[75] Simon Müller et al. “Quantification and modeling of mechanical degradation in lithium-ion batteries based on nanoscale imaging”. en. In: *Nature communications* 9.1 (June 2018), p. 2340 (cit. on p. 24).

[76] Geun-Chang Chung et al. “Origin of graphite exfoliation an investigation of the important role of solvent cointercalation”. In: *Journal of the Electrochemical Society* 147.12 (2000), p. 4391 (cit. on p. 24).

[77] Vijay A Sethuraman et al. “Surface structural disordering in graphite upon lithium intercalation/deintercalation”. In: *Journal of power sources* 195.11 (June 2010), pp. 3655–3660 (cit. on p. 24).

[78] Thomas Waldmann, Björn-Ingo Hogg, and Margret Wohlfahrt-Mehrens. “Li plating as unwanted side reaction in commercial Li-ion cells–A review”. In: *Journal of power sources* 384 (2018), pp. 107–124 (cit. on p. 24).

[79] Qianqian Liu et al. “Understanding undesirable anode lithium plating issues in lithium-ion batteries”. en. In: *RSC advances* 6.91 (Sept. 2016), pp. 88683–88700 (cit. on p. 25).

[80] Kenji Takahashi and Venkat Srinivasan. “Examination of Graphite Particle Cracking as a Failure Mode in Lithium-Ion Batteries: A Model-Experimental Study”. In: *Journal of the Electrochemical Society* 162.4 (Jan. 2015), A635–A645 (cit. on p. 25).

[81] Tao Cheng et al. “Cracks Formation in Lithium-Rich Cathode Materials for Lithium-Ion Batteries during the Electrochemical Process”. en. In: *Energies* 11.10 (Oct. 2018), p. 2712 (cit. on p. 25).

[82] Chun Zhan et al. “Dissolution, migration, and deposition of transition metal ions in Li-ion batteries exemplified by Mn-based cathodes–a critical review”. In: *Energy & environmental science* 11.2 (2018), pp. 243–257 (cit. on p. 25).

[83] Simon F Schuster et al. “Nonlinear aging characteristics of lithium-ion cells under different operational conditions”. In: *Journal of Energy Storage* 1 (June 2015), pp. 44–53 (cit. on p. 25).

[84] Matthieu Dubarry, Cyril Truchot, and Bor Yann Liaw. “Synthesize battery degradation modes via a diagnostic and prognostic model”. In: *Journal of Power Sources* 219 (2012), pp. 204–216 (cit. on pp. 25, 26, 31).

[85] Kohei Honkura, Ko Takahashi, and Tatsuo Horiba. “Capacity-fading prediction of lithium-ion batteries based on discharge curves analysis”. In: *Journal of power sources* 196.23 (Dec. 2011), pp. 10141–10147 (cit. on p. 25).

[86] Matthieu Dubarry and Bor Yann Liaw. “Identify capacity fading mechanism in a commercial LiFePO4 cell”. In: *Journal of power sources* 194.1 (Oct. 2009), pp. 541–549 (cit. on pp. 25, 31).

[87] M S Hossain Lipu et al. “A review of state of health and remaining useful life estimation methods for lithium-ion battery in electric vehicles: Challenges and recommendations”. In: *Journal of cleaner production* 205 (Dec. 2018), pp. 115–133 (cit. on pp. 26, 39).

[88] Tianheng Feng et al. “Online identification of lithium-ion battery parameters based on an improved equivalent-circuit model and its implementation on battery state-of-power prediction”. In: *Journal of power sources* 281 (May 2015), pp. 192–203 (cit. on p. 26).

[89] Jürgen Remmlinger et al. “State-of-health monitoring of lithium-ion batteries in electric vehicles by on-board internal resistance estimation”. In: *Journal of power sources* 196.12 (June 2011), pp. 5357–5363 (cit. on p. 26).

[90] Xueyuan Wang, Xuezhe Wei, and Haifeng Dai. “Estimation of state of health of lithium-ion batteries based on charge transfer resistance considering different temperature and state of charge”. In: *Journal of Energy Storage* 21 (Feb. 2019), pp. 618–631 (cit. on pp. 26, 57).

[91] Grietus Mulder et al. “Enhanced test methods to characterise automotive battery cells”. In: *Journal of power sources* 196.23 (Dec. 2011), pp. 10079–10087 (cit. on p. 27).

[92] Carlos Pastor-Fernández et al. “A Comparison between Electrochemical Impedance Spectroscopy and Incremental Capacity-Differential Voltage as Li-ion Diagnostic Techniques to Identify and Quantify the Effects of Degradation Modes within Battery Management Systems”. In: *Journal of Power Sources* 360 (2017), pp. 301–318 (cit. on pp. 27, 38).

[93] Gabriele Sordi. “Thermodynamic and kinetic analysis of commercial lithium ion battery for identification of degradation mechanisms”. MA thesis. Polytechnic of Milan, Apr. 2019 (cit. on pp. 28, 31, 41, 45, 55, 59, 85).

[94] Venkatasailanathan Ramadesigan et al. “Parameter Estimation and Capacity Fade Analysis of Lithium-Ion Batteries Using Reformulated Models”. In: *J. Electrochem. Soc.* 158.9 (2011) (cit. on p. 28).

[95] M Petzl and M A Danzer. “Advancements in OCV Measurement and Analysis for Lithium-Ion Batteries”. In: *IEEE Transactions on Energy Conversion* 28.3 (Sept. 2013), pp. 675–681 (cit. on p. 31).

[96] Matthieu Dubarry, Cyril Truchot, and Bor Yann Liaw. “Cell degradation in commercial LiFePO4 cells with high-power and high-energy designs”. In: *Journal of power sources* 258 (July 2014), pp. 408–419 (cit. on p. 31).

[97] Zeyu Ma et al. “Investigation of path dependence in commercial lithium-ion cells for pure electric bus applications: Aging mechanism identification”. In: *Journal of power sources* 274 (Jan. 2015), pp. 29–40 (cit. on p. 31).

[98] C R Birkl et al. “A Parametric Open Circuit Voltage Model for Lithium Ion Batteries”. In: *Journal of the Electrochemical Society* 162.12 (Jan. 2015), A2271–A2280 (cit. on p. 32).

[99] Maria Angeles Cabañero et al. “Direct Determination of Diffusion Coefficients in Commercial Li-Ion Batteries”. In: *Journal of The Electrochemical Society* 165.5 (2018), A847–A855 (cit. on p. 32).

[100] Wei Shi et al. “Analysis of Thermal Aging Paths for Large-Format LiFePO4/Graphite Battery”. In: *Electrochimica acta* 196 (Apr. 2016), pp. 13–23 (cit. on p. 32).

[101] Lars Ole Valøen and Jan N Reimers. “Transport Properties of LiPF6-Based Li-Ion Battery Electrolytes”. en. In: *Journal of the Electrochemical Society* 152.5 (Mar. 2005), A882 (cit. on pp. 33, 52, 53).

[102] Huiwen Ji et al. “Hidden structural and chemical order controls lithium transport in cation-disordered oxides for rechargeable batteries”. en. In: *Nature communications* 10.1 (Feb. 2019), p. 592 (cit. on p. 33).

[103] Kandler Smith and Chao-Yang Wang. “Solid-state diffusion limitations on pulse operation of a lithium ion cell for hybrid electric vehicles”. In: *Journal of Power Sources* 161.1 (2006), pp. 628–639 (cit. on pp. 33, 66, 70, 72).

[104] Stefan Schindler et al. “Voltage relaxation and impedance spectroscopy as in-operando methods for the detection of lithium plating on graphitic anodes in commercial lithium-ion cells”. In: *Journal of power sources* 304 (Feb. 2016), pp. 170–180 (cit. on p. 34).

[105] Anup Barai et al. “A study of the influence of measurement timescale on internal resistance characterisation methodologies for lithium-ion cells”. en. In: *Scientific reports* 8.1 (Jan. 2018), p. 21 (cit. on pp. 34, 35).

[106] Anup Barai et al. “A study on the impact of lithium-ion cell relaxation on electrochemical impedance spectroscopy”. In: *Journal of power sources* 280 (Apr. 2015), pp. 74–80 (cit. on pp. 34, 70, 75).

[107] J Dambrowski. “Validation of Impedance-Data and of Impedance-Based Modeling Approach of Electrochemical Cells by Means of Mathematical System Theory”. In: *39th Annual Conference of the IEEE Industrial.* Vol. 60. 2013, pp. 1–7 (cit. on p. 35).

[108] Jeremy P Meyers et al. “The Impedance Response of a Porous Electrode Composed of Intercalation Particles”. In: *Journal of the Electrochemical Society* 147.8 (Aug. 2000), pp. 2930–2940 (cit. on pp. 36, 45, 75, 98, 116, 140).

[109] Isabel Jiménez Gordon et al. “Electrode contributions to the impedance of a high-energy density Li-ion cell designed for EV applications”. In: *Solid State Ionics* 237 (Apr. 2013), pp. 50–55 (cit. on p. 36).

[110] I A Jiménez Gordon et al. “Electrochemical Impedance Spectroscopy response study of a commercial graphite-based negative electrode for Li-ion batteries as function of the cell state of charge and ageing”. In: *Electrochimica acta* 223 (Jan. 2017), pp. 63–73 (cit. on pp. 36, 77, 140).

[111] Matt Lacey. *Diffusion impedance. http://lacey.se/science/eis/diffusion-impedance/.* Accessed: 2020-3-15. Mar. 2020 (cit. on p. 37).

[112] Haifeng Dai, Bo Jiang, and Xuezhe Wei. “Impedance Characterization and Modeling of Lithium-Ion Batteries Considering the Internal Temperature Gradient”. en. In: *Energies* 11.1 (Jan. 2018), p. 220 (cit. on p. 38).

[113] Ulrike Krewer et al. “Review—Dynamic Models of Li-Ion Batteries for Diagnosis and Operation: A Review and Perspective”. In: *Journal of The Electrochemical Society* 165.16 (2018), A3656–A3673 (cit. on p. 39).

[114] Y Hu et al. “Electro-thermal battery model identification for automotive applications”. In: *Journal of power sources* 196.1 (Jan. 2011), pp. 449–457 (cit. on p. 39).

[115] Min Chen and Gabriel A Rincon-Mora. “Accurate electrical battery model capable of predicting runtime and IV performance”. In: *IEEE Transactions on Energy Conversion* 21.2 (2006), pp. 504–511 (cit. on p. 39).

[116] Meng-Ting Chang et al. “Identification of the Parameters in Equivalent Circuit Model of Lithium-Ion Batteries”. In: *ECS Transactions* 61.27 (2014), pp. 125–130 (cit. on p. 40).

[117] Caihao Weng et al. “On-board state of health monitoring of lithium-ion batteries using incremental capacity analysis with support vector regression”. In: *Journal of power sources* 235 (Aug. 2013), pp. 36–44 (cit. on p. 40).

[118] G You, S Park, and D Oh. “Real-time state-of-health estimation for electric vehicle batteries: A data-driven approach”. In: *Applied energy* (2016) (cit. on p. 40).

[119] Datong Liu et al. “Prognostics for state of health estimation of lithium-ion batteries based on combination Gaussian process functional regression”. In: *Microelectronics Reliability* 53.6 (2013), pp. 832–839 (cit. on p. 40).

[120] Kristen A Severson et al. “Data-driven prediction of battery cycle life before capacity degradation”. In: *Nature Energy* 4.5 (May 2019), pp. 383–391 (cit. on p. 40).

[121] Zheng Chen et al. “Online battery state of health estimation based on Genetic Algorithm for electric and hybrid vehicle applications”. In: *Journal of power sources* 240 (Oct. 2013), pp. 184–192 (cit. on p. 40).

[122] Todd R Ferguson and Martin Z Bazant. “Phase Transformation Dynamics in Porous Battery Electrodes”. In: *Electrochimica acta* 146 (Nov. 2014), pp. 89–97 (cit. on p. 40).

[123] Priya Gambhire et al. “A reduced order electrochemical thermal model for lithium ion cells”. In: *Journal of power sources* 290 (Sept. 2015), pp. 87–101 (cit. on p. 41).

[124] Meng Guo and Ralph E White. “An approximate solution for solid-phase diffusion in a spherical particle in physics-based Li-ion cell models”. In: *Journal of power sources* 198 (Jan. 2012), pp. 322–328 (cit. on p. 41).

[125] Thomas F Fuller, Marc Doyle, and John Newman. “Simulation and optimization of the dual lithium ion insertion cell”. In: *Journal of the Electrochemical Society* 141.1 (1994), pp. 1–10 (cit. on pp. 41, 70, 89).

[126] Xuebing Han et al. “Simplification of physics-based electrochemical model for lithium ion battery on electric vehicle. Part I: Diffusion simplification and single particle model”. In: *Journal of power sources* 278 (Mar. 2015), pp. 802–813 (cit. on p. 41).

[127] Nan Lin, Fridolin Röder, and Ulrike Krewer. “Multiphysics Modeling for Detailed Analysis of Multi-Layer Lithium-Ion Pouch Cells”. en. In: *Energies* 11.11 (Nov. 2018), p. 2998 (cit. on p. 41).

[128] Gregory L Plett. *Battery Management Systems, Volume I: Battery Modeling.* en. Artech House, Sept. 2015 (cit. on p. 41).

[129] Parthasarathy M Gomadam, Ralph E White, and John W Weidner. “Modeling Heat Conduction in Spiral Geometries”. en. In: *Journal of the Electrochemical Society* 150.10 (Aug. 2003), A1339 (cit. on p. 48).

[130] Manuel Garcıa-Villalba, Guillermo Palau-Salvador, and Wolfgang Rodi. “Forced Convection Heat Transfer from a Finite-Height Cylinder”. In: *Flow, Turbulence and Combustion* 93.1 (July 2014), pp. 171–187 (cit. on p. 50).

[131] S J Drake et al. “Measurement of anisotropic thermophysical properties of cylindrical Li-ion cells”. In: *Journal of power sources* 252 (Apr. 2014), pp. 298–304 (cit. on p. 50).

[132] Michael J Lain, James Brandon, and Emma Kendrick. “Design Strategies for High Power vs. High Energy Lithium Ion Cells”. en. In: *Batteries* 5.4 (Oct. 2019), p. 64 (cit. on pp. 58, 84, 85).

[133] Frank M Kindermann et al. “Measurements of lithium-ion concentration equilibration processes inside graphite electrodes”. In: *Journal of power sources* 342 (Feb. 2017), pp. 638–643 (cit. on pp. 70, 72).

[134] Veronika Zinth et al. “Inhomogeneity and relaxation phenomena in the graphite anode of a lithium-ion battery probed by in situ neutron diffraction”. In: *Journal of Power Sources* 361 (2017), pp. 54–60 (cit. on pp. 70, 75).

[135] A H Zimmerman. “Self-discharge losses in lithium-ion cells”. In: *IEEE Aerospace and Electronic Systems Magazine* 19.2 (Feb. 2004), pp. 19–24 (cit. on p. 73).

[136] K M Shaju, G V Subba Rao, and B V R Chowdari. “Li ion kinetic studies on spinel cathodes, Li (M 1/6 Mn 11/6) O 4 (M= Mn, Co, CoAl) by GITT and EIS”. In: *Journal of materials chemistry* 13.1 (2003), pp. 106–113 (cit. on pp. 75, 77, 140).

[137] Young-Min Choi and Su-Il Pyun. “Effects of intercalation-induced stress on lithium transport through porous LiCoO2 electrode”. In: *Solid State Ionics* 99.3 (Aug. 1997), pp. 173–183 (cit. on p. 75).

[138] De Li and Haoshen Zhou. “Two-phase transition of Li-intercalation compounds in Li-ion batteries”. In: *Materials Today* 17.9 (Nov. 2014), pp. 451–463 (cit. on p. 76).

[139] Guus Ten Broeke, George Van Voorn, and Arend Ligtenberg. “Which sensitivity analysis method should I use for my agent-based model?” In: *Journal of Artificial Societies and Social Simulation* 19.1 (2016) (cit. on p. 82).

[140] Nan Lin et al. “Efficient Global Sensitivity Analysis of 3D Multiphysics Model for Li-Ion Batteries”. In: *Journal of the Electrochemical Society* 165.7 (Jan. 2018), A1169–A1183 (cit. on pp. 82, 83).

[141] S Zhao and D A Howey. “Global Sensitivity Analysis of Battery Equivalent Circuit Model Parameters”. In: *2016 IEEE Vehicle Power and Propulsion Conference (VPPC).* Oct. 2016, pp. 1–4 (cit. on p. 82).

[142] Feng Guo et al. “The equivalent circuit battery model parameter sensitivity analysis for lithium-ion batteries by Monte Carlo simulation”. In: *International Journal of Energy Research* 43.15 (Dec. 2019), pp. 9013–9024 (cit. on p. 82).

[143] Xin Lai et al. “Parameter sensitivity analysis and simplification of equivalent circuit model for the state of charge of lithium-ion batteries”. In: *Electrochimica Acta* 330 (2020), p. 135239 (cit. on p. 82).

[144] Alexander P Schmidt et al. “Experiment-driven electrochemical modeling and systematic parameterization for a lithium-ion battery cell”. In: *Journal of power sources* 195.15 (Aug. 2010), pp. 5071–5080 (cit. on pp. 82, 83).

[145] C Edouard et al. “Parameter sensitivity analysis of a simplified electrochemical and thermal model for Li-ion batteries aging”. In: *Journal of power sources* 325 (Sept. 2016), pp. 482–494 (cit. on pp. 82–84, 87).

[146] Shriram Santhanagopalan, Qingzhi Guo, and Ralph E White. “Parameter Estimation and Model Discrimination for a Lithium-Ion Cell”. In: *Journal of the Electrochemical Society* 154.3 (Mar. 2007), A198–A206 (cit. on pp. 82, 131).

[147] Liqiang Zhang et al. “Parameter Sensitivity Analysis of Cylindrical LiFePO4 Battery Performance Using Multi-Physics Modeling”. In: *Journal of the Electrochemical Society* 161.5 (Jan. 2014), A762–A776 (cit. on pp. 82–84, 87, 131, 139).

[148] Ning Jin et al. “Parameter estimation of an electrochemistry-based lithium-ion battery model using a two-step procedure and a parameter sensitivity analysis”. In: *International Journal of Energy Research* 42.7 (2018), pp. 2417–2430 (cit. on pp. 82, 131).

[149] Matthew D Murbach and Daniel T Schwartz. “Analysis of Li-Ion Battery Electrochemical Impedance Spectroscopy Data: An Easy-to-Implement Approach for Physics-Based Parameter Estimation Using an Open-Source Tool”. In: *Journal of The Electrochemical Society* 165.2 (2018), A297–A304 (cit. on p. 83).

[150] Johannes Schmalstieg and Dirk Uwe Sauer. “Full Cell Parameterization of a High-Power Lithium-Ion Battery for a Physico-Chemical Model: Part II. Thermal Parameters and Validation”. In: *Journal of The Electrochemical Society* 165.16 (2018), A3811–A3819 (cit. on pp. 84, 85, 136).

[151] Johannes Schmalstieg et al. “Full Cell Parameterization of a High-Power Lithium-Ion Battery for a Physico-Chemical Model: Part I. Physical and Electrochemical Parameters”. In: *Journal of The Electrochemical Society* 165.16 (2018), A3799–A3810 (cit. on pp. 84, 85, 98).

[152] Jason B Quinn et al. “Energy density of cylindrical Li-ion cells: A comparison of commercial 18650 to the 21700 cells”. In: *Journal of the Electrochemical Society* 165.14 (2018), A3284–A3291 (cit. on pp. 84, 85).

[153] Chia-Chin Chang, Sin-Yi Huang, and Wei-Hsin Chen. “Thermal and solid electrolyte interphase characterization of lithium-ion battery”. In: *Energy* 174 (May 2019), pp. 999–1011 (cit. on p. 84).

[154] Atsushi Funabiki et al. “Impedance study on the electrochemical lithium intercalation into natural graphite powder”. In: *Journal of the Electrochemical Society* 145.1 (1998), pp. 172–178 (cit. on p. 84).

[155] A Van der Ven and G Ceder. “Lithium Diffusion in Layered Li x CoO2”. en. In: *Electrochemical and Solid State Letters* 3.7 (May 2000), p. 301 (cit. on p. 84).

[156] Jaephil Cho et al. “Electrochemical Properties and Thermal Stability of Li a Ni1- x CO x O 2 Cathode Materials”. In: *Journal of the Electrochemical Society* 147.1 (2000), pp. 15–20 (cit. on p. 84).

[157] Ajit Kumar Dutta. “Electrical Conductivity of Single Crystals of Graphite”. In: *Physics Review* 90.2 (Apr. 1953), pp. 187–192 (cit. on p. 84).

[158] M Wakihara et al. “Chemical diffusion coefficients of lithium in LiMyMn2-yO4 (M= Co and Cr)”. In: *Solid State Ionics* 86 (1996), pp. 907–909 (cit. on p. 84).

[159] J Marzec et al. “Conduction mechanism in operating a LiMn2O4 cathode”. In: *Solid State Ionics* 146.3 (Feb. 2002), pp. 225–237 (cit. on p. 84).

[160] Dany Carlier, Michel Ménétrier, and Claude Delmas. “7Li MAS NMR study of electrochemically deintercalated LixNi0.30Co0.70O2 phases: evidence of electronic and ionic mobility, and redox processes”. en. In: *Journal of materials chemistry* 11.2 (2001), pp. 594–603 (cit. on p. 84).

[161] Sang Woo Han. “Transport and Kinetic Phenomena Linked to Power Performance of Lithium-Ion Batteries”. PhD thesis. 2014 (cit. on p. 84).

[162] Sarah Stewart and John Newman. "Measuring the Salt Activity Coefficient in Lithium-Battery Electrolytes". en. In: *Journal of the Electrochemical Society* 155.6 (Apr. 2008), A458 (cit. on p. 84).

[163] Moses Ender et al. "Anode microstructures from high-energy and high-power lithium-ion cylindrical cells obtained by X-ray nano-tomography". In: *Journal of power sources* 269 (Dec. 2014), pp. 912–919 (cit. on p. 84).

[164] Frank M Kindermann et al. "Long-term equalization effects in Li-ion batteries due to local state of charge inhomogeneities and their impact on impedance measurements". In: *Electrochimica Acta* 185 (2015), pp. 107–116 (cit. on pp. 86, 142).

[165] J Sturm et al. "Modeling and simulation of inhomogeneities in a 18650 nickel-rich, silicon-graphite lithium-ion cell during fast charging". In: *Journal of Power Sources* 412 (2019), pp. 204–223 (cit. on pp. 86, 142).

[166] Eric W Weisstein. "Fast Fourier Transform". en. In: *http://mathworld.wolfram.com/* () (cit. on p. 87).

[167] James Taylor et al. "An insight into the errors and uncertainty of the lithium-ion battery characterisation experiments". In: *Journal of Energy Storage* 24 (2019), p. 100761 (cit. on p. 99).

[168] Saehong Park et al. "Optimal Experimental Design for Parameterization of an Electrochemical Lithium-Ion Battery Model". In: *Journal of the Electrochemical Society* 165.7 (Jan. 2018), A1309–A1323 (cit. on pp. 131, 139).

[169] Jun Li et al. "Parameter Identification of Lithium-Ion Batteries Model to Predict Discharge Behaviors Using Heuristic Algorithm". In: *Journal of the Electrochemical Society* 163.8 (Jan. 2016), A1646–A1652 (cit. on pp. 131, 139).

[170] Joel C Forman et al. "Genetic identification and fisher identifiability analysis of the Doyle–Fuller–Newman model from experimental cycling of a LiFePO4 cell". In: *Journal of power sources* 210 (July 2012), pp. 263–275 (cit. on p. 131).

[171] Bernardo Severino et al. "Multi-objective optimal design of lithium-ion battery packs based on evolutionary algorithms". In: *Journal of power sources* 267 (Dec. 2014), pp. 288–299 (cit. on p. 131).

[172] Md Ashiqur Rahman, Sohel Anwar, and Afshin Izadian. "Electrochemical model parameter identification of a lithium-ion battery using particle swarm optimization method". In: *Journal of Power Sources* 307 (2016), pp. 86–97 (cit. on p. 131).

[173] Xiao Yang et al. "Parameter Identification of Electrochemical Model for Vehicular Lithium-Ion Battery Based on Particle Swarm Optimization". In: *Energies* 10.11 (2017), p. 1811 (cit. on pp. 131, 139).

[174] Daniele Peri, Matteo Diez, and Giovanni Fasano. "Comparison between Deterministic and Stochastic formulations of Particle Swarm Optimization, for Multidisciplinary Design Optimization". In: *12th AIAA Aviation Technology, Integration, and Operations (ATIO) Conference and 14*th *AIAA/ISSMO Multidisciplinary Analysis and Optimization Conference*. Aviation Technology, Integration, and Operations (ATIO) Conferences. American Institute of Aeronautics and Astronautics, Sept. 2012 (cit. on p. 133).

[175] Hiroki Kondo et al. "Influence of the active material on the electronic conductivity of the positive electrode in lithium-ion batteries". In: *Journal of the Electrochemical Society* 166.8 (2019), A1285–A1290 (cit. on p. 137).